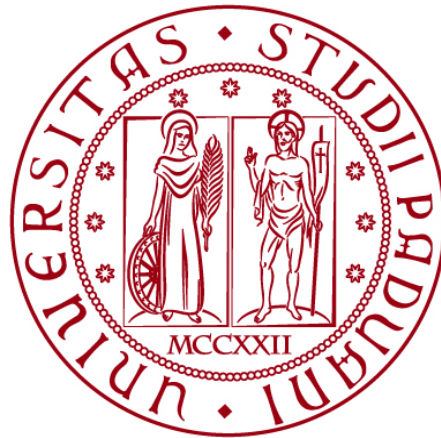


UNIVERSITÀ DEGLI STUDI DI PADOVA

DIPARTIMENTO DI INGEGNERIA CIVILE, EDILE E AMBIENTALE

Department Of Civil, Environmental and Architectural Engineering

Corso di Laurea Magistrale in Ingegneria Civile



Tesi di Laurea

Instability effects due to wind and snow combinations on transmission line systems

Relatore: Chiar.ma PROF. VALENTINA SALOMONI

Controrelatore: Chiar.mo PROF. FRANCESCO MAROTTI DE SCIARRA

Laureando: LUCA PESCARIN

Matricola: 1236709

ANNO ACCADEMICO 2021-2022

Preface

This Thesis embodies the outcome of the final project for Master's Degree in Civil Engineering at the University of Padua (Università degli Studi di Padova).

I am very thankful to my Supervisor at Unipd Structural research team, Professor Valentina Salomoni, who made this project possible thanks to her passion, perseverance and professionalism.

Hence, I would like to express my great gratitude to her contribute, accompanied by the appreciated and valuable help offered by Professor Francesco Marotti De Sciarra, who accepted to give his contribute in terms of personal valuation about this project.

A special gratitude is due to Alvisè Rossi, whose Thesis has given important input dataset for the analysis and several guidelines for a continuity project in terms of Galloping studying.

Lastly, my deepest gratefulness goes to my friends and my family, my parents and my sister, who constantly supported me during a difficult historical period of pandemic and international tensions, showing me always their faith, love, pride and motivation.

Padova, April 2022

Luca Pescarin

Abstract

In Civil Engineering, wind and snow effects are often solved according to static loads that hit our structures as an equivalent weight generating forces not dependent on time.

Galloping phenomenon is an example in which this assumption, most of times supported by legislation, is actually not valid anymore and incorrect. In fact, its non-linear dynamic effects are closely linked to several conditions that may yield to structural unstable behaviour.

Galloping mechanism is based on a steady state flow hitting an asymmetric profile, leading to swinging pressure load giving rise to vortex shedding. The alteration of the flow conditions generates dangerous vibrating conductors, mostly due to power interruptions, loss of revenue, system reliability and quality of service.

In transmission line systems, asymmetry is conceived by the icing and wet snow layers covering power networks in winter. Their accretion is not uniform and changes dynamic parameters of the span when hit by an airflow, recording a set of displacements that may be not acceptable.

This Thesis is focused on a Canadian transmission line, which was investigated by a Research Institute in 2018, now revisited in terms of aerodynamics and mechanical combinations leading to low frequencies and large amplitudes oscillations.

A presentation of Galloping and wind induced phenomena are given in Chapter 1, where also a detailed description of the case of study is proposed.

Chapter 2 has the purpose of pointing out literature and physical models offered on this field, highlighting in particular Den Hartog's instability criterion and Nigol's theory with Clarke. The dynamics response of the wire is conducted thanks to the linear theory of free vibrations of a suspended cable established by Irvine.

In Chapter 3 an input collection is presented with a statistical Canadian investigation, dealing with a climatic dataset in terms of wind velocity and icing load in its density. Moreover, a numerical validation for FEM model is described in both terms of aerodynamic and structural analysis.

Eventually, Chapter 4 highlights output results obtained by STRAUS7 and ANSYS software, with the aim to reproduce structural characteristics of the conductor on which the typical mechanical wire's behaviour is combined with a harmonic external forcing coming from the aerodynamic effect of wind and ice-shaped transverse section.

In the final Chapter 5 some conclusions are made on the base of possible resolution methods in order to contain sag displacements into an acceptable range.

Contents

Preface	I
Abstract	III
Contents	V
List of Figures	VII
List of Tables	XIII
Chapter 1	1
Introduction to Galloping	1
1.1 Historical background	2
1.2 Wind as a fluid body.....	6
1.2.1 Wind-induced instability phenomena	10
1.2.2 Flow-induced vibrations	12
1.3 Mechanism of Galloping	15
1.4 Case of study	18
Chapter 2	23
Dynamic approach to Galloping	23
2.1 Kinds of icing accretion.....	24
2.2 Ice accretion model.....	27
2.3 Hamilton’s Principle revisited	30
2.4 Den Hartog’s criterion	36
2.5 Torsional Galloping.....	40
2.5.1 Ampliation to two directions problems	43
2.6 Linear theory of cable free vibrations.....	46
2.6.1 Static Model.....	46
2.6.2 Dynamic Model	49
2.7 Non-Linear Analysis	54
2.7.1 Non-Linear Geometry.....	55
2.7.2 Non-Linear Material	56
Chapter 3	59
Data collection and Numerical Analysis	59

3.1 Climatic data set – Icing Load.....	60
3.1.1 Ice shape and eccentricity.....	62
3.2 Climatic data set – Wind Load.....	67
3.2.1 Wind tunnel test.....	69
3.3 Frequency-combining Analysis.....	72
3.4 Fluid dynamic model.....	78
3.4.1 Computational resolution methods.....	83
3.4.2 Boundary layer.....	86
3.5 Computational model.....	88
3.5.1 Validation model – Structural feature.....	89
3.5.2 Modes of vibration.....	96
3.5.3 Validation model - CFD.....	109
Chapter 4.....	119
Results and Discussion.....	119
4.1 CFD results.....	119
4.2 Structural results.....	138
4.3 Resolution Tools.....	151
Chapter 5.....	155
Conclusions.....	155
5.1 Summary.....	155
5.2 Future developments.....	157
References.....	159

List of Figures

- Figure 1.1 Examples of damages caused by galloping effects [4]
- Figure 1.1.1 Number of recorded events of galloping in German during 1979-1999 [5]
- Figure 1.1.2 Number of recorded events of galloping in German during 1979-1999 [5]
- Figure 1.1.3 Locations of galloping events in Germany during winter 1998-1999 [5]
- Figure 1.1.4 Number of galloping events related to conductor size and span length [5]
- Figure 1.1.5 Number of galloping events related to temperature and wind direction [5]
- Figure 1.1.6 Number of galloping events related to altitude (left) and wind speed (right) [5]
- Figure 1.2.1 Examples of friction effects on wind velocity trend [33]
- Figure 1.2.2 Evolution of a wake on a cylindrical body [33]
- Figure 1.3.1 Aerodynamic forces acting on an iced conductor [5]
- Figure 1.3.2 Conductors damage at clamp due to fatigue problems [4]
- Figure 1.3.3 Development of isobars in case of wind current hitting a cylindrical obstacle [7]
- Figure 1.4.1 Project localization [8]
- Figure 1.4.2 Location and geographical development of towers transmission line [1]
- Figure 1.4.3 Picture of a Y-frame steel tower of transmission line in Long Lake Hydro [1]
- Figure 1.4.4 OPPC section view [8]
-
- Figure 2.1 Oscillation modes of conductor bundles [3]
- Figure 2.1.1 Difference between Soft rime (left), Glaze (center) and Hard rime (right) [11]
- Figure 2.1.2 Example of Glaze ice in form of icicles growing at a roof rail [3]
- Figure 2.1.3 Example of Wet snow accretion on a transmission line [3]
- Figure 2.1.4 Dry ice growth (left) and wet ice growth (right) [3]
- Figure 2.1.5 Rime on a 22 kV overhead line in Voss, Norway, 18 April 1961 [6]
- Figure 2.2.1 Air streamlines and droplet trajectories around a cylindrical object [6]
- Figure 2.2.2 Collision efficiency [3]
- Figure 2.2.3 Collection efficiency [3]
- Figure 2.2.4 Accretion efficiency [3]
- Figure 2.2.5 Growth of rime ice (dry growth) on the left and growth of glaze ice (wet growth) on the right [6]
- Figure 2.3.1 Simple oscillator as dynamic reference model [30]
- Figure 2.3.2 The open control surface, closed and the open one [26]
- Figure 2.4.1 Geometry of a bluff section indicating lift and drag forces (L, D), relative angle of attack (α) and principal structural axes (x, y) [13]

- Figure 2.4.2 Trend set example of Den Hartog's coefficient [1]
- Figure 2.5.1 Torsional galloping reference model [20]
- Figure 2.6.1.1 Definition diagram for cable vibrations [21]
- Figure 2.6.1.2 Definition diagram for sagging cable [23]
- Figure 2.6.2.1 Longitudinal and vertical components of the first two anti-symmetric in plane modes [21]
- Figure 2.6.2.2 Graphical solution for first non-zero root of equation [21]
- Figure 2.6.2.3 Possible forms of the first symmetric vertical modal components [21]
- Figure 2.7.1.1 Large deflections effect on a cantilever beam
- Figure 2.7.1.2 Overlapping effects Principle [36]
- Figure 2.7.1.3 Non-linear relation between forces and displacements (material) [36]
-
- Figure 3.1.1 WRF4km and WRF500m models, respectively [1]
- Figure 3.1.2 In-cloud ice accretion for different wind directions [kg/m/hour] [1]
- Figure 3.1.3 Wet snow accretion wind rose [1]
- Figure 3.1.1.1 Typical Crescent shape; Wing shape; Wing shape and eccentric circle [12]
- Figure 3.1.1.2 Typical Eccentric oval shape; Eccentric round shape; Wing shape and round shape [12]
- Figure 3.1.1.3 Typical ice-shapes along the longitudinal direction of the wire [1]
- Figure 3.1.1.4 Accretion on a torsionally rigid stranded wire (axial growth) [10]
- Figure 3.1.1.5 Accretion on a stranded wire having low torsional stiffness (cylindrical-sleeve growth) [10]
- Figure 3.1.1.6 Accretion on a smooth wire having low torsional stiffness [10]
- Figure 3.1.1.7 Semi-elliptical model adopted for crescent shape profile [1] and evidence about the ice deposit on a cylinder-shape wire [11]
- Figure 3.1.1.8 Crescent profile for wet snow and rime ice accretion [1]
- Figure 3.1.1.9 Trend of ice weight according to eccentricities
- Figure 3.2.1 Wind speed distribution for wet snow [1]
- Figure 3.2.2 Excerpt from Eurocode about Factor of galloping instability [39]
- Figure 3.2.1.1 Set of increasing angle of attack adopted in the experiment [1]
- Figure 3.2.1.2 Representation of the Boundary layer wind tunnel test [1]
- Figure 3.2.1.3 Results of ice profiles made by specific machine [1]
- Figure 3.2.1.4 Schematic representation of the SDOF system [20]
- Figure 3.3.1 In-cloud icing types [1]
- Figure 3.3.2 Histogram of frequency analysis
- Figure 3.3.3 Frequency analysis of wet snow
- Figure 3.3.4 Joint frequency distribution function for wet snow

- Figure 3.3.5 Frequency analysis of soft rime
- Figure 3.3.6 Joint frequency distribution function for soft rime
- Figure 3.3.7 Frequency analysis of hard rime
- Figure 3.3.8 Joint frequency distribution function for hard rime
- Figure 3.4.1 Infinitesimal control volume and its Cartesian coordinates [29]
- Figure 3.4.1 Boundary layer around a cylinder creating vortex shedding [15]
- Figure 3.4.2 Excerpt from Eurocode 1 about Strouhal number for several cross sections [39]
- Figure 3.4.1.1 Representation of RANS concept both steady and unsteady [17]
- Figure 3.4.1.2 Prediction method for turbulent models [28]
- Figure 3.4.2.1 Law of the wall [18]
- Figure 3.4.2.2 Law of the wall [19]
- Figure 3.5.1.1 Representation of simple supported beam static scheme [22]
- Figure 3.5.1.2 Straus7 initial model
- Figure 3.5.1.3 Constitutive bond for Aluminum assumed
- Figure 3.5.1.4 Definition diagram for cable vibrations [21]
- Figure 3.5.1.5 Comparison between Finite Elements for self-weight in wire
- Figure 3.5.1.8 Parabolic curve model [34]
- Figure 3.5.2.1 Natural Frequency results for modes of vibration analysis
- Figure 3.5.2.2 Representation of the first eigenmodes corresponding to modes of vibration
- Figure 3.5.2.3 Normalized eigenmodes corresponding to the first four modes of vibration
- Figure 3.5.2.4 Graphical approach in solving transcendental equation for anti-symmetric motion
- Figure 3.5.2.5 First two Symmetric modes of vibration according to theoretical results
- Figure 3.5.2.6 First two Anti-symmetric modes of vibration according to theoretical results
- Figure 3.5.2.7 Plot of resonance function load by Straus7
- Figure 3.5.2.8 Resonance response simulation of the conductor
- Figure 3.5.2.9 Static solution for self-weight load
- Figure 3.5.2.10 Development of theoretical $R(t)$ in relation with numeric one
- Figure 3.5.2.11 Plot of non-resonance function load by Straus7
- Figure 3.5.2.12 Non-resonance response simulation of the conductor
- Figure 3.5.3.1 Geometry and measures of the numerical model domain
- Figure 3.5.3.2 Boundary Conditions naming conventions
- Figure 3.5.3.3 Implementation of Boundary Conditions plot on ANSYS software
- Figure 3.5.3.4 Overview of the air-domain mesh adopted and detail of the mesh-refinement around the wire region
- Figure 3.5.3.5 Drag coefficients for 2D transverse shape bodies [32]

- Figure 3.5.3.6 Plot of numerical model's convergence
- Figure 3.5.3.7 Trend of Drag coefficient obtained by the analysis
- Figure 3.5.3.8 Trend of Lift coefficient obtained by the analysis
- Figure 3.5.3.9 Trend of Moment coefficient obtained by the analysis
- Figure 3.5.3.10 Convergence of Drag coefficient trending to theoretical value of 1.17
- Figure 3.5.3.11 Contouring dealing with Pressure of wind flow [Pa]
- Figure 3.5.3.12 Contouring dealing with Velocity of wind flow [m/s]
- Figure 3.5.3.13 Contouring dealing with Turbulence of wind flow [m^2/s^2]
- Figure 3.5.3.14 Contouring dealing with Velocity's vectors [m/s]
-
- Figure 4.1.1 Aerodynamics coefficients related to Wind Tunnel Tests results for e025
- Figure 4.1.2 Aerodynamics coefficients related to Wind Tunnel Tests results for e050
- Figure 4.1.3 Aerodynamics coefficients related to Wind Tunnel Tests results for e100
- Figure 4.1.4 Aerodynamics coefficients related to Wind Tunnel Tests results for e150
- Figure 4.1.5 Aerodynamics coefficients related to Wind Tunnel Tests results for e200
- Figure 4.1.6 Comparison between the several trends of aerodynamic coefficients for all the eccentricities studied, in relation to the variation of angle of attack
- Figure 4.1.7 Contouring dealing with Pressure [Pa], Velocity [m/s] and Turbulence [m^2/s^2] respectively, for ice eccentricities of 150% (e150) and AoA=0°
- Figure 4.1.8 Contouring dealing with Pressure [Pa], Velocity [m/s] and Turbulence [m^2/s^2] respectively, for ice eccentricities of 150% (e150) and AoA=20°
- Figure 4.1.9 Contouring dealing with Pressure [Pa], Velocity [m/s] and Turbulence [m^2/s^2] respectively, for ice eccentricities of 150% (e150) and AoA=45°
- Figure 4.1.10 Contouring dealing with Pressure [Pa], Velocity [m/s] and Turbulence [m^2/s^2] respectively, for ice eccentricities of 150% (e150) and AoA=60°
- Figure 4.1.11 Contouring dealing with Pressure [Pa], Velocity [m/s] and Turbulence [m^2/s^2] respectively, for ice eccentricities of 150% (e150) and AoA=90°
- Figure 4.1.12 Contouring dealing with Pressure [Pa], Velocity [m/s] and Turbulence [m^2/s^2] respectively, for ice eccentricities of 150% (e150) and AoA=110°
- Figure 4.1.13 Contouring dealing with Pressure [Pa], Velocity [m/s] and Turbulence [m^2/s^2] respectively, for ice eccentricities of 150% (e150) and AoA=135°
- Figure 4.1.14 Contouring dealing with Pressure [Pa], Velocity [m/s] and Turbulence [m^2/s^2] respectively, for ice eccentricities of 150% (e150) and AoA=160°
- Figure 4.1.15 Contouring dealing with Pressure [Pa], Velocity [m/s] and Turbulence [m^2/s^2] respectively, for ice eccentricities of 150% (e150) and AoA=180°
- Figure 4.1.16 Trend of vortex shedding according to theoretical solution
- Figure 4.1.17 Comparison between vortex shedding frequencies with Wind Tunnel Results

Figure 4.2.1	Load cases combination
Figure 4.2.2	Sag oscillation and forces discharged to supports, for the case of e025
Figure 4.2.3	Sag oscillation and forces discharged to supports, for the case of e050
Figure 4.2.4	Sag oscillation and forces discharged to supports, for the case of e100
Figure 4.2.5	Sag oscillation and forces discharged to supports, for the case of e150
Figure 4.2.6	Sag oscillation and forces discharged to supports, for the case of e200
Figure 4.2.7	Dynamic amplification factor trend
Figure 4.2.8	DAF vs Mean velocity for a different case of study [38]
Figure 4.2.9	Dynamic amplification factor trend for forces on supporting towers
Figure 4.2.10	Axial forces discharged to towers for a particular case of cable rupture [37]
Figure 4.2.11	Comparison between self-weight configuration and e025-e200 cases
Figure 4.2.12	Comparison between self-weight configuration and other profile cases
Figure 4.3.1	Stockbridge damper
Figure 4.3.2	The two ways of motions of a Stockbridge [42]
Figure 4.3.3	Typical functionality of Stockbridge [42]

List of Tables

Table 1.1.1	Galloping report [5]
Table 3.1.1.1	Values dealing with transverse feature of every asymmetric shape and the corresponding values of weight per meter
Table 3.2.1	Wind speeds reference data [1]
Table 3.5.1.1	Illustration of Input-geometry Data
Table 3.5.1.2	Illustration of Input-rheological Data
Table 3.5.1.3	Parabolic curve model [34]
Table 3.5.1.4	Parabolic curve model [34]
Table 4.1.1	Calculation of characteristic length and vortex shedding frequencies
Table 4.1.2	Aerodynamic numbers and parameters according to Eurocode
Table 4.1.3	Aerodynamic critical speeds for ice shapes adopted
Table 4.2.1	Values of strain state for each case of ice eccentricity
Table 4.2.2	Comparison between icing load cases in terms of dynamic response

Chapter 1

Introduction to Galloping

Of all the wind induced motions of overhead transmission line conductors or other suspended cable systems, Galloping is the most significant one due to its economic and social relevance. Galloping is a low frequency, high amplitude wind induced vibration in both the horizontal and vertical directions of both single and bundle conductors, with a single or a few loops of standing waves per span [5]. Frequencies can range from 0.1 to 3 Hz and amplitudes from ± 5 to ± 300 multiples of the conductor's diameter [25]. It is not a forced oscillation, but a self-excited vibration phenomenon and it occurs when wind flow hits an asymmetry transverse profile and sectional shape, leading to a significant alteration of stream conditions such that a swinging pressure load is generated on the whole line. The reason for lack of symmetry for transverse section of wires, although they are always designed for circular cables, is due to ice or wet snow covered overhead power line in winter. Most of cases demonstrate that the presence of ice accretion on the conductor yields to make it aerodynamically unstable. The damages associated with galloping events can deal with power interruptions, loss of revenue, system reliability and quality of service, social impacts, impact on hospitals, on production industry and on population confidence and safety [5]. Figure 1.1 gives an example of fatigue damage to conductors and support towers.

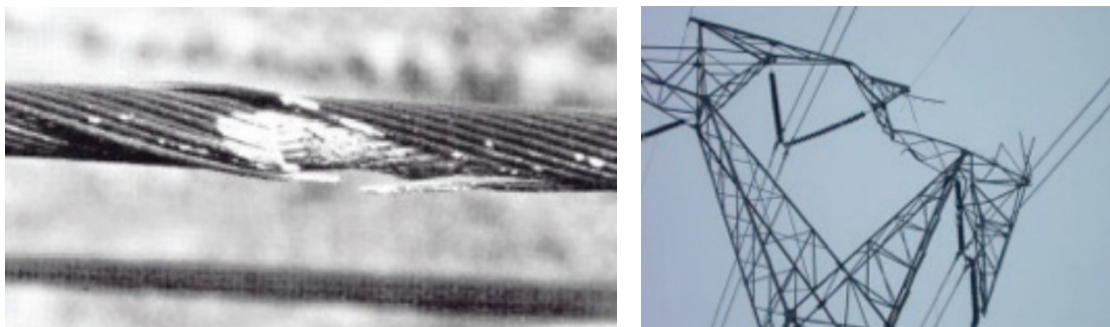


Figure 1.1 – Examples of damages caused by galloping effects [4]

The galloping of iced conductors has been a design and operating problem since early of 1900 [25]. Over the years, it has been the subject of several investigations and research programs, in order to understand its mechanisms and development [5]. The aim was always to design devices or take best initiatives with the purpose of avoid it or minimize its effects at least. In fact, Galloping is not just a natural phenomenon that impact our structures as well as other kinds of loads, both static and dynamic, but it may have very costly consequences. It has been estimated that the average annual cost of repairs to all Canadian utilities for galloping is about \$ 400,000 [25]. Moreover, several million dollars may be spent every ten years, when a significant case of galloping takes place and leads to catastrophic consequences. This means that galloping problem is quite far from being secondary in terms of engineering attention, since it deserves to be studied and faced with appropriate requirement.

1.1 Historical background

Although the galloping phenomenon would be considered as rare, it seriously may cover a key role in both terms of occurring and structural stability. Moreover, it is more frequent than we think, particularly in those countries where atmospheric precipitations in terms of snow and icing events are by no means indifferent. Even if it occurs just one time in a country not incline to this kind of natural events, it can be the trigger of a long and dangerous list of problems, as said, not only in the field of engineering. It is true so much so that during the last decades this theme led to several analytical investigations and researches, gone along with wind-tunnel tests and thus experimental field, across North America (Transmission line reference book 1979, Richardson 1981, Havard and Pon 1987, Rawlins 1988), in Europe (Dienne et. al. 1985, Gheorghita 1987, Lilien and Ponthot 1987), the USSR (Van'ko 1987), and in Japan (Sasaki et. al. 1986) [25].

Hence, can we really say Galloping is not so frequent? Table 1.1.1 shows a list of just some of several cases recorded around the world, where O means “No activity to report”, X means “Activity to report” and - means “No report”. It summarizes 192 verbal reports on galloping from 28 countries over the 20 meetings of TFG since 1988 [5]. North America was by far the most active with 38 reports followed by Norway with 18 reports, Belgium with 16 reports, the UK with 15 reports, Germany (East, West and United) with 14 reports and Japan with 12 reports [5]. Also Italy is involved in the list with its 10

reports that demonstrate Galloping can occur also where we might not expect. In fact, a 130 kV single conductor line was subjected to Galloping in the South of Italy and a tower collapsed, also due to a large magnitude of ice load [5]. Eventually, in 2002, six galloping events were reported on other bundle lines around Italy [5].

Table 1.1.1 – Galloping report [5]

Countries reporting at meetings listed	Paris 9/88	Opatija 10/89	Paris 8/90	Oslo 5/91	Paris 8/92	Montreal 9/93	Eveux 8/94	Madrid 9/95	Paris 8/96	Sandvi 10/97	Avignon 8/98	Chester 4/99	Sydney 10/99	Kolding 5/00	Quebec 5/01	Krakow 4/02	Moscow 5/03	Oslo 5/04	Bilbao 4/05	Rio de Janeiro 9/05	
Austria	X	-	-	-	-	-	-	-	O	-	-	-	-	-	-	-	-	-	-	-	O
Belgium	O	X	X	X	O	O	X	X	X	X	O	X	-	-	O	-	X	X	X	X	-
Brazil	-	-	-	-	-	-	-	-	-	-	-	-	-	-	-	-	-	-	-	X	X
Canada	X	X	X	X	X	X	X	X	X	X	X	X	-	X	X	X	X	X	X	X	X
Chile	-	-	-	-	-	-	-	-	-	-	-	-	-	-	X	-	-	-	-	-	-
China	-	-	-	-	-	-	-	X	-	-	-	-	-	-	-	-	-	-	-	-	-
Croatia (Yugoslavia)	X	X	X	-	O	-	-	-	-	-	X	-	-	-	-	-	-	-	X	-	-
Denmark	-	-	-	O	O	O	-	O	X	-	O	O	-	O	-	-	-	-	-	-	-
Finland	-	-	-	-	-	-	-	-	-	-	-	-	-	-	-	-	X	-	-	-	-
France	-	-	-	-	-	-	-	-	-	-	-	-	-	-	-	-	-	-	-	-	O
Germany (East&West)	X	-	X	X	X	-	X	X	X	X	X	X	X	O	-	-	O	-	X	-	-
Greece	-	-	O	-	-	-	-	-	-	-	-	-	-	-	-	-	-	-	-	-	-
Holland	O	X	O	O	O	X	-	-	X	-	O	X	-	-	-	-	-	-	-	-	-
Iceland	-	-	-	-	-	-	-	-	-	-	X	-	-	-	-	-	-	-	-	-	-
India	-	-	X	-	-	-	-	-	-	-	-	-	-	-	-	-	-	-	-	-	-
Iran	-	-	-	-	-	-	-	-	-	-	-	-	-	-	-	-	-	-	-	-	X
Italy	X	O	-	-	-	-	O	O	-	O	O	-	O	O	-	O	X	-	-	X	O
Japan	X	-	-	X	X	X	X	X	X	X	-	-	X	O	X	-	-	O	-	-	-
New Zealand	-	-	-	-	-	-	-	-	-	-	-	-	-	-	-	-	-	-	-	X	-
Norway	X	X	O	X	O	X	X	X	X	X	X	X	-	X	-	X	O	X	X	X	X
Poland	-	-	-	-	-	-	-	-	-	-	O	-	O	O	-	X	-	O	-	-	-
Russia (USSR)	-	O	O	-	X	-	-	-	-	X	X	-	X	X	X	X	X	X	O	-	-
South Africa	-	-	-	-	-	-	O	-	-	-	-	-	-	-	-	-	-	-	-	-	-
Spain	O	-	-	-	-	-	-	-	-	-	-	-	-	-	-	-	-	-	-	X	-
Sweden	-	X	O	O	-	X	X	-	X	-	-	X	-	X	O	X	-	X	-	-	-
Turkey	-	-	-	-	-	-	-	-	-	-	-	-	-	-	-	-	-	-	-	X	-
UK	X	X	O	X	O	O	-	X	O	-	O	X	-	X	X	-	-	O	O	X	-
USA	X	X	X	X	X	X	X	X	X	X	X	X	-	X	O	X	X	X	X	X	O

The cases of Germany and Japan appear particularly interesting, since an extensive collection of galloping data have been pursued. Germany covers a 20 years observation and recording of 46 events, most of which induced a short-circuit, meaning that the amplitudes of conductor motions were very significant. Figure 1.1.1 and Figure 1.1.2 show histograms dealing with the recorded events between 1979 and 1999, while Figure 1.1.3 gives a geographic representation of galloping instabilities recorded between 1998 and 1999.

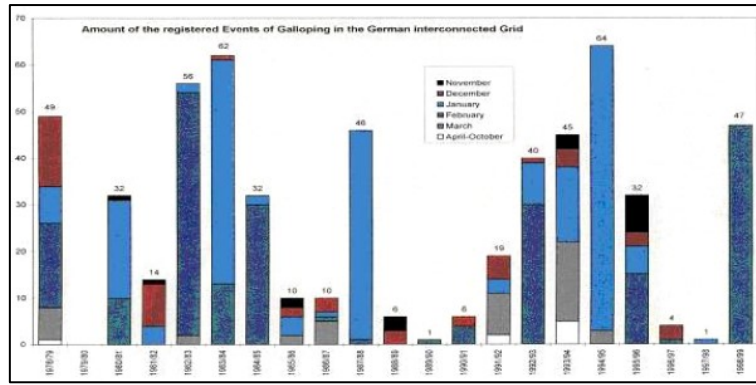


Figure 1.1.1 – Number of recorded events of galloping in German during 1979-1999 [5]

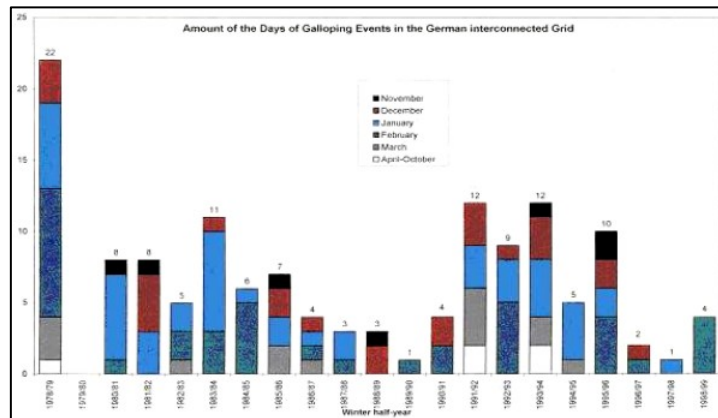


Figure 1.1.2 – Number of recorded events of galloping in German during 1979-1999 [5]

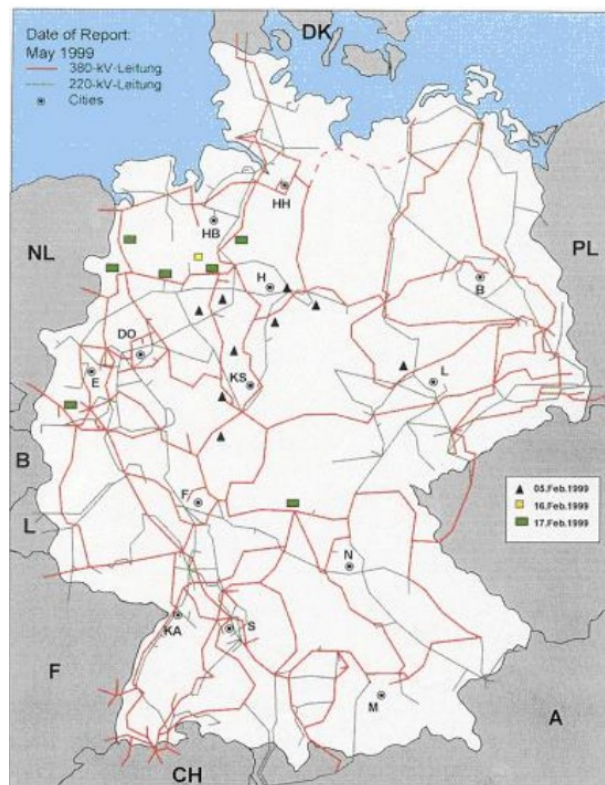


Figure 1.1.3 – Locations of galloping events in Germany during winter 1998-1999 [5]

The next images show recorded data about galloping events occurred in Japan, where interesting and detailed information were discovered and researched, in a total of 776 demonstrations. There are several places where this kind of instability was observed, in some cases also in a reference period of 30 years. Figure 1.1.4, Figure 1.1.5, Figure 1.1.6 show histograms dealing with the number of galloping events in dependence of conductor size of the transmission line, the span length, temperature, wind direction, altitude and wind velocity, respectively.

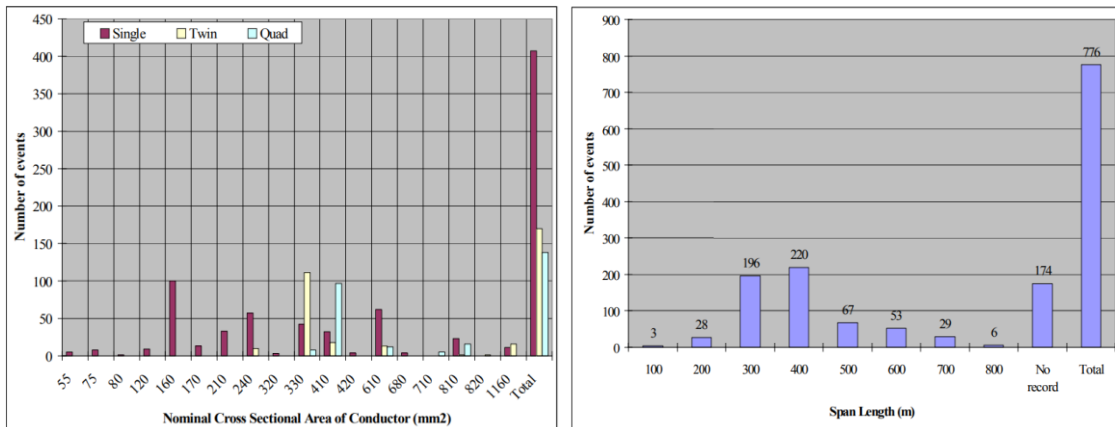


Figure 1.1.4 – Number of galloping events related to conductor size (left) and span length (right) [5]

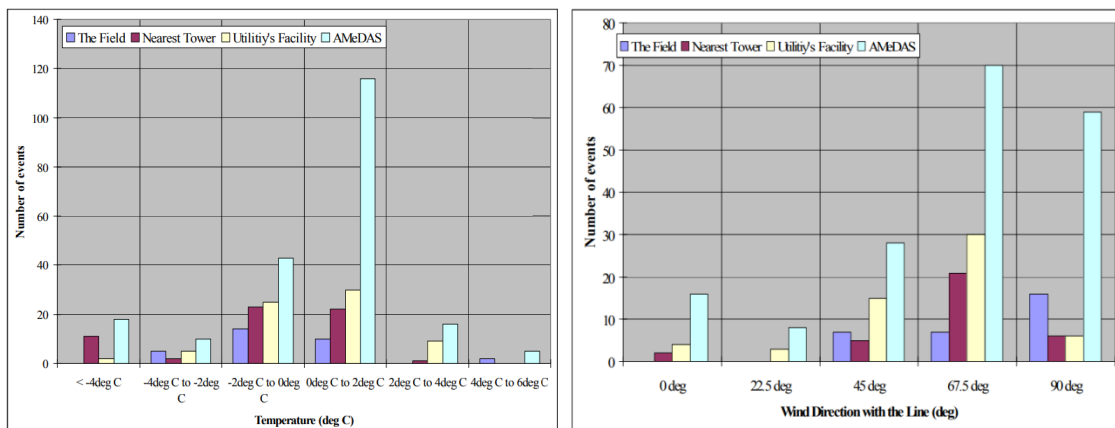


Figure 1.1.5 – Number of galloping events related to temperature (left) and wind direction (right) [5]

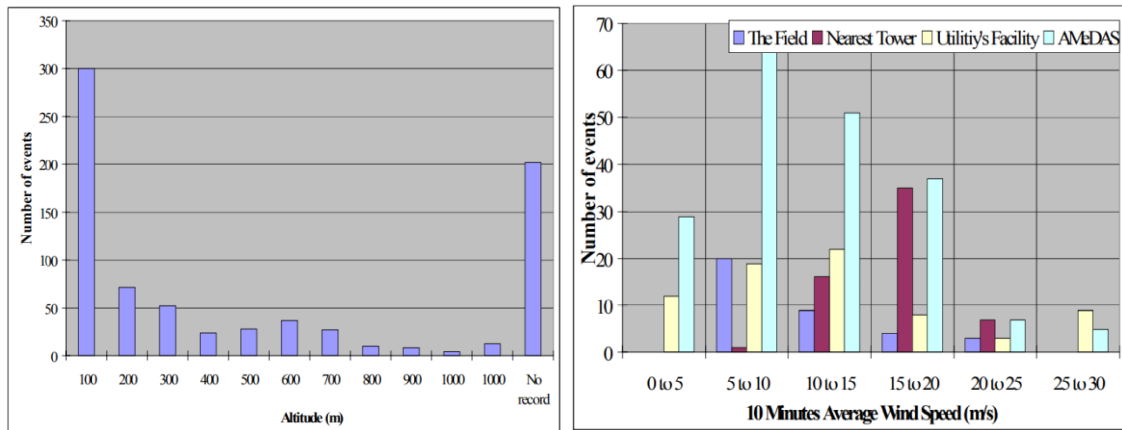


Figure 1.1.6 – Number of galloping events related to altitude (left) and wind speed (right) [5]

Several theories were carried out in order to explain and predict galloping problems, during the years. From Davidson, Den Hartog to Nigol or Chadha it seemed that a shortcoming governed between each position. This fact is explained by the biggest problem that really hits galloping theme, otherwise it is not fundamentally understood completely. Many attempts to create devices like Stockbridge dampers and their not complete satisfaction at engineers' eyes demonstrate that Galloping is still a debated problem. Furthermore, neither its development and occurring condition parameters are equally shared by the global scientific scene. Hence, the challenge for research in this field is open and requires to be probed widely with the purpose to give answers and safety network systems.

1.2 Wind as a fluid body

In civil engineering, wind is a horizontal motion of air particles induced by pressure gradients, mostly generated by thermodynamics and mechanical reasons [7]. Wind load is one of the major actions for structures dealing with high lightness and low stiffness, such as tensile structures, long bridges and steel buildings. On the other hand, the results of wind action are not so significant for the ones characterized by high weight and remarkable stiffness. In fact, what really cares in physical problems in this field is structure-wind interaction because of its deformability, which can amplify wind effects even leading to resonance phenomenon. Moreover, the wind load depends on the shape of the structure and it is strictly linked to friction coefficient of the ground, on which the turbulent development and trend of flow velocity depend on. Interaction between flow

and structure is such important and significant in this field that the best way to evaluate it is to reproduce the phenomenon during the so called Wind Tunnel tests, where measurements of wind velocity and its transformation in a pressure variable field can be calculated and recorded.

The response of a structure in relation to a wind load case is closely linked to its stiffness [33]: globally, rigid structures are more prone to generate vibrations along the longitudinal direction (*along-wind* behaviour), the same of the wind speed, while flexible ones are more prone to vibrate along the orthogonal direction (*across-wind* behaviour), which is highly dependent on vortex shedding and creation of Von Karmann street.

The force that triggers air motion is directly linked to pressure gradient and so its name is “*Gradient Force*”, thus defined:

$$P = -m \frac{1}{\rho} \frac{\partial p}{\partial n} \quad (1.2.1)$$

In absence of disturbing actions, the wind’s particles should blow perpendicularly to the isobars. These are subjected to deviations due to Earth’s rotation, irregularity of the ground and friction both internal and external. For this reason, wind particles are diverted through the *Coriolis Force*, thus explained:

$$F_c = 2m(v \times \omega) \quad (1.2.2)$$

Where m is the particle’s mass, v is wind velocity tangent to the Earth’s surface and ω is Earth’s rotation speed along Earth’s axis.

At low altitudes, the friction of air masses with the ground produces a slowdown in the movement itself [7]. This one is transmitted, due to the progressively decreasing with the share, until it becomes negligible ranging from a few hundred metres to a few kilometres. As Figure 1.2.1 reveals, the region where this kind of flow retardant effect is produced is called *Atmospheric Boundary Level*.

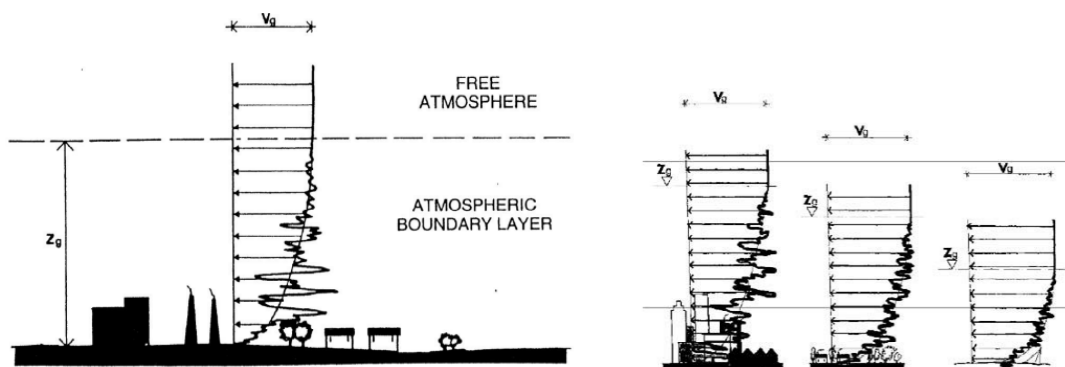


Figure 1.2.1 – Examples of friction effects on wind velocity trend [33]

From a civil engineering point of view, Atmospheric Boundary Level is extremely important as well as the knowledge of wind motions in this area, because it gives place to the type of air movement and phenomena in which our buildings are interested in. Civil constructions, in fact, are regarded as an obstacle for a stationary undisturbed wind current, and they lead to changes dealing with pressure and velocity distributions yielding to vortex risk generation. When the wind approaches the building, it gradually diverges, leading to a separation bubble or recirculation zone characterized by low velocity and high turbulence intensity [27]. Eventually, the dimension of this Boundary Level is once again linked to ground's roughness and gives birth to all the several literatures about it that generates *friction length* in legislations.

As can be noticed in Figure 1.2.1, the trend of velocity is very similar to the exponential one, thus the first model for wind velocity profile was the following one:

$$U(z_{g1}) = U(z_{g2}) \left(\frac{z_{g1}}{z_{g2}} \right)^\alpha \quad (1.2.3)$$

Where α is a coefficient depending on the roughness of the ground, while z_{g1} and z_{g2} are two different heights in relation to the base ground [33]. By assuming $z_{g2} = z_{ref}$ and by making z_{g1} possible to vary simply in z , the original Canadian trend of wind-speed profile can be obtained:

$$U(z) = U(z_{ref}) \left(\frac{z}{z_{ref}} \right)^\alpha \quad (1.2.4)$$

As a fluid, wind is interested in the classification of the fluid forces, that may be viscous or inertial. If the formers are called to maintain the order of fluid particles and thus a laminar nature of the motion, the latters have the role to generate turbulence and assign high values of cinematic energy. The ratio between them is represented by *Reynolds number*, thus expressed:

$$Re = \frac{\rho v^2 l^2}{\mu v l} = \frac{\rho v l}{\mu} \quad (1.2.5)$$

Where ρ is the flow density [about 1.25 kg/m^3], v is the relative velocity of the flow respect to the conductor, μ is the viscosity [about $1.81 \times 10^{-5} \text{ kg/m s}$] and l is the characteristic length [m], used to relate the spatial extension of the geometry to the fluid properties (it is equal to the diameter for cylindrical bodies, such as the wire in this case of study). Reynolds number has also the role to classify the flows in several regions; for instance, a cylindrical body is characterized by these evolution steps [33] and Figure 1.2.2 gives a representation of it.

- For $Re < 5$, the isobars follow the side of section;
- For $5 < Re < 40$, the flow separates at the end of the circle and a couple of symmetric vortexes are generated;
- For $40 < Re < 150$, the wake becomes unstable and vortexes start to detach in an alternating way (*Laminar Regime*);
- For $150 < Re < 300$, the wake starts to become turbulent;
- For $300 < Re < 3 \cdot 10^5$, the whole wake is completely turbulent (*Subcritical Regime*);
- For $3 \cdot 10^5 < Re < 3.5 \cdot 10^6$, the vortex shedding is not observable anymore (*Critic Regime*);
- For $Re > 3.5 \cdot 10^6$, the vortex shedding appears once again but inside of a highly turbulent wake (*Supercritical Regime*).

The frequency of vortex shedding follows the *Strouhal number*, thus defined:

$$St = f \frac{D}{U} \quad (1.2.6)$$

Where f is the frequency of vortex shedding [Hz] and D the characteristic length [m]. However, Strouhal number and other several fluid dynamics concept will be resumed in Subsection 3.4.

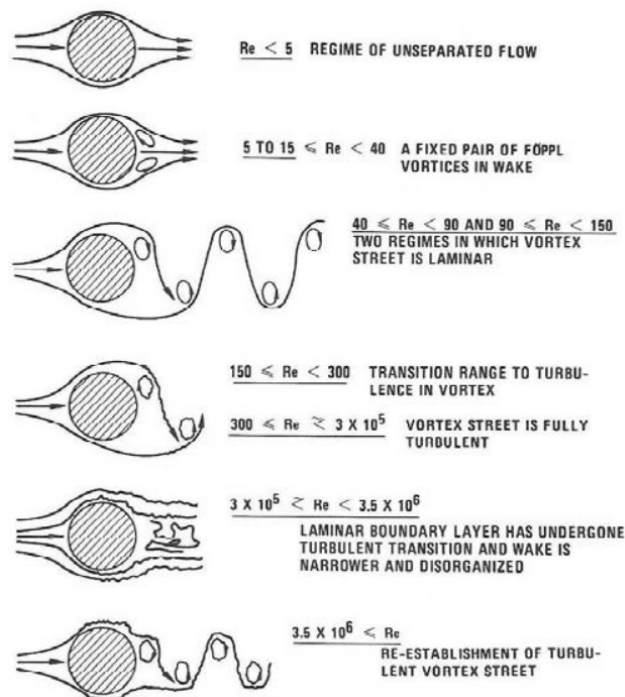


Figure 1.2.2 – Evolution of a wake on a cylindrical body [33]

1.2.1 Wind-induced instability phenomena

Many times engineers solve wind problems in a simplified way, based on the set of a statically equivalent system for wind global force hitting the structure. It is clear that a such approach gets lost all fluid dynamics hitches and fluid-structure interaction, dropping the complex problem into just a force balance one. Aero-instability challenges, instead, requires to set up a deeper kind of analysis, since several problems come from vortex shedding and divergence that basically link the two fields of mechanics world, structural and fluid. Moreover, this subject has been known to man since ancient times: the vibration of a wire at its natural frequency in response to vortex shedding was known in ancient Greece as Aeolian tones [24].

During the last decades several scientific researches dealing with aeroelastic and aerodynamics behaviour of cylindrical objects inserted in a fluid current were carried out. The interest of this theme gradually developed more and more because of lot of structural problems, starting from the trend of new buildings projects making these ones slender and thus more susceptible to vibrations. Other actual reasons yielding to an always greater interest for fluid dynamic interaction are the following:

- Use of building materials in extreme conditions
- Structures characterized by high lightness and low stiffness
- Poorly dumped structures
- The development of advanced nuclear power reactors

In a broad sense, flow-induced vibration covers all topics on the dynamic responses of structures immersed in fluid, containing fluid, or subjected to external flow [24].

Typical aeroelastic phenomena that focused engineers' attention on this field are now presented:

- Vortex shedding
- Galloping
- Torsional divergence
- Flutter

They are all treated differently in literature, even if quite similar or linked each other.

Vortex shedding

Vortex shedding is particularly important in the presence of slender structures and cylindrical buildings. Vortex-shedding occurs when vortices are shed alternately from

opposite sides of the structure. This gives rise to a fluctuating load perpendicular to the wind direction. Structural vibrations may occur if the frequency of vortex-shedding is the same as a natural frequency of the structure. Typically, the critical wind velocity is a frequent wind velocity indicating that fatigue, and thereby the number of load cycles, may become relevant [39]. The critical wind velocity for bending vibration mode- i is defined as the wind velocity at which the frequency of vortex shedding equals the natural frequency (mode i) of the structure or the structural element [39] and it is given by the following expression suggested by Eurocode 1:

$$v_{crit,i} = \frac{b n_{1,y}}{St} \quad (1.2.1.1)$$

Where b is the reference width of the cross-section at which resonant vortex shedding occurs and where the modal deflection is maximum for the structure or structural part considered; $n_{1,y}$ is the natural frequency of the considered flexural mode i of cross-wind vibration; St is the Strouhal number, as defined before.

However, the effects of vortex shedding need not to be investigated if the value of critical wind velocity is bigger than 1.25 times the medium velocity ($v_{crit,i} > 1.25 v_m$), defined as the characteristic 10 minutes mean wind velocity specified at the cross section where vortex shedding occurs, described and specified by Eurocode.

Galloping

Galloping swings are a typical phenomenon of aerodynamics instability for slender structures having non-circular section. In correspondence with so called critical speed, large amplitude oscillations can occur frequencies much lower than those corresponding to the vortex shedding. It happens when the shape of the object or torsional movement might cause asymmetry of the flows oscillating pressure. Thus it amplifies the initial motion of the body, giving rise the so called galloping swings crisis. It is usually found in tall buildings, lighting poles and overhead lines when the formation and accretion of ice in winter generates a section different from the circular one.

Torsional divergence

Torsional divergence is the one that is not characterized by oscillations. It consists of a static instability linked to lack of stiffness for the system. It's quite similar to the buckling phenomenon in steel structures. It is usually found in structures having an aerodynamic profile or bridge deck in which as the speed increases, the torsion increases

more and more. Thus the bridge section rotates until it diverges because torque is no longer balanced by torsional stiffness, so the bridge collapses.

Flutter

Flutter is a typical example of self-excitation structures, characterized by a significant torsional component. This kind of crisis is associated with dumping capacity of structures. In fact, wind load increases the quantity of energy of the structure, leading to an ampliation of motion. This phenomenon affects typically bridges with large spans or very light ones, such as walkways, as they respond with first torsional way of vibrating. The structure, subjected to a wind and due to asymmetries on the detachment of vortices, begins to swing vertically and torsionally absorbing energy from the wind and expanding its torsional oscillation until collapse. A famous example of this kind of instability effects is Tacoma Narrow bridge; a suspension bridge with span of 850 metres, built in 1940 and collapsed just 4 months later. The collapse occurred a few hours after the induced vibrational process established by a constant wind of 65 km/h. It induced torsional oscillations of inexorably increasing amplitude in central span, reaching over 45 degrees above the horizontal, thus breaking one of the cables which immediately changed the dynamic behaviour of the bridge until it broke.

1.2.2 Flow-induced vibrations

As it is regarded as a flow with its own viscosity and density, wind deals with fluid mechanics and fluid dynamics when it hits a manufacture. Flow-induced vibration is a term to denote those phenomena associated with the response of structures placed in or conveying fluid flow [24]. In these terms, the study around wind-induced behaviour is closely linked to all features yielding to structural and fluid mechanics.

There are several behaviours as response of a structure, when it is immersed in a flowing fluid. First of all, it experiences a distributed force on which displacements are based, creating a static or dynamic reaction. In fact, according to [24], the structure may: deflect statically; become unstable by divergence in flow; resonate with periodic excitation of the flow; respond to random fluid excitation; be subjected to dynamic instability by flutter.

A computational classification is now reported, carting all the possible structural behaviour just presented.

Several mathematical models and approaches were carried out during the years, in order to predict and control structural response at flow excitation, but one stands out for its significance on a practical and intuitive field. This one is based on recording and studying the macroscopic way to respond in terms of large displacements, and thus placing attention on instability conditions with corresponding parameters yielding to it.

If structural displacements components were defined by a column vector $\{\mathbf{Q}\}$, then the derivative vectors $\{\dot{\mathbf{Q}}\}$ and $\{\ddot{\mathbf{Q}}\}$ would define velocity and acceleration of the system, respectively.

On this way, the interaction between fluid and structure can be described by the following equation:

$$[\mathbf{K}]\{\mathbf{Q}\} + [\mathbf{C}]\{\dot{\mathbf{Q}}\} + [\mathbf{M}]\{\ddot{\mathbf{Q}}\} = \{\mathbf{G}\} \quad (1.2.2.1)$$

The equation itself could be developed as follows:

$$[\mathbf{K}_S + \mathbf{K}_F]\{\mathbf{Q}\} + [\mathbf{C}_S + \mathbf{C}_F]\{\dot{\mathbf{Q}}\} + [\mathbf{M}_S + \mathbf{M}_F]\{\ddot{\mathbf{Q}}\} = \{\mathbf{G}\} \quad (1.2.2.2)$$

where $[\mathbf{M}]$ is the mass matrix, including structural mass \mathbf{M}_S and added fluid mass \mathbf{M}_F ; $[\mathbf{C}]$ is the damping matrix, including structural damping \mathbf{C}_S and fluid damping \mathbf{C}_F ; $[\mathbf{K}]$ is the stiffness matrix, including structural stiffness \mathbf{K}_S and fluid stiffness \mathbf{K}_F ; $\{\mathbf{G}\}$ is the excitation forces, including vortex shedding, turbulence, etc [24].

On a general consideration, the three matrices are dependent on displacements $\{\mathbf{Q}\}$, thus the non-linearity of the problem is evident. However, in many engineering problems, this dependence can be neglected.

By pre-multiplying $\{\dot{\mathbf{Q}}\}^T$ the two terms on the left and on the right in Equation (1.2.2.2) and establishing the symmetric and antisymmetric components of the matrices studied [24], it can be written as follows:

$$[\mathbf{M}_1] = \frac{1}{2}([\mathbf{M}] + [\mathbf{M}]^T) \quad (1.2.2.3)$$

$$[\mathbf{C}_1] = \frac{1}{2}([\mathbf{C}] + [\mathbf{C}]^T) \quad (1.2.2.4)$$

$$[\mathbf{K}_1] = \frac{1}{2}([\mathbf{K}] + [\mathbf{K}]^T) \quad (1.2.2.5)$$

$$[\mathbf{M}_2] = \frac{1}{2}([\mathbf{M}] - [\mathbf{M}]^T) \quad (1.2.2.6)$$

$$[\mathbf{C}_2] = \frac{1}{2}([\mathbf{C}] - [\mathbf{C}]^T) \quad (1.2.2.7)$$

$$[\mathbf{K}_2] = \frac{1}{2}([\mathbf{K}] - [\mathbf{K}]^T) \quad (1.2.2.8)$$

The final separated description of the problem is given by the Equation thus defined:

$$\begin{aligned} & \{\dot{\mathbf{Q}}\}^T [\mathbf{K}_1] \{\mathbf{Q}\} + \{\dot{\mathbf{Q}}\}^T [\mathbf{C}_2] \{\dot{\mathbf{Q}}\} + \{\dot{\mathbf{Q}}\}^T [\mathbf{M}_1] \{\ddot{\mathbf{Q}}\} \\ & = \{\dot{\mathbf{Q}}\}^T \{\mathbf{G}\} - (\{\dot{\mathbf{Q}}\}^T [\mathbf{K}_2] \{\mathbf{Q}\} + \{\dot{\mathbf{Q}}\}^T [\mathbf{C}_1] \{\dot{\mathbf{Q}}\} + \{\dot{\mathbf{Q}}\}^T [\mathbf{M}_2] \{\ddot{\mathbf{Q}}\}) \end{aligned} \quad (1.2.2.9)$$

Equation (1.2.2.9) governs the interaction challenge and it is used to point out the flow-induced vibration mechanisms and classification. The right terms are representative of the non-conservative components of the forces, since they give a non-zero value for network resultant when integrated over a closed path through the spare linked to displacements $\{\mathbf{Q}\}$ [24]. On the other side, the terms on the left are representative of conservative components of the forces, since they give rise to a zero work resultant over any closed path.

As explained before, in relation to the different parameters playing in this field, the structural response can be classified consequently and following lines show the split into static and dynamic behaviour, with the respective instability condition.

Static behaviour

- Static displacement: Structural deflections are induced by steady-state fluid conditions, characterized by a frequency much lower than the structural natural one. The formulation of displacement in this case is written below:

$$\{\mathbf{Q}\} = [\mathbf{K}]^{-1} \{\mathbf{G}\} \quad (1.2.2.10)$$

- Static instability (divergence): Instability in this case arises due to fluid stiffness and it is belonging to static field. Typical instance for static instability is buckling phenomenon, in particular with pipes systems. The values within critical velocity of the flow ranges in order to generate large unstable displacements are derived by solving the following condition:

$$Det([\mathbf{K}_S] + [\mathbf{K}_F]) = 0 \quad (1.2.2.11)$$

Dynamic behaviour

- Dynamic response: Structural response is influenced by a periodic excitation, born from several fluid phenomena, such as vortex shedding or turbulence. Once noted the excitation, the structural configuration is directly derived.

- Dynamic instability: This field encloses the set of all that high velocities of the flow, causing different kinds of dynamic instabilities, according to the predominant term in Equation (1.2.2.9) [24]:

- *Fluid-damping-controlled instability (single mode flutter)*: A negative dumping is caused by fluid dynamic forces and dominant terms are referred to symmetric matrix $[C_1]$;

- *Fluid-stiffness-controlled instability (coupled-mode flutter)*: It is the so called coupled-mode flutter, since a minimum of two modes of vibrations are necessary for it. The dominant terms in governing equation are linked to antisymmetric matrix $[K_2]$.

Correlated to the two types of mode flutter, there may be a parametric or a combination resonance if the fluid flow has a periodic function along time:

- *Parametric resonance*: It occurs when the period of the flow is a multiple of one of the natural frequencies of the body;

- *Combination resonance*: It occurs when the period of the flow is a result of sum or difference divided by an integer number coming from the natural frequency of the body.

However, all the mechanisms just explained may occur at the same time, and thus another kind of interaction in terms of static or dynamic instability modes might take place.

1.3 Mechanism of Galloping

Overhead transmission line conductors are subjected to all the types of unsteady wind-induced loading presented before. In this kind of structural elements, it is very significant the role of both wind and ice or wet snow accretion and their interaction together. In fact, if Aeolian vibrations are small amplitude and high frequency oscillations induced by the wind flow and the vortex shedding, the ice accretion can induce to a larger quantity of weight and an increase of internal tensional estate. This gives birth to a variation of the oscillation frequency, which may be not covered by the capacity of structure as it was designed for. For the majority of cases observed, it occurs on iced-accreted conductors and in particular it causes several important structural damages. These one are also linked to dynamic loads, which can lead to fatigue damages, more dangerous features of this phenomenon. Figure 1.3.2 shows this kind of damage.

Galloping motions require an asymmetric cross section of the body, which expose this one to aerodynamic instability. In conductors of transmission line systems, this kind of section is usually provided by atmospheric icing, since as ice builds up, mainly on the top and windward side of the wire, the circular shape is modified yielding to aerodynamically unstable structure.

Complex interactions of aerodynamic instability and iced overhead transmission lines can produce lift and drag force on conductors, as Figure 1.3.1 highlights, with consequently modification of the flow pattern and pressure distribution along the wire. The aerodynamic forces and mass effects also increase with the thickness of the ice layer.

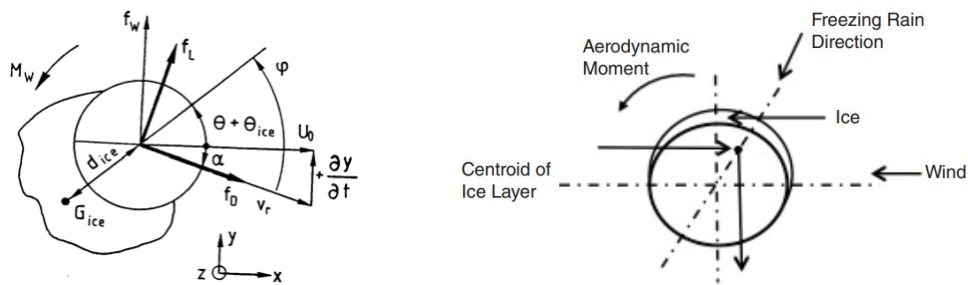


Figure 1.3.1 – Aerodynamic forces acting on an iced conductor [5]

The galloping motion of the conductor can be seen as standing waves or traveling waves or a combination of both [4]. The standing waves consist of forced nodes at the support structure and intermediate nodes spaced along the span at intervals that depend on the particular natural frequencies at which the conductor is vibrating [4].

From an energetic point of view, the amplitude of galloping vibrations are the result of continuous balance between energy obtained by the wind flow and the one dissipated in oscillation thanks to damping capacity of the structure. Most of cases reported demonstrate that this kind of dynamic instability occurred in relation with wet snow and freezing rain. This yields to the thought on which Galloping may set up in conditions of temperatures between -5°C and 2°C [1], as will be explained in Chapter 2, dealing with kinds of ice accretion.

Moreover, the thickness of snow or ice layers formed which cause the instability is often moderate and it has never exceeded the value of two times the conductor diameter [1]. However, Galloping can occur even with very low values of ice thickness of the order of millimeters.

Eventually, even the range of wind velocities at which the instability can occur is limited [1]. In fact, many facts recorded a wind speed never greater than 25 m/s. The main factor in the field of blowing wind that contribute mostly is the angle of attack. This one is

closely linked to the wire shape, because the trigger of instability depends on the ice eccentricity formed by the layers accreted and thus the most critical directions along which the wind can cause the phenomenon.



Figure 1.3.2 – Conductors damage at clamp due to fatigue problems [4]

From a hydraulic and aerodynamic point of view, if a steady stream current hits an obstacle that is not a classic building but a cylindrical one, representing for instance the transverse section of cables in transmission lines, several considerations can be made. Figure 1.3.3 shows what happens to isobars in this case of hitting.

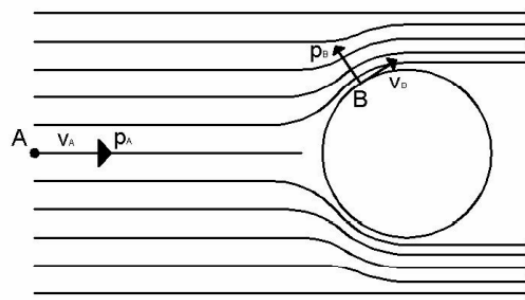


Figure 1.3.3 – Development of isobars in case of wind current hitting a cylindrical obstacle [7]

Where A and B are a point on the undisturbed zone and a point lying on the obstacle, respectively.

The *Bernoulli Theorem* admits the following formulation dealing with energy storage:

$$p + \rho \frac{v^2}{2} = \text{const} \quad (1.3.1)$$

$$p_A + \rho \frac{v_A^2}{2} = p_B + \rho \frac{v_B^2}{2} \quad (1.3.2)$$

$$p_A - p_B = \frac{\rho}{2} v_A^2 \left(1 - \frac{v_B^2}{v_A^2} \right) = C_p \rho \left(1 - \frac{v_B^2}{v_A^2} \right) \quad (1.3.3)$$

where C_p is called shape coefficient and it ranges in terms of time and space, in particular with swirling areas. It can assume values both positive and negative, in particular for the cases of vortex shedding, where it continues to vary in its sign due to alternating formation of vortexes that gives a highly turbulent nature to the phenomenon. Its value

depends actually on the aerodynamics of the body around which the steady flow runs. In other words, it deals with body's shape and the position of the reference point studied.

Wind behaviour is strictly related to the presence of obstacles and Reynolds number, that determine the permanence or transition for Boundary Layer, as Subsection 3.4 will point out. Passed laminar motion condition, a system of vortexes is created, dissipating the exceeded energy that was not spent on viscous deformation. The magnitude of vortex divergence is governed by Reynolds number.

When a vortex breaks off, an orthogonal force on the wind direction is created. This fluid forcing has the characteristic to be pseudo-harmonic and changes in dependence of the body's orientation [33]. If the structural body swings, then its position changes in time and thus also the fluid forcing. If this development tends to increase the amplitude of body's oscillations, the structural behaviour becomes unstable and it diverges.

As bigger is the flow velocity, as bigger is the frequency of vortex shedding [7], which gradually approaches the natural frequency of the structure yielding to resonance instability and structural divergence. In these terms, since the cyclic arrangement of the mutual interactions between fluid motions and structural vibrations, the problem is strongly non-linear and dynamic.

1.4 Case of study

This thesis is based on a real case of study, that allowed to analyze galloping phenomenon with a realistic approach in terms of both values and utility. The research is closely linked to Alvisè Rossi's Thesis, who completed the Double Degree in Master Science of Civil Engineering at the University of Padua and the Technical University of Denmark in 2018, discussing a project dealing with Galloping instability and leaving future development direction lines of his work. This one was conducted at the WindEEE Research Institute in London Ontario, Canada, from January 2018 until June 2018 [1].

Thus his project is here reworked with similar but different dataset and thorough, in order to extend the analysis set up during the foreign permanence in collaboration with the University of Denmark, also on the base of Alvisè's Chapter 5 in which he explains what could be the main directions towards which to orientate a further development of the project [1].

It is clear that all the information needed to resume a complete and further analysis are gradually presented and associated to new developments proposed. For this reason, input data are extremely important and necessary in order to create a real field of application and comparison in terms of results of the analysis.

The work deals with the power network designed of a 138 kV transmission line near Stewart in British Columbia, Canada, as Figure 1.4.1 shows. This line connects the Long Lake hydroelectric generating station to the BC Hydro network [8]. The structure has been operating since 2013 and it crosses an 800-metre-wide river, a mountainous terrain from 50 m to 1,500 m and several valleys [8], for a total length of 10 km.

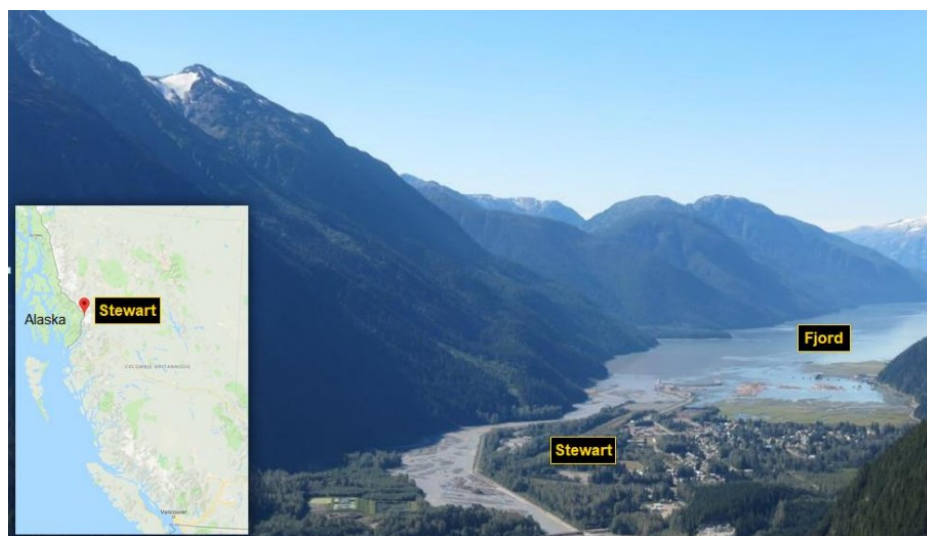


Figure 1.4.1 – Project localization [8]

Since it consists of the unique power line transmission for a local mine site and being the energy deliver of the BC Hydro [1], it has a significant importance in terms of both social and economic fields. Following Figure 1.4.2 highlights the geographical area in which the site arises and a scheme of power towers positions along the line way.

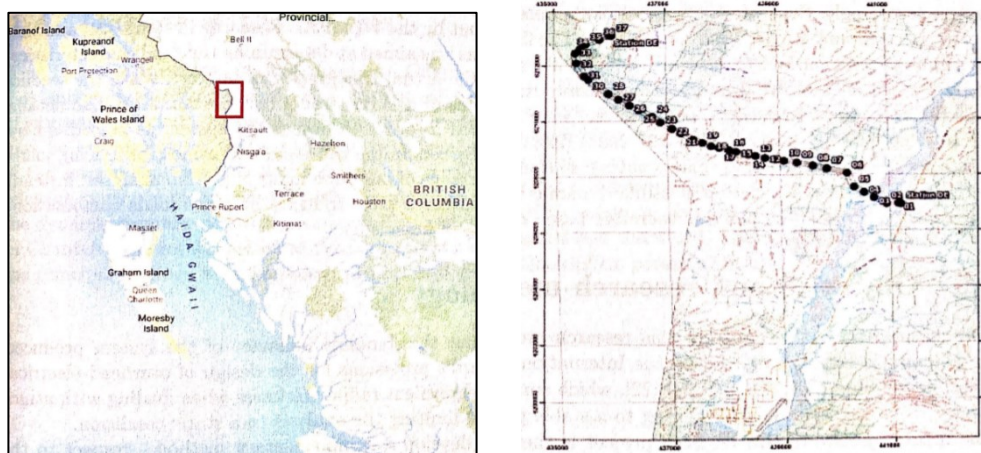


Figure 1.4.2 – Location and geographical development of towers transmission line [1]

Figures show that the line develop thanks to 37 towers composed by single pole Y-frame steel structure and variable height, placed at different altitudes and with relative spans of variable length. These towers are supported by a steel structure foundation with post tensioned anchors [8]. The maximum value of the span is 509 m, dealing with towers number 5 and number 6, while the minimum one is 35 m, at the final span. The mid span sag ranges between 2 m and 28 m, while the tallest tower is 44 m height, number 31, and the lowest one is 20.20 m, number 12. Figure 1.4.3 gives a representation of what just described above.

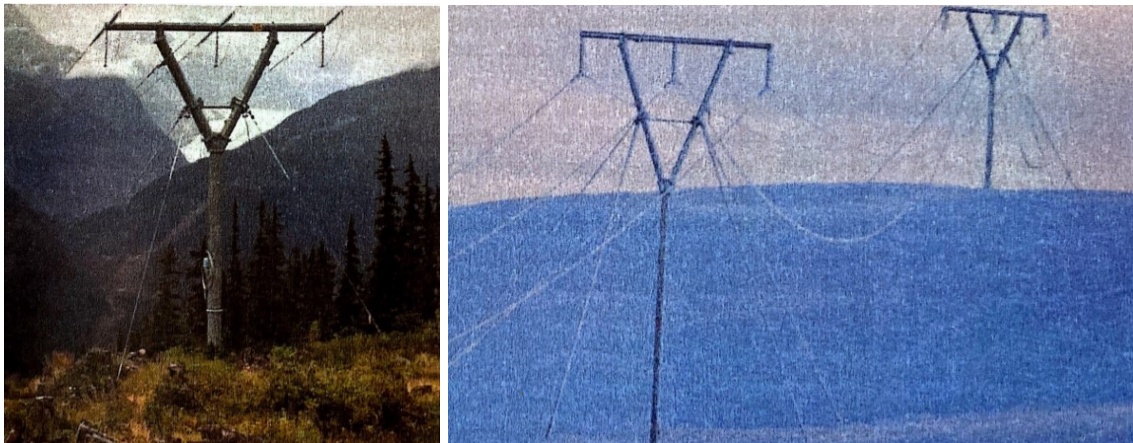


Figure 1.4.3 – Picture of a Y-frame steel tower of transmission line in Long Lake Hydro [1]

Eventually, the conductor is composed by a single aluminium clad steel wire and it is characterized by a diameter of 23.55 mm. An optical ground wire (OPGW) cable was used, then replaced by the innovative optical phase conductor (OPPC) technology, which permitted to reduce structural loads in a significant way thanks to its properties. An OPPC is a conductor similar to OPGW, designed to be energized and to transport both electricity and telecom data [8]. The OPPC used for this project was made of aluminium-clad steel strands, one of which is replaced by a stainless steel tube containing fibres [8]. Unlike OPGW, where the cable is not carrying a continuous current, OPPC is energized along high-voltage power lines [8]. This OPPC section view is presented in Figure 1.4.4:

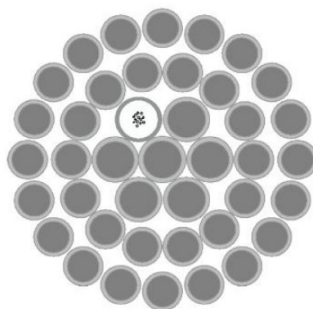


Figure 1.4.4 – OPPC section view [8]

It is clear, on the base of its position and physical development, the transmission line system is highly exposed to critic atmospheric and climatic conditions, due to strong wind flows and significant magnitude of icing accumulation in the site.

Separate loads assessment were established for each tower and span, through studying wind characteristics in terms of physical and numerical models. Then, a second study dealing with the combination of both wind and ice accretion was made thanks to a WRF model. Wind and atmospheric iceloads were combined with aim to achieve the worst scenario with an occurrence of one time in 50 years. However, these design values were the results of static approach analysis and thus the power line system is not calculated in reference of a dynamic behaviour and time-dependent loads combinations. Hence, Alvise carried out a thesis that could take care of this gap of knowledge [1] and here the work is developed with the aim of capturing effects on the structural system produced by the coupling behaviour of different types of motions during the galloping instability.

Chapter 2

Dynamic approach to Galloping

Several motions can be ensued by galloping instability. All of them may be grouped and divided into translational and rotational. The former leads to vertical galloping and represents the greatest part of this phenomenon's events, while the latter leads to torsional galloping. Of course, the real oscillations are the result of the composition of both vertical and torsional motions, both in plane and out of plane of line. Figure 2.1 gives an example of how transmission line system may respond in real conditions.

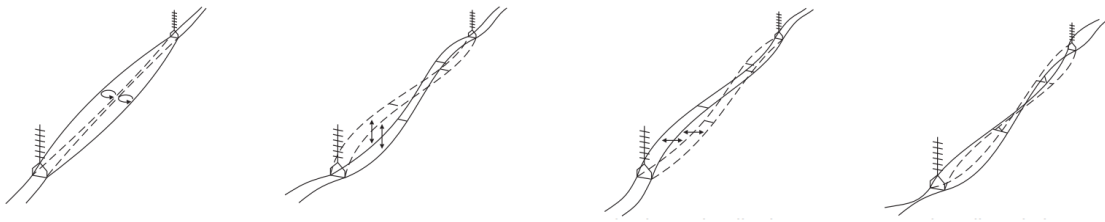


Figure 2.1 – Oscillation modes of conductor bundles [3]

Although the figure above shows several out of plane vibrating modes, in this Thesis only the vertical in-plane galloping instability will be investigated, according to Den Hartog's theory subsequently explained. The choice to pay attention to just this kind of vibration behaviour is linked to the fact that vertical oscillations are more frequent and dangerous than torsional or out-of-plane ones. Furthermore, this is the most characterization for lines made by a single conductor, as the case of study examined.

For the reasons just explained, the need to investigate the dynamic behaviour of a power network. The aim of this Section is in fact to give a report of the several ice and snow events in which transmission lines are interested in, since galloping phenomenon starts with it as said, and eventually to describe the dynamic characterization of a single wire line, starting from several analytical considerations and developments in literature.

2.1 Kinds of icing accretion

Atmospheric icing is a kind of terminology used to define natural processes linked to the change of form of the water that freezes and adheres to a body exposed to the air. This type of meteorological phenomenon may threaten classical structures as well as infrastructure systems, such as power transmission lines. Its magnitude and intensity can vary in relation with geographic conditions as distance to the coast, altitude above sea level and the local topography, in addition to high precipitation and low temperatures. As said before, the ice accretion plays a central role in galloping effects due to its contribution in varying the transverse section of the wire, which exposes this one to aerodynamically instability. There are several conditions that lead to different types of ice and snow deposits. Icing and snow accretion are apparently quite similar, but there are several differences between them in terms of temperature, forms and meteorological conditions that make the natural precipitation possible. First of all, icing is the result of the repeated impingement and freezing of fog particles transported by the wind on an object [11]. It requires liquid-water droplets and strong winds [11]. On the other hand, snow accretion is the result of the continuous of wet snow near 0°C [11]. It requires snowflakes and weak winds [11].

However, from an engineering point of view it is resolved as a state of both static and dynamic load that can be catalogued into classes. A classification of icing forms has been proposed in Technical Brochure number 179, by a CIGRE working group (CIGRE TB179, 2000) [5], and Figure 2.1.1 gives a graphical distinction of classification. They divided icing into the following six different types:

Precipitation icing

- Glaze (Freezing rain)
- Wet snow
- Dry snow

In-cloud icing

- Glaze due to super cooled cloud/fog droplets
- Hard rime
- Soft rime

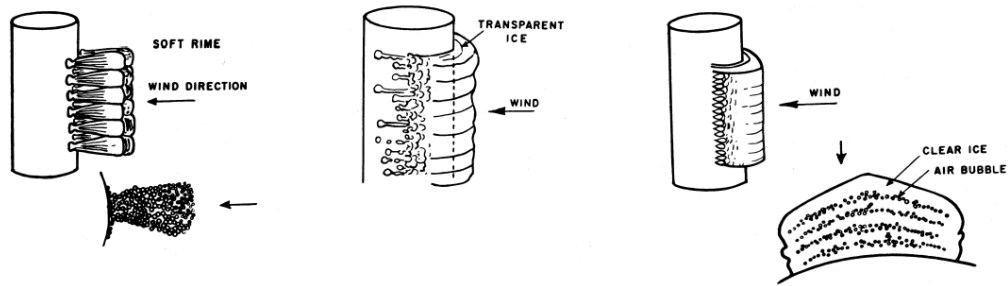


Figure 2.1.1 – Difference between Soft rime (left), Glaze (center) and Hard rime (right) [11]

Glaze

Glaze, also known as Freezing rain, takes place when falling raindrops meet cold air, meaning an air layer at a temperature below zero. Raindrops cool down but they remain in a physical state of liquid. Supercooled droplets go down to the surface of a body, on which they freeze [1]. The process of accretion is governed by the surface itself, in particular by its conditions that define heat flux. Glaze ice is usually smooth, dense and transparent. Its density can reach 800-900 kg/m³ [1]. Accretion temperature conditions is around -1°C to -5°C [5]. Meteorological conditions for glaze ice formation usually show high liquid water content in the air and freezing rain with droplets ranging from 0,5 to 4 mm [3]. Eventually, glaze is generally identified by typical ice drop formations, called icicles, caused by the freezing of the running off water on the surface, like Figure 2.1.2 highlights. It does not contain air bubbles, even if air pockets can occur in particular condition of strong wind [1].

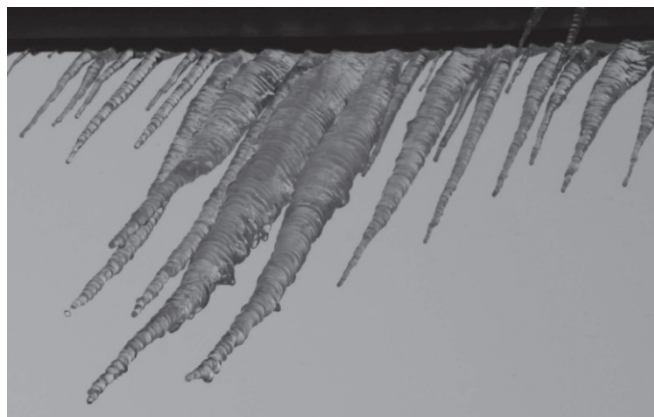


Figure 2.1.2 – Example of Glaze ice in form of icicles growing at a roof rail [3]

Wet snow

It occurs when snowflakes get through a layer characterized by warm air, with a variation of temperature between -2°C and +5°C [3]. Obviously, the water content in wet snow is quite high, thus its capacity to adhere on an object is significant, even though it is closely

linked to meteorological conditions and temperature. Figure 2.1.3 gives a representation of it. Density of wet snow can range between 200 and 990 kg/m³, thus it can exceed the density of pure glaze ice [3].



Figure 2.1.3 – Example of Wet snow accretion on a transmission line [3]

Dry snow

Dry snow accretion happens when wind flow conditions are moderate, since it requires a wind velocity very low, such as 2 m/s [1]. It occurs when the snowflakes settle on the object before passing through the 0°C isotherm, at subfreezing temperatures, like Figure 2.1.4 shows. This kind of precipitation does not have significant weight, since its density can be approximately 100 kg/m³ [1].

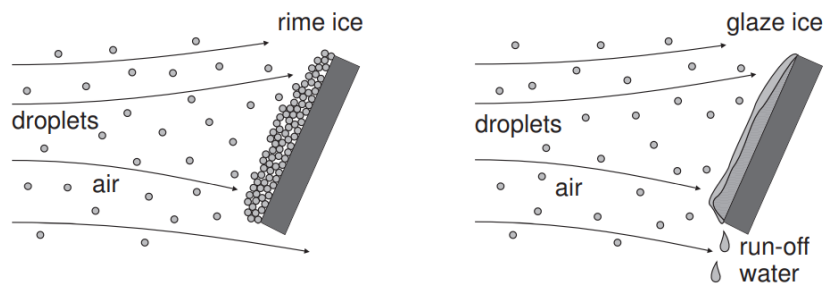


Figure 2.1.4 – Dry ice growth (left) and wet ice growth (right) [3]

Hard and soft rime

Rime ice forms when super cooled water droplets hit a surface with a temperature less than 0°C [3]. It belongs to in-cloud icing type due to freezing fog or freezing drizzle. The typical droplet diameter of fog droplets is about 10 µm in a range from 1 to 50 µm [3]. Hard and soft rime in both terms of internal structure and density. First one is characterized by a densely packed crystal matrix leading to a relatively high density varying from 700 to 900 kg/m³ [1]. It contains a mixture of clear ice and ice incorporating bubbles. On the other hand, soft rime is characterized by a granular

structure with high content of air bubbles, thus its density is lower and can vary between 200-600 kg/m³ [1]. It occurs when droplets with a small momentum freeze instantaneously on the surface. For this reason, the temperature usually needs to be below -5°C at moderate wind velocities. In this conditions air voids are left between the frozen droplets leading to densities of less than 100 μm [3]. Figure 2.1.5 offers an example of Rime deposit.



Figure 2.1.5 – Rime on a 22 kV overhead line in Voss, Norway, 18 April 1961 [6]

2.2 Ice accretion model

In this section a model about how ice accretion grows on transmission line system is provided. However, even if this kind of research is not the main object of the thesis, it is important to highlight the theoretical method on which the data series and investigations are based. These last one will be widely presented in Chapter 3, as a main data input in order to simulate meteorological condition for galloping instability.

The model that follows was established by Lasse Makkonen and it is a tool with the aim of computing the ice mass variation per unit length M [kg/m], which accretes on an object. Figure 2.2.1 gives the ideal model from which his theory starts. According to Makkonen, extreme icing events are rare results of complex combinations of various atmospheric and geographic factors, and may not follow an occurrence probability distribution [6], thus it's quite difficult to predict iceloads. Moreover, when a mathematical or numerical distribution is occurred and obtained, it will be probably not suitable enough for other similar consequence events. Anyway, as Makkonen says, in structural engineering the designer is always interested in extreme events that we may not yet have experienced [6].

However, the purpose of this section is to offer a general overview about modeling of icing events. The fundamental equation of icing, on which the author refers to, is the following one:

$$\frac{dM}{dt} = \alpha_1 \alpha_2 \alpha_3 \omega v A \quad (2.2.1)$$

Where A is the sectional area of the object, v is the velocity particle vector, ω is the mass concentration that identifies the liquid water content and finally the correction factors α_1 , α_2 and α_3 which represent different processes that may reduce dM/dt from its maximum value, since they vary between 0 and 1. Factor α_1 denotes the collision efficiency, α_2 the sticking efficiency and α_3 the accretion efficiency.

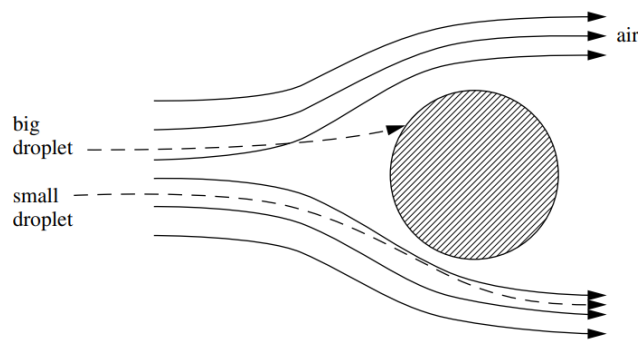


Figure 2.2.1 – Air streamlines and droplet trajectories around a cylindrical object [6]

Factor α_1 represents the efficiency of collision of the particles, and it describes the ratio of the flux density of the particles that collide with the object to the maximum flux density [1]. The collision efficiency is reduced respect to the unity, because of particles that follow the air streamlines and may be deflected from their path towards the object [6]. Figure 2.2.2 gives a representation of it.

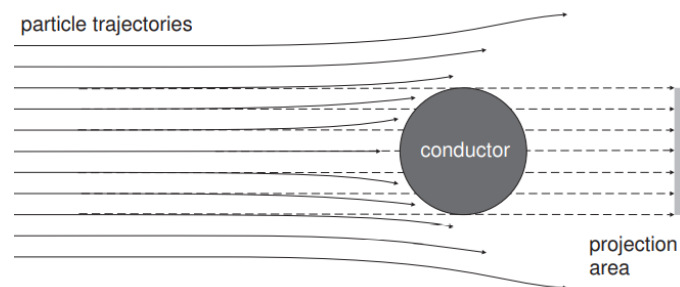


Figure 2.2.2 – Collision efficiency [3]

Factor α_2 represents the collection efficiency, or sticking, of those particles that stick on the object to the totality of particles [1]. The sticking efficiency α_2 is reduced respect to the unity, when the particles bounce from the surface [6], and it is well represented by

Figure 2.2.3. Only particles with enough residence time on the surface to affect the icing are considered and take part to the computation and variation of this coefficient.

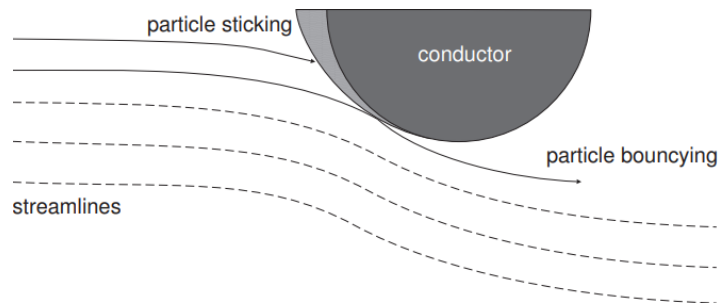


Figure 2.2.3 – Collection efficiency [3]

Factor α_3 represents the efficiency of accretion, and it defines the ratio of those particles which contribute to the accretion of the mass and the totality of particles themselves. The accretion efficiency α_3 is given by Figure 2.2.4 and it is reduced respect to the unity when the heat flux from the accretion is too small to cause sufficient freezing to incorporate all the sticking particles into the accretion [6]. The condition in which $\alpha_3=1$ defines a state called “*dry-growth*”, that represents an absence of liquid layer and leads to the creation of rime ice. On the other hand, when the situation develops ($\alpha_3<1$) there is a liquid layer on the surface which gives birth to glaze ice. Obviously it is called “*wet-growth*”. Figure 2.2.5 explains this diversity.

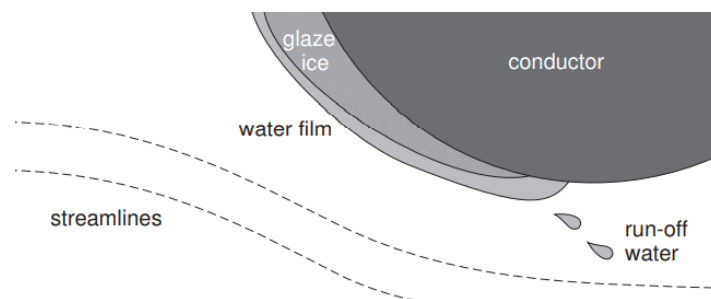


Figure 2.2.4 – Accretion efficiency [3]

It is clear that this kind of process depends widely on the time and on the conditions of the surface, such that it requires an iterative analysis able to define the combination of factors that lead to icing rate at each step. However, according to [6], the value obtained by the time-dependent analysis can be transformed in a radial thickness as the result of accretion of wire section. Thus the equivalent shape of iced accreted geometry section is provided.

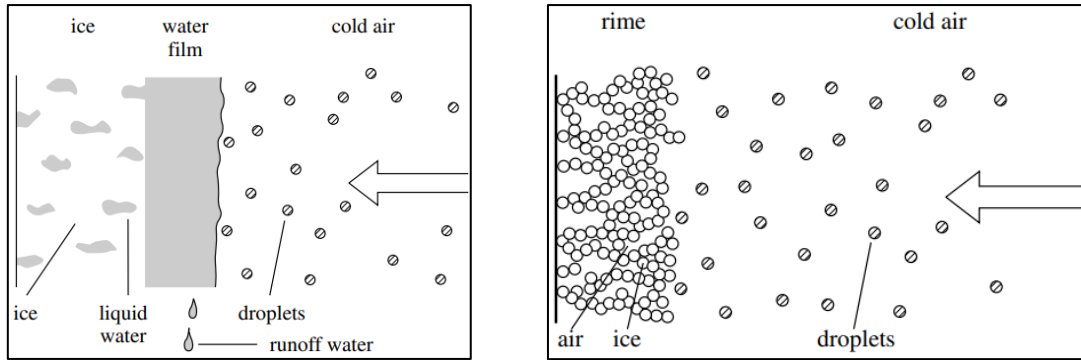


Figure 2.2.5 – Growth of rime ice (dry growth) on the left and growth of glaze ice (wet growth) on the right [6]

2.3 Hamilton’s Principle revisited

This subsection has the purpose to give a dynamic model approach, in order to establish a formal writing for next analytical developments.

A dynamic system is a mathematical model, typically following a partial differential equation, that embodies a natural object evolving along time. It is fundamental highlighting that a dynamic analysis is strictly dependent not only on time but also on masses movements, that give birth to inertial forces not definable in static field, as well as dumping forces. Hence, the formal dynamic balance equation needs to take care of this new kind of forces playing their role as state variables, since they characterizes the state of the system with its dynamic features at every time step.

The reference body has degrees of freedom that have dynamic meaning and represent motion’s displacement range. The simplest model is represented by oscillator, defined in Figure 2.3.1:

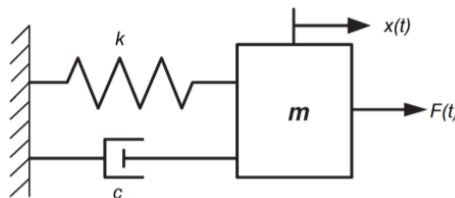


Figure 2.3.1 – Simple oscillator as dynamic reference model [30]

The oscillator is supposed to be excited by an external time-dependent forcing $F(t)$ and characterized by its own elastic stiffness K , a dumping coefficient c and a determined mass m . With the hypothesis of a single degree-of-freedom, SDOF in literature, the problem solution is $x(t)$ as body’s displacements after forcing excitation. From this

assumption, it derives that the derivatives versus time of model movement is velocity $\dot{x}(t)$ and acceleration $\ddot{x}(t)$, respectively.

By using *d'Alembert* principle, which establishes that every dynamic state of motion can be regarded as a static equivalent mechanical state with its own balance according to external forces and inertial ones, it derives the dynamic balance equation researched:

$$m\ddot{x}(t) + c\dot{x}(t) + Kx(t) = F(t) \quad (2.3.1)$$

Where the first two terms are inertial and dumping forces, introduced above, and the third one is the elastic force, the only one just known in static field. Moreover, from equation (2.3.1) it is clear that the left contributes are always against the motion, and thus of resistive nature.

In this thesis, as mentioned in the previous chapter, fluid dynamics and its relation with structures play a key role. Hence, a fluid-structure archetypal is required and now provided, since it is demonstrated that flow-oscillator models are a subclass of the general physical-based framework [26]. In fact, according to Haym Benaroya and Rene Gabbai, a flow-oscillator model is a coupled of two reduced-order mechanical, one representing structural behaviour and the other non-linear one based on fluid interaction with structural development [26]. This analytical tool can be derived from a variational approach linked to *Hamilton's* principle. The extension of the set governing equations coming from this principle can be used for generalize multiple degrees-of-freedom problems in this field.

Starting from d'Alembert's principle, it can be written as follows:

$$\sum_{i=1}^n \left(m_i \frac{d^2 \mathbf{r}_i}{dt^2} + \frac{\partial \Pi}{\partial \mathbf{r}_i} - \mathbf{F}_i \right) \delta \mathbf{r}_i = 0 \quad (2.3.2)$$

Where Π is a function of $\Pi(\mathbf{r}_1, \mathbf{r}_2, \dots, \mathbf{r}_n)$ and it is the potential energy; \mathbf{F}_i represents forces acting on the i_{th} particle; \mathbf{r}_i is the position vector of the particle of mass m_i ; $\delta \mathbf{r}_i$ is a virtual displacement.

Developing Π function:

$$\delta \Pi = \sum_{i=1}^n \left(\frac{\partial \Pi}{\partial \mathbf{r}_i} \right) \delta \mathbf{r}_i \quad (2.3.3)$$

and considering the virtual work performed on the system by non-conservative forces undergoing virtual displacements:

$$\delta W = \sum_{i=1}^n (\mathbf{F}_i) \delta \mathbf{r}_i \quad (2.3.4)$$

the d'Alembert principle becomes the following one:

$$\delta \mathcal{L} + \delta W - \frac{d}{dt} \left[\sum_{i=1}^n \left(m_i \frac{d\mathbf{r}_i}{dt} \right) \delta \mathbf{r}_i \right] = 0 \quad (2.3.5)$$

where $\mathcal{L} = \Pi - T$ is the Lagrangian of the system and T is the kinetic energy of the particles.

With the aim to write equation (2.3.5) from a discrete form to a continuous one, it follows:

$$\delta \mathcal{L} + \delta W - \frac{d}{dt} \left[\int_v (\rho \mathbf{U}) \delta \mathbf{r} dv \right] = 0 \quad (2.3.6)$$

where ρ represents density; $\mathbf{U} = \frac{d\mathbf{r}}{dt}$ is the velocity field of the system at time t ; \mathcal{L} is the Lagrangian of the continuous system. v denotes a fixed material system enclosed in a volume, over which the integration is made [26].

Hamilton's principle is obtained by integrating equation (2.3.6) within a time interval $[t_1; t_2]$:

$$\delta \int_{t_1}^{t_2} \mathcal{L} dt + \delta \int_{t_1}^{t_2} \delta W dt - \left[\int_v (\rho \mathbf{U}) \delta \mathbf{r} dv \right]_{t_1}^{t_2} = 0 \quad (2.3.7)$$

Having a prescribed conditions for instants t_1, t_2 then it must be $\delta \mathbf{r} = 0$ [26]. Thus, the third term is neglected and equation (2.3.7) becomes:

$$\delta \int_{t_1}^{t_2} \mathcal{L} dt + \delta \int_{t_1}^{t_2} \delta W dt = 0 \quad (2.3.8)$$

Even though equation (2.3.8) is written and devised properly, it does not explain generally fluid-structure interaction, since it is linked to cases when boundary conditions or system configuration are prescribed. Thus a generalization is needed. This one was given by McIver (1973), who published a work yielding to an approach that extends the just presented principle. In fact, if Hamilton's traditional form is referred to a system containing same materials at all times and where the positions of masses could be known at different times, McIver's extension deals with control volumes where the material is allowed to cross the boundaries and thus to modify their quantity along time.

Considering the case of uniform flow U_o past a stationary circular cylinder of radius R , the extended form of Hamilton's principle for a system of changing mass is given by the following equation and Figure 2.3.2 shows the reference graphic volume:

$$\delta \int_{t_1}^{t_2} (\mathcal{L})_o dt + \delta \int_{t_1}^{t_2} (\delta W)_o dt - \int_{t_1}^{t_2} \int_{B_o} \int_{(t)} \rho (\mathbf{u}_{rel} \cdot \delta \mathbf{r}) (\mathbf{u} \cdot \mathbf{n}) ds dt = 0 \quad (2.3.9)$$

It is referred for an open an open control volume $R_o(x, t)$, which has a bounding surface $B(x, t)$ having a part open for the flow particles $B_o(x, t)$ and a part closed to them $B_c(x, t)$ described by the circumference $x^2 + y^2 = R^2$ if the center of the reference system is chosen in the middle of the circle, as shown.

In equation (2.3.9), $(\mathcal{L})_o = (\mathcal{K} - \mathcal{E})_o$ is the Lagrangian of the open system and $(\delta W)_o$ is the virtual work performed by non-potential forces on the same system [26]. $ds = ds(x, t)$ is used here to represent a differential surface element: at position x and time t , the density is ρ and the velocity is u [26]. Eventually, \mathbf{u}_{rel} is the relative fluid velocity in relation to the one of control surface. Moreover, the kinetic energy of the open system is called $(\mathcal{K})_o$, while the sum of gravitational potential energy, buoyancy potential energy, strain energy and internal energy is called $(\mathcal{E})_o$.

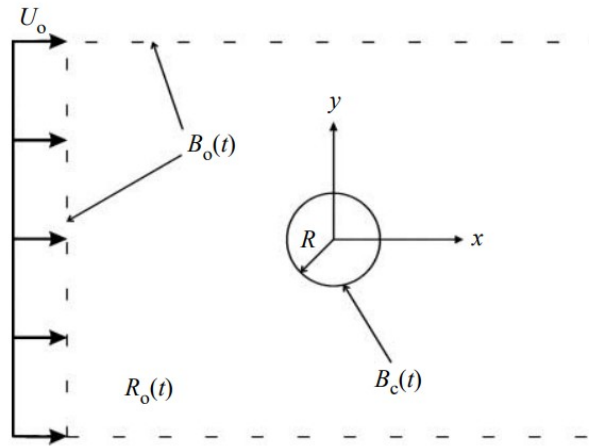


Figure 2.3.2 – The open control surface, closed and the open one [26]

The kinetic energy of the open system is written as follows:

$$(\mathcal{K})_o = (\mathcal{K}_{fluid})_o = \int \int \int_{R_o(t)} \frac{1}{2} \rho (\mathbf{u} \cdot \mathbf{u}) dv \quad (2.3.10)$$

where $dv = dv(x, t)$ is the differential volume element.

Furthermore, the differential potential energy of the system is given by:

$$\delta(\mathcal{E})_o = \delta(\mathcal{E}_{fluid})_o = \delta \int \int \int_{R_o(x,t)} \rho e(\rho, T) dv = 0 \quad (2.3.10)$$

where e is the specific internal energy and $T(x, t)$ is the thermodynamic temperature field.

After several considerations included in [26], it can be written as follows:

$$\delta \int_{t_1}^{t_2} (\mathcal{L})_o dt = \delta \int_{t_1}^{t_2} (\mathcal{K})_o dt = \delta \int_{t_1}^{t_2} \int \int \int_{R_o(t)} \frac{1}{2} \rho (\mathbf{u} \cdot \mathbf{u}) dv dt \quad (2.3.11)$$

The virtual work done by the normal and tangential stresses in the fluid during a virtual displacement is given by a formulation introduced by Dost and Tabarrok (1979):

$$\delta(W)_o = \delta(W_{fluid})_o = - \int \int \int_{R_o(t)} \sigma_{ij} \delta \varepsilon_{ij} dv \quad (2.3.12)$$

where σ_{ij} is the natural or Eulerian stress tensor:

$$\sigma_{ij} = \frac{1}{2} \left[\frac{\partial(\delta r_i)}{\partial x_j} + \frac{\partial(\delta r_j)}{\partial x_i} \right] \quad (2.3.13)$$

and $\delta \varepsilon_{ij}$ is the Lagrangian variation of Cauchy's infinitesimal and linear strain tensor:

$$\varepsilon_{ij} = \frac{1}{2} \left[\frac{\partial r_i}{\partial x_j} + \frac{\partial r_j}{\partial x_i} \right] \quad (2.3.14)$$

Due to the symmetric property of the stress tensor, it can be written as follows:

$$\frac{1}{2} \sigma_{ij} \left[\frac{\partial(\delta r_i)}{\partial x_j} + \frac{\partial(\delta r_j)}{\partial x_i} \right] = \sigma_{ij} \frac{\partial(\delta r_i)}{\partial x_j} \quad (2.3.15)$$

Hence, equation (2.3.12) becomes:

$$\delta(W)_o = - \int \int \int_{R_o(t)} \sigma_{ij} \frac{\partial(\delta r_i)}{\partial x_j} dv \quad (2.3.16)$$

Now, using equation (2.3.11) and equation (2.3.16), equation (2.3.9) can be written as follows:

$$\begin{aligned} & \delta \int_{t_1}^{t_2} \int \int \int_{R_o(t)} \frac{1}{2} \rho (\mathbf{u} \cdot \mathbf{u}) dv dt - \int_{t_1}^{t_2} \int \int \int_{R_o(t)} \sigma_{ij} \frac{\partial(\delta r_i)}{\partial x_j} dv dt + \\ & + \int_{t_1}^{t_2} \int \int_{B_o(t)} \rho (\mathbf{u} \cdot \delta \mathbf{r}) (\mathbf{u} \cdot \mathbf{n}) ds dt = 0 \end{aligned} \quad (2.3.17)$$

Eventually, a development form for stress tension and continuity equation is now provided.

Currie (2003) shows that the relation between the stress tensor σ to the density field $\rho(x, t)$, the thermodynamic pressure field $p(x, t)$ and the velocity gradient tensor $L = [\nabla \mathbf{u}(x, t)]^T$ in a Newtonian fluid is given by the following formulation:

$$\sigma = [-p + \lambda(\nabla \cdot \mathbf{u})] \mathbf{I} + \mu [(\nabla \mathbf{u}) + (\nabla \mathbf{u})^T] \quad (2.3.18)$$

where \mathbf{I} is the identity tensor and μ and ρ are used to define the dynamic viscosity coefficient and the second viscosity coefficient, respectively. It is noted that all properties of p, μ, λ depend on (ρ, T) .

Equation (2.3.18) follows the general form below:

$$\boldsymbol{\sigma} = -p\mathbf{I} + \mathbf{G}(\nabla\mathbf{u}) \quad (2.3.19)$$

where \mathbf{G} is a linear tensor valued function, $\nabla\mathbf{u}$ can be written as the sum of a symmetric tensor \mathbf{D} and a skew-symmetric tensor \mathbf{W} , which are now provided:

$$\mathbf{D} = \frac{1}{2}[(\nabla\mathbf{u}) + (\nabla\mathbf{u})^T] \quad (2.3.20)$$

$$\mathbf{W} = \frac{1}{2}[(\nabla\mathbf{u}) - (\nabla\mathbf{u})^T] \quad (2.3.21)$$

In a fluid, a rigid body rotation cannot be followed by shear stresses, since there is no shear action in it. Thus the shear stresses are described only by \mathbf{W} . By using the assumption of an isotropic fluid, the stress tension can be written as follows:

$$\boldsymbol{\sigma} = -p\mathbf{I} + \lambda \operatorname{tr}(\mathbf{D}) \mathbf{I} + 2\mu\mathbf{D} \quad (2.3.22)$$

Eventually, the mass balance is solved by McIver through the following necessary condition:

$$\rho \int \int \int_{R_o(t)} \rho(\cdot) dv = \int \int \int_{R_o(t)} \rho\delta(\cdot) dv \quad (2.3.23)$$

where (\cdot) is an arbitrary function of space and time.

Thanks to McIver's statement, continuity equation can be written as follows:

$$\frac{D\rho}{Dt} + \rho \left(\frac{\partial u_k}{\partial x_k} \right) = \frac{\partial \rho}{\partial t} + \frac{\partial(\rho u_k)}{\partial x_k} = 0 \quad (2.3.24)$$

Using these developments, equation (2.3.18) can be reformed as follows:

$$\begin{aligned} & \int_{t_1}^{t_2} \int \int \int_{R_o(t)} \rho \left[\mathbf{u} \cdot \delta \left(\frac{D\mathbf{r}}{Dt} \right) \right] dv dt \\ & = \int_{t_1}^{t_2} \int \int \int_{R_o(t)} \rho \left[\mathbf{u} \cdot \frac{D(\delta\mathbf{r})}{Dt} \right] dv dt \end{aligned} \quad (2.3.25)$$

Using Dost and Tabarrok results, continuity equation and some considerations contained in [26], it derives that:

$$\begin{aligned}
& \delta \int_{t_1}^{t_2} \iiint_{R_o(t)} \rho [\mathbf{u} \cdot \mathbf{u}] dv dt \\
& = \int_{t_1}^{t_2} \iiint_{R_o(t)} \rho \left[\mathbf{u} \cdot \delta \left(\frac{D\mathbf{r}}{Dt} \right) \right] dv dt \\
& - \int_{t_1}^{t_2} \iiint_{R_o(t)} \rho \left[\left(\frac{D\mathbf{u}}{Dt} \right) \cdot \delta \mathbf{r} \right] dv dt
\end{aligned} \tag{2.3.26}$$

This finally leads to the rewriting of equation (2.3.17), that becomes:

$$\begin{aligned}
& - \int_{t_1}^{t_2} \iiint_{R_o(t)} \rho \left[\left(\frac{D\mathbf{u}}{Dt} \right) \cdot \delta \mathbf{r} \right] dv dt \\
& - \int_{t_1}^{t_2} \iiint_{R_o(t)} \sigma_{ij} \frac{\partial(\delta r_i)}{\partial x_j} dv dt \\
& + \int_{t_1}^{t_2} \iint_{B_o(t)} \rho (\mathbf{u} \cdot \delta \mathbf{r}) (\mathbf{u} \cdot \mathbf{n}) ds dt = 0
\end{aligned} \tag{2.3.27}$$

Other analytical developments of this theme are included in [26].

2.4 Den Hartog's criterion

The first model of galloping phenomenon was established by Den Hartog in 1932 [13]. According to his analysis, the system could be modelled as a single-degree-of-freedom (SDOF) one simply capable of vertical motions. The hypothesis on which this theory is based on is that the flow is considered as quasi-steady, that means that the force acting on the body is only linked to the airflow velocity and to the angle of attack [13]. This one is the angle formed by the wind direction velocity and a reference line of the body. The reason behind this assumption is that the frequency of the transmission line under galloping is quite lower than the wind speed one [13]. This simplified hypothesis is widely applied when a single line conductor is subjected by the phenomenon, while it doesn't deal with bundled ones, as it is not possible to take into account the dynamic effect of the whole system. The oscillation that the transmission line system experiences is major caused by the ice accretion and aerodynamics features of the resulting profile section, other than its dynamic characteristics. As usually happens in aerodynamic analyses, the resulting wind force is split into two components, called Drag and Lift. Figure 2.4.1 gives a graphic illustration of these components:

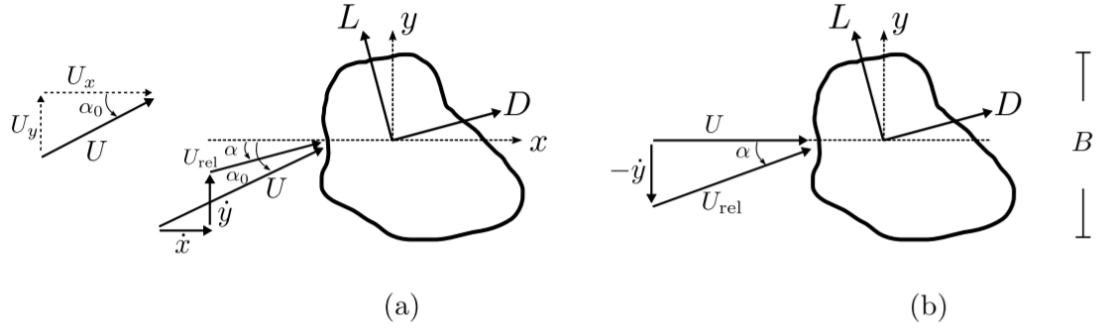


Figure 2.4.1 – Geometry of a bluff section indicating lift and drag forces (L , D), relative angle of attack (α) and principal structural axes (x , y) [13]

The Drag force D acts parallel to the flow direction and represents the sum of the resulting pressure on the body, while the Lift one L is perpendicular to the wind and is linked to the pressure and velocity gradients between the two sides of the object. Their formulations are presented by the following equations, respectively:

$$D = \frac{1}{2} \rho U^2 A C_D \quad (2.4.1)$$

$$L = \frac{1}{2} \rho U^2 A C_L \quad (2.4.2)$$

Where: C_D is the aerodynamic drag coefficient; C_L is the aerodynamic lift coefficient; ρ is the air density; U is the wind speed; A is the projected area in a plane perpendicular to the flow direction, also known as frontal area.

The classical Den Hartog derivation starts typically by writing the mean aerodynamic force, per unit length, along the y -axis, as a function of the mean drag and lift forces:

$$-F_y = L \cos(\alpha) + D \sin(\alpha) \quad (2.4.3)$$

As and U_{rel} is the relative velocity and α the angle of attack thus defined:

$$\alpha = \tan^{-1} \left(\frac{\dot{y}}{U} \right) \quad (2.4.4)$$

Based on the quasi-steady assumption, F_y varies as a function of the body velocity \dot{y} , and thus of the angle of attack. In these terms, an unstable condition has been achieved.

Therefore, Den Hartog criterion is expressed by the following one:

$$\frac{dF_y}{d\alpha} > 0 \quad (2.4.5)$$

According to (2.4.5), and considering small angles so that $\cos(\alpha)$ and $\sin(\alpha)$ can be approximated to unity and zero, respectively, the (2.4.5) unstable condition can be written in this way:

$$\frac{dL}{d\alpha} + D < 0 \quad (2.4.6)$$

The (2.4.6) derivation can be easily obtained by a series of mathematical steps, now expressed. If Taylor series expansion is used on F_y around $\dot{y} = 0$, ignoring the higher order terms, which is acceptable for small amplitude motion, the standard damped equation of motion of the body can be written as:

$$m\ddot{y} + c\dot{y} + m\omega_y^2 y = F_y \approx F_y|_{\dot{y}=0} + \dot{y} \left. \frac{dF_y}{d\dot{y}} \right|_{\dot{y}=0} \quad (2.4.7)$$

where m is the cylinder mass per unit length, ω_y^2 is the circular natural frequency, c is the structural damping coefficient.

Exclusively when the free-stream wind velocity U and the motion velocity \dot{y} are orthogonal and thus $\alpha = \tan^{-1}\left(-\frac{\dot{y}}{U}\right)$:

$$F_y \approx -D - D\alpha \approx -\left(L_0 + \frac{dL}{d\alpha}\alpha\right) - \left(D_0 + \frac{dD}{d\alpha}\alpha\right)\alpha \quad (2.4.8)$$

By neglecting the second order α^2 , since the α is assumed as small:

$$F_y \approx -L_0 - \left(D_0 + \frac{dL}{d\alpha}\right)\alpha \approx -L - \left(D + \frac{dL}{d\alpha}\right)\frac{\dot{y}}{U} \quad (2.4.9)$$

The term inside the bracket can be substituted in (2.4.7) as a component of damping element, thus:

$$m\ddot{y} + \left[c + \left(D + \frac{dL}{d\alpha} \right) \frac{1}{U} \right] \dot{y} + m\omega_y^2 y = -L \quad (2.4.10)$$

The term inside the square brackets defines the global damping. It consists of the base of aerodynamic analysis, since an unsteady on this field occurs when the total damping becomes zero. Hence, it is necessary that the aerodynamic damping split under the zero value becoming negative. Thus the (2.4.6) condition is proved. Hartog criterion is often expressed in terms of coefficients, rather than forces, so it can be written as follows:

$$S_{DH} = C_D + \frac{dC_L}{d\alpha} < 0 \quad (2.4.11)$$

S_{DH} is defined as Den Hartog's coefficient. Figure 2.4.2 gives an example of its development.

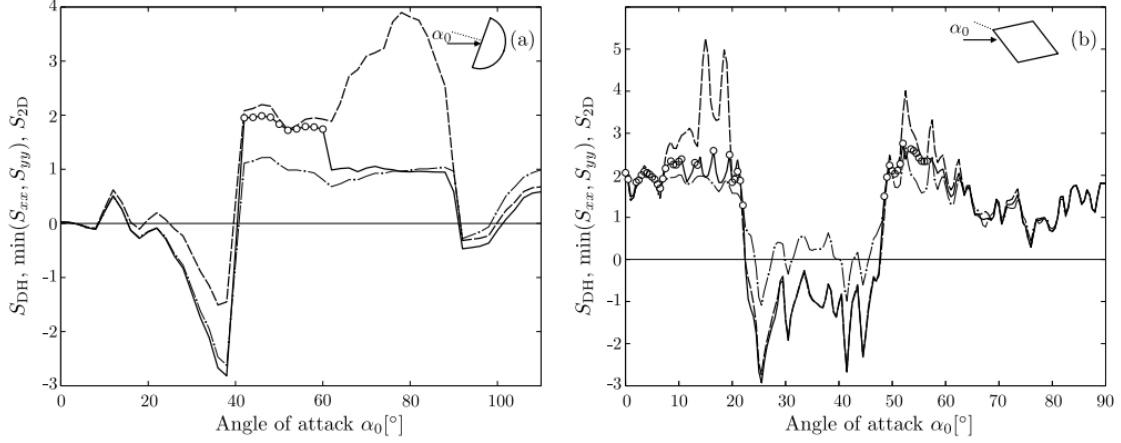


Figure 2.4.2 – Trend set example of Den Hartog's coefficient [1]

As previously mentioned, Den Hartog's criterion highlights the ranges of values of the angle of attack where galloping instability may occur, but it doesn't explain its development. In order to explain the whole condition of this kind of crisis's occurrence, it is necessary to introduce the so called "critical velocity for galloping" U_c , thus defined:

$$U_c = - \frac{2c}{\left(C_D + \frac{dC_L}{d\alpha}\right) \frac{1}{2} \rho} \quad (2.4.12)$$

Which gives the following derivation, if rewritten inside the damping element of (2.4.10) equation and imposing this one to vanishing:

$$c + \left(D + \frac{dL}{d\alpha}\right) \frac{1}{U_c} = c + \left(C_D + \frac{dC_L}{d\alpha}\right) \frac{1}{2} \rho U_c A = 0 \quad (2.4.13)$$

By introducing damping ratio ξ and natural angular frequency ω_n , the equation of motion (2.4.10) becomes the following one:

$$m\ddot{y} + \left[\xi + \left(C_D + \frac{dC_L}{d\alpha}\right) \frac{\rho UA}{4m\omega_n}\right] \dot{y} + \omega_n^2 y = 0 \quad (2.4.14)$$

Where the right term is null since the mass is rotating around its static position and the new terms introduced are such defined:

$$\xi = \frac{c}{2m\omega_n} \quad (2.4.15)$$

$$\omega_n = \sqrt{\frac{K}{m}} \quad (2.4.16)$$

Therefore, the critical wind velocity can be formulated as follows:

$$U_c = - \frac{4 m \xi \omega_n}{\left(C_D + \frac{dC_L}{d\alpha}\right) A \rho} = - \frac{4 m \delta f_n}{\left(C_D + \frac{dC_L}{d\alpha}\right) A \rho} \quad (2.4.17)$$

In fact the logarithmic decrement of structural damping $\delta = 2\pi\xi$ and the circular natural frequency f_n have been introduced in the formulation.

It is very interesting to notice that Eurocode 1, EN 1991-1-4 [39], establishes that the galloping instability starts at a typical value of wind speed named U_{CG} , thus defined:

$$U_{CG} = \frac{2S_C}{a_g} f_n b \quad (2.4.18)$$

Where S_C is defined as the Scruton Number, calculated as follows:

$$S_C = \frac{2 \delta_s m_{n,e}}{\rho b^2} \quad (2.4.19)$$

Coefficient a_g represents the minimum value of Den Hartog's coefficient calculated within a range of values for the angle of attack in which instability takes place, and $b = A$ is the width of the body along the wind-speed direction.

Finally, by introducing the expression of S_C (2.4.19) in the equation (2.4.18) we can immediately obtain the equality $U_C = U_{CG}$.

However, it is necessary to highlight that Den Hartog's criterion is quite simplified, such that it cannot explain all galloping instabilities and real cases. For instance, as the theory admits just vertical motions for the wire, its torsional capacity and stiffness is neglected. This simplification can lead to unreliable results in several cases, since all the instabilities linked to torsional movements are ignored. The next subsection gives an approach that includes also this kind of behaviour.

On the other hand, even though Den Hartog analysis has clear limits on the field of application, experimental observations underline that the most important and the most frequent galloping events occurring on single wire follow this theory and instability conditions. In fact, frequently the conductor does not require to be rigid about rotations, as it follows just vertical displacements.

2.5 Torsional Galloping

Den Hartog's theory is not able to catch and explain all the wire instability from wind effects, due to its imposition to consider just one single degree-of-freedom (SDOF). Therefore, in this subsection a multiple-degrees-of-freedom theoretical model is carried out and discussed, thanks to Nigol and Clarke's mechanism. This one is based on the torsional freedom and its central role played in the triggering of Galloping instability

through the derivative of the moment coefficient C_M , subsequently explained. The develop of this approach is much more difficult than transverse galloping, since fluid forces depend on both the angle and angular velocity. Nigol's model explains the so called coupled translational and rotational galloping, also called "Flutter-Galloping" since it involves vertical and torsional motions through mutual interactions.

The theoretical explanation begins with Figure 2.5.1 that shows torsional model for this kind of galloping motion.

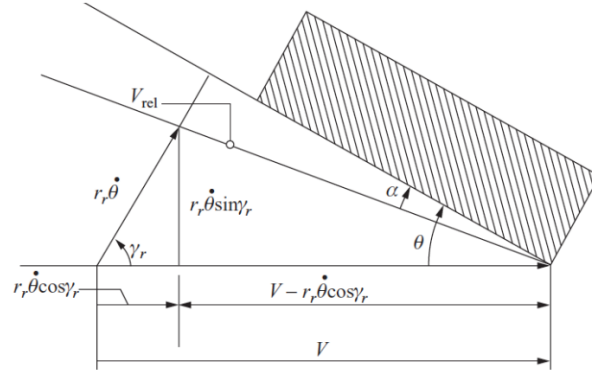


Figure 2.5.1 – Torsional galloping reference model [20]

Figure 2.5.1 allows to write these following relations between parameters such defined:

$$\theta - \alpha = \tan^{-1} \left(\frac{r_r \dot{\theta} \sin \gamma_r}{U_\infty - r_r \dot{\theta} \cos \gamma_r} \right) \quad (2.5.1)$$

$$V_{rel}^2 = (r_r \dot{\theta} \sin \gamma_r)^2 + (U_\infty - r_r \dot{\theta} \cos \gamma_r)^2 \quad (2.5.2)$$

By assuming a small angle of attack, these one become:

$$\alpha \approx \theta - \frac{r_r \dot{\theta} \sin \gamma_r}{U_\infty} = \theta - \frac{R \dot{\theta}}{U} \quad (2.5.3)$$

$$R = r_r \sin \gamma_r \quad (2.5.4)$$

$$V_{rel} \approx U_\infty \quad (2.5.5)$$

According to Nigol and Clarke, Flutter Galloping occurs when the derivative of C_M respect to the angle of attack, also named Nigol's coefficient δ_N , becomes negative. Moment coefficient and its variation on α are now expressed by the following formulations:

$$C_M = \frac{M}{\frac{1}{2} \rho U^2 A d} \quad (2.5.6)$$

$$\delta_N = \frac{\partial C_M}{\partial \alpha} < 0 \quad (2.5.7)$$

Where M is the torque and d is the conductor diameter.

The equation of torsional motion is explained by the following one, in total analogy with transverse Galloping:

$$J\ddot{\theta} + c\dot{\theta} + k\theta = M = \frac{1}{2} \rho U^2 d^2 C_M \quad (2.5.8)$$

Where J represents the moment of inertia, c is the torsional damping and k is the torsional stiffness. All the variables represented by θ and its derivatives $\dot{\theta}$, $\ddot{\theta}$ are torsional rotation, velocity and acceleration, respectively. It is allowed, as usual, to expand the coefficient C_M according to Taylor series, similarly to the transverse one:

$$C_M = C_M|_{\alpha=0} + \left(\frac{\partial C_M}{\partial \alpha}\right)|_{\alpha=0} \alpha + \dots \quad (2.5.9)$$

By assuming once again a small angle of attack, (2.5.9) becomes as follows:

$$C_M \approx \left(\frac{\partial C_M}{\partial \alpha}\right)|_{\alpha=0} \alpha = \left(\frac{\partial C_M}{\partial \alpha}\right) \left(\theta - \frac{R\dot{\theta}}{U}\right) \quad (2.5.10)$$

Since R represents the characteristic radius linked to a reference point in which the angle of attack is calculated. Hence, the (2.5.8) equation is reformulated by introducing (2.5.10) in it and by using the typical dynamic parameters ξ and ω :

$$c = 2 \xi J \omega \quad (2.5.11)$$

$$\omega = \sqrt{\frac{K}{J}} \quad (2.5.12)$$

Thus the equation (2.5.8) becomes:

$$\ddot{\theta} + \left[2 \xi \omega + \frac{1}{2} \rho \frac{U R A d}{J} \frac{\partial C_M}{\partial \alpha}\right] \dot{\theta} + \left[\omega^2 - \frac{1}{2} \rho \frac{U R A d}{J} \frac{\partial C_M}{\partial \alpha}\right] \theta = 0 \quad (2.5.13)$$

It is necessary to recognize the second term on the left as the torsional galloping and the third one as static divergence. Galloping instability is carried out when torsional galloping is null, thus:

$$2 \xi \omega + \frac{1}{2} \rho \frac{U R A d}{J} \frac{\partial C_M}{\partial \alpha} = 0 \quad (2.5.14)$$

Obtaining the criterion, that does not require a negative derivative of lift to give the galloping the possibility to occur, in opposition to what Den Hartog said:

$$U = -\frac{2 \xi \omega}{\frac{1}{2} \rho \frac{R A d}{J} \frac{\partial C_M}{\partial \alpha}} \quad (2.5.15)$$

$$\frac{\partial C_M}{\partial \alpha} < 0 \quad (2.5.16)$$

While by imposing null the static divergence it becomes:

$$\omega^2 - \frac{1}{2}\rho \frac{U R A d}{J} \frac{\partial C_M}{\partial \alpha} = 0 \quad (2.5.17)$$

Which yields to the opposite criterion:

$$U = \sqrt{\frac{\omega^2}{\frac{1}{2}\rho \frac{R A d}{J} \frac{\partial C_M}{\partial \alpha}}} \quad (2.5.18)$$

$$\frac{\partial C_M}{\partial \alpha} > 0 \quad (2.5.19)$$

2.5.1 Ampliation to two directions problems

If the motion is not normal to the wind direction, equation (2.5.13) does not hold and the formulation of the angle α is not valuable no longer. For the general case of arbitrary orientation and for extending the analysis to cover two orthogonal translational DOFs, which potentially can lead to coupled response, the derivation follows. Note that x and y are the principal structural axes, which may or may not align with axes of symmetry of the cross-section. Rotation of the body has not been included. In the general 2DOF translational case the equation that defines F_y still holds and also the following one about F_x :

$$F_x = -L \sin(\alpha) + D \cos(\alpha) \quad (2.5.1.1)$$

after Taylor series expansion of F_y and F_x , again for small amplitude motion only retaining the linear viscous damping terms with the aim of identifying the stability of the initial at rest state, similar to before:

$$F_x = F_x|_{\dot{x}=\dot{y}=0} + \dot{x} \frac{dF_x}{d\dot{x}}|_{\dot{x}=\dot{y}=0} \quad (2.5.1.2)$$

$$F_y = F_y|_{\dot{x}=\dot{y}=0} + \dot{y} \frac{dF_y}{d\dot{y}}|_{\dot{x}=\dot{y}=0} \quad (2.5.1.3)$$

For evaluating the derivatives we employ the chain rule:

$$\frac{d()}{d\dot{x}} = \frac{\partial ()}{\partial U_{rel}} \frac{\partial U_{rel}}{\partial \dot{x}} + \frac{\partial ()}{\partial \alpha} \frac{\partial \alpha}{\partial \dot{x}} \quad (2.5.1.4)$$

and similarly for \dot{y} .

Keeping in mind the relations:

$$U_{rel} = \sqrt{(U_y - \dot{y})^2 + (U_x - \dot{x})^2} \quad (2.5.1.5)$$

$$\tan(\alpha) = \frac{U_y - \dot{y}}{U_x - \dot{x}} \quad (2.5.1.6)$$

$$\tan(\alpha_0) = \frac{U_y}{U_x} \quad (2.5.1.7)$$

finally the unit length full 2×2 aerodynamic damping matrix of a bluff section is obtained:

$$\frac{\partial C_M}{\partial \alpha} > 0 \quad (2.5.1.8)$$

$$C_{aero} = \begin{bmatrix} c_{xxa} & c_{xya} \\ c_{yxa} & c_{yya} \end{bmatrix} = \left[\begin{array}{cc} -\frac{dF_x}{d\dot{x}} & -\frac{dF_x}{d\dot{y}} \\ \frac{dF_y}{d\dot{x}} & \frac{dF_y}{d\dot{y}} \end{array} \right]_{\dot{x}=\dot{y}=0} = \frac{\rho B U}{2} \begin{bmatrix} S_{xx} & S_{xy} \\ S_{yx} & S_{yy} \end{bmatrix} \quad (2.5.1.7)$$

Where:

$$S_{xx} = C_D(1 + \cos^2 \alpha_0) - (C_L + C_L') \sin \alpha_0 \cos \alpha_0 + C_L' \sin^2 \alpha_0$$

$$S_{xy} = -C_L(1 + \sin^2 \alpha_0) + (C_D - C_L') \sin \alpha_0 \cos \alpha_0 + C_D' \cos^2 \alpha_0$$

$$S_{yx} = C_D(1 + \cos^2 \alpha_0) + (C_D - C_L') \sin \alpha_0 \cos \alpha_0 - C_D' \sin^2 \alpha_0$$

$$S_{yy} = C_D(1 + \sin^2 \alpha_0) + (C_L - C_D') \sin \alpha_0 \cos \alpha_0 + C_L' \cos^2 \alpha_0$$

Where over dots represent differentiation with respect to the angle of attack α .

The derivation is also valid for wind skewed to the cylinder axis, by employing the wind component normal to the cylinder and the force coefficients with respect to that component, as long as the independence principle is a viable approximation. For the instability condition of the coupled response, an eigenvalue analysis has to be performed for the 2DOF system, which is a function of the structural, as well as the aerodynamic, parameters. In general a numerical solution is required, but for special cases a closed form result is derived as follows. Since rotations are not included in this analysis potential inertial coupling of the degrees of freedom due to eccentricity of the centre of mass is not allowed for and the mass per unit length, m , associated with the two degrees of freedom is the same. The equations of motion:

$$m\ddot{x} + [c_x + c_{xxa}]\dot{x} + m\omega_x^2 x = -c_{xya}\dot{y} \quad (2.5.1.8)$$

$$m\ddot{y} + [c_y + c_{yya}]\dot{y} + m\omega_y^2 y = -c_{yxa}\dot{x} \quad (2.5.1.9)$$

with ω_x , ω_y and c_x , c_y the natural frequencies and structural damping coefficients for the 2DOF respectively, are assumed to possess a solution of the form that follows:

$$x = X e^{\lambda t} \quad (2.5.1.10)$$

$$y = Y e^{\lambda t} \quad (2.5.1.11)$$

where the eigenvalues λ and the amplitudes X, Y are in general complex-valued. The equation (2.4.1.8) yields to the following formulation:

$$\frac{Y}{X} = -\frac{\lambda^2 + \frac{c_{xx}}{m}\lambda + \omega_x^2}{\frac{c_{xya}}{m}\lambda} = -\frac{\frac{c_{yxa}}{m}\lambda}{\lambda^2 + \frac{c_{yy}}{m}\lambda + \omega_y^2} \quad (2.5.1.12)$$

$$\begin{aligned} \lambda^4 + \left(\frac{c_{xx} + c_{yy}}{m}\right)\lambda^3 + \left(\frac{c_{xx}c_{yy} - c_{xya}c_{yxa}}{m^2} + \omega_x^2 + \omega_y^2\right)\lambda^2 \\ + \left(\frac{c_{xx}\omega_y^2 + c_{yy}\omega_x^2}{m}\right)\lambda + \omega_x^2\omega_y^2 = 0 \end{aligned} \quad (2.5.1.13)$$

where $c_{xx} = c_x + c_{xxa}$ and $c_{yy} = c_y + c_{yya}$. On the stability boundaries the eigenvalues are purely imaginary ($\lambda = i\omega$). When $\omega_x = \omega_y = \omega_n$, solving the biquadratic equation (2.5.1.13) for marginal stability gives the two following possibilities:

$$eq. \begin{cases} \omega_n = \omega, & c_{xx}c_{yy} - c_{xya}c_{yxa} = 0 \\ \omega_n \neq \omega, & c_{xx} + c_{yy} = 0 \end{cases} \quad (2.5.1.14)$$

For no structural damping ($c_x = c_y = 0$) equation (2.4.1.1) translates to the criterion for coupled galloping:

$$S_{2D} = \frac{1}{2} \left[3C_D + C'_L \pm \sqrt{(C_D - C'_L)^2 + 8C_L(C'_D - C_L)} \right] < 0 \quad (2.5.1.15)$$

where S_{2D} represents the non-dimensional effective aerodynamic damping coefficient of the coupled motion, corresponding to S_{xx} and S_{yy} for the uncoupled problem.

The solution in equation (2.5.1.14) is called complex response, which arises when the term under the square root in equation (2.5.1.15) is negative [13]. Then the criterion for coupled galloping (for no structural damping) becomes the following ones:

$$S_{2D} = \frac{1}{2} [3C_D + C'_L] < 0 \quad (2.5.1.16)$$

This solution is often missed by constraining X and Y to be real. From equation (2.5.1.12), for $\lambda = i\omega$ with $\omega_n \neq \omega$, Y/X is complex, writing elliptical trajectories [13]. Since the two modal responses occur simultaneously at different frequencies, a 2D beating-type behaviour occurs.

2.6 Linear theory of cable free vibrations

The aim of this subsection is to give a simple linear theory for cable free vibrations, in order to explain dynamic behaviour of a wire belonging to a transmission line system. On this field, Irvine and Caughey gave a huge contribute due to their linear approach developed in 1974 [21]. Certainly the validity of this model has several limits, since it is based on a case of study which is a uniform suspended cable with dead-end spans rigidly constrained at each support and the ratio of sag to span is about 1:8, or less [21]. Both in-plane and out-of-plane motions are considered, thus it establishes a 2 degrees-of-freedom model (2DOF).

2.6.1 Static Model

The following Figure 2.6.1.1 shows a uniform cable which hangs in a static equilibrium in a vertical plane through supports which are at the same level.

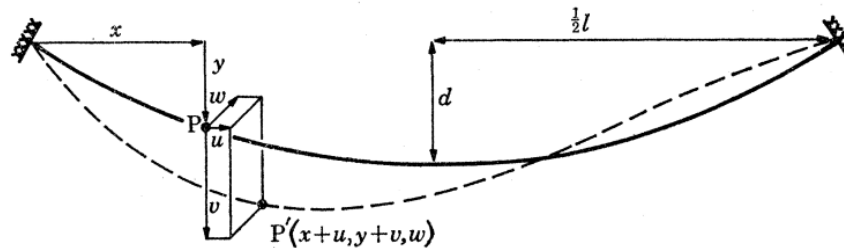


Figure 2.6.1.1 – Definition diagram for cable vibrations [21]

The equation of static equilibrium of a cable's element is the following one, in both directions:

$$\begin{cases} \frac{d}{ds} \left(T \frac{dy}{ds} \right) = -mg \\ \frac{d}{ds} \left(T \frac{dx}{ds} \right) = 0 \end{cases} \quad (2.6.1.1)$$

Where m is the mass of the cable per unit length, g is the acceleration due to gravity and T is the cable tension [N]. Moreover, $\frac{dx}{ds}$ is the cosine of the angle of inclination and $\frac{dy}{ds}$ the sine of the same one.

The solution of the two-equations system is given by the following formulation and it represents the profile adopted by the cable in static condition:

$$y = \frac{mgl^2}{2H} \left[\frac{x}{l} - \left(\frac{x}{l} \right)^2 \right] \quad (2.6.1.2)$$

Where l is the span and H is the horizontal component of cable tension T , such defined:

$$H = \frac{mgl^2}{8d} \quad (2.6.1.3)$$

Where d is the sag of the cable.

Before dealing with the dynamic behaviour, it is quite interesting how the Irvine's theory above could be extended into the case of a cable having supports not lying on the same level. Hence, the model is named sagging cable model, also known as elastic catenary model. A summary treatment of this general static sagging model is now given below. It describes the static profile of a cable by a set of non-linear equations and it has been studied and used in civil engineering since 1930s [23].

Figure 2.6.1.2 gives a representation of the so called inclined cable diagram.

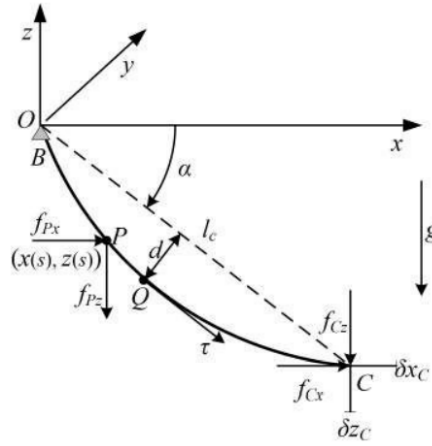


Figure 2.6.1.2 – Definition diagram for sagging cable [23]

In this theory, one of the cable ends is fixed, while an external force is applied to the other end. On the base of both external force and gravity contributes, the shape of the cable between points C and B will be not a straight line, but a sagging curve in the xOz plane [23].

Considering an arbitrary point named P, several analytical considerations can be pointed out, as follows:

Geometric constraint

$$\left(\frac{dx}{dp}\right)^2 + \left(\frac{dz}{dp}\right)^2 = 1 \quad (2.6.1.4)$$

Constraint for static equilibrium

$$f_p \frac{dx}{dp} = f_{Px} = f_{Cx} \quad (2.6.1.5)$$

$$f_p \frac{dz}{dp} = f_{pz} = f_{Cz} - \rho g(L_{us} - s) \quad (2.6.1.6)$$

Hooke's Law

$$f_p = EA \left(\frac{dp}{ds} - 1 \right) \quad (2.5.1.7)$$

Where: (x,z) is the Cartesian coordinate of point P; L_{us} and L_s are the unstrained and strained cable length between points C and B, respectively; s and p are the Lagrangian coordinate in the unstrained and strained cable profile, respectively, within the conditions $0 \leq s \leq L_{us}$ and $0 \leq p \leq L_s$; f_C is the cable force on point C; f_{Cx} and f_{Cz} are the components of f_C along x and z axis, respectively; f_p is the cable force on point P; f_{px} and f_{pz} are the components of f_p along x and z axis respectively; ρ is the cable mass per unit length; g is the gravitational acceleration; A is unstrained cross-sectional area; E is the Young's modulus.

Relating Equations (2.5.4) and (2.5.6), it derives that the force on P point f_p can be written as follows, since it is the combinations of its components according to Pythagorean Theorem:

$$f_p = \sqrt{(f_{px})^2 + (f_{pz})^2} = \sqrt{(f_{Cx})^2 + [f_{Cz} - \rho g(L_{us} - s)]^2} \quad (2.6.1.8)$$

Then, Equations (2.6.1.5) and (2.6.1.7) allows to write the differential ratios as functions of the force f_p , as follows:

$$\frac{dx}{dp} = \frac{dx}{dp} \frac{dp}{ds} = \frac{f_{Cx}}{f_p} \left(\frac{f_p}{EA} + 1 \right) \quad (2.6.1.9)$$

Now, substituting (2.6.1.8) into (2.6.1.9), it leads to:

$$\frac{dx}{ds} = \frac{f_{Cx}}{EA} + \frac{f_{Cx}}{\sqrt{(f_{Cx})^2 + [f_{Cz} - \rho g(L_{us} - s)]^2}} \quad (2.6.1.10)$$

The same reasoning is carried for the other incremental ratio, and thus:

$$\frac{dz}{ds} = \frac{f_{Cz} - \rho g(L_{us} - s)}{EA} + \frac{f_{Cz} - \rho g(L_{us} - s)}{\sqrt{(f_{Cx})^2 + [f_{Cz} - \rho g(L_{us} - s)]^2}} \quad (2.6.1.11)$$

Eventually, integration with the boundary condition $x(0)=0$ and $z(0)=0$ can be applied, and the static cable profile can be described by the two following equations:

$$x(s) = \frac{f_{Cx}s}{EA} + \frac{|f_{Cx}|}{\rho g} \left\{ \sinh^{-1} \left[\frac{f_{Cz} - \rho g(L_{us} - s)}{f_{Cx}} \right] - \sinh^{-1} \left[\frac{f_{Cz} - \rho g L_{us}}{f_{Cx}} \right] \right\} \quad (2.6.1.12)$$

$$z(s) = \frac{f_{Cz}s}{EA} + \frac{\rho g}{EA} \left(\frac{s^2}{2} - L_{us}s \right) + \frac{1}{\rho g} \left\{ \sqrt{(f_{Cx})^2 + [f_{Cz} - \rho g(L_{us} - s)]^2} - \sqrt{(f_{Cx})^2 + [f_{Cz} - \rho g L_{us}]^2} \right\} \quad (2.6.1.13)$$

2.6.2 Dynamic Model

If a small displacement from its static position is assigned, then the equilibrium of a generic infinitesimal element requires what follows:

$$\begin{cases} \frac{\partial}{\partial s} \left[(T + \tau) \left(\frac{dx}{ds} + \frac{\partial u}{\partial s} \right) \right] = m \frac{\partial^2 u}{\partial t^2} , \\ \frac{\partial}{\partial s} \left[(T + \tau) \left(\frac{dy}{ds} + \frac{\partial v}{\partial s} \right) \right] = m \frac{\partial^2 v}{\partial t^2} - mg , \\ \frac{\partial}{\partial s} \left[(T + \tau) \frac{\partial w}{\partial s} \right] = m \frac{\partial^2 w}{\partial t^2} , \end{cases} \quad (2.6.2.1)$$

Where u and v are the longitudinal and vertical components of the in-plane motion, while w is the transverse component one, perpendicular to the vertical plane, and τ is the additional cable tension due to the motion. It is clear that these different components are functions of both space and time.

A simplified formulation of vertical motion problem is provided:

$$H \frac{\partial^2 v}{\partial x^2} + h \frac{\partial^2 y}{\partial x^2} = m \frac{\partial^2 v}{\partial t^2} \quad (2.6.2.2)$$

$$H \frac{\partial^2 \omega}{\partial x^2} = m \frac{\partial^2 \omega}{\partial t^2} \quad (2.6.2.3)$$

The longitudinal component of the equations (2.6.2.1) is less important and can be ignored, since the analyses validity is just for cables with ratios of sag to span of about 1:8, or less [21]. Moreover, in equation (2.6.2.1) terms of the second order have been dropped.

The linearized cable equation is provided by the following:

$$\frac{h \left(\frac{ds}{dx} \right)^3}{E_c A_c} = \frac{\partial u}{\partial x} + \frac{dy}{dx} \frac{\partial v}{\partial x} \quad (2.6.2.4)$$

Where A_c and E_c are the area and the modulus of elasticity of the cable, respectively.

Thus equations (2.6.2.2), (2.6.2.4) and (2.6.2.4) are the ones that govern the dynamic problem.

The two component of motion, transverse and in-plane ones, are uncoupled because, to first order, the transverse horizontal motion is not linked to additional tension in cable. Moreover, the analysis of the conductor in-plane oscillations has to be split into other two components, which are symmetric and antisymmetric modes. Basically, in total analogy with just noticed for transverse motion, this separation is explained by the fact that to the first order, no additional tension τ is induced to the cable by the motion for the antisymmetric modes. On the other hand, it does for symmetric ones. Thus it is clear that the analysis induces two different levels of solution.

The transverse horizontal motion

It is the easiest motion between the all ones. Called ω the natural circular frequency of vibration, and by introducing a formulation of $w(x, t)$ like $w(x, t) = \tilde{w}(x)e^{i\omega t}$, the equation (2.6.2.3) is rewritten as follows:

$$H \frac{d^2 \tilde{w}}{dx^2} + m\omega^2 \tilde{w} = 0 \quad (2.6.2.5)$$

The boundary conditions are the following ones, from the nature of the restrains on the opposite sides of the wire, both perfectly rigid:

$$\tilde{w}(0) = \tilde{w}(l) = 0 \quad (2.6.2.6)$$

This gives the possibility to find the natural frequencies of vibrations, that are:

$$\omega_n = \frac{n \pi}{l} \sqrt{\frac{H}{m}} \quad n = 1, 2, 3, \dots \quad (2.6.2.7)$$

And also the transverse modes, represented by the following occurrence:

$$\tilde{w}_n(x) = A_n \sin\left(\frac{n \pi x}{l}\right) \quad n = 1, 2, 3, \dots \quad (2.6.2.8)$$

It is to highlight that $n = 1, 2, 3, \dots$ identifies the sequence of modes. For instance, the first transverse horizontal mode (the one represented by $n = 1$) is the lowest one.

The in-plane antisymmetric motion

For the case of the antisymmetric motion, the equation (2.6.2.2) can be simplified as follows, since the additional horizontal component of cable tension is zero:

$$H \frac{d^2 \tilde{v}}{dx^2} + m\omega^2 \tilde{v} = 0 \quad (2.6.2.9)$$

Where a formulation of $v(x, t)$ was introduced like $v(x, t) = \tilde{v}(x)e^{i\omega t}$:

$$\frac{d^2 \tilde{u}}{dx^2} + \frac{dy}{dx} \frac{d\tilde{v}}{dx} = 0 \quad (2.6.2.10)$$

Where the substitution of $u(x, t) = \tilde{u}(x)e^{i\omega t}$ is also made.

The following boundary conditions yield to a solution of the eigenvalue problem, in terms of natural frequencies:

$$\tilde{v}(0) = \tilde{v}\left(\frac{l}{2}\right) = 0 \quad (2.6.2.11)$$

$$\omega_n = \frac{2 n \pi}{l} \sqrt{\frac{H}{m}} \quad n = 1, 2, 3, \dots \quad (2.6.2.12)$$

And also the antisymmetric vertical modes, represented by the following occurrence:

$$\tilde{v}_n(x) = A_n \sin\left(\frac{2 n \pi x}{l}\right) \quad n = 1, 2, 3, \dots \quad (2.6.2.13)$$

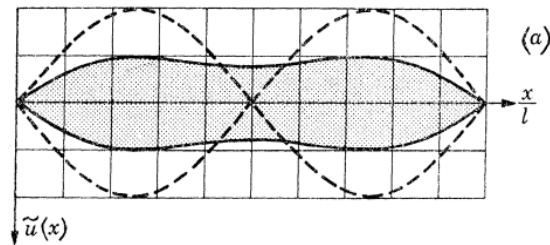
It is to highlight that $n = 1, 2, 3, \dots$ identifies the sequence of n-antisymmetric modes and A_n the amplitude corresponding.

The longitudinal components of motion are found from the equation (2.6.2.9) and symmetric since $\frac{dy}{dx}$ is null at mid-span, and by substituting the equation (2.6.2.12) and with rearrangement [21], it leads to:

$$\tilde{u}_n(x) = -4 \left(\frac{d}{l}\right) A_n \left\{ \left[1 - 2 \left(\frac{x}{l}\right)\right] \sin\left(\frac{2 n \pi x}{l}\right) + \frac{1}{n \pi} \left[1 - \cos\left(\frac{2 n \pi x}{l}\right)\right] \right\} \quad (2.6.2.14)$$

These kind of components become very small more and more the cable becomes flatter, so that $\frac{d}{l} \rightarrow 0$. Their maximum displacement occurs at the quarter span points and not at mid-span, where there is a local minimum as Figure 2.6.2.1 shows.

However, some authors showed that the assumption $h = 0$ is not so strict, in particular for cables with a ratio of sag to span of 1:8, like the one examined by Irvine's theory, since it conduces to an error of less than 4%.



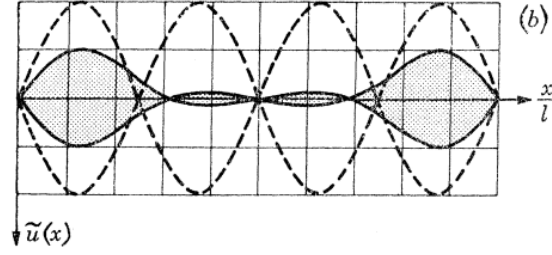


Figure 2.6.2.1 – Longitudinal and vertical components of the first two anti-symmetric in plane modes [21]

The in-plane symmetric motion

In this component, additional tension arises, as said before. The equation (2.6.2.2) can be rearranged as follows:

$$H \frac{d^2 \tilde{v}}{dx^2} + m\omega^2 \tilde{v} = \frac{8d}{l^2} \tilde{h} \quad (2.6.2.15)$$

Where a formulation of $v(x, t)$ was introduced like $v(x, t) = \tilde{v}(x)e^{i\omega t}$, $h(t) = \tilde{h}(x)e^{i\omega t}$ and $\frac{d^2 y}{dx^2} = -\frac{8d}{l^2}$. The cable equation is:

$$\frac{\tilde{h} \left(\frac{ds}{dx} \right)^3}{E_c A_c} = \frac{d\tilde{u}}{dx} + \frac{dy}{dx} \frac{d\tilde{v}}{dx} \quad (2.6.2.16)$$

The boundary conditions here are the following ones, leading to the formulation of the solution in terms of eigenvalues and thus natural frequencies:

$$\tilde{u}(0) = \tilde{u}(l) = 0 \quad (2.6.2.17)$$

$$\tilde{v}(0) = \tilde{v}(l) = 0 \quad (2.6.2.18)$$

$$\frac{\tilde{v}(x)}{8d} = \frac{\tilde{h}}{H} \frac{1}{(\beta l)^2} \left\{ 1 - \tan\left(\frac{1}{2}\beta l\right) \sin(\beta x) - \cos(\beta x) \right\} \quad (2.6.2.19)$$

Where $\beta = \sqrt{\frac{m\omega^2}{H}}$ and the value of (βl) has the role to identify the particular symmetric vertical mode component.

By using boundary conditions to the cable equation, this one can be expressed like the following one:

$$\frac{\tilde{h} L_e}{E_c A_c} = \frac{8d}{l^2} \int_0^l \tilde{v}(x) dx \quad (2.6.2.20)$$

Where L_e is defined as follows:

$$L_e = \int_0^l \left(\frac{ds}{dx} \right)^3 dx \approx l \left[1 + 8 \left(\frac{d}{l} \right)^2 \right] \quad (2.6.2.21)$$

Usually there is the aim to delete \tilde{h} from the equation (2.6.2.19) in order to obtain the following transcendental equation, from which natural frequencies and modes are given:

$$\tan\left(\frac{1}{2}\beta l\right) = \left(\frac{1}{2}\beta l\right) - \left(\frac{4}{\lambda^2}\right)\left(\frac{1}{2}\beta l\right)^3 \quad (2.6.2.22)$$

The parameter λ^2 is known as Irvine's parameter and it is introduced by the following expression:

$$\lambda^2 = \left(\frac{8d}{l}\right)^2 \frac{l}{H \frac{L_e}{E_c} A_c} \quad (2.6.2.23)$$

Which involves cable geometry and elasticity, so that it governs the nature of the roots of the equation. When λ^2 is very big, it occurs that the cable might be assumed inextensible and the equation (2.5.24) is reduced to:

$$\tan\left(\frac{1}{2}\beta l\right) = \frac{1}{2}\beta l \quad (2.6.2.24)$$

And the roots of this case are the following, distinguishing between the first ones and the others:

$$(\beta l)_{1,2} = 2,86\pi ; 4,92\pi \quad (2.6.2.25)$$

$$(\beta l)_n = (2n + 1)\pi \quad n = 3,4,5, \dots \quad (2.6.2.26)$$

The other limiting value and condition on λ^2 is when it is very small. The general transcendental equation becomes:

$$\tan\left(\frac{1}{2}\beta l\right) = -\infty \quad (2.6.2.27)$$

And the roots of this case corresponds to symmetric modes of the taut string:

$$(\beta l)_n = (2n - 1)\pi \quad n = 1,2,3, \dots \quad (2.6.2.28)$$

Figure 2.6.2.2 gives a representation of what just said about limits of values for λ^2 .

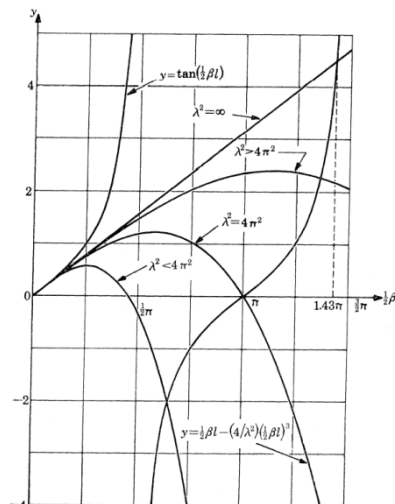


Figure 2.6.2.2 – Graphical solution for first non-zero root of equation [21]

In these terms, three important cases are made:

- (a) If $\lambda^2 < 4\pi^2$, the frequency of the first symmetric in-plane mode is less than the frequency of the first antisymmetric in-plane mode. The first symmetric vertical modes component has no internal nodes along the span.
- (b) If $\lambda^2 = 4\pi^2$, the frequency of the first symmetric in-plane mode is less than the frequency of the first antisymmetric in-plane mode. The first symmetric vertical modes component is tangential to the static cable profile at each support.
- (c) If $\lambda^2 > 4\pi^2$, the frequency of the first symmetric in-plane mode is less than the frequency of the first antisymmetric in-plane mode. The first symmetric vertical modes component has two internal nodes along the span.

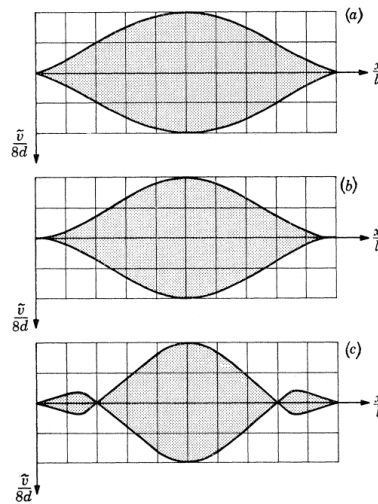


Figure 2.6.2.3 – Possible forms of the first symmetric vertical modal components [21]

2.7 Non-Linear Analysis

Since galloping problem involves conductors of aerial lines, the system is affected by highly non-linearity, perhaps in both terms of geometry and material. The former deals with abandonment of the key hypothesis on which the balance of the system is written on the undeformed configuration, while the latter concerns mechanical feature of materials, developing and changing along the load subjection.

As every single type of analysis can be split into two big pitches, static and dynamic, each of these might be split again into linear or nonlinear. Nonlinear behaviour of

structures depends analytically on the relation between forces and state of stress, that leads to non-linearity of balance equations.

The world of non-linearity may be caused by second order effects, due to large structural deflections, and a list of phenomena dealing with materials that changes the mechanical performances of the system. Elasto-plasticity, cracking, viscosity are just a few examples in which nonlinearity has a central role.

Actually, there are three kinds of non-linearity:

- Non Linear Geometry
- Non Linear Material
- Non Linear Boundary

In this Thesis only the first two classes will be considered, since they represent the most involved tool in civil engineering researches.

This Subsection is aimed to give an acknowledgement about this kind of analysis, that necessary moves away from basics concerning linear elasticity.

2.7.1 Non-Linear Geometry

Basically, the non-linear geometry bases its validity on the circumstance related to changes in geometry of the structure during the analysis. In this case, displacements affects the whole solution in terms of structural response to loads applied. It is mainly caused by large deflections yielding to a different shape of the model in relation to the initial one. Figure 2.7.1.1 highlight graphically what happens.

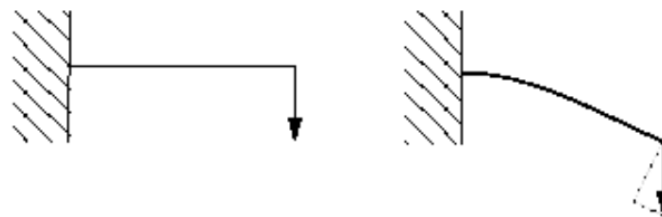


Figure 2.7.1.1 – Large deflections effect on a cantilever beam

As long as the magnitude of displacements, and thus deflections, remains small, the unloaded shape and the loaded one are approximately the same. This hypothesis is the base of linear analysis. However, if the intensity of deformations becomes bigger such to overcome the rational approximation of the two configurations, the stiffness of the system changes and the balance must to be written on the new shape acquired.

In fact, the load applied will start to generate other components acting on the beam, if it does not remain orthogonal to beam longitudinal development. As it deflects, the load is solved as a component perpendicular to the beam and a component acting along its longitudinal direction.

This situation is what actually happens in cable elements, representing transmission line's conductors, since deformed shape is extremely far from the unloaded one. Moreover, the deflections registered, in particular during dynamic oscillation response, are very significant and a linear approach would not explain the real characterization of the structure.

2.7.2 Non-Linear Material

The hypothesis on which linear attitude is based are the following ones:

- Deflections and displacements increase proportionally to the increase of load;
- Structural displacements are such small to allow to ignore the deformed shape obtained for acquiring balance;
- Boundaries are bilateral, thus they do not depend on load entity.

If all these conditions are respected and verified, the solution in terms of structural response is unique and the overlapping effects principle is valid.

Figure 2.7.1.2 gives a representation of what just explained.

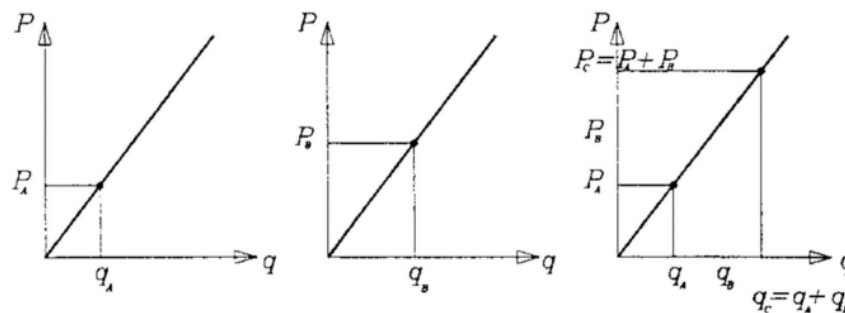


Figure 2.7.1.2 – Overlapping effects Principle [36]

In nature there is not any material that behaves in this way, due to constitutive bond which always implies a non-proportional relation between forces and deflections. A clear example is given by concrete, which is characterized by a strict nonlinear mechanical performance between stress and strain, but also steel with the critical point of yielding phenomenon.

Hence, Hooke Law in these terms should be not applied without any approximate conditions, much more how much the structural stiffness varies in relation to its deformed state. Figure 2.7.1.3 points out the non-linear bond, in which overlapping effects Principle is not valid anymore and the solution might not exist or not be unique.

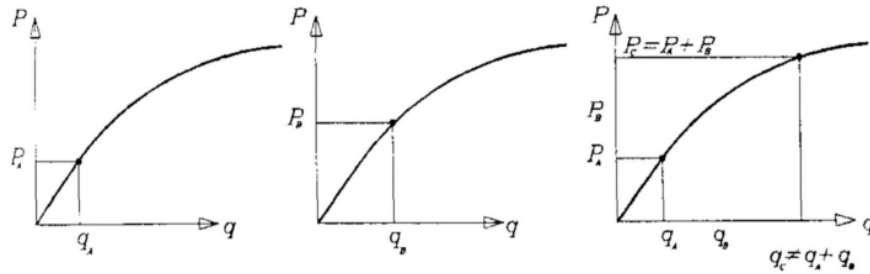


Figure 2.7.1.3 – Non-linear relation between forces and displacements (material) [36]

For this reason, there is a clear possibility that the wire studied will enter into plasticity field during dynamic oscillations. Furthermore, it has to be highlighted again that the transmission line studied in this Thesis was not designed for this kind of combination load. Thus, perhaps conductors would be subjected to stress forces that were not predicted in these terms, leading to an underestimation of the structural problem.

Chapter 3

Data collection and Numerical Analysis

This chapter deals with an overview of the input data collection with the aim of setting up the numerical analysis, loyal to real experiments carried out and case of study. Thus a description of the tools and numerical mean to rework the structural problem are provided and all the investigations to get through the aerodynamic conditions for the transmission line system are presented too.

Clearly, due to the reworking nature of the Thesis, input data are necessary derivative from tests and values yet collected by the foreign studies of Canada and Denmark. Among these we can find important several data, such as climatic one and atmospheric icing loads investigated through frequency analysis in order to reproduce in a loyal way the peculiar conditions of the site. For this reason, also a wind tunnel test was carried out, aimed at knowing the aerodynamic characteristics of the system wire-wind with even the determination of the influence of profile's geometry in air flow.

Eventually, a description of which kind of numerical model was used is given, also with the list of choices needed to adopt aimed at simplifying the problem in 1D and 2D space of work. Substantially, the numerical study was set with the mean of STRAUS7 at the beginning starting with a 1D-model aimed at verifying the theoretical solution; hence a 2D-model was settled with the software ANSYS in order to get through the aerodynamic behaviour of the system wire-air flow, so keeping attention to the conductor as an obstacle for the flow free direction; finally, an ideal 3D-model is given to reply all the contributes from both structural and aerodynamics behaviour, by the fusion of these two initial independent models.

3.1 Climatic data set – Icing Load

Climatic data used for the project were provided by the Norwegian company Kjeller Vindteknikk [1,14]. According to the company, both wind and ice loadings are obtained with the approach of WRF model (Weather Research and Forecasting), which is a numerical weather prediction (NWP) and an atmospheric simulation system designed for both research and operational applications [14]. Two models scales were adopted with the purpose of calculating weather loads. The former is a 4 km x 4 km wide grid and it was firstly employed with a temporal resolution of 1 hour for 20 years-reference period of observation, between 1995 and 2015. The latter is a 500 m x 500 m wide grid, employed with the aim to correct, scale and rotate wind speed and direction values coming from the first one. Respectively they are named WRF4km and WRF500m. Hence these collection datasets reproduce the reference values for the site studied in terms of atmospheric conditions both for ice and wind loading. Following Figure 3.1.1 represents an overview of the two models proposed.

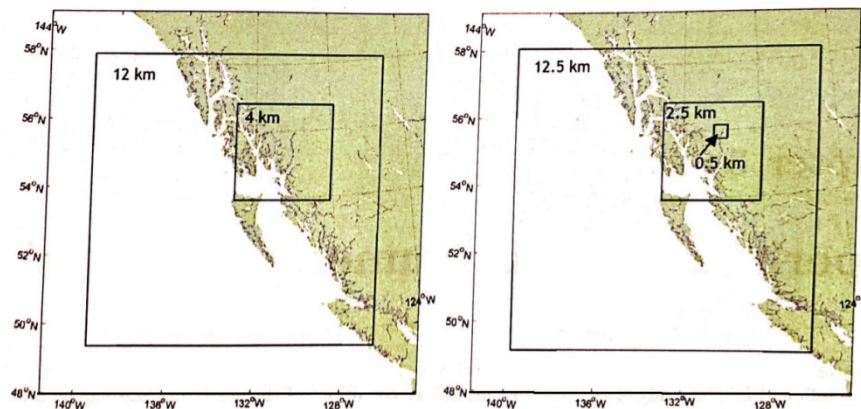


Figure 3.1.1 – WRF4km and WRF500m models, respectively [1]

The dataset is thus composed by time series of wind speeds and directions, temperatures and atmospheric liquid water content [1]. Wind load was directly computed by the meaning of this simulation, while ice load was needed to be completed with the use of the numerical ice accretion model based on the equation of icing, presented in Section 2.3).

It's important to highlight that both of these kind of loads were evaluated at an altitude of 20 m and were applied as hourly mean values to the whole relative span. According to dataset, the biggest magnitude in terms of wet snow accumulation was recorded at the point of Tower n°11, which is 1075 m a.s.l., and it was 5.50 cm thick, while the biggest

in-cloud icing formation was recorded at Tower n°16, which is 1485 m.a.s.l., with its 12 cm thick ice. Figure 3.2 gives a representation of what just said.

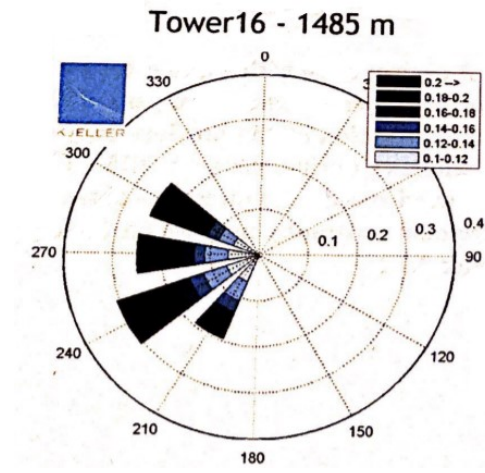


Figure 3.1.2 – In-cloud ice accretion for different wind directions [kg/m/hour] [1]

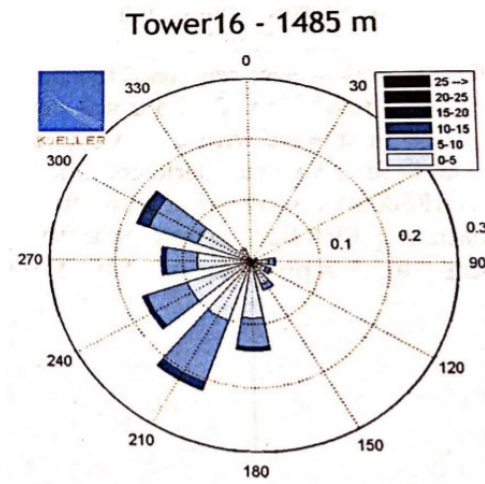


Figure 3.1.3 – Wet snow accretion wind rose [1]

Therefore, a statistical analysis was carried out by the Norwegian company Kjeller Vindteknikk, who kept just the extreme values of wind and ice datasets, with a return period of 50 years. As the International Standard establishes, these values correspond to the reference design one for the transmission line system. On the basis of this concept, the static design load, which corresponds to the maximum value obtained as the engineering approach wants, is associated with Tower n°16. This last one, hence, becomes the reference point and therefore the main field of applying analysis for all the research.

Anyway, it is very important to clear that the maximum load transferred to the towers in static conditions has the only role to be a yardstick for dynamic behaviour during galloping phenomenon on the line. This fact was due to the different conditions in which

the dynamic analysis was performed, firstly because the aerodynamic instabilities have been observed at atmospheric icing and wind conditions much lower than the ones referring to the worst static combination. Moreover, the will presented by the research group was to keep multiple combination of loads effects, not just one.

It is clear that aerodynamic analysis should have been based on a parametric set of values, dealing with firstly the different shapes acquired by the conductor section due to several combination of icing load, and secondly the wind load, considering different air flow conditions, speeds and angles of attack.

3.1.1 Ice shape and eccentricity

An ice profile in conductor section is considered by the two combination of ice shape and its eccentricity, defined as the ratio between the maximum ice thickness to the diameter of the wire conductor. In order to keep more comprehensive the work, the term eccentricity is referred to both the cases of wet snow and in-cloud icing.

It's important to highlight that according to International Standard, during the design phase of the transmission line system, a simplified ice-shape section was considered as the result of a constant radial ice formation. Certainly, this is a strong hypothesis since we all know that the ice accrete in an asymmetric way, yielding to an anti-symmetric profile section of the wire. Hence, the research was conducted on the base of the reference values of literature and experimental observations of different icing events. Also the magnitude of the eccentricity was referred to the literature and data available. The aim of this approach is to discover a limit value of eccentricity beyond which the galloping is less likelihood to develop [1]. Clearly, the results were compared to climatic datasets with the aim to compare them with the case of study.

The cross-sectional shape of the iced conductor depends on wind speed, the water droplets size and torsional stiffness of conductors [12], which plays a key role at defining a non-uniform distribution of ice shape along the wire longitudinal direction. This has to be explained in terms of hypothesis on which the theoretical approach of the theme is based, since the conductor is supposed to be fixed at the tower-anchorage, representing the extreme restraints. This condition leads to consider an infinite torsional stiffness at them, while it decreases more and more going at the mid span, where the torsional stiffness acquires the lowest value and the profile can rotate around its axis due to the

gravity load and ice-eccentricity. Figure 3.1.1.1 and Figure 3.1.1.2 show typical ice profiles at the mid span observed at wire tests carried out in Chinese experiments on overhead transmission line.

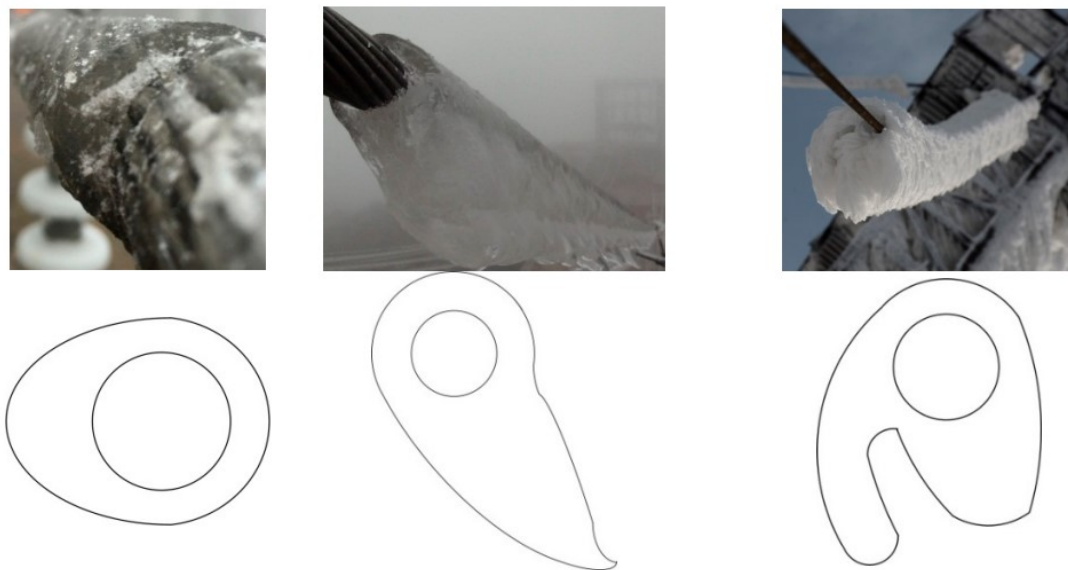


Figure 3.1.1.1 – Typical Crescent shape; Wing shape; Wing shape and eccentric circle [12]

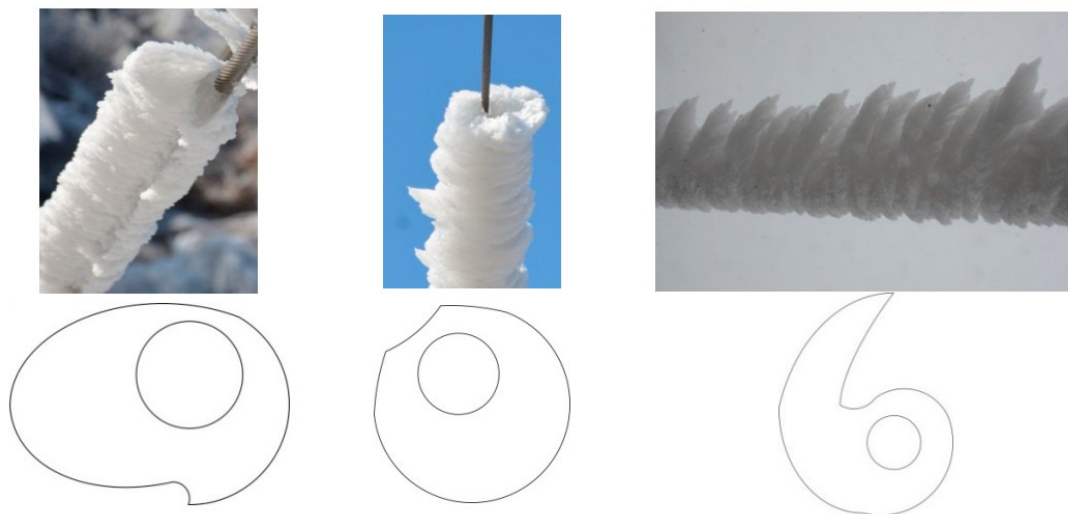


Figure 3.1.1.2 – Typical Eccentric oval shape; Eccentric round shape; Wing shape and round shape [12]

The fixed-anchorage hypothesis and its consequences just reported above give the following consideration: in fixed points the wire is not allowed to rotate and so it resists the torque, leading to expose always the same side to the atmospheric event and thus yielding the snow accreting along the wind axial direction (*axial growth*); on the other hand, the finite torsional stiffness recorded, more and more moving away from the limit points, makes rotations that allow snow precipitation to deposit on different sides of the profile, leading to a cylindrical-sleeve growth. The concept just presented is given by

Figure 3.1.1.3, showing the ice-accretion typical shapes along the longitudinal direction of the overhead wire.

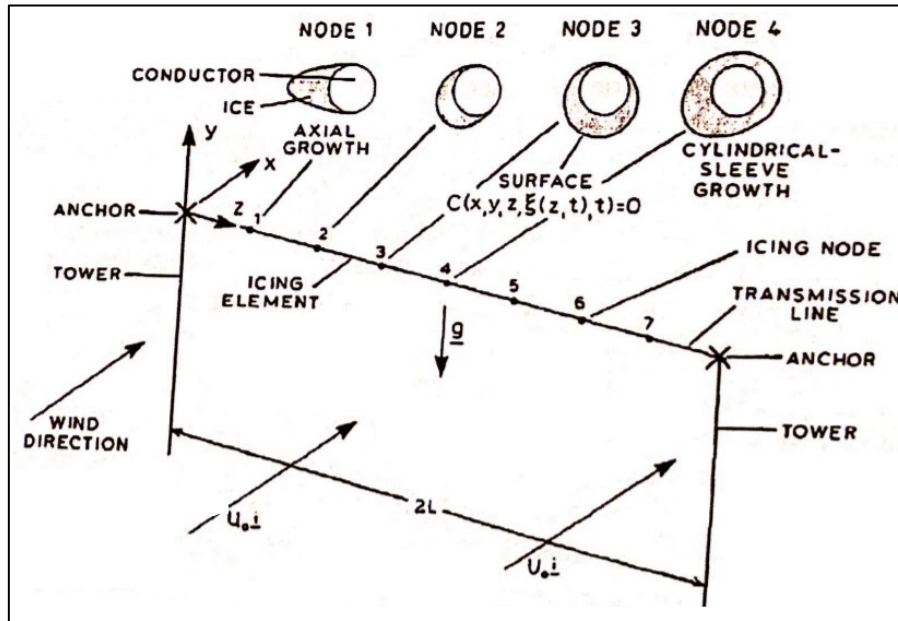


Figure 3.1.1.3 – Typical ice-shapes along the longitudinal direction of the wire [1]

The latter consideration is confident with the International Standard assumption on ice accretion design load, since it almost reproduces a uniform circular layer around the wire section and thus able to be represented by an equivalent radial thickness.

The difference between these two limit kinds of section profiles is well highlighted by Sakamoto [10] in which a graphic development of ice accretion is given and reported in Figure 3.1.1.4 and Figure 3.1.1.5.

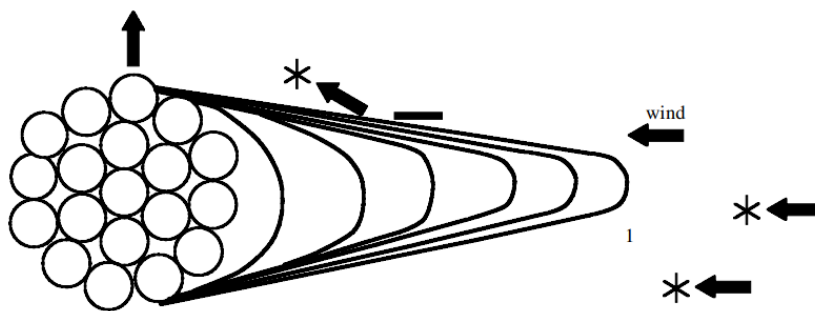


Figure 3.1.1.4 – Accretion on a torsionally rigid stranded wire (axial growth) [10]

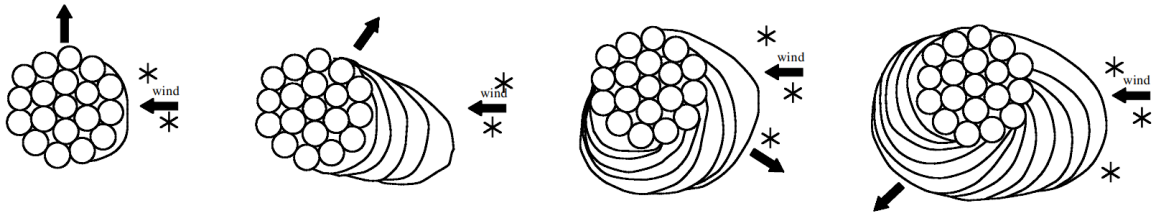


Figure 3.1.1.5 – Accretion on a stranded wire having low torsional stiffness (cylindrical-sleeve growth) [10]

According to him, the shape of snow accreted on overhead wires is governed by many factors, including stranding condition of the wire. The shape of the accreted snow may enhance the formation of cylindrical sleeve growth and lead to significant overload [10]. A different accretion is seen on a smooth wire of transmission line, as Figure 3.1.1.6 shows.

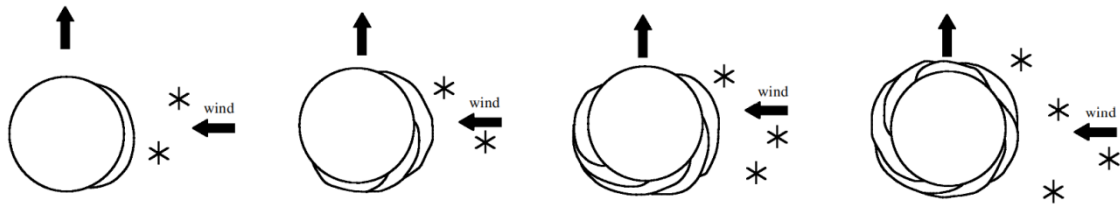


Figure 3.1.1.6 – Accretion on a smooth wire having low torsional stiffness [10]

However, in the project a stranded cylindrical wire is adopted and considered. Experimental evidences show that glaze ice shape is very irregular and quite different from the other kinds of ice and snow accretions, making itself difficult to predict and model with a sufficient precision. This fact led to ignore this natural contribute of precipitation, also due to its very low frequency in terms of occurring event, as will be explained next. Conversely, wet snow and rime ice accretions are closely similar in terms of section profile. Hence, a common shape for both events was regarded as the reference and equal to a semi-elliptical one, as also several previous authors suggested and adopted in order to rework an easier field of analysis. The semi-elliptical model adopted by the analysis set up during this Thesis is given by Figure 3.1.1.7.

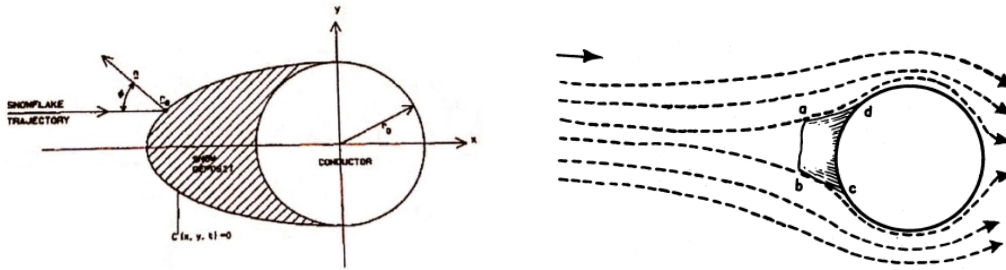


Figure 3.1.1.7 – Semi-elliptical model adopted for crescent shape profile [1] and evidence about the ice deposit on a cylinder-shape wire [11]

As the *State of the art of conductor Galloping* [5] records, all the galloping instabilities occurred did not exceed an eccentricity of 2 times the diameter of the conductor (e200 in Figure 3.1.1.8). This evidence may be expressed and explained by two reasons. First of all, more the ice accrete on the wire section, more the adhesion of snow and ice itself decrease and thus it leads to breaking the mass involved not only due to gravity but also because of the wind pressure. Moreover, thicker accretion on one side of the wire yields to move into rotation the all transverse section, which starts rotating on the base of its torsional stiffness. This fact leads to a creation of a new snow or ice layer on another side, which makes the whole section seeming to a cylindrical profile and thus not being exposed to galloping instability anymore.

Five different eccentricity were considered, as Figure 3.1.1.8 highlights.

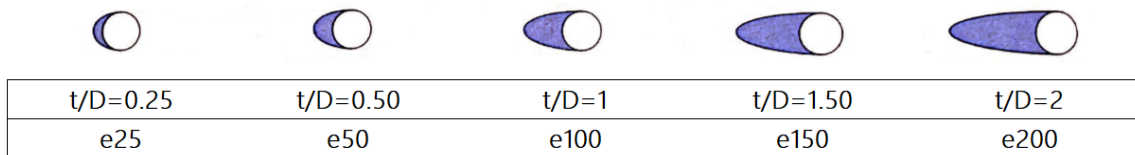


Figure 3.1.1.8 – Crescent profile for wet snow and rime ice accretion [1]

By assuming an ice-load density equal to the value of 916.80 kg/m^3 , corresponding to the general case of wet snow freezing after settled on the conductor, the calculation of its weight is immediate. Moreover, this value is quite in favor of safety as the distribution of other types of snow precipitation's density extends particularly below this limit.

According to the development of ice eccentricity and thus its ratio with the diameter of the wire which yields to a different transverse area, the weight per meter is gained by multiplying the density by the value of corresponding area. The set of this series of calculation is reported in Table 3.1.1.1 and its trend is showed in Figure 3.1.1.9.

Table 3.1.1.1 – Values dealing with transverse feature of every asymmetric shape and the corresponding values of weight per meter

<i>t/D ratio</i>		<i>Area</i>	<i>Density</i>	<i>Ice weight</i>
<i>e025</i>	25%	0,00055	0,50424	0,00494659
<i>e050</i>	50%	0,00065	0,59592	0,00584598
<i>e100</i>	100%	0,00085	0,77928	0,00764474
<i>e150</i>	150%	0,00105	0,96264	0,0094435
<i>e200</i>	200%	0,00125	1,146	0,01124226
		<i>mq</i>	<i>kg/m</i>	<i>kN/m</i>

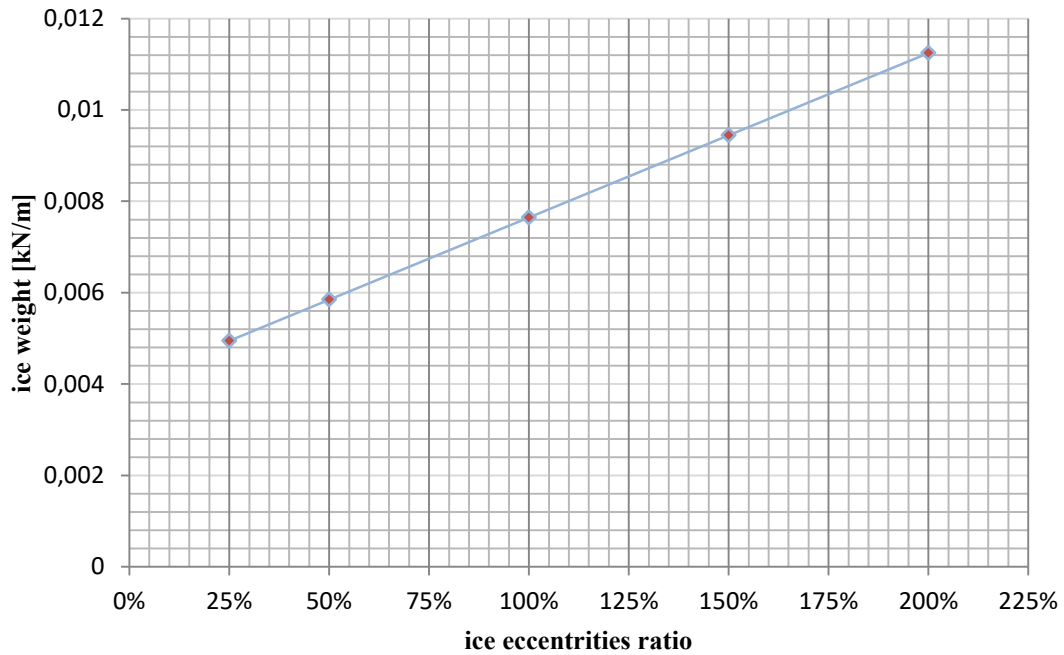


Figure 3.1.1.9 – Trend of ice weight according to eccentricities

3.2 Climatic data set – Wind Load

The reference values for wind speeds were considered on the base of literature and dataset about climatic conditions of the site during the 20 years observation period described in the reference document for this Thesis. The aim was to achieve the set of values below and beyond which galloping phenomenon generally does not occur. Table 3.2.1 gives an introduction of them.

Table 3.2.1 – Wind speeds reference data [1]

Case 1	Case 2	Case 3	Case 4
U=5 m/s	U=10 m/s	U=15 m/s	U=20 m/s

Although the set of wind Dataset contains four reference values of wind velocity, the nature of this kind of analysis is parametric, since it is strictly depending on the choice in terms of what kind of variable should vary and what not. Hence, it was needed to maintain the wind speed value constant and observing the phenomenon by varying all the other factors.

The reference value for wind flow velocity was chosen to 10 m/s, since it sums up a big part of wind speed distribution according to the hourly event, as Figure 3.2.1 shows, associated to the case of wet snow and eccentricity within e050 and e100.

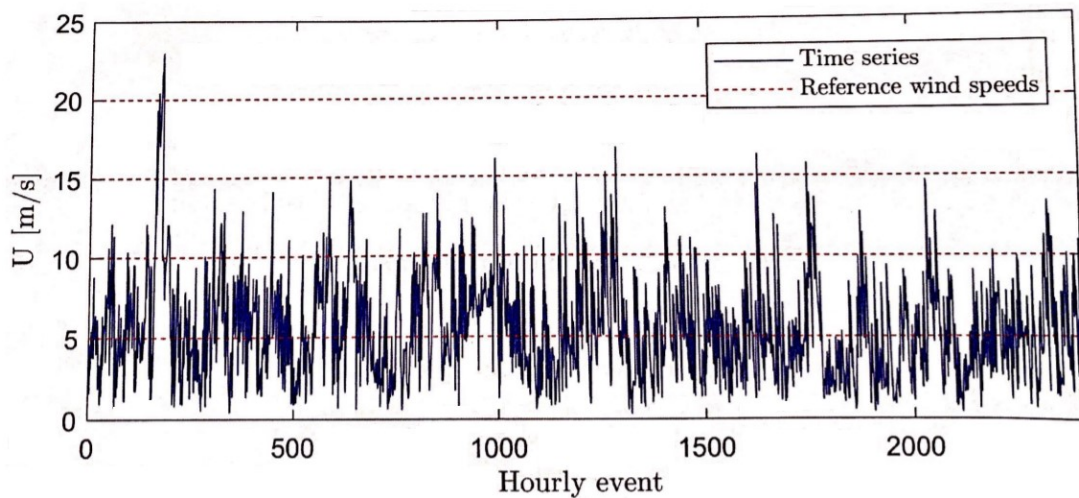


Figure 3.2.1 – Wind speed distribution for wet snow [1]

As Eurocode 1 states, Galloping oscillation starts at a special onset wind velocity U_{CG} and normally the amplitudes increase rapidly with increasing wind velocity [39]. This value is given by the following expression:

$$U_{CG} = \frac{2 Sc}{a_g} n_{1,y} b \quad (3.2.1)$$

Where Sc is the Scruton number as defined in [39]; $n_{1,y}$ is the cross-wind fundamental frequency of the structure; b is the width; a_g is the factor of galloping instability highlighted by Figure 3.2.2.

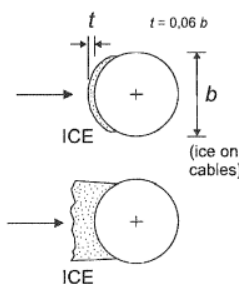
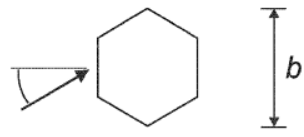
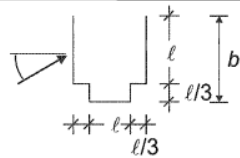
Cross-section	Factor of galloping instability a_G	Cross-section	Factor of galloping instability a_G
	1,0		1,0
			4

Figure 3.2.2 – Excerpt from Eurocode about Factor of galloping instability [39]

3.2.1 Wind tunnel test

In order to discover the trend of aerodynamic parameters dealing with the conductor studied in this contest of research, an experiment was set up in terms of Wind Tunnel test at the University of Western Ontario, Canada. The results were then reproduced and modeled thanks to the computational software ANSYS, which allowed to compare them and the precision level of both methods.

The will to investigate the trend of aeroelastic properties of the transmission line was translated thanks to a boundary layer wind tunnel facility, in which Den Hartog's coefficients were studied in relation to angles of attack and to several combination of wind and precipitation icing events. These properties have been calculated with a force-moment sensor, related to a reference system based on the coincidence of the x -axis and y -axis that lie on the horizontal plane and z -axis on the vertical direction. The convention here adopted was to make the x direction equal to the direction of the wind speed when the angle of attack is 0° , and thus the y -axis perpendicular to it. Then, varying the value of the angle of attack in anticlockwise direction, a set of angle of attacks were determined and used as reference magnitude for it. Figure 3.2.1.1 gives the set of intervals here used. As mentioned and explained in Chapter 2, the drag and lift forces were calculated in relation to the formulations already treated:

$$D = F_x \cos(\alpha) + F_y \sin(\alpha)$$

$$L = -F_x \sin(\alpha) + F_y \cos(\alpha)$$

Where α concerns the angle of attack, defined as the angle formed by the longitudinal direction of the wire and the free stream velocity of the wind.

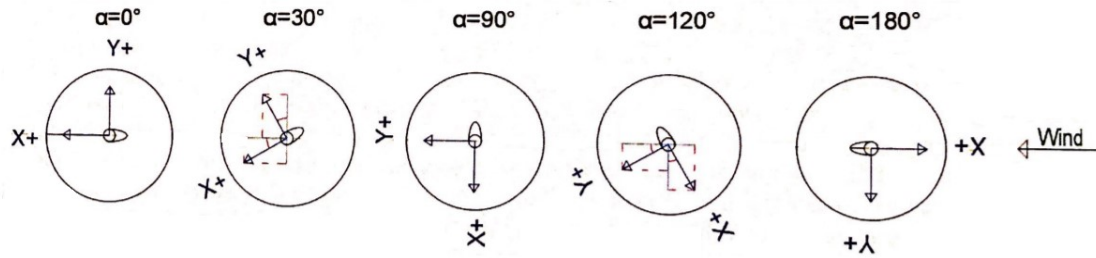


Figure 3.2.1.1– Set of increasing angle of attack adopted in the experiment [1]

The facility is a 33 m long open circuit wind tunnel [1], which means that it can reproduce realistic wind conditions, with a rectangular cross section that varies from 2.4x1.5 m to 2.4x2.15 m [1]. The capacity of this wind tool ends with a wind speed that acquires a maximum value of 55 km/h, which is about 15.3 m/s.

The principle on the base of which the experiment was conducted is a static force balance research. The model was mounted in a vertical way and made supportive to a plate able to record drag force, lift force and torque. Since the aim of the experiment was not to investigate the dynamic behaviour of the transmission line itself, but just in case its role as a body creating disturb to an airflow, supposed in a quasi-steady condition as Den Hartog's hypothesis highlights. Hence, the characteristics of the whole line were not reproduced, but just a realistic geometry of the iced wire section and air flow properties in a scale 1:1. Thus, the transverse section of the conductor was made by a cylindrical aluminum with the real diameter studied, 23.55 mm, and a length of 0.457 m. Figure 3.2.1.2 gives a representation of the wind facility.

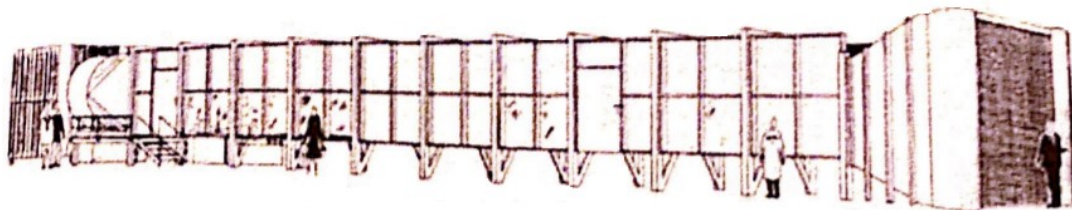


Figure 3.2.1.2– Representation of the Boundary layer wind tunnel test [1]

The choice of 23.55 mm length is linked to a will in order to avoid an overload on the plate balance, since the model is thought as a cantilever beam with the balance plate as the element reproducing the fix node and joint. The ice-shaped conductor was made possible thanks to a high precision hot wire cutting machine. The results of the profile eccentricities is given by Figure 3.2.1.3.

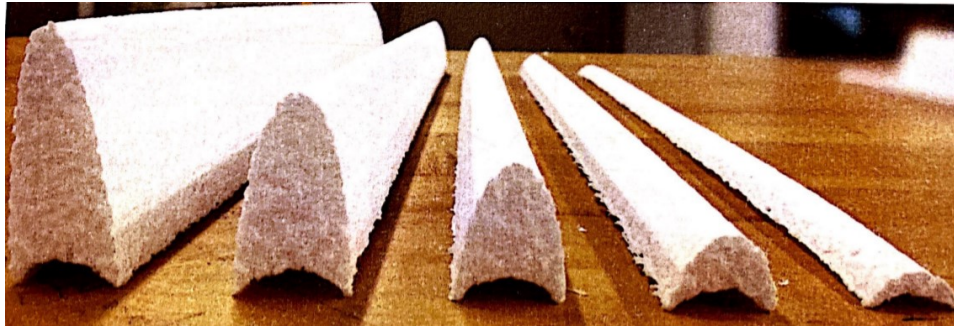


Figure 3.2.1.3– Results of ice profiles made by specific machine [1]

Furthermore, the choice of the model material was linked by the need to avoid the so called lock-in phenomena, dealing with resonance conditions caused by vortex shedding. In fact, if the frequency of the vortex induced vibrations hits the one of the model, several damaging vibrations occur and resonance conditions would take place. In this case, drag and lift values would be compromised, since they would be influenced by variation caused by additional inertia loads due to resonance. This aim was achieved through the use of a material like aluminum thanks to its significant stiffness and lightness at the same time.

The schematic representation of the model is given by Figure 3.2.1.4 and it concerns the SDOF system of the reverse pendulum.

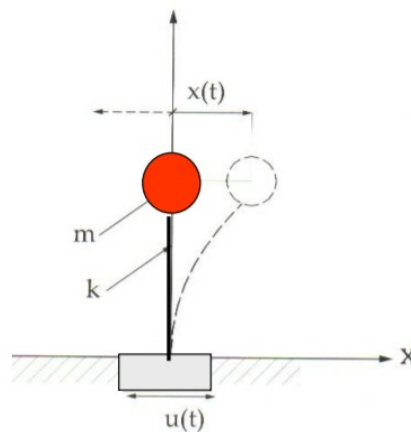


Figure 3.2.1.4– Schematic representation of the SDOF system [20]

According to dynamic formulation of SDOF system, the natural frequency of the model can be calculated as follows:

$$f_n = \frac{\omega}{2\pi} = \frac{1}{2\pi} \sqrt{\frac{K}{m}}$$

Where K and m are respectively the stiffness and the mass of the body.

The eigenfrequencies were obtained by hitting the model several times with and studying its behaviour and response, while the frequencies coming from the vortex shedding f were estimated by solving the equation introducing the Strouhal number, widely described in Subsection 3.4:

$$f = \frac{St U}{D}$$

Where U defines the free stream velocity, D is the reference length and St is the Strouhal number, defined as the non-dimensional form of the shedding frequency [15]. As in Subsection 3.4 will be reported, the value well-fitting with this case of study is 0.18, since it is linked to the profile of a crescent shape and Eurocode 1 suggests this kind of number for it. Clearly, all the parameters that assumed a key role in this test were several, such as wind speed, angle of attack and ice eccentricity. From the comparison of the eigenfrequencies analysis, it can be noted that more the wind speed increases, more the two kinds of frequencies intersect each other. The most dangerous risk is present in the case of $U=15$ m/s, the maximum value adopted for wind free stream velocity, where the second and third main eigenfrequencies of the model overlap the trend of the vortex shedding frequencies for all the eccentricities and for all the values of angle of attack [1]. Hence, in order to avoid this lock-in phenomena, it was decided to assume $U=10$ m/s as a reference value, where the risk of overlapping frequencies is quite rare.

3.3 Frequency-combining Analysis

While a quality analysis of both wind and atmospheric icing loads was presented, here a quantity review in terms of occurrence is given. In fact, in the reference of the observation period of 20 years a separated frequency analysis was carried out, then combined in order to give a complete information about the frequency occurrence of a particular load combination in terms of both wind and ice. Thus, firstly a singular study will follow dealing with every single type of icing forms and wet snow, associated with the relative wind speed distribution. Eventually, for every combination a 2D distribution is presented to consider a probabilistic density function for each natural event.

The in-cloud icing observations is presented in Figure 3.3.1 within the division of the events that characterize this kind of precipitation. Moreover, Figure 3.3.2 gives a representation of the histogram dealing with frequency distribution of different icing events considered.

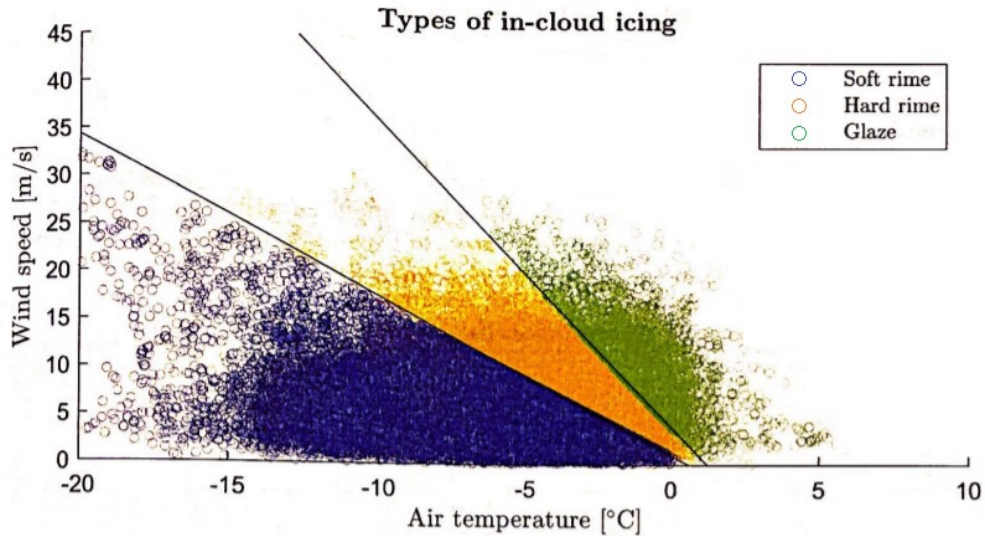


Figure 3.3.1 – In-cloud icing types [1]

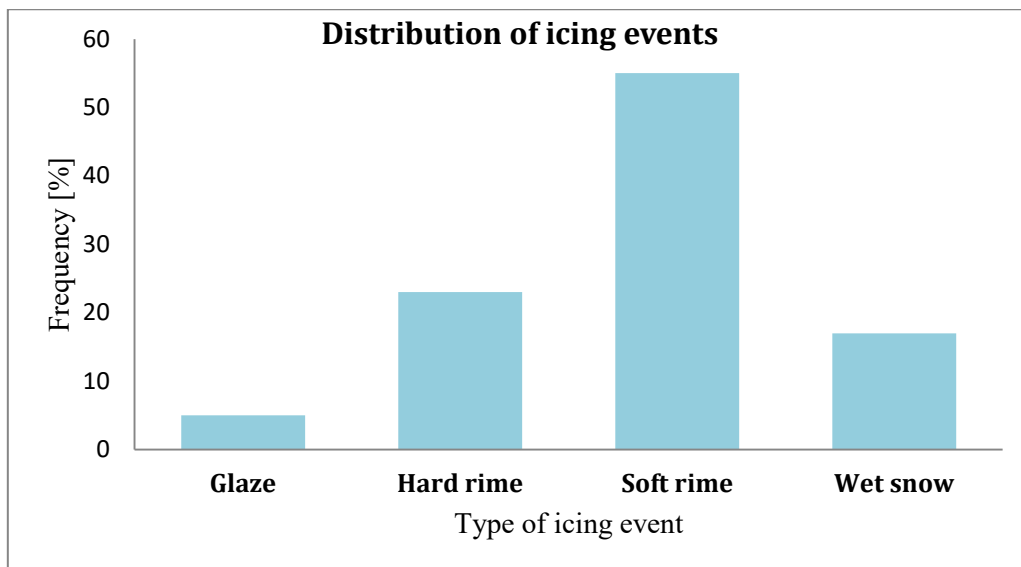


Figure 3.3.2 – Histogram of frequency analysis

The latter figure demonstrate that rime ice is the most frequent icing event observed, in particular Soft rime. Moreover, the figure highlights also how the Glaze condition represents less than the 10% of the overall icing precipitations observed, in particular the 6% [1]. This justifies the will to ignore the contribute of Glaze during the analysis, due to both its low significance and the necessary to simplify the analysis, reducing it to the worst and significant condition linked to galloping effects.

Eventually, a frequency analysis of the occurrence of a certain ice profile was carried out for each ice-event group. The mass per unit length was regarded as the reference quantity to calculate icing layers, first of all the magnitude of the mass related to each ice profile was calculated as follows:

$$M = A \rho$$

Where A is the transverse area of ice layer accumulated [m²] and ρ is ice density [kg/m³]. Clearly, the value of density depends on the kind of icing event.

For each weight class, and thus for each section of ice profiles, an analysis of wind speed occurrence was set up to be related with every kind of eccentricity.

It is important to highlight that wind load was considered blowing perpendicular to the line. Hence, the direction respect to the network was neglected in order to simplify the analysis, in particular for the 2-D numerical model. However, a joint frequency distribution of both the variables was studied with the aim to have a better interpretation and precision of the phenomenon.

Figure 3.3.3 shows the results of the frequency analysis dealing with wet snow in terms of eccentricity and wind speed.

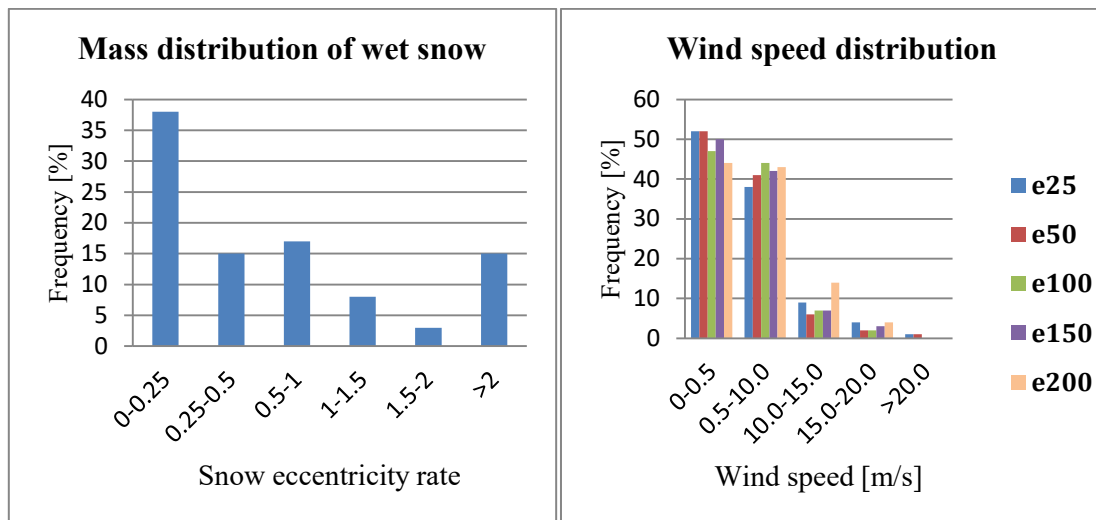


Figure 3.3.3 – Frequency analysis of wet snow

Figure above highlights that the majority values of eccentricities recorded during the reference period of observation of 20 years are distributed around the 25% of the conductor diameter, with a frequency occurrence of almost 40%. Just in a few cases, covering the 15 % singularly of the whole observation, the ice shape may arrive to reach 1 time and even 2 times the diameter. In terms of wind speed, it is clear how the values of wind velocity reach magnitude equal or lower than 10 m/s. Almost null is the frequency to have a speed higher than 20 m/s.

A joint analysis distribution is given in Figure 3.3.4, where a 3-D histogram is presented.

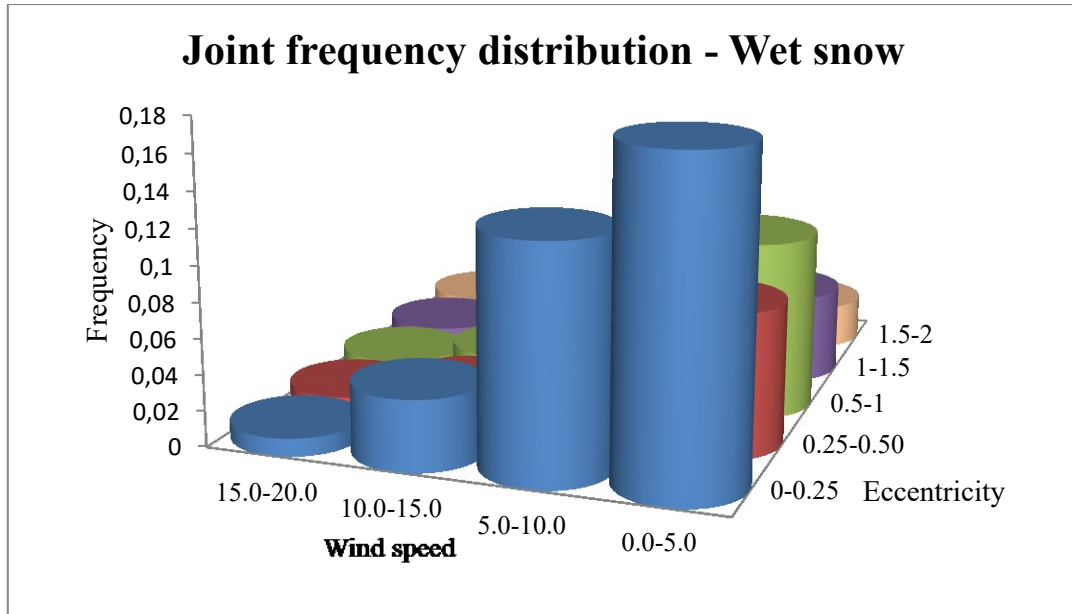


Figure 3.3.4 – Joint frequency distribution function for wet snow

Figure 3.3.4 clearly highlights how the most significant load combinations for wet snow are linked to configurations where the ice eccentricity and wind speed are small. In fact, the highest frequency of occurrence covers 20% of the whole cases [1] and it is recorded in the case of the e25 ice profile and wind speed with $U=5$ m/s, the lowest values considered according to datasets of the site and International Standards.

Figure 3.3.5 shows the results of the frequency analysis dealing with soft rime in terms of eccentricity and wind speed.

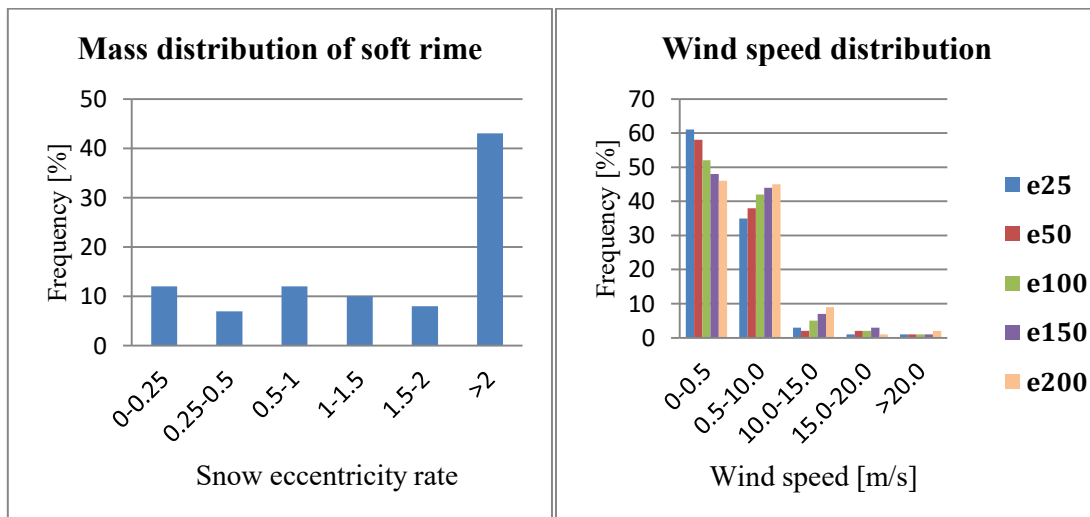


Figure 3.3.5 – Frequency analysis of soft rime

Figure above highlights that the majority values of eccentricities recorded during the reference period of observation of 20 years are distributed around the 200% of the

conductor diameter, so to times the diameter, with a frequency occurrence of more than 40%. Just in a few cases, covering the 15 % singularly of the whole observation, the ice shape may reach 1 time the diameter, or lower, but the smaller cases cover the majority of all cases considered. This consideration is extremely in contrast whit the study dealing with wet snow, since soft rime yields to a configuration less prone to galloping effects due to its larger ice load occurrence, and thus less interesting. In terms of wind speed, it is clear how the values of wind velocity reach magnitude equal or lower than 10 m/s. Almost null is the frequency to have a speed higher than 20 m/s, very similar to wet snow case.

A joint analysis distribution is given in Figure 3.3.6, where a 3-D histogram is presented.

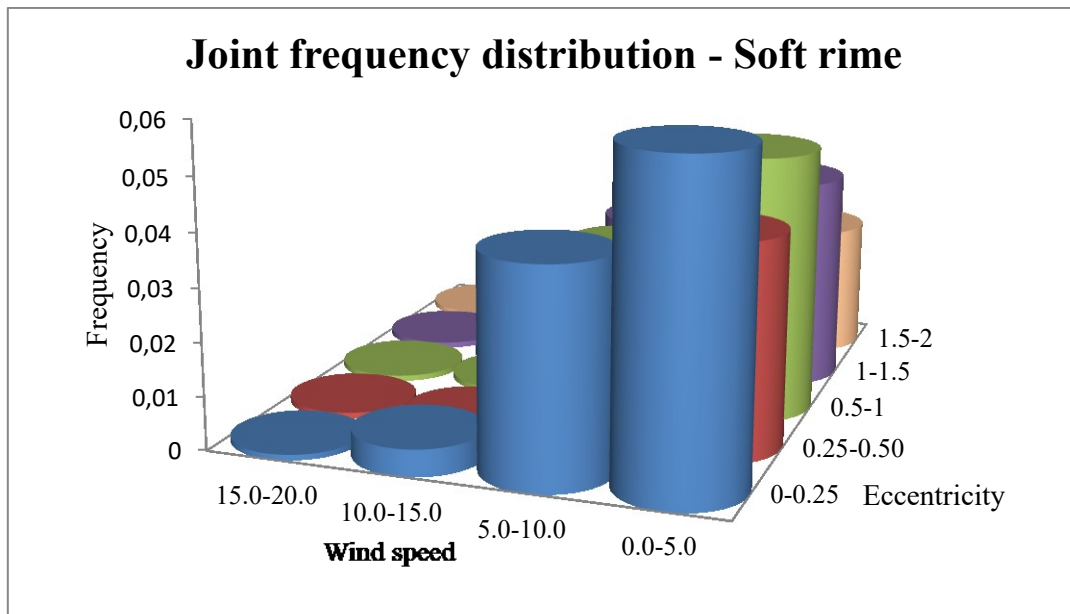


Figure 3.3.6 – Joint frequency distribution function for soft rime

Figure 3.3.6 clearly highlights how the most significant load combinations for soft rime are linked to configurations where the ice eccentricity and wind speed are small. In fact, the highest frequency of occurrence covers 7,5% of the whole cases [1] and it is recorded in the case of the e25 ice profile and wind speed with $U=5$ m/s, the lowest values considered according to datasets of the site and International Standards.

Figure 3.3.7 shows the results of the frequency analysis dealing with hard rime in terms of eccentricity and wind speed.

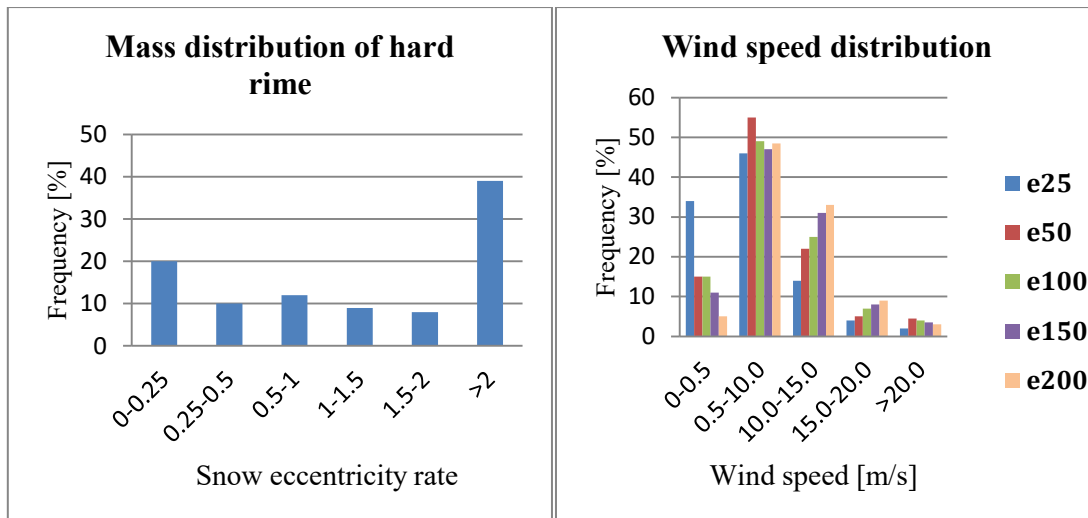


Figure 3.3.7 – Frequency analysis of hard rime

Figure above highlights that the majority values of eccentricities recorded during the reference period of observation of 20 years are distributed around the 200% of the conductor diameter, so to times the diameter, with a frequency occurrence of more than 40%. The result is very similar to the one of soft rime. In terms of wind speed, it is clear how the values of wind velocity reach magnitude equal or lower than 10 m/s. However, in this case the range most frequent is 5-10 m/s, rather than 0-5 m/s seen in soft rime. This fact is explained by the nature itself of hard rime, which requires bigger magnitude of wind speed to occur.

A joint analysis distribution is given in Figure 3.3.8, where a 3-D histogram is presented.

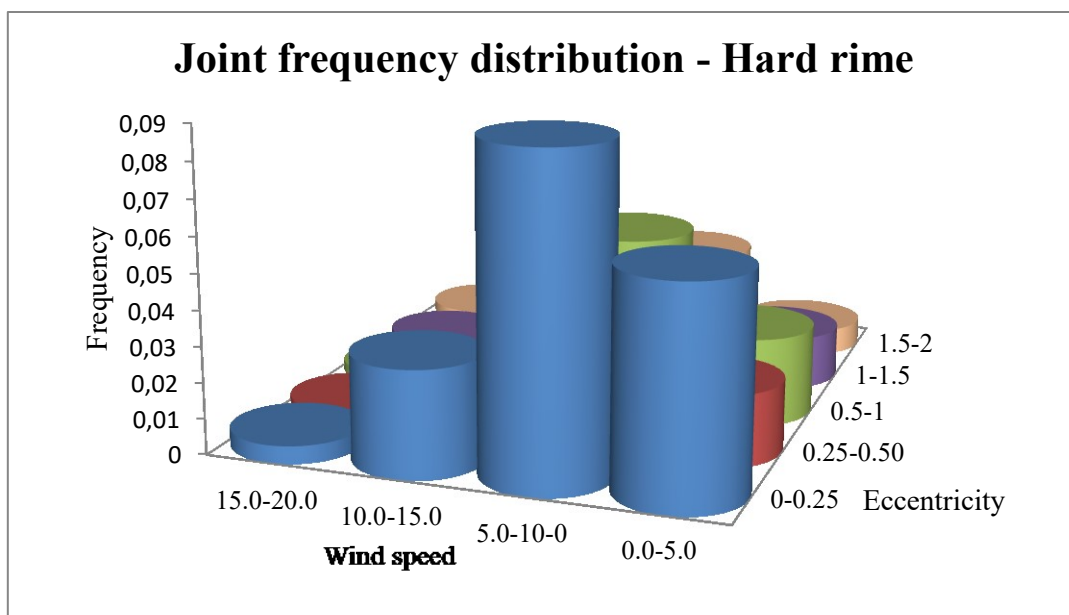


Figure 3.3.8 – Joint frequency distribution function for hard rime

Figure 3.3.8 clearly highlights how the most significant load combinations for hard rime are linked to configurations where the ice eccentricity and wind speed are not so big. In fact, the highest frequency of occurrence covers 9,6% of the whole cases [1] and it is recorded in the case of the e25 ice profile and wind speed with $U=10$ m/s.

By studying joint frequency occurrence of icing events in both terms of ice eccentricity and wind speed it can be clearly highlighted how the main responsible of galloping events is wet snow. Moreover, this consideration is in line with field observations about the kind of icing event that mainly yields to galloping instability [5].

3.4 Fluid dynamic model

In this section the fluid dynamics principles are presented and discussed in order to introduce the fluid behaviour with its mechanics and to explain the alternative aerodynamic analysis of the flow.

A fluid has the main feature of inability to endure shear stresses when at rest [29]. Any deviatoric stress can be supported by the fluid, but only hydrostatic or pressure one. The main variable related to a flow motion is velocity u . The strain rate $\dot{\epsilon}$ can be expressed as follows:

$$\dot{\epsilon} = \mathbf{S}u \quad (3.4.1)$$

Where \mathbf{S} is the strain operator.

A Newtonian fluid is regarded as characterized by a linear isotropic features, and its stress-strain relations require two important parameters [29].

The first one is the deviatoric stress, thus defined:

$$\tau_{ij} = \sigma_{ij} - \delta_{ij} \frac{\sigma_{kk}}{3} = 2\mu \left(\dot{\epsilon}_{ij} - \delta_{ij} \frac{\dot{\epsilon}_{kk}}{3} \right) \quad (3.4.1)$$

Where μ is the dynamic viscosity of the fluid, in total analogy with the shear modulus G in solid linear elasticity.

The second one is the definition of pressure, linked to the relation between the mean stress changes and the volumetric strain rates:

$$p = \frac{\sigma_{ij}}{3} = -\kappa \dot{\epsilon}_{ii} + p_0 \quad (3.4.1)$$

Where κ is the volumetric viscosity coefficient, in total analogy with the Bulk modulus in linear elasticity, and p_0 is the hydrostatic pressure.

Hence, it can be written as follows:

$$\sigma_{ij} = 2\mu \left(\dot{\varepsilon}_{ij} - \delta_{ij} \frac{\dot{\varepsilon}_{kk}}{3} \right) + \delta_{ij} \kappa \dot{\varepsilon}_{ii} - \delta_{ij} p_0 = \tau_{ij} - \delta_{ij} p_0 \quad (3.4.1)$$

Or in another way:

$$\sigma_{ij} = 2\mu \dot{\varepsilon}_{ij} + \delta_{ij} \left(\kappa - \frac{2}{3}\mu \right) \dot{\varepsilon}_{ii} + \delta_{ij} p_0 \quad (3.4.1)$$

Eventually, reminding the definition of strain ratio [29], it can be such written:

$$\tau_{ij} = 2\mu \left(\dot{\varepsilon}_{ij} - \delta_{ij} \frac{\dot{\varepsilon}_{kk}}{3} \right) = \mu \left[\left(\frac{\partial u_i}{\partial x_j} + \frac{\partial u_j}{\partial x_i} \right) - \delta_{ij} \frac{2}{3} \frac{\partial u_k}{\partial x_k} \right] \quad (3.4.1)$$

If we consider the fluid density named ρ , the balance of the mass flow ρu_i , in relation to an infinitesimal control volume [29], such as in Figure 3.4.1, can be written as follows:

$$\frac{\partial \rho}{\partial t} + \frac{\partial}{\partial x_i} (\rho u_i) = \frac{\partial \rho}{\partial t} + \nabla^T (\rho \mathbf{u}) = 0 \quad (3.4.1)$$

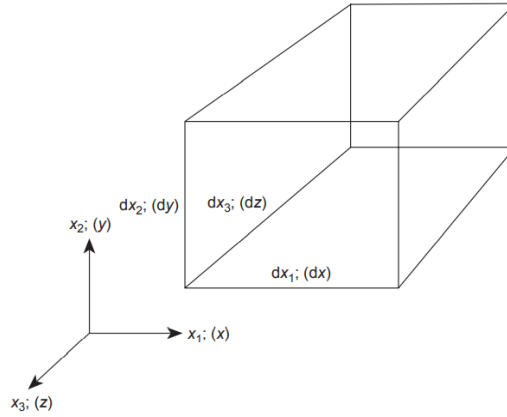


Figure 3.4.1 – Infinitesimal control volume and its Cartesian coordinates [29]

The momentum balance is linked to $(\rho u_j)u_i$ and can be expressed in j-direction as follows:

$$\frac{\partial (\rho u_j)}{\partial t} + \frac{\partial}{\partial x_i} [(\rho u_j)u_i] - \frac{\partial}{\partial x_i} (\sigma_{ij}) - p f_i = 0 \quad (3.4.1)$$

In terms of energy conservation, pressure and density are linked to absolute temperature by the following expression:

$$\rho = \rho(p, T) = \frac{p}{RT} \quad (3.4.1)$$

Where R is the universal gas constant. The introduction of intrinsic energy allows to define total energy of the problem:

$$e = e(p, T) \quad (3.4.1)$$

$$E = e + \frac{u_i u_i}{2} \quad (3.4.1)$$

Thus, enthalpy is now defined:

$$h = e + \frac{p}{\rho} \quad ; \quad H = E + \frac{p}{\rho} \quad (3.4.1)$$

Thanks to the conductive heat flux law:

$$q_i = -k \frac{\partial}{\partial x_i} T \quad (3.4.1)$$

Where k is the isotropic thermal conductivity.

By a series of mathematical passages included in [29], it can be finally written energy balance like follows:

$$\frac{\partial(\rho E)}{\partial t} + \frac{\partial}{\partial x_i}(\rho u_j H) - \frac{\partial}{\partial x_i} \left(k \frac{\partial T}{\partial x_i} \right) + \frac{\partial}{\partial x_i}(\tau_{ij} u_j) - \rho f_i u_i - q_H = 0 \quad (3.4.1)$$

The motion of a fluid is governed by a set of equations in terms of continuity, momentum and energy. They are well-known as Navier-Stokes equations and describe the behaviour of a generic flow in the 3D space, keeping in mind its viscosity, turbulence, thermal effects and compressibility. They are now written in the general conservative form:

$$\frac{\partial \Phi}{\partial t} + \nabla \mathbf{F} + \nabla \mathbf{G} + \mathbf{Q} = 0 \quad (3.4.1)$$

In some cases, the flow can be treated as incompressible with the aim to simplify the problem. This assumption leads to decoupling continuity and momentum equations from the energy one, written as follows:

$$\frac{\partial \rho}{\partial t} + \nabla(\rho u) = 0 \quad (3.4.1)$$

$$\rho \frac{\partial u}{\partial t} + \rho(u \cdot \nabla)u = -\nabla p + F + \nabla \cdot \mu(\nabla u + (\nabla u)^T) = 0 \quad (3.4.2)$$

Where ρ is the flow density, u is the fluid velocity vector, p is the pressure, μ is the viscosity and F the external force acting to the fluid. In the latter equation, there is an implicit term known as stress tensor and such defined:

$$\tau = \mu(\nabla u + (\nabla u)^T) \quad (3.4.3)$$

This term allows to rewrite equation (3.4.1) through the toll of tensors as follows [31]:

$$\frac{\partial}{\partial t} \begin{bmatrix} \rho \\ \rho \mathbf{U} \\ \rho E \end{bmatrix} + \nabla \begin{bmatrix} (\rho \mathbf{U})^T \\ \rho \mathbf{U} \mathbf{U} + p \mathbf{I} - \boldsymbol{\tau} \\ (\rho H \mathbf{U} - \boldsymbol{\tau} \mathbf{U} + \mathbf{q})^T \end{bmatrix} = 0 \quad (3.4.4)$$

The hypothesis of incompressible airflow studied in this section allows also to reduce the first equation in the following one, since the density variation with the pressure is such small that it can be considered as constant in the gradient term, as well as the viscosity:

$$\frac{\partial \rho}{\partial t} + \nabla(\rho u) = 0 \rightarrow \nabla u = 0 \quad (3.4.4)$$

The flow behaviour is also closely linked to several dimensionless quantity numbers such as Reynolds and Strouhal numbers. The former is the ratio of inertial to viscous forces of a flow and it gives information of the flow condition:

$$Re = \frac{\rho U D}{\mu} \quad (3.4.5)$$

Where ρ is the flow density [kg/m^3], U is the relative velocity of the flow respect to the conductor, μ is the viscosity [kg/m s] and D is the characteristic length [m], used to relate the spatial extension of the geometry to the fluid properties.

The conditions expressed by Reynolds number are basically used to define a fluid as laminar or turbulent. The transition zone from laminar to turbulent depends strictly on the theoretical model or the reference author, but also it varies in relation to the nature of the obstacle for the flow. In this case, which is related to an airflow pasting a cylinder corresponding to the wire conductor, the flow could be regarded as fully turbulent if $Re > 2 \cdot 10^5$. Laminar flows have smaller Reynolds numbers and above a critical Reynolds number the flow turns into a turbulent regime [3]. A turbulent condition is characterized by a boundary level becoming turbulent forming disorganized and narrow wakes on the downside of the cylinder. This kind of flow is described by stochastic velocity fluctuations in both magnitude and directions. Figure 3.4.1 shows two examples of vortex shedding with a cylindrical conductor:

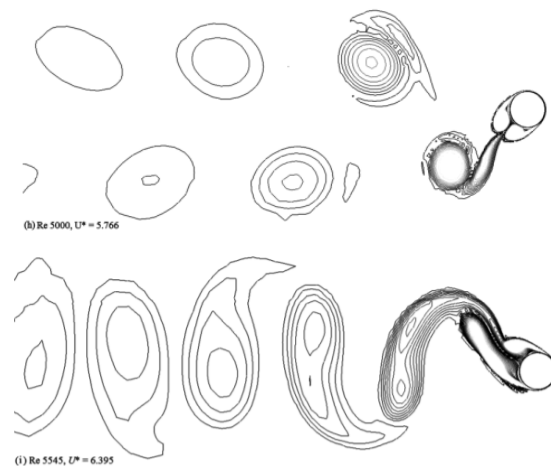


Figure 3.4.1 – Boundary layer around a cylinder creating vortex shedding [15]

The latter number, Strouhal one, describes the transient flow mechanisms based on the vortex shedding frequency f and the ratio of the characteristic length and the flow velocity. It is such defined:

$$St = f \frac{D}{U} \quad (3.4.6)$$

Where f is the vortex shedding frequency, U is the relative velocity of the flow respect to the conductor and D is the characteristic length [m]. A value of 0.18 for the Strouhal number fits well for cylindrical structures such as a cable in transmission line systems. Indeed, Eurocode 1 suggests this kind of number for circular cross sections, as Figure 3.4.2 highlights.


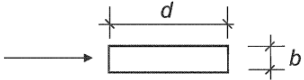
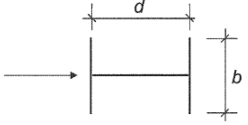
Cross-section	St
 for all Re -numbers	0,18
 $0,5 \leq d/b \leq 10$	from Figure E.1
 linear interpolation	$d/b = 1$ 0,11 $d/b = 1,5$ 0,10 $d/b = 2$ 0,14

Figure 3.4.2 – Excerpt from Eurocode 1 about Strouhal number for several cross sections [39]

Another important number in fluid dynamics is Scruton number, which describes the susceptibility of vibrations depends on the structural damping and the ratio of structural mass to fluid mass [39]. In other words, it is a non-dimensional number representing the trend of a structure to be susceptible to vortex shedding and in particular to lock-in phenomena. Its formulation is given by (3.4.7).

$$Sc = \frac{2 \delta_s m_{i,e}}{\rho b^2} \quad (3.4.7)$$

where δ_s is the structural damping expressed by the logarithmic decrement; ρ is the air density under vortex shedding conditions; $m_{i,e}$ is the equivalent mass per unit length and b is the reference width of the cross-section at which resonant vortex shedding occurs [39].

About structural dumping, it has been observed that transmission lines has a dumping coefficient equal to 0.04 (4%) [40]. This value will be considered in terms of comparison between undumped cable response and dumping effect to vibrations.

3.4.1 Computational resolution methods

Several methods can be set up in order to find a solution for the set of Navier-Stokes equations. The first intuitive approach that can be assumed is the directed one, based on a total simulation of the motion. In his theory, A. N. Kolmogorov, established that the factors playing a key role in a turbulent fluid are just ϵ and ν . The former represents the mean value of dissipated energy, while the latter is the kinematic viscosity of the fluid. According to him, for every single L length, where L is defined as a ratio of the body's dimension, there should be a number of nodes equal to $N \approx Re^{3/4}$ [31]. Hence, for a single cube of volume L^3 there should be a number of nodes equal to $N^3 \approx Re^{9/4}$ [31]. Moreover, the time step requires to be chosen according to the fluid dynamic phenomenon investigated, in order to catch every significant feature of the motion. The method just introduced is also known as Direct Numerical Simulation (**DNS**), and it needs a very refined mesh and 3-D grid, since vortex fluctuations are three-dimensional and also small scales of a turbulent flow are important [3]. This kind of numerical method requires a very high computational cost, solving both spatial and temporal fields of the equations, and the range of applicability is limited to small values of Reynolds number. Hence, also for modest values of Reynolds it can become an important challenge for modern calculators, so it cannot be always applied.

A valid alternative can be Large Eddy Simulation (**LES**), which gives only a spatial solution to the problem. The main feature of this approach is that the largest scales are directly simulated with an opportune dense grid, while the smallest ones are parameterized with a model [31]. The cost is reduced due to modeling eddies smaller than the mesh size and considering the most of kinetic energy as transported by the larger turbulent scales [1]. The derivation of equations for LES modeling is performed in a very similar way to Reynolds approach, defining a so called filter function:

$$\bar{u}(x, t) = \int u(y, t) G(x - y, t) dy \quad (3.4.1.1)$$

Where $G(x - y, t)$ is the filter. In this way, it is allowed to split the velocity field into a filtered part and a sub-grid one [31]:

$$u(x, t) = \bar{u}_i(x, t) + u'_i(x, t) \quad (3.4.1.2)$$

Since LES method could be expensive in terms of computational cost for many practical applications, even if requires a lower demand than DNS, most of times the Reynolds-Averaged Navier-Stokes method (**RANS**) is used. This approach uses time-averaged

flow variables, which reduces the numerical cost more than the other solutions. It consists of a split of the flow into two components which are the time-average and its fluctuations. This kind of solution is also called Reynolds decomposition and with this approach the deformation stresses is separated, in a total analogy of what happens in LES equations. The latter term in (3.4.1.2), $u'_i(x, t)$, is linked to the deviation from the former one, $\bar{u}_i(x, t)$, which is derived by the average of the following instantaneous quantities:

$$\bar{U}_i(x, t) = \lim_{N \rightarrow \infty} \frac{1}{N} \sum_{n=1}^N U_i^{(n)}(x, t) \quad (3.4.1.3)$$

The splitting variables can be also named as follows, with the aim to give a general description of the method:

$$\phi = \bar{\phi} + \phi' \quad (3.4.1.4)$$

where $\bar{\phi}$ is the time-average and ϕ' the fluctuating component. This allow to give a graphic representation of the RANS solution way, that can be expressed in both terms of steady and unsteady conditions. Figure 3.4.1.1 shows what just said:

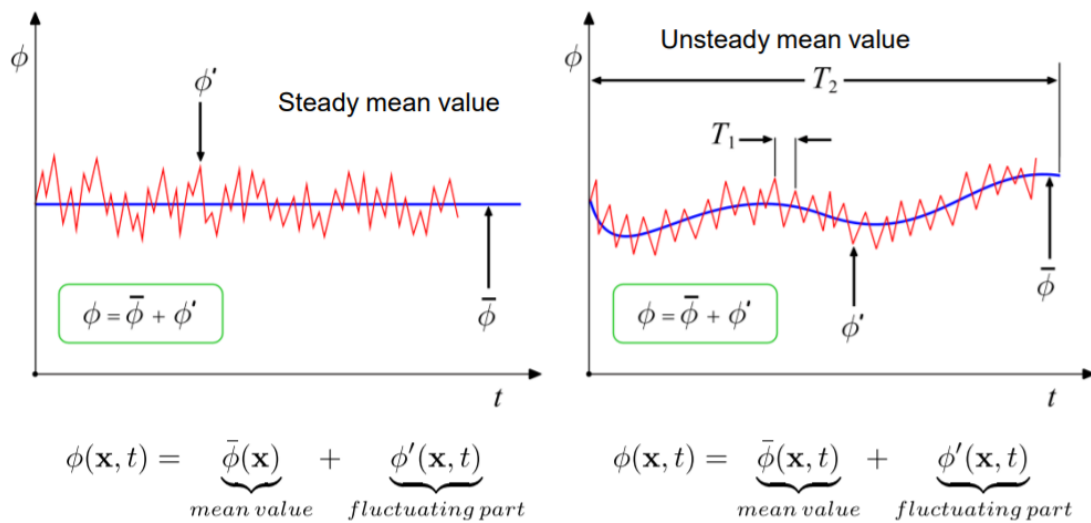


Figure 3.4.1.1 – Representation of RANS concept both steady and unsteady [17]

Substituting these expressions in time-average continuity and momentum equations, a formulation of the average flow is reached. It is quite important to highlight that if the continuity equation does not change its nature, the momentum one gets an additional term, which makes the equation itself not close. This unknown term is also called Reynolds stress [16], since it produces an additional stress to the flow. Momentum equation is now thus expressed:

$$\rho U \cdot \nabla U = -\nabla p + \nabla \cdot \mu(\nabla U + (\nabla U)^T) - \nabla(\rho \overline{U' \otimes U'}) \quad (3.4.1.5)$$

The Reynolds stress itself needs to be solved through the meaning of several alternative methods that could yield a closure formulation for momentum equation. One of them is based on the Boussinesq hypothesis [16], according to which Reynolds stress varies linearly with the velocity, in analogy with shear stress in a viscous fluid [3]. It introduces the eddy viscosity μ_t , even if it requires simple turbulent shear flows to be applied. The equation (3.4.1.4) becomes:

$$\rho U \cdot \nabla U = -\nabla p + \nabla \cdot ((\mu + \mu_t) \cdot (\nabla U + (\nabla U)^T)) \quad (3.4.1.6)$$

The eddy viscosity is determined by the standard k- ϵ turbulence model and thus defined:

$$\mu_t = \rho C_\mu \frac{k^2}{\epsilon} \quad (3.4.1.7)$$

where $C_\mu=0.09$ is a model constant, k the turbulent kinetic energy and ϵ the turbulent dissipation rate.

Other turbulence methods are based on RANS equations (time averaged) and now introduced:

- Zero equation model
- One-equation model
- Two-equations model: k- ϵ models, k- ω models, ASM
- Seven-equations model: Reynolds stress model

The number of equations highlights the number of additional PDE that are solved [28].

The most used method is therefore k- ω one, also used in this thesis and applied in CFD software for flow simulations. Figure 3.4.1.2 shows the just introduced approaches in solving turbulence scales.

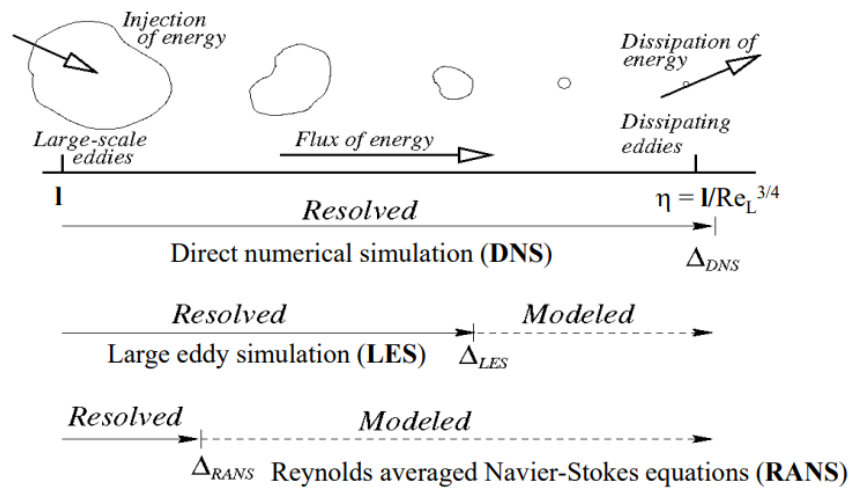


Figure 3.4.1.2 – Prediction method for turbulent models [28]

Eventually, another method can be performed as an hybrid between LES and RANS models. It is called Detached Eddy Simulation (**DES**) and it is consisted of a split of modeling. In these terms, the motion of the flow near walls is simulated through a RANS model, while the far areas follow a LES model [31]. With this approach, the fluid domain is separated into two macro areas in which the discretization does not require a constant development and thus it can reduce the computational cost.

3.4.2 Boundary layer

The boundary layer is the region in which viscous forces are dominant over the inertial ones. Even if it consists of a very small layer, in the boundary level the velocity rapidly turns from null into undisturbed values, when inertial forces are bigger than viscous effects, which cannot damp fluctuation anymore. These last one are significant only at the surface of the body, or at very low distance from this. Hence, chaotic and turbulent motion born after the instability of laminar boundary layer, which rapidly is subjected to posting and energy dissipation.

There are two strategies to model the turbulent flow in this region. The first one is the Low Reynolds method, which requires a very fine mesh solving the RANS equations and accounting increasing effect of the viscosity with damping functions. The second one is Wall Function method, where a wall function is used to describe the flow in the near wall region. It is also called Logarithmic Law of the Wall, since its logarithmic trend in describing flow development, as Figure 3.4.2.1 shows.

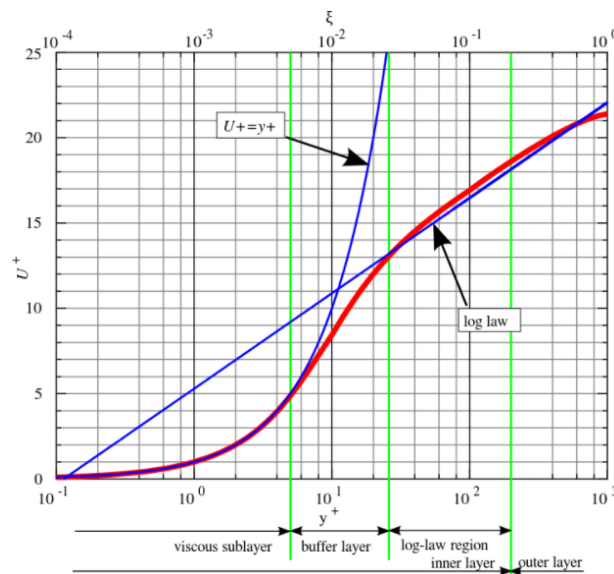


Figure 3.4.2.1 – Law of the wall [18]

The wall function describes the tangential velocity in correspondence of the surface in relation to the distance from the body (see Figure 3.4.2.2).

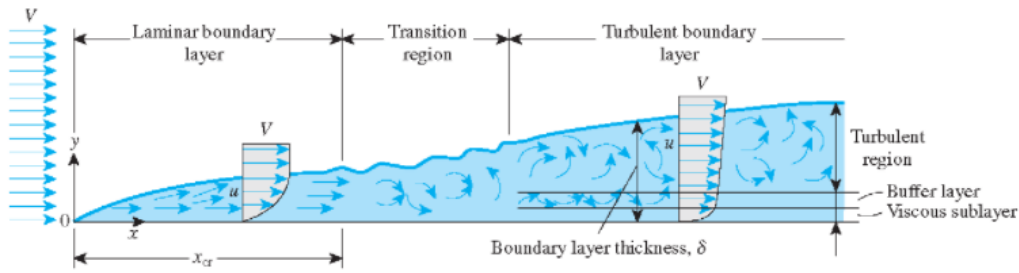


Figure 3.4.2.2 – Law of the wall [19]

The law is written in dependence of dimensionless quantities, describing the velocity of the turbulent parallel flow u^+ and the boundary layer depth, in its development, y^+ . They are introduced by the following formulations:

$$u^+ = \frac{U_T}{u_t} \quad (3.4.2.1)$$

$$y^+ = \frac{y u_t}{\nu} \quad (3.4.2.2)$$

Where U_T is the tangential velocity of the flow, y is the wall distance, ν is the kinematic viscosity and u_t is the friction velocity expressing the intensity of speed fluctuations within the wall-bounded flow and thus formulated:

$$u_t = \sqrt{\frac{\tau_\omega}{\rho}} \quad (3.4.2.3)$$

With ρ the flow density, here the air flow density, and τ_ω such defined:

$$\tau_\omega = (\mu + \mu_t) \frac{\partial U}{\partial y} \quad (3.4.2.4)$$

It has to be highlighted that this approach is closely linked to the domain in which it is valid, namely all the values of wall distance that are within the range of logarithmic wall function. This condition is translated through the range $30 < y^+ < 300$ and it is highlighted Figure 3.4.2.1 by the so called Log-law Region. The corresponding velocity profile in this field is expressed by the following equation:

$$u^+ = \frac{1}{\kappa} \ln(y^+) + C^+ \quad (3.4.2.5)$$

Which has obviously a logarithmic trend and where κ corresponds to Von Karman's constant and C^+ is a model constant. For smooth surfaces it can be adopted as values $\kappa=0.42$ and $C^+=5.5$ [1].

This method has the advantage according to which it requires a coarse mesh since it does not solve cases dealing with significant pressure and velocity gradients. Thus, its computational cost is limited. However, the other method proposed, the Low Reynolds Number approach, seems to be more suited since it deals with the resolution of the viscous sublayer in order to be able to catch the important flow gradients and variation in this zone. For this reason, it requires a very fine mesh and RANS equations are solved right down to the wall [3] considering viscous and damping properties, that are determinant in this layer. This method requires another kind of domain for the wall distance, which is now $y^+ < 1$ in order to maintain the range within the viscous sublayer (see Figure 3.4.2.1).

The will to adopt this second approach in the case of study here presented is based on the kind of the problem considered. In fact, for low velocities, as the ones related to this experiment, the wall spacing tends to increase [1]. If low velocities and large values of y^+ are adopted, then the corresponding wall spacing gets a value closely compared with the one of the conductor section profile ($D=23.55$ mm) [1].

3.5 Computational model

The numerical analysis was conducted through two different commercial finite element modeling software, that are Straus7 and Ansys 2021. First of all, the challenge was to point out the correct way to represent and model the wire in its parabolic geometry and rheological characteristics, as it is a kind of structural member that only reacts to positive states of tension. Thus, compressions are not allowed in it, since its stiffness linked to negative forces is null. Hence, several alternative solutions were probed and then compared. They included the use of finite elements such as beam, truss, cable. It is important to highlight the fact that the convergence researched with truss or cable elements required a non-linear analysis, since the former led to a discretization that formed a catenary and thus a labile structure, while the latter are born as non-linear elements and they don't reach the equilibrium on the static field.

In order to study the aerodynamics features of the conductor and the possible creations of vortex shedding that may cause ampliation to amplitude of vibrations, a CFD analysis was carried out thanks to ANSYS software, and then compared with Wind Tunnel Test results, as said.

A flow domain was created in order to reproduce the real conditions of undisturbed wind velocity that gradually encounters the transverse section of the wire, shaped in its variation forms as previously mentioned. Hence, starting from the simple circular section of the conductor, the analysis was repeated with the different hole shape of the circle with the addition of semi-elliptical form representing the icing load, in its magnitude of 0.25 - 0.5 - 1 - 1.5 - 2 times the conductor diameter, as just pointed out in Subsection 3.1.1.

Finally, the results obtained by the CFD model were deduced and processed into the Straus7 numerical model, in order to study the global effects of aerodynamic loads and instabilities along the whole longitudinal development of the wire span. This third and last computational step was crucial and particularly important, since the results in terms of pressure and velocity with vortex shedding events needed to be elaborated and translated into dynamic force distribution along the transmission line system. This way allowed to join the 1D and 2D two models, creating the last numerical complete model which could give a panoramic overview to the galloping phenomenon and its unstable effects on transmission line system of the case of study.

3.5.1 Validation model – Structural feature

As just mentioned, the numerical approach started with a 1D model with the use of Straus7 in order to validate the theoretical solution of the static condition in the wire due to self-weight. Even though the parabolic geometry may be downloaded from an Autocad sketch, it should be interfaced with an important consideration on the field of stress state. In fact, if the static configuration was uploaded directly in the finite element software, the tension in the wire would be null since no load is applied on it, but it is known that the shape assumed by the conductor is necessary due to its self-weight. It is a kind of static, gravitational load and thus it leads to a stress state different from the null value. Hence, the need to reproduce a static scheme equal to simple supported beam was clear. In other words, the parabolic form assumed by the line became the starting static configuration on with dynamic consideration and the other kinds of load were applied, in total analogy with the straight shape of a simple beam. Moreover, this simple structural approach has allowed to have a deep control on the solution and a significant awareness on the results.

Figure 3.5.1.1 allows to have an illustration of what just explained, in particular the expectation of the model qualitative behaviour after self-weight load.

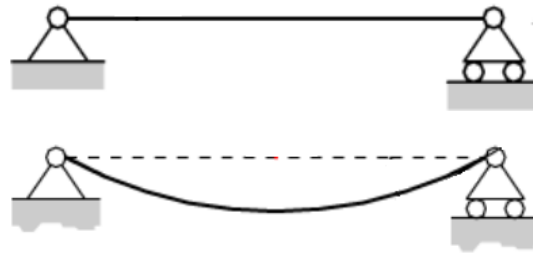


Figure 3.5.1.1 – Representation of simple supported beam static scheme [22]

From a quantitative point of view, the displacements recorded should be in line with the real span of the case of study. Since the transmission line system studied has several dimensions in terms of longitudinal development and sag of span, it was decided to keep a reference on the database coming from Alvisè Rossi's Thesis, in order to have a clear and immediate comparison with the results. The data are presented in the following Table 3.5.1.1.

Table 3.5.1.1 – Illustration of Input-geometry Data

Input-geometric Data	Values
<i>Span length</i>	160 m
<i>Sag</i>	2.27 m
<i>Conductor Diameter</i>	0.02355 m

The beam model required a modification of its stiffness since it is generally used for elements that have both behaviour in terms of bending moment and axial forces, while in this case it would be used as a finite element representing a structural member having just the latter one. Thus, the need to change the characteristics of the bending moment stiffness, in particular to decrease it as much as the response would have given the correct shape of the static deformation, in terms of span. In that case, in fact, it means that the wire correctly reproduce the conductor under its self-weight and so the model is ready to be studied on the base of mass and stiffness for dynamic loads.

The material used for the numeric model, as mentioned before, is Aluminum, presented in Table 3.5.1.2 that gives a summary of the modified characteristics of the wire-beam equivalent:

Table 3.5.1.2 – Illustration of Input-rheological Data

Input-rheological Data	Values	Measuring unit
Conductor Diameter D	0.02355	m
Transverse section Area A	$4.35 \cdot 10^{-4}$	m^2
Density ρ	$2.7 \cdot 10^3$	kg/m^3
Mass per unit length m	1.35	kg/m
Elasticity Modulus E	70 000	MPa
Ultimate tensile strength σ_{max}	220	MPa
Yield deformation ϵ_y	0.2	%
Ultimate deformation ϵ_u	8.0	%
Fusion temperature T_f	643	$^{\circ}C$
Electrical resistance Ω	0.0285	Ω/mm^2m

On the opposite side, with the aim to use a cable element to model the conductor, it is necessary only to define the section area and no other values in terms of geometry data. Figure 3.5.1.2 shows the Straus7 model in terms of full beam 160 m length and its discretization every 2 meters.

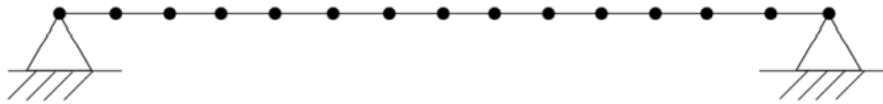


Figure 3.5.1.2 – Straus7 initial model

The trend of Aluminum’s mechanical features is reported in Figure 3.5.1.3, where its rheological and constitutive bond is given. As it can be noticed, the nonlinearity is clear and reflects what just mentioned and explained in Subsection 2.7 in the previous Chapter.

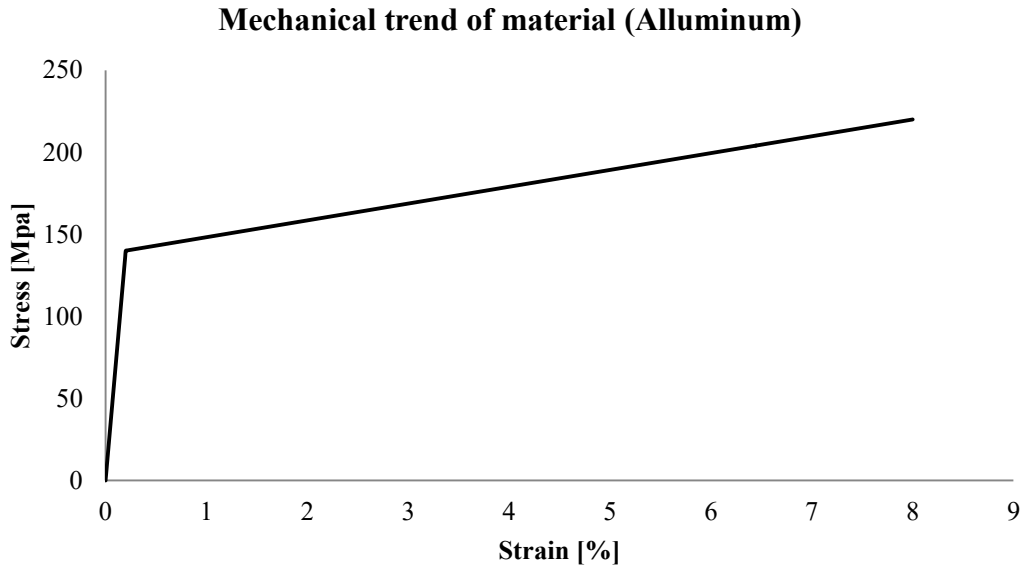


Figure 3.5.1.3 – Constitutive bond for Aluminum assumed

The theoretical solution follows the approach established by Irvine and Caughey, as reported in Section 2. The resolution of the two-equations system is given by the following formulation and it represents the profile adopted by the cable in static condition, now given by Figure 3.5.1.4 just treated.

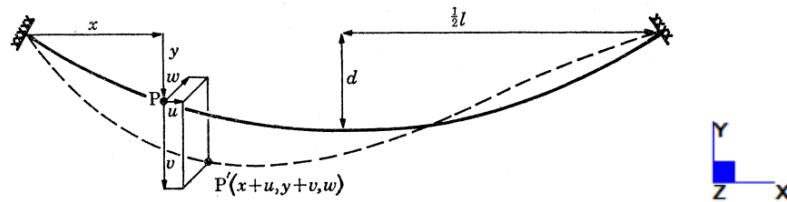


Figure 3.5.1.4 – Definition diagram for cable vibrations [21]

$$y = \frac{mgl^2}{2H} \left[\frac{x}{l} - \left(\frac{x}{l} \right)^2 \right] \quad (2.5.2)$$

Where m is the mass of the cable per unit length, g is the acceleration due to gravity l is the span and H is the horizontal component of cable tension T , such defined:

$$H = \frac{wl^2}{8s} \quad (2.5.3)$$

Where d is the sag of the cable and w is the force per unit length of cable and load.

Maximum Horizontal tension is instead given by the following formulation:

$$H = \frac{mgl^2}{8d} \quad (2.5.4)$$

Here in Figure 3.5.1.5 follows the comparison between the different finite elements used for self-weight load and the theoretical solution, in order to point out the difference and the powerful of numerical approach in its varies.

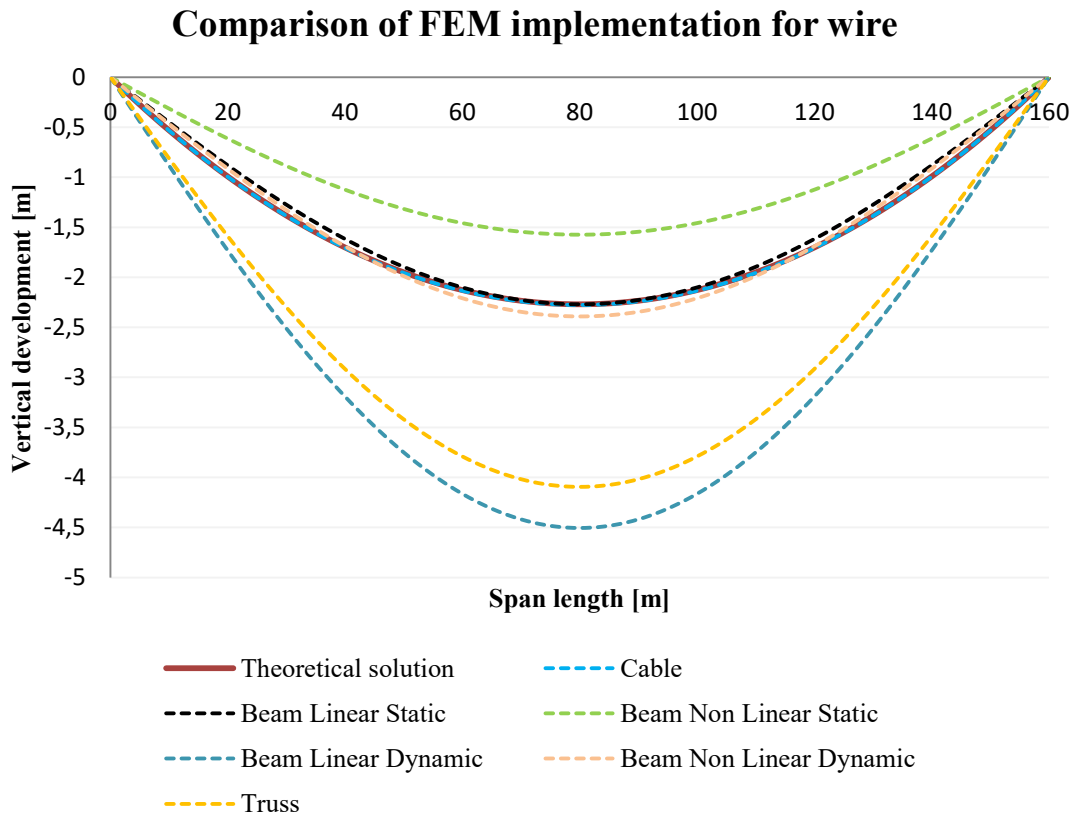


Figure 3.5.1.5 – Comparison between Finite Elements for self-weight in wire

As the Figure 3.5.1.5 shows, the use of beam and cable elements may be the best way to model the conductor, since they fit the theoretical solution very well.

It has to be highlighted that the linear dynamic approach does not interpolate the correct trend of the span. Hence, in these terms the geometric non-linearity of the problem nature is clear.

Moreover, truss catenary is quite far from the real analytical solution, even if it seems to be theoretically an alternative of cable. Instead, cable element has the best fit for conductor span trend.

The choice to continue the analysis below with the use of beam elements is justified by the will to control more complex considerations, such as the modes of vibration investigation, and the need to have simple output data as possible. Even though beam is maybe the best way to investigate dynamic analysis, also cable solution was used with the aim to compare and give a more comprehensive overview of the problem.

Validation phase continued with the comparison also in terms of static forces at the supports of the conductor. In fact, the analytical solution of the wire allows to compute these components in order to have an idea of the inclination and orientation of the cable at the extreme towers. On this field, there are two kinds of method useful: the *parabola* and the *catenary*. The former is often used because it simplifies the calculations and may be applied to every single case, while the latter is better when the span length are very short. On the other hand, in its 6th chapter for [35], A. Guell explains that these two methods are exchangeable for all practical purpose.

When a wire is assumed to conform to the curve of the parabola, the mass of the wire or cable is assumed to be uniformly distributed along its horizontal projection (the horizontal span length), while for the catenary, the mass of the conductor is assumed to be uniformly distributed along the arc of it [34]. For the parabolic solution, it is safe to assume that the sag will vary as the square of the span length for spans that are at least double the length of the ruling span [34]. Figure 3.5.1.6 shows the reference model for analytical restitutions.

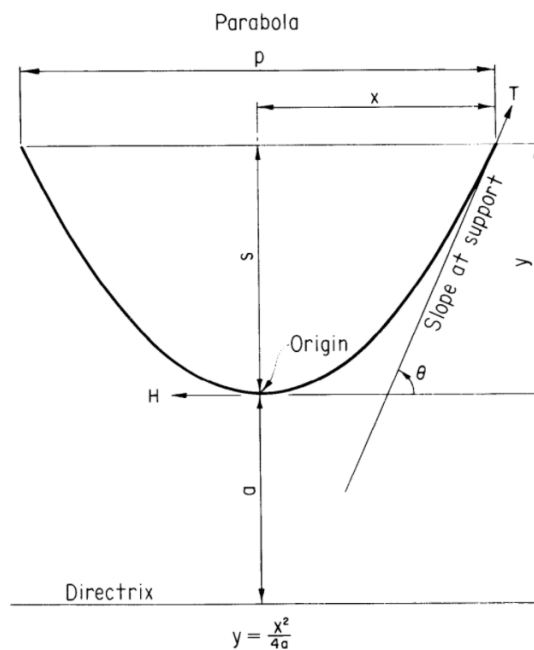


Figure 3.5.1.6 – Parabolic curve model [34]

The governing equations dealing with the parabolic balance are now reported.

w : Force per unit length

$$L = p + \frac{8s^2}{3p} : \text{Length of cable}$$

$$H = 2aw = \frac{wp^2}{8s} : \text{Horizontal tension}$$

$$V = \frac{w(3p^2+8s^2)}{6p} : \text{Vertical tension}$$

$$T = \frac{wp}{8s} \sqrt{p^2 + 16s^2} : \text{Maximum tension}$$

$$S_l = \frac{wx^2}{2H} : \text{Sag at any point}$$

$$S = \frac{wp^2}{8H} : \text{Maximum sag}$$

By considering dataset of the case of study, the load applied consists of self-weight of the conductor, and thus $w = m g = \rho A g = 13.24 \text{ N/m}$.

Taking on the break tension adopted for Aluminum used in the aerial line, it follows that the static configuration must indulge the trend of self-weight load solution, but also be characterized by an internal tension less than the 50% of the ultimate tensile strength. This last one is the maximum tensile stress which a material is able to sustaining. According to American legislation, its half value has to be greater than the ultimate stress assumed during design. Hence, for this case of study, it must not to exceed a value of 110 Mpa, according to Table 3.5.1.2.

Table 3.5.1.3 shows the procedure in order to highlight limit values for accepting initial static sag of span and its consequent tensile stress.

Table 3.5.1.3 – Parabolic curve model [34]

Maximum tension	σ_{max}	110	MPa
Conductor's area	A	0.0005	m ²
Self-weight load	w	13.24	N/m
Span length	L	160	m
Maximum Horizontal tension	H_{max}	55000	N
Minimum sag	f	0.77	m

Thus, a minimum value of sag of 0.77 for this type of conductor must be respected.

Actually the real sag registered for self-load case is 2.27 m, so this condition is prized. At the same time, the configuration adopted by the cable has to remain in the elastic field displacements and deformations. Hence, Table 3.5.1.4 gives a recalculation of the design values with the corresponding initial deformation, that must be lower than the one at yield state (0.2%).

Table 3.5.1.4 – Parabolic curve model [34]

Sag value	f	2.27	m
Conductor's area	A	0.0005	m ²
Self-weight load	w	13.24	N/m
Span length	L	160	m
Maximum Horizontal tension	H	18669.25	N
Maximum Vertical tension	V	1060.05	N
Maximum Tension in cable	T	18700.03	N
Maximum tension	σ	37.34	MPa
Total length	L	160.085	m
Elongation	ΔL	0.085	m
Deformation ϵ	\mathcal{E}	0.0536	%

As it can be noticed, deformation ratio is lower than 0.2%, the limit of elastic domain, and obviously the internal tensile tension respects the upper limit for ultimate one. Thus, the whole conductor is in an elastic state condition when snow accretion starts to generate, in combination with wind dynamic forcing.

3.5.2 Modes of vibration

Once decided to proceed with beam elements, the next step is to investigate the magnitude of the main conductor frequencies and its corresponding modes of vibration.

It is to highlight that this kind of analysis is based on two important factors of a structure, that we need to know: Mass and Stiffness. Once again, beam modeling helps to simplify the work, since it internal reproduce all this features as a representative of an extrusion of transverse section wire in its longitudinal development. This way allows to keep in consideration the density of the member material and its inertial characteristics in an implicit method.

On the analytical field, the dynamic problem of the mode of shapes is a free-undumped vibrations analysis. If the general dynamic balance equation can be expressed by the following formulation, just introduced in Chapter 2:

$$m\ddot{s} + c\dot{s} + Ks = p(t) \quad (3.5.2.1)$$

Mode of shapes research can be written with the following one:

$$m\ddot{s} + Ks = 0 \quad (3.5.2.2)$$

Where m, c, K are mass, dumping coefficient and stiffness of the system, respectively, while s is the response function in the domain of time $s(t)$ for the structure excited by the dynamic load $p(t)$.

The solution of the partial differential equation of the second order is given in complex numbers domain with the following expression:

$$s(t) = G_1 e^{i\omega t} + G_2 e^{-i\omega t} \quad (3.5.2.3)$$

By introducing the Eulerian formulation, it becomes:

$$e^{i\omega t} = \cos(\omega t) \pm i \cdot \sin(\omega t) \quad (3.5.2.4)$$

$$s(t) = A \cdot \sin(\omega t) + B \cdot \cos(\omega t) \quad (3.5.2.5)$$

Where G_1, G_2, A and B are the amplitude of the motion, while ω is the natural frequency of the system.

Another form of the solution above can be written as follows:

$$s(t) = \frac{s(\dot{t} = 0)}{\omega} \cdot \sin(\omega t) + s(t = 0) \cdot \cos(\omega t) \quad (3.5.2.6)$$

Where $s(\dot{t} = 0)$ and $s(t = 0)$ are the initial values of the system in terms of velocity and displacement, respectively.

With the aim to point out several succeeding considerations, it is given also the general solution for a damped system excited by a dynamic sinusoidal load in the form $p(t) = p_0(\sin \bar{\omega} t)$:

$$\begin{aligned} s(t) = e^{-\xi\omega t} [& A \sin(\omega_D t) + B \cos(\omega_D t)] \\ & + \frac{p_0}{K} \frac{1}{(1 - \beta^2)^2 + (2\xi\beta)^2} [(1 - \beta^2) \sin(\bar{\omega} t) \\ & - 2\xi\beta \cos(\bar{\omega} t)] \end{aligned} \quad (3.5.2.7)$$

Where p_0 and $\bar{\omega}$ are the amplitude and the cyclic frequency of the dynamic external load, β is the ratio between the load frequency and the natural one, while ω_D is the frequency of damped vibration, thus defined:

$$\omega_D = \omega \sqrt{1 - \xi^2} \quad (3.5.2.8)$$

Eventually, ξ is the dumping ratio, thus defined:

$$\xi = \frac{c}{c_c} = \frac{c}{2m\omega} \quad (3.5.2.9)$$

Where c_c is named “critic dumping” and its formulation is $2m\omega$. Obviously, dumping ratio is null in case of undumped system ($c=0$).

Hence, a natural frequency analysis was carried out and its results are presented below in Figure 3.5.2.1:

FINAL FREQUENCY RESULTS			
Mode	Eigenvalue	Frequency (rad/s)	Frequency (Hertz)
1	3.34639902E+00	1.82931655E+00	2.91144771E-01
2	5.33871438E+01	7.30665066E+00	1.16288957E+00
3	2.68961328E+02	1.64000405E+01	2.61014751E+00
4	8.44241417E+02	2.90558328E+01	4.62437941E+00
5	2.04286919E+03	4.51981105E+01	7.19350270E+00
6	4.18970089E+03	6.47278989E+01	1.03017651E+01
7	7.66012829E+03	8.75221588E+01	1.39295842E+01
8	1.02810998E+04	1.01395758E+02	1.61376361E+01
9	1.28669511E+04	1.13432584E+02	1.80533565E+01
10	2.02448011E+04	1.42284227E+02	2.26452380E+01
11	3.02321640E+04	1.73873989E+02	2.76729048E+01
12	4.10117573E+04	2.02513598E+02	3.22310401E+01
13	4.32511203E+04	2.07969037E+02	3.30993002E+01
14	5.96850353E+04	2.44305209E+02	3.88823817E+01
15	7.98545808E+04	2.82585528E+02	4.49748837E+01
16	9.18552810E+04	3.03076362E+02	4.82361011E+01
17	1.03992669E+05	3.22478943E+02	5.13241179E+01
18	1.32219125E+05	3.63619479E+02	5.78718375E+01
19	1.62254797E+05	4.02808636E+02	6.41089855E+01
20	1.64516218E+05	4.05605989E+02	6.45541981E+01

Figure 3.5.2.1 – Natural Frequency results for modes of vibration analysis

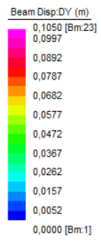
As it can be easily highlighted in Figure 3.5.2.1, just the first four eigenvalues are the main representative modes of vibration, since the other are just a combination of the first ones. They give a significant and important key of lecture for the wire structural problem. Theoretically, the structure has infinite vibrating modes, but the first four ones can well describe the dynamic behaviour.

First of all, the first natural frequency that excites the whole conductor for span is pointed out and has a magnitude of 0.29 Hz. The other main values are presented below:

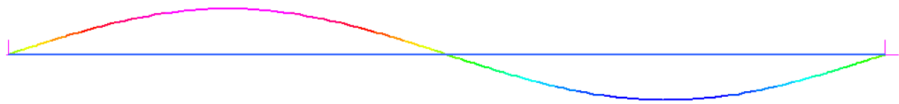
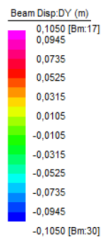
- 1) $f_1 = 0.2911 \text{ Hz}$
- 2) $f_2 = 1.1628 \text{ Hz}$
- 3) $f_3 = 2.6101 \text{ Hz}$
- 4) $f_4 = 4.6243 \text{ Hz}$

The shape of the corresponding eigenmodes are now reported in Figure 3.5.2.2, and it's quite clear how the configurations after the fourth mode are just a complex elaboration of the first modes of vibration

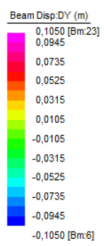
MODE 1



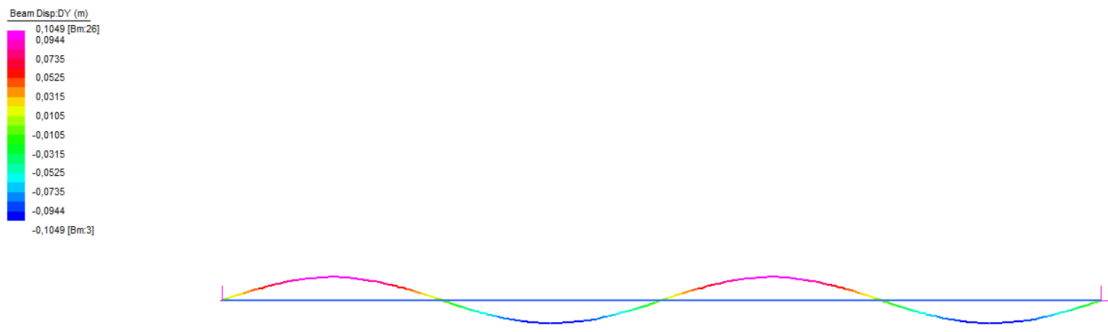
MODE 2



MODE 3



MODE 4



MODE 5

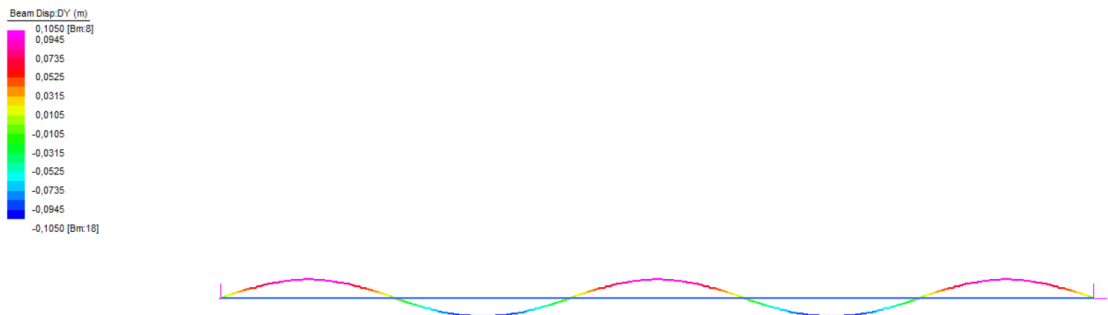


Figure 3.5.2.2 – Representation of the first eigenmodes corresponding to modes of vibration

The plot of the normalized eigenmodes are given in Figure 3.5.2.3.

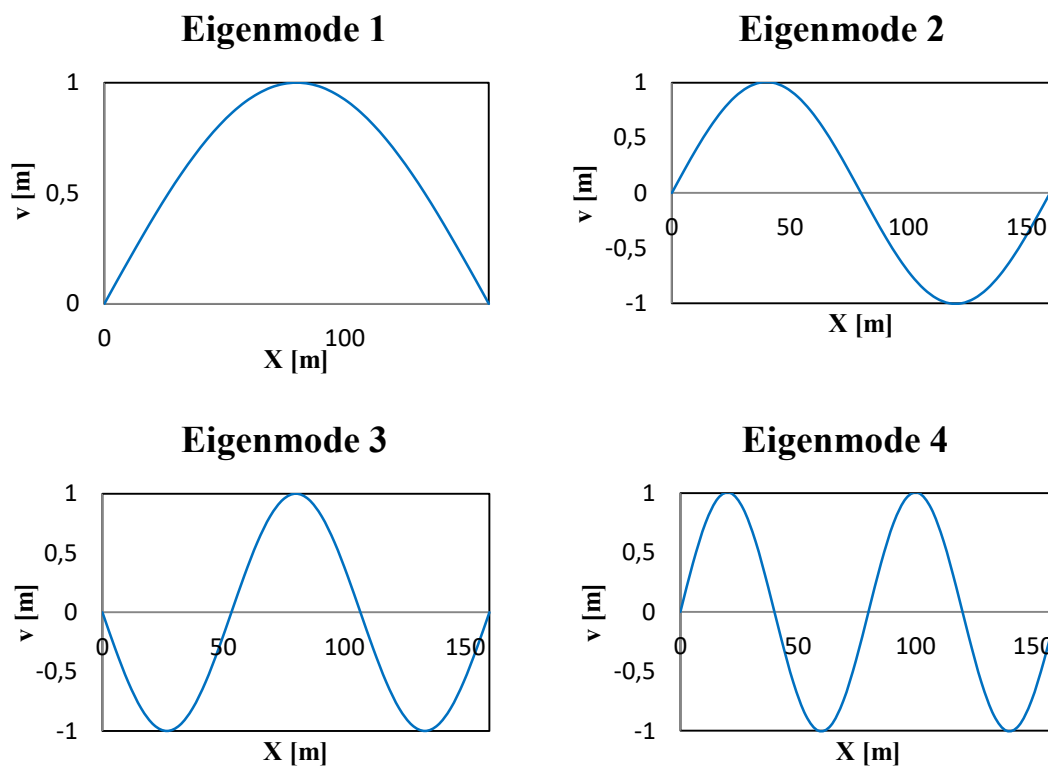


Figure 3.5.2.3 – Normalized eigenmodes corresponding to the first four modes of vibration

With the purpose of studying the analytical configuration of modes of vibration found in literature, the in-plane symmetric and anti-symmetric motions equations drive the comparison with numerical results. In these terms, Eigenmode 1 and Eigenmode 3 are evidently symmetric in relation to the middle of the span, while Eigenmode 2 and Eigenmode 4 are anti-symmetric related to the same position. For this reason, the comparison with theoretical equations (2.6.2.9) and (2.6.2.15) is immediate.

The former, related to eigenmodes 2 and 4, follow the eigenvalues problem by an easy formulation as just mentioned in Chapter 2 and now rewritten below:

$$H \frac{d^2 \tilde{v}}{dx^2} + m\omega^2 \tilde{v} = 0 \quad (3.5.2.10)$$

Which gives the theoretical solution as follows:

$$\tilde{v}_n(x) = A_n \sin\left(\frac{2n\pi x}{l}\right) \quad n = 1, 2, 3, \dots \quad (3.5.2.11)$$

On the other side, the latter equation related to eigenmodes 1 and 3 is characterized by a more complex formulation given by the following one:

$$H \frac{d^2 \tilde{v}}{dx^2} + m\omega^2 \tilde{v} = \frac{8d}{l^2} \tilde{h} \quad (3.5.2.12)$$

Which gives the theoretical solution as follows:

$$\frac{\tilde{v}(x)}{8d} = \frac{\tilde{h}}{H(\beta l)^2} \left\{ 1 - \tan\left(\frac{1}{2}\beta l\right) \sin(\beta x) - \cos(\beta x) \right\} \quad (3.5.2.13)$$

Where $\beta = \sqrt{\frac{m\omega^2}{H}}$ and the value of (βl) has the role to identify the particular symmetric vertical mode component. As just mentioned in Chapter 2, the aim to delete \tilde{h} from the equation (3.5.2.13), in order to obtain the following transcendental equation, leads to natural frequencies and modes given by this equation:

$$\tan\left(\frac{1}{2}\beta l\right) = \left(\frac{1}{2}\beta l\right) - \left(\frac{4}{\lambda^2}\right) \left(\frac{1}{2}\beta l\right)^3 \quad (3.5.2.14)$$

It's evident the transcendental nature of the equation above and thus the way to solve it requires to be graphic. Figure 3.5.2.4 shows the graphical approach in solving equation (3.5.2.14).

Graphical solution of trascendental equation of modes of vibration

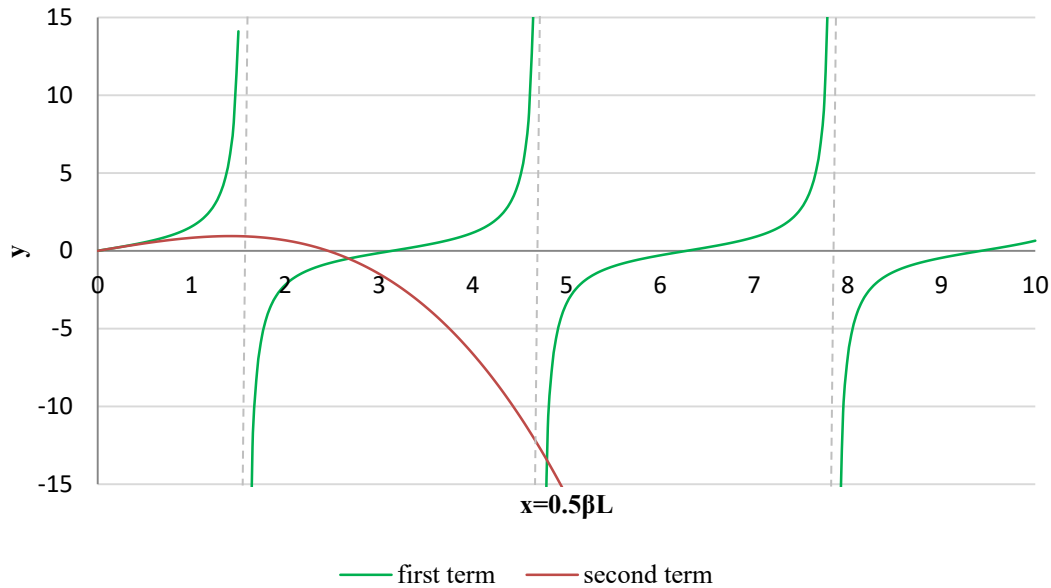


Figure 3.5.2.4 – Graphical approach in solving transcendental equation for anti-symmetric motion

First of all, the Irvine’s parameter λ^2 was calculated. According to the geometrical and structural properties of the conductor line, it was found $\lambda^2 = 67.59$.

As reported in subsection 2.6.2, the value of Irvine’s parameter λ^2 reflects what theory explains. In fact, if $\lambda^2 > 4\pi^2$, the frequency of the first symmetric in-plane mode is less than the frequency of the first antisymmetric in-plane mode. The value recorded is $\lambda^2 = 67.59 > 4\pi^2 = 39.43$, and the frequency of the first symmetric mode is actually lower than the one of the first antisymmetric mode ($0.31 < 0.73$).

The non-zero roots visible in Figure 3.5.2.4 are 2.65 and 4.75, which yield to a magnitude of frequency of 0.3101 Hz and 0.5559 Hz. As 0.2911 Hz is the numerical natural frequency for the first mode of vibration of the structure calculated, it has to be highlighted that the difference is not quite significant, but not imperceptible.

Thus, it deserves to be investigated to understand why the theoretical value is higher than the numerical one.

First of all, the reason why the two values are different is obviously the gap existing between numerical and theoretical fields, which always governs all kinds of analysis and which has to be accepted first. Moreover, the model has been implemented in terms of plane freedom case, thus the behaviour of the span is investigated only along its longitudinal development and recording vertical displacements according to x and y axis contained in that plane. On the other hand, the theoretical solution takes care also to

contributions coming from the transverse section area, which can be replaced by numerical data in terms of inertia, but it evidently gives birth to other components of stiffness that globally increase the rigidity of the whole model. For this reason, according to the analytical description of oscillation period, a higher value for K yields to a lower value for T , leading to a lower value for frequency f since period plays the role of denominator in frequency formulation. Thus, the numerical plane model seems to be less stiff than the analytical one, but this statement may be used in favor of safety.

Furthermore, the theoretical results are written under the hypothesis of linear cable vibration, while the problem is affected by a non-linearity feature.

Ultimately, equation (3.5.2.12) does not present a null known term, as the formal structure of free vibrations analysis would require. Thus, its solution is strictly linked to this additional term, which physically represents an external forcing due to cable development. The traditional form of free vibration system is instead maintained by the anti-symmetric motion, as equation (3.5.2.10) shows.

Hence, the modal shapes for analytical approach in the case of symmetric and anti-symmetric behaviour is now given by Figure 3.5.2.5 and Figure 3.5.2.6, respectively.

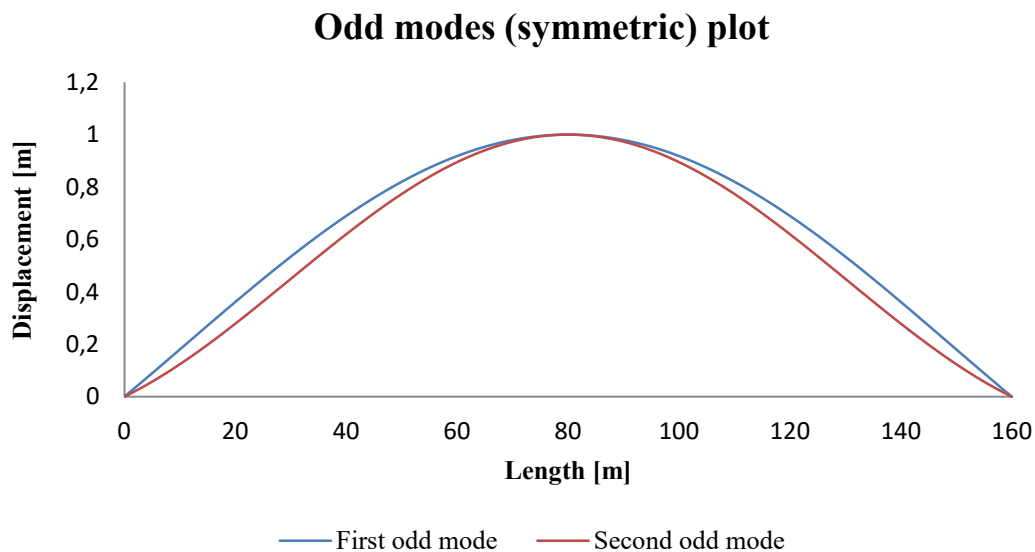


Figure 3.5.2.5 – First two Symmetric modes of vibration according to theoretical results

Even modes (anti-symmetric) plot

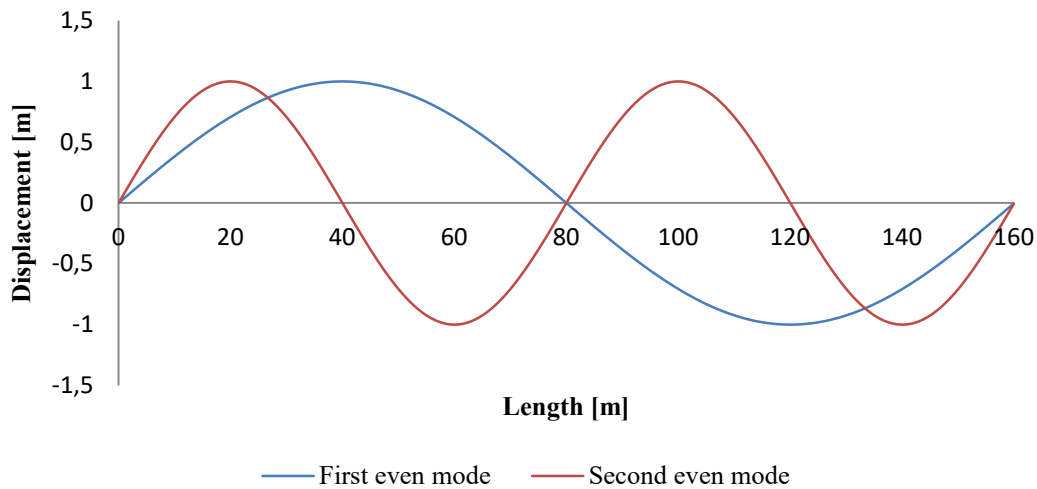


Figure 3.5.2.6 – First two Anti-symmetric modes of vibration according to theoretical results

In order to validate one more time the frequency results obtained above, a resonance simulation was carried out. The will to reproduce the resonance effect required the research of a sinusoidal dynamic load, having the same frequency of the first shape of mode of the structure. Hence, the frequency ratio β is equal to 1 in this condition ($\beta=1$), since it is a fraction between two same values.

A common and easy formulation for a function that has a sinusoidal development is the following one:

$$y = A \sin(\omega x + \varphi) + B \quad (3.5.2.15)$$

By placing $B = \varphi = 0$ and $A = 1$, it becomes:

$$y = \sin(\omega x) \quad (3.5.2.16)$$

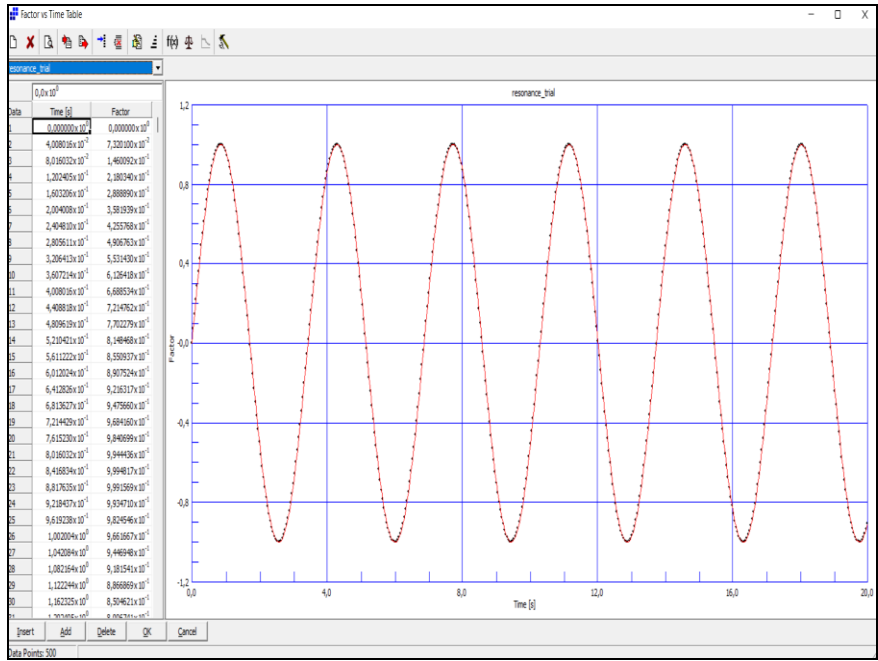
The value of natural frequency, ω , is the link with dynamic features of the structures. Since the first structural mode of shape is excited by $f_1=0.2911$ Hz, the relation with function period is expressed by the following writing, and it needs to be the same value in load frequency for resonance condition:

$$T = \frac{2\pi}{\omega} = \frac{1}{f_1} = \frac{1}{0.2911} \quad (3.5.2.17)$$

And thus:

$$\omega = 0,2911 \cdot 2\pi = 1.8281 \text{ rad/s}$$

Hence, the formulation of the researched load is $y = \sin(1.8281x)$ and Figure 3.5.2.7 shows its plot in Straus7.



A measure to define the dynamic feature of a load is the ratio response, or factor response, $R(t)$ and it can be always expressed in a SDOF system. It can be also regarded as a magnitude of how much the dynamic response is amplified in relation to the static one.

Its formulation is the following one and points out the ratio between the dynamic response of the structure and the equivalent static one:

$$R(t) = \frac{s(t)}{s_{st}} \quad (3.5.2.18)$$

It follows that the advance of $R(t)$ is the same of the model displacements but reduced by the static solution of the problem.

This last one, in the case of study, is obtained by solving the simply static load case considering self-weight as a uniformly distributed load on the wire and recording its enlargement along the longitudinal axis. Figure 3.5.2.9 allows to see what just explained in the Straus7 contour.

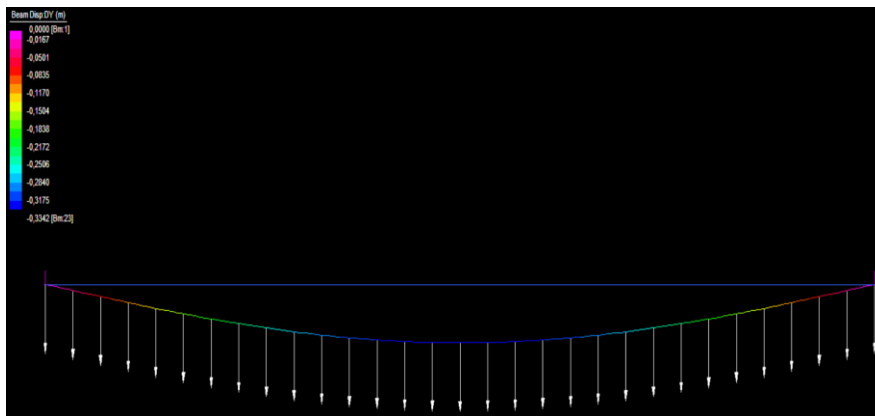


Figure 3.5.2.9 – Static solution for self-weight load

The maximum value recorded is $s_{st} = -0.3342 \text{ m}$ and it is used to define ratio response. On the analytical field, the solution of a resonant dumping system is obtained by considering the unitary value of β and hence the equality between natural and cyclic frequency ($\omega = \bar{\omega}$). The formulation becomes the following, by imposing the initial conditions at rest:

$$s(t) = \frac{p_0}{K} \frac{1}{2\xi} (e^{-\xi\omega t} - 1) \cos(\omega t) \quad (3.5.2.19)$$

For low-dumped structures ($0 < \xi < 1$), the analytic expression for $R(t)$ in case of resonance is obtained by decreasing the (3.5.2.19) equation by the static solution $s_{st} = \frac{p_0}{K}$.

$$R(t) = \frac{s(t)}{s_{st}} \cong \frac{1}{2\xi} (e^{-\xi\omega t} - 1) \cos(\omega t) \quad (3.5.2.20)$$

Eventually, considering the absence of dumping during this validation test, $\xi \rightarrow 0$ and the De L'Hospital Theorem is applied:

$$R(t) = \frac{1}{2} [\sin(\omega t) - \omega t \cdot \cos(\omega t)] \quad (3.5.2.21)$$

Figure 3.5.2.10 shows the advance of $R(t)$ for the examined case:

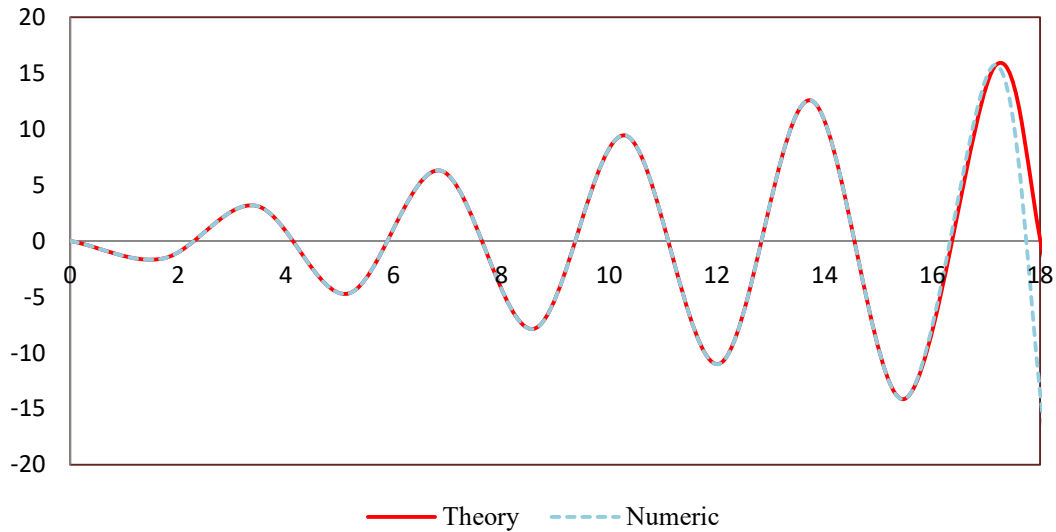


Figure 3.5.2.10 – Development of theoretical $R(t)$ in relation with numeric one

As the plot highlights, numeric solution and theoretic one fit very well each other. Another relevant consideration is made about the oblique asymptote, which is the clear sign of a divergence response typical for undamped structure, instead of a horizontal asymptotic limit to $\frac{1}{2\xi}$ that would be appreciated if the system was characterized by a non-zero dumping coefficient.

On the contrary field, a normal condition of dynamic load was applied, with the aim to certificate that a different frequency of temporal development would give a non-resonance response and behaviour. Thus, a value of 5 was given to load frequency ω , with the same initial hypothesis mentioned before, obtaining a sinusoidal load defined by the law $y = \sin(5x)$. Figure 3.5.2.11 gives a plot of its development in the domain of time, clearly highlighting the significant bigger frequency also by drawing.

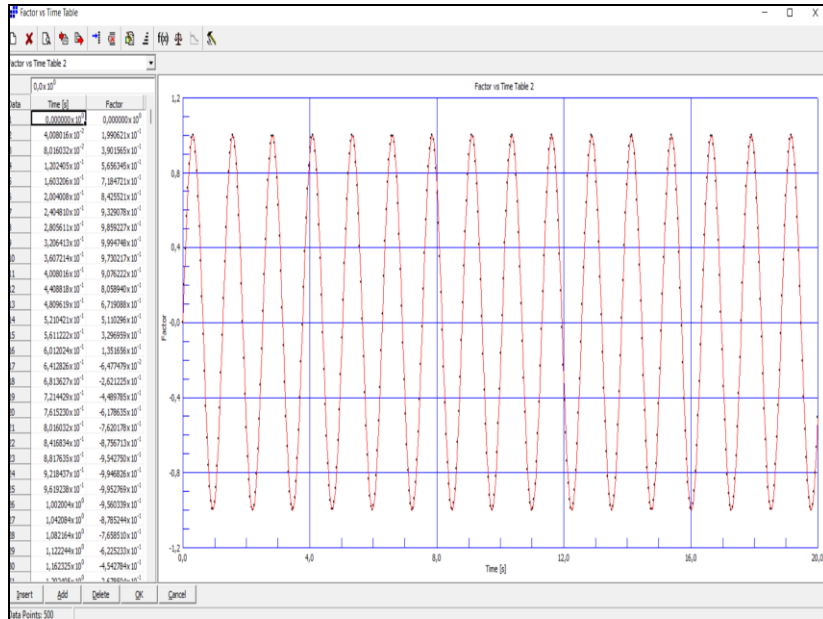


Figure 3.5.2.11 – Plot of non-resonance function load by Straus7

The model response is evaluated in terms of dropping amplitude in the middle of the span. Dropping development is reported in Figure 3.5.2.12, which clearly shows the emblematic divergence that characterizes resonance instability.

Wire response in non-resonance condition ($\xi=0, \beta \neq 1$)

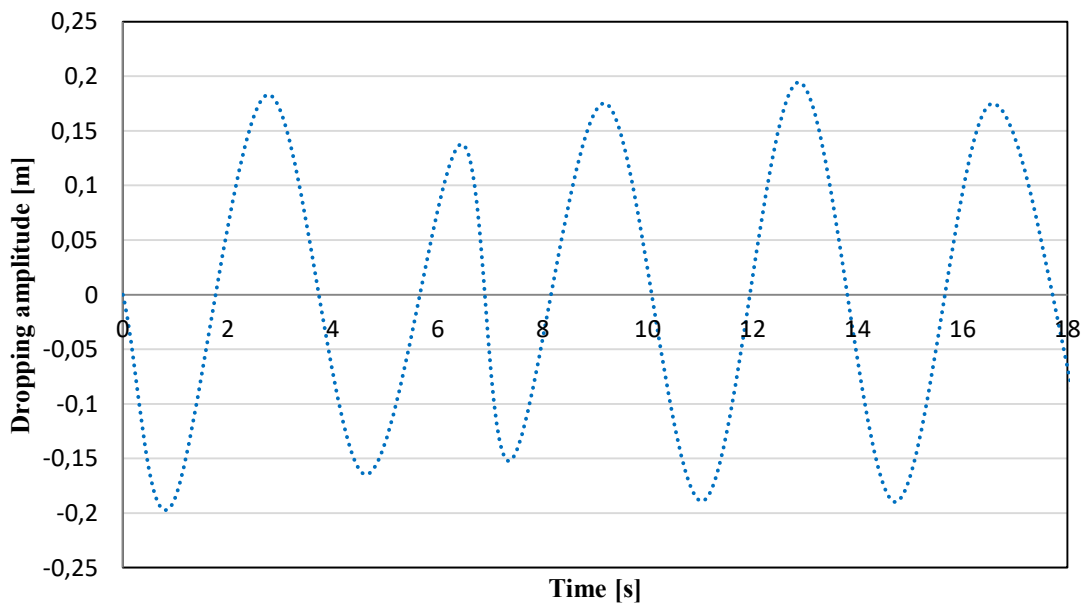


Figure 3.5.2.12 – Non-resonance response simulation of the conductor

The figure above points out the horizontal asymptote that is typical of a response belonging to the field of stability behaviour. Moreover, also its magnitude is extremely circumscribed within modest standards that touch the realistic value of 0.20 m.

3.5.3 Validation model - CFD

As mentioned in Subsection 3.5, the Computational Fluid Dynamic (CFD) analysis was carried out through the commercial FEM software ANSYS, version Workbench 2021 R2. CFD simulation of wind flow around buildings started with fundamental studies for isolated buildings, often with a cubical shape, to analyze the velocity and pressure fields (Vasilic-Melling 1977, Hanson et al. 1986, Paterson and Apelt, 1986, 1989, 1990, Murakami et al. 1987, 1990, 1992, Murakami and Mochida, 1988, 1989, Baskaran and Stathopoulos, 1989, 1992, Stathopoulos and Baskaran 1990, Murakami 1990a, 1990b, 1993, Baetke et al. 1990, Mochida et al. 1993) [27].

The aim of using this important and efficient tool was based on the will to reproduce and study widely the aerodynamic characteristics of the wire section, in its different shapes. Several geometries were adopted, in fact, according to the set of eccentricities due to ice and snow accretion but also in terms of angles of attack that made necessary a rotation of the transverse section model following the angle dataset intervals given in Subsection 3.2.1.

The numerical model was then modified with a hole in a particular position, subsequently presented, with the role of reproducing the transverse section, just mentioned above. This was set up thanks to specific rotations made to the starting hole representing the initial 0°-shape till the last one of 180°-shape.

Since ANSYS software does not require a 3D model to run the fluid dynamics analysis, a 2D numerical model was created, representing the air domain around the transverse section of the wire. This last one was orientated according to *x-axis* in its main development and in flow stream direction, along which the Drag coefficient was calculated, while *y-axis* is the orthogonal direction along which Lift coefficient was calculated. Eventually, *z-axis* is the ideal depth for three-dimensional simulations, here neglected.

The dimensions of geometry had to be such that all critical phenomena and fluid dynamics features could be appreciated and not cut off by surrounding domain's limits. Hence, the geometry was chosen according to multiples scales of the wire's diameter, as shown in Figure 3.5.3.1 with the representation of air domain and section proportions.

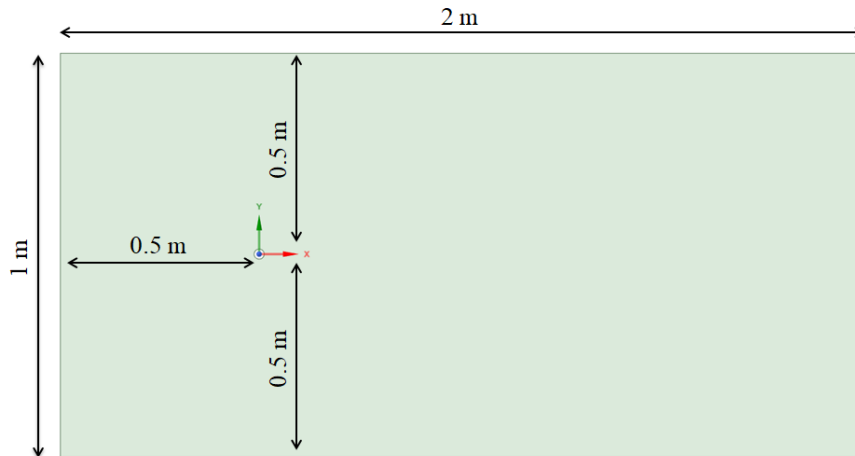


Figure 3.5.3.1 – Geometry and measures of the numerical model domain

Clearly, the boundary conditions remained constant with changing the several cases of wire profile in its orientation and eccentricity. On top of that, they were assigned to each of external walls and the cut body. Figure 3.5.3.2 gives a common illustration of conventions dealing with naming Boundary Conditions Fluent’s standard.

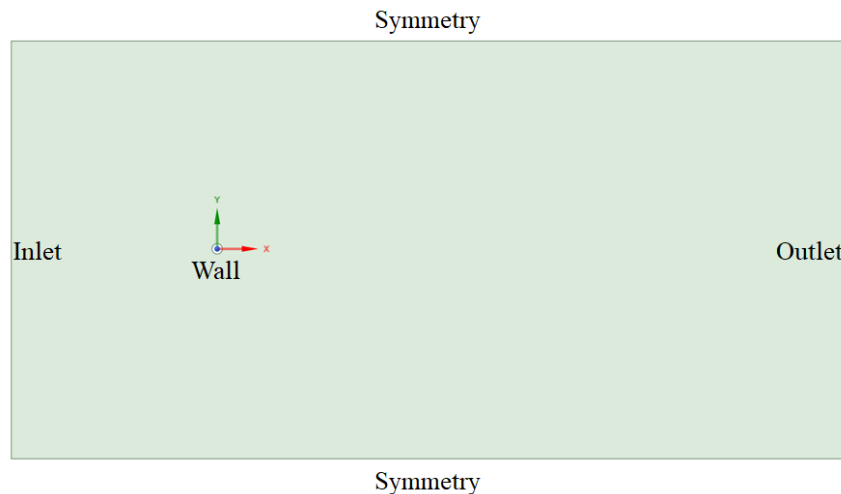


Figure 3.5.3.2 – Boundary Conditions naming conventions

Where the different naming standards mean the following descriptions:

- Inlet BC : the entrance of stream undisturbed flow of wind, at the input velocity ;
- Outlet BC : the leaving of the flow, after hitting the transverse section. Pressure assigned equal to zero ($p = 0 \text{ Pa}$) ;
- Wall BC : creation of a non-penetrable site for wind flow, assigning default values ;
- Symmetry BC : velocity assigned only according to inlet direction stream of wind ;

Figure 3.5.3.3 shows BCs plot on ANSYS software model, highlighting wind direction, the same for all CFD simulations studied.

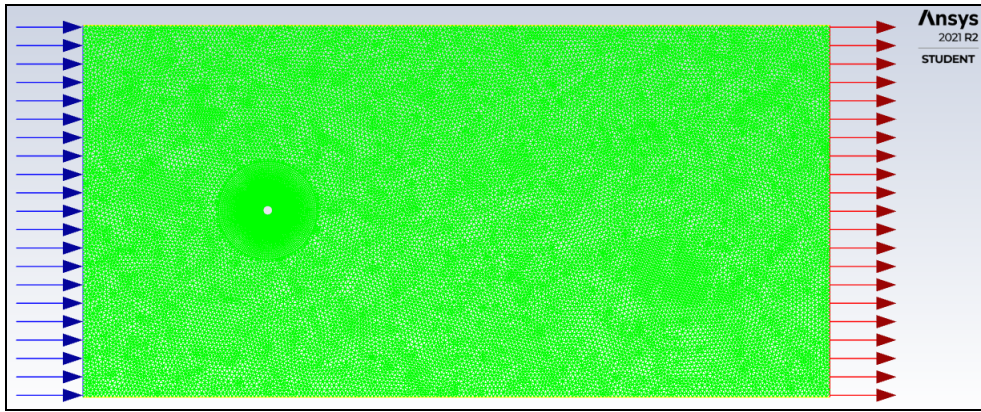


Figure 3.5.3.3 – Implementation of Boundary Conditions plot on ANSYS software

Regarding mesh refinement, it has to be highlighted that two were the main objectives line-guides leading to a correct mesh choice. Firstly, the need of a high number of finite elements necessary to well interpolate numerical output results of CFD analysis and thus a quite significant number of nodes, as just explained in Subsection 3.4.1, but at the same time the need to contain this number under the software running capacity, lined to its computational burden or cost. Hence, a triangular method was adopted, except for edge sizing and inflation dealing with the hole representing the wire, where ANSYS allows to set the first layer thickness of the finite element and then create a second domain made by regular mesh surrounding the hole. This tool is very fundamental for all FEM method's parts where high gradients are expected, in every kind of terms, here dealing with gradient of pressure, velocity and turbulence. For the cases studied, it was chosen a first layer of half millimeter (0.0005 m) and let it growing till 60 radius maximum layers. For the remaining part of flow-domain, it was established a 0.01 m maximum dimension for the elements, since the accuracy of the solution far from the critical point oh the wire is less strict. Figure 3.5.3.4 highlights the final mesh used, with a detail focused on the mesh-refinement around the wire.

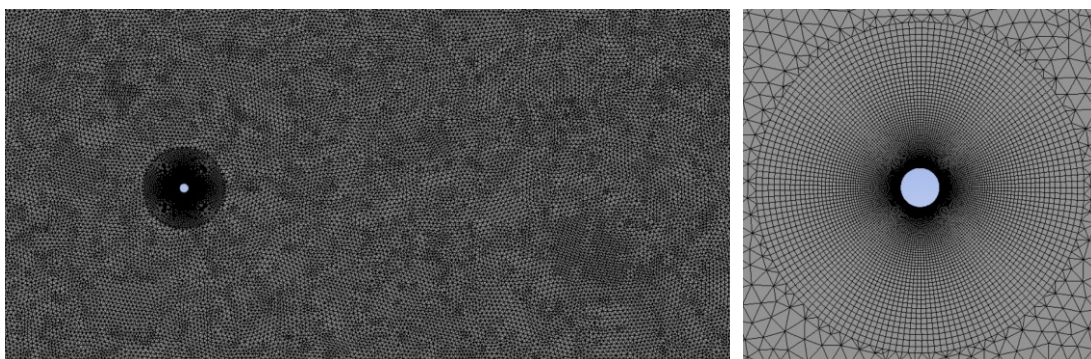


Figure 3.5.3.4 – Overview of the air-domain mesh adopted and detail of the mesh-refinement around the wire region

The validation reference was adopted by theoretical solutions for simple shape, like the circular one. The analytical response in terms of Drag coefficient is given by Sighard F. Hoerner (1965) in [32], where the two-dimensional problem for a steady stream hitting a circular body is treated. Figure 3.5.3.5 shows the part of the document where several simple Drag coefficients are tabled, including 1.17 as reference value for circular shape section.

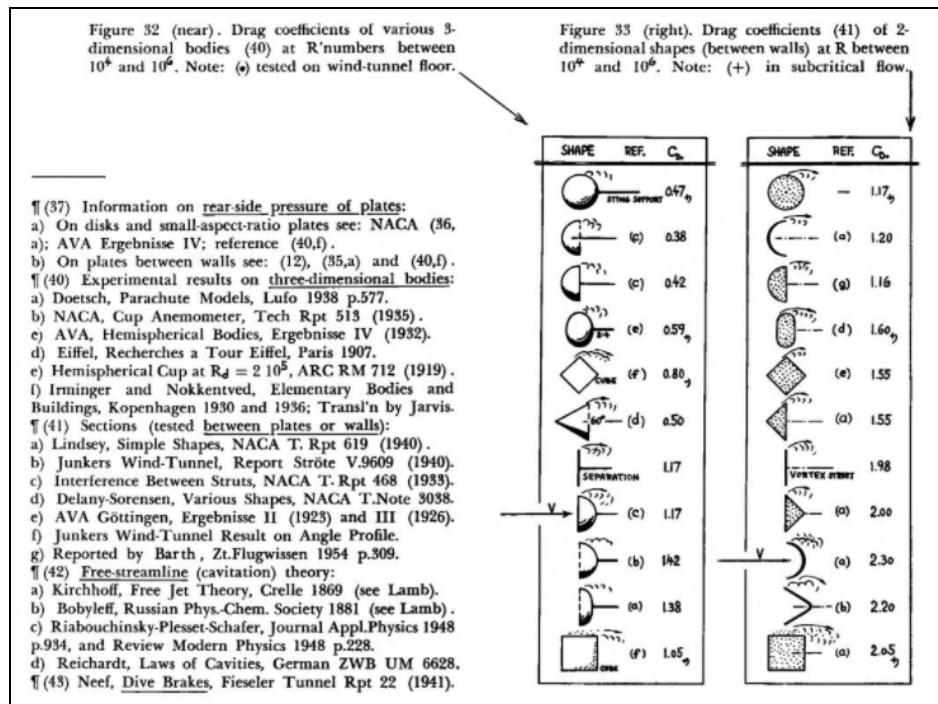


Figure 3.5.3.5 – Drag coefficients for 2D transverse shape bodies [32]

It is quite important to highlight that 1.17 is the reference value Drag coefficient in a particular conditions of the flow, characterized by a Reynolds number included between $10^4 < Re < 10^6$. Thus, the needed value of velocity had to be such in order to verify this hypothesis. The mean value assumed of $U=10$ m/s was optimal, since the Reynolds derived by the dataset correctly respected the requiring conditions ($D=0.02355$ m ; $\rho=1.225$ kg/m³ ; $\mu=1.81 \times 10^{-5}$ Pa s):

$$Re = \frac{\rho U D}{\mu} = 15803,17 \quad (3.5.3.1)$$

The value corresponding to equation (3.5.3.1) shows that the flow lies in the region included between $10^4 < Re < 10^6$.

The time step for dynamic development of the problem was evaluated by considering two different fields of choice: firstly, the need to have a significant accuracy of the solution required to have a very small time step, also as reported in Subsection 3.4.1, but

at the same time the need to have a low computational demand and thus its cost. A conservative hypothesis states from the experimental results made by Wind tunnel test and recorded in [1], where a reference frequency of 100 Hz was adopted as the representative for all the cases studied. Thus, a value of time for a single cycle in vortex-shedding was calculated $T=1/f=0.01$ s and so the time step needed to be lower than this value. Hence, it was chosen a time step of 0.001 s and the analysis was carried out for a total time of 1 s, since it was observed that 1 second is sufficient to achieve convergence and stable mean values for aerodynamics coefficients like C_D, C_L, C_M [1].

Hence, the validation analysis was carried out. Figure 3.5.3.6 shows the plot of convergence achieved, in terms of residuals between the different iterations. As it can be seen, the precision of the numerical model turns around 10^{-6} and 10^{-7} , which is a very significant level.

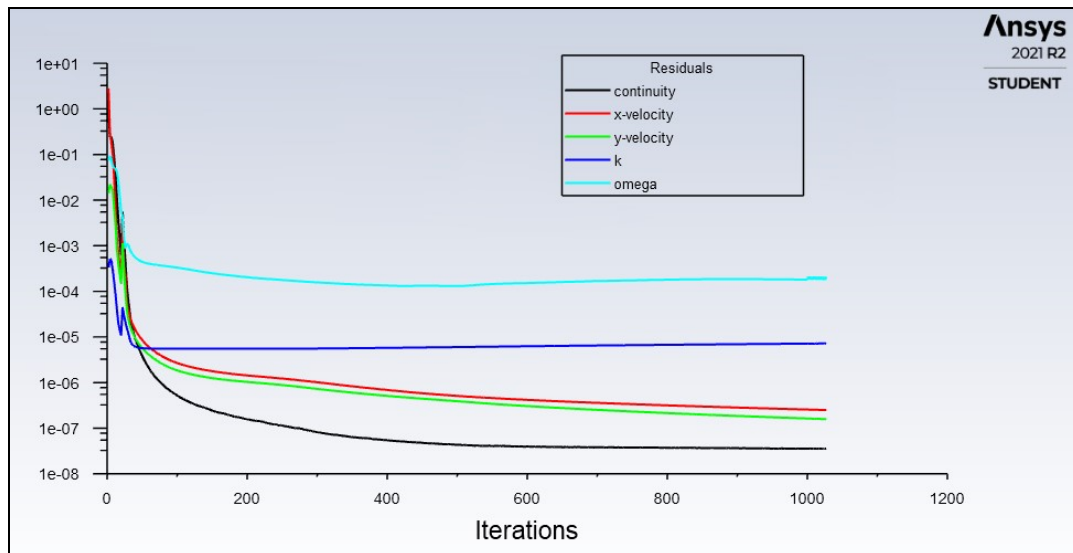


Figure 3.5.3.6 – Plot of numerical model's convergence

Eventually, Figure 3.5.3.7, Figure 3.5.3.8 and Figure 3.5.3.9 highlights the values obtained in terms of aerodynamics coefficients.

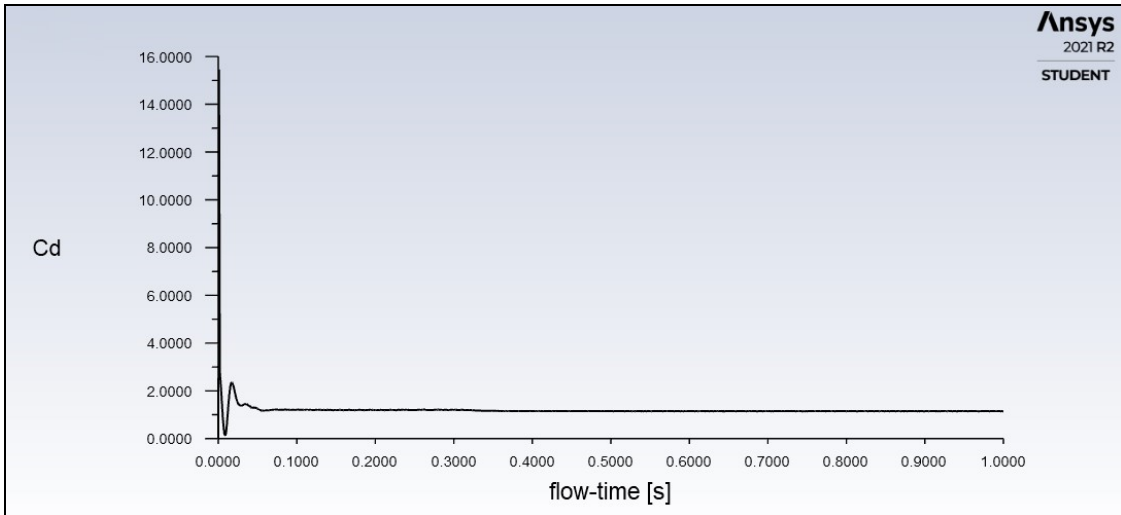


Figure 3.5.3.7 – Trend of Drag coefficient C_D obtained by the analysis

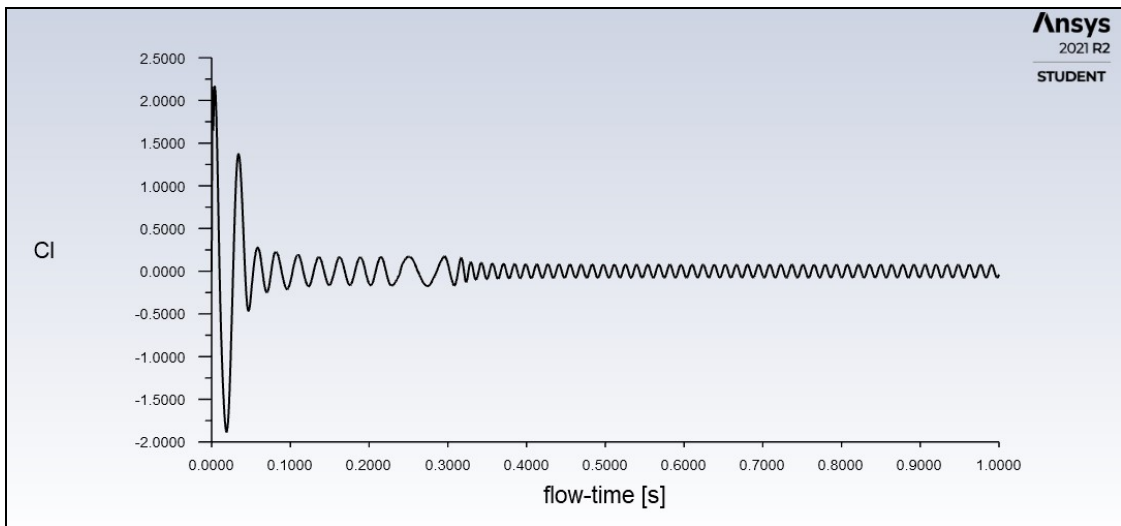


Figure 3.5.3.8 – Trend of Lift coefficient C_L obtained by the analysis

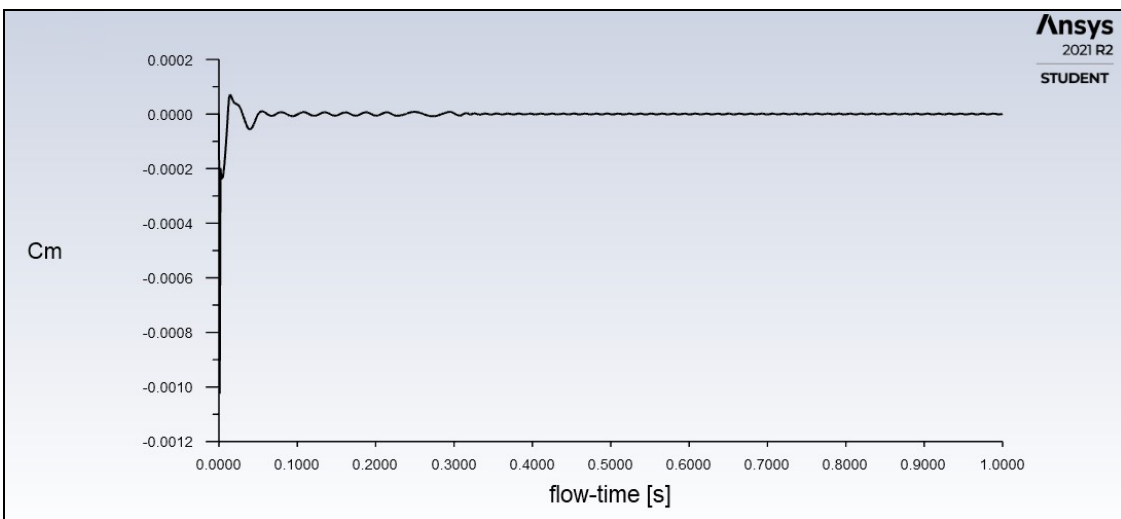


Figure 3.5.3.9 – Trend of Moment coefficient C_M obtained by the analysis

Figure 3.5.3.10 below shows the convergence of Drag coefficient in demonstration of validation for the whole numerical model, since it tends to the theoretical value of 1.17.

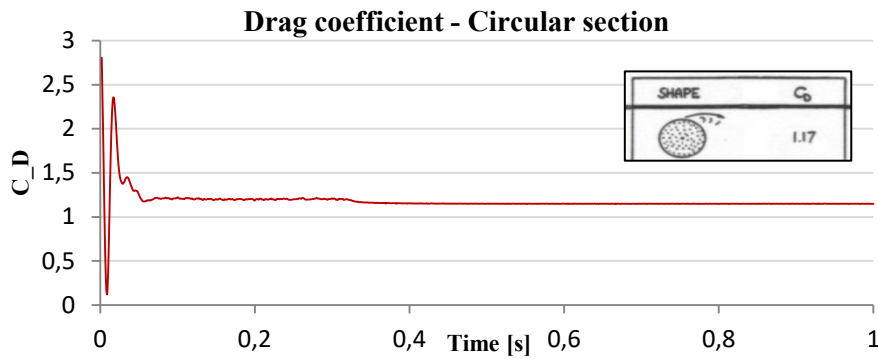


Figure 3.5.3.10 – Convergence of Drag coefficient trending to theoretical value of 1.17

At the end of this chapter, a series of contouring plot is presented in order to introduce in which terms the results of the CFD analysis will be reported.

The several plots deal with the uniform distribution of pressure [Pa], velocity [m/s] and Turbulence [Turbulent Kinetic energy $J/kg=m^2/s^2$], respectively presented in Figure 3.5.3.11, Figure 3.5.3.12 and Figure 3.5.3.13 with their own configuration also in terms of meshing interpolation. Eventually, a contour of velocity's vectors is given to complete the results framework in Figure 3.5.3.14.

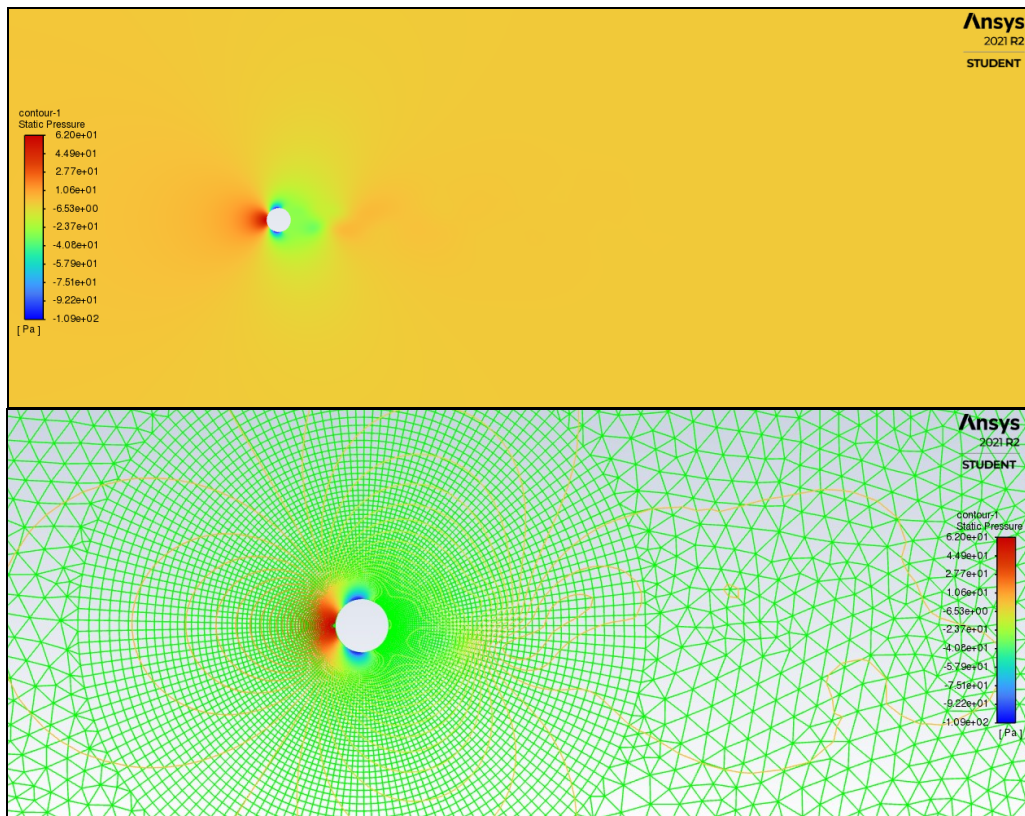


Figure 3.5.3.11 – Contouring dealing with Pressure of wind flow [Pa]

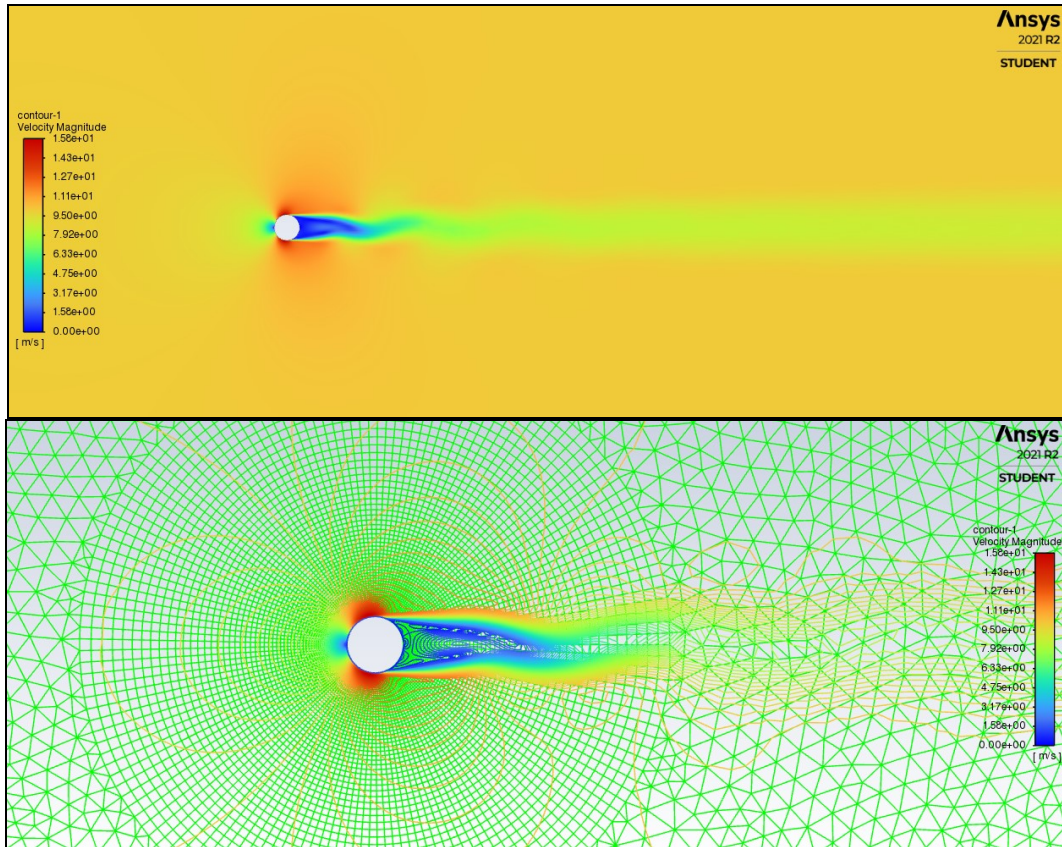


Figure 3.5.3.12 – Contouring dealing with Velocity of wind flow [m/s]

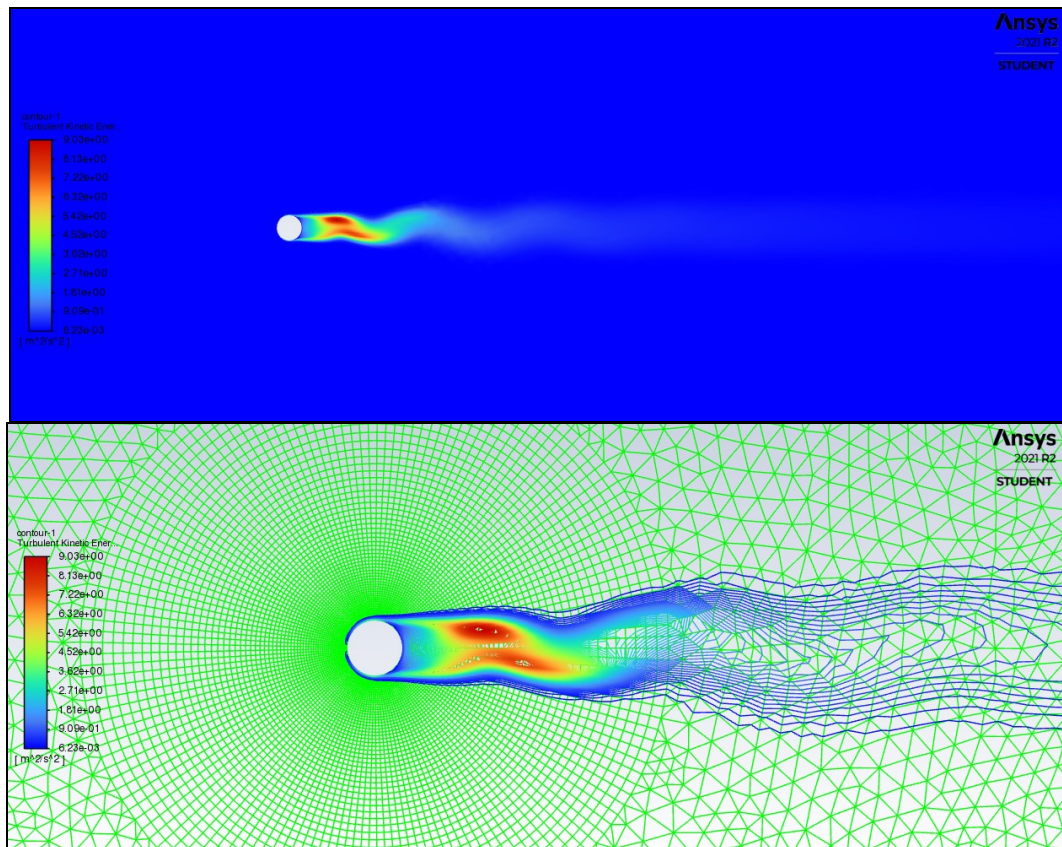


Figure 3.5.3.13 – Contouring dealing with Turbulence of wind flow [m²/s²]

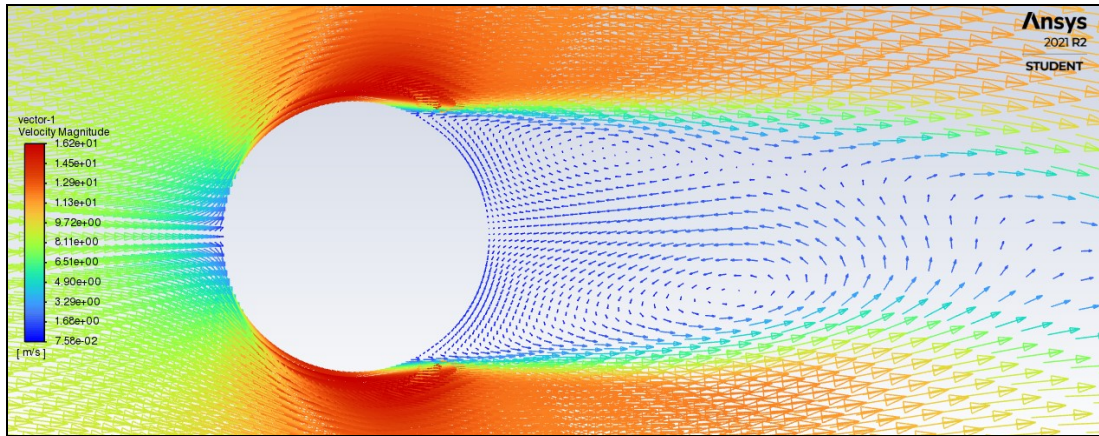


Figure 3.5.3.14 – Contouring dealing with Velocity's vectors [m/s]

Chapter 4

Results and Discussion

This chapter has the aim to report the results achieved through the several analysis in both their fluid dynamics and structural nature.

As just mentioned and explained before, the computational models were divided into three phases: the first one, dealing with the research of how model the wire in its stiffness and mechanical behaviour, also through a dynamic analysis to validate it; the second one, the fluid dynamics analysis (CFD) carried out thanks to the commercial software ANSYS 2021 R2, in order to plot study the aerodynamic behaviour of all the single transverse section thought in their own eccentricities due to ice load accretion; the third one, once again dealing with the structural part of the problem, but now with the combined effects coming from CFD analysis of ice and wind on the longitudinal development of the wire span, with several combination cases and distribution possibilities of ice load along the conductor.

In other words, the three-dimensional real behaviour of the structure studied in this Thesis was simplified and split into a part dealing with the 2D field in terms of transverse section of the wire, and a part dealing with the 1D longitudinal development of the span conductor. The fusion of these two separated models should give the approximated solution representing the global behaviour of the body examined.

4.1 CFD results

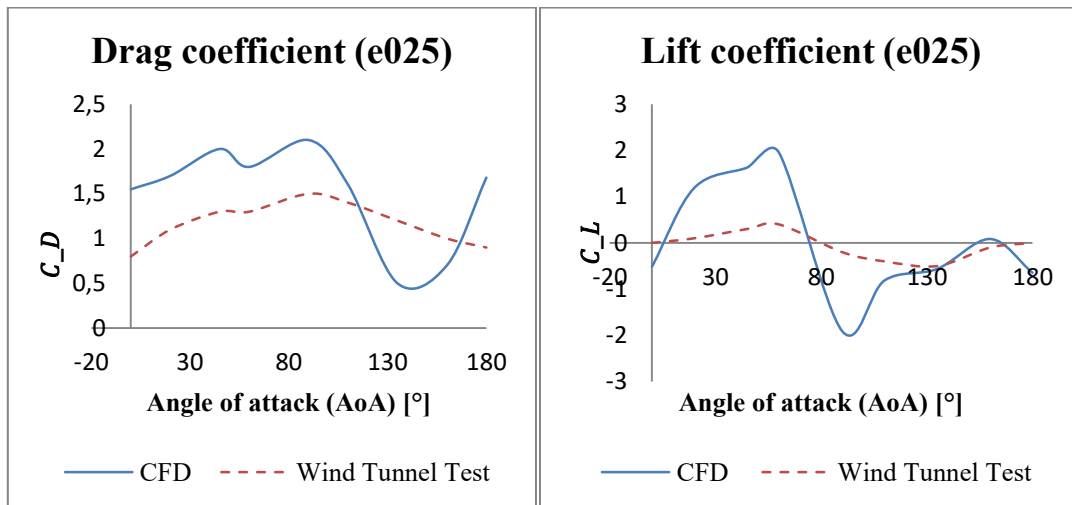
Computational Fluid Dynamics analysis has just started with the validation model reported at the end of Chapter 3. Now a series of contouring plot is presented and also the center of the whole analysis linked to the search of Lift Coefficients.

This value was calculated for every single transverse profile and for every orientation angle (Angle of Attack – AoA) between ice shape development and steady stream wind direction. About this, a choice was made for its variation, thus increments of 15°-20° were adopted for a total range between 0° and 180°. In fact, it is quite evident that other angles bigger than 180° would return anti-symmetric results in relation to the ones obtained since that last value of angle of attack.

The following graphics show the trend and the development of Computational Analysis results, compared with values recorded during Wind Tunnel Test simulations. These last ones belong to the Dataset available from the foreign studies made by Alvisè Rossi.

As said before, the plots are dealing with aerodynamics coefficients in relation to the variation of angle of attack. Eventually, evidentially the most important parameter is the Lift coefficient, since it will generate Lift Force needed to be applied on the structural model in Straus7 with its own variation and amplitude.

Figure 4.1.1 highlights these trends referring to a value of ice-eccentricity of 25% (*e025*), Figure 4.1.2 to *e050*, Figure 4.1.3 to *e100*, Figure 4.1.4 to *e150*, Figure 4.1.5 to *e200* respectively.



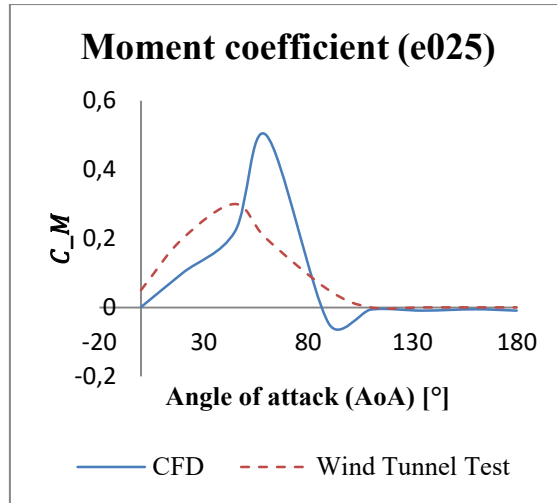


Figure 4.1.1 – Aerodynamics coefficients related to Wind Tunnel Tests results for e025

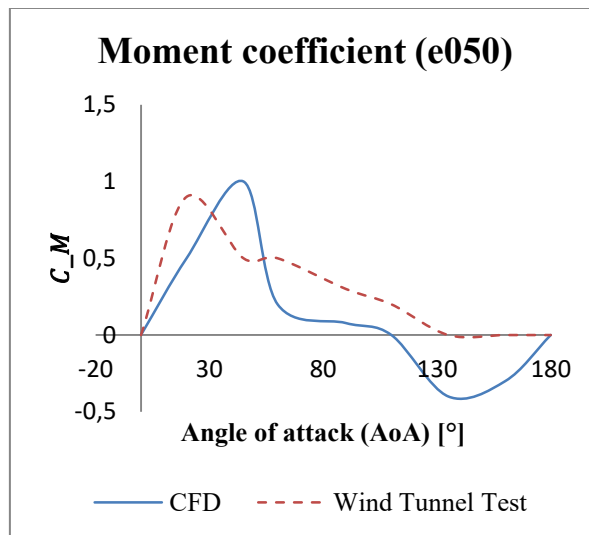
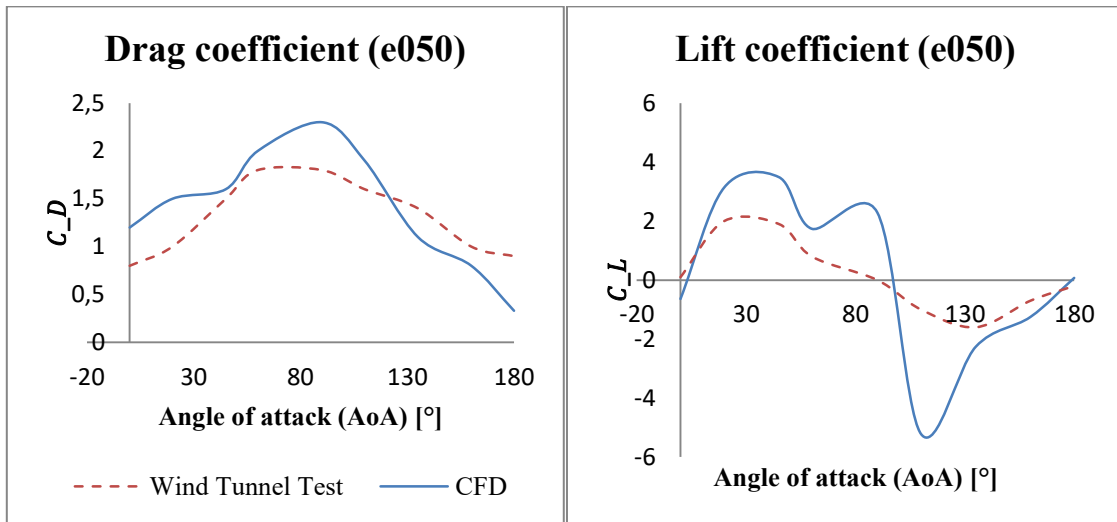


Figure 4.1.2 – Aerodynamics coefficients related to Wind Tunnel Tests results for e050

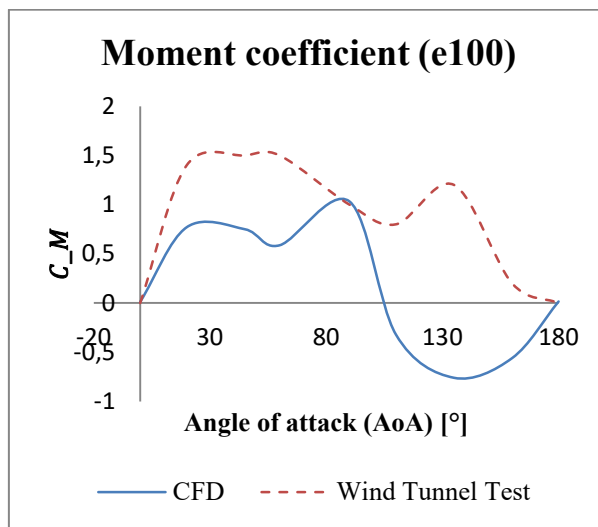
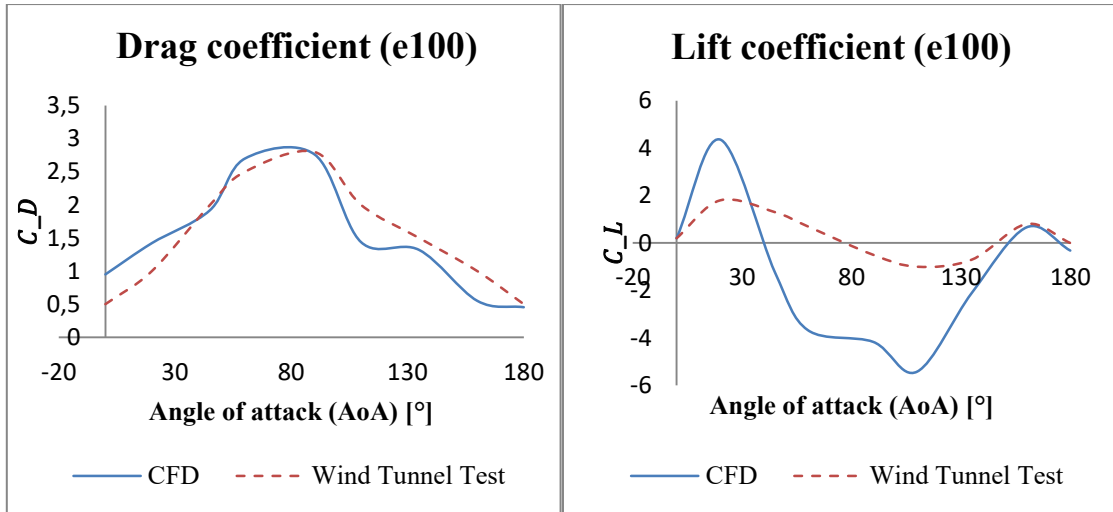
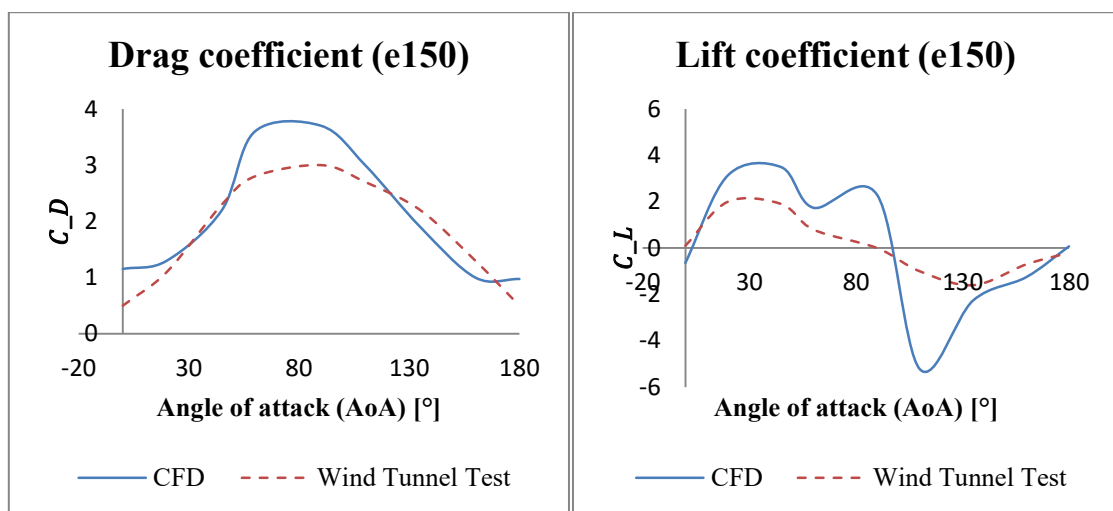


Figure 4.1.3 – Aerodynamics coefficients related to Wind Tunnel Tests results for e100



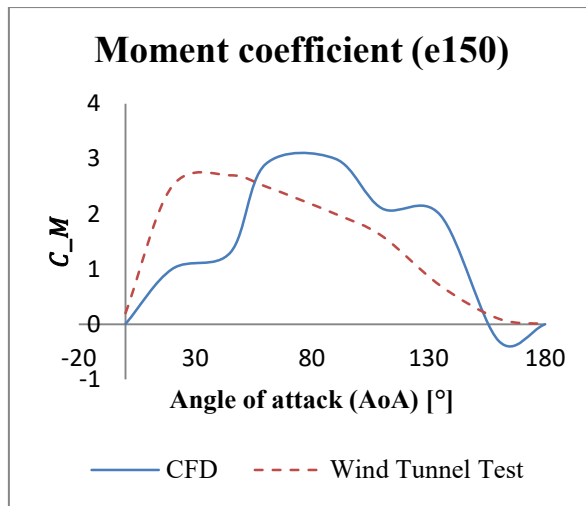


Figure 4.1.4 – Aerodynamics coefficients related to Wind Tunnel Tests results for e150

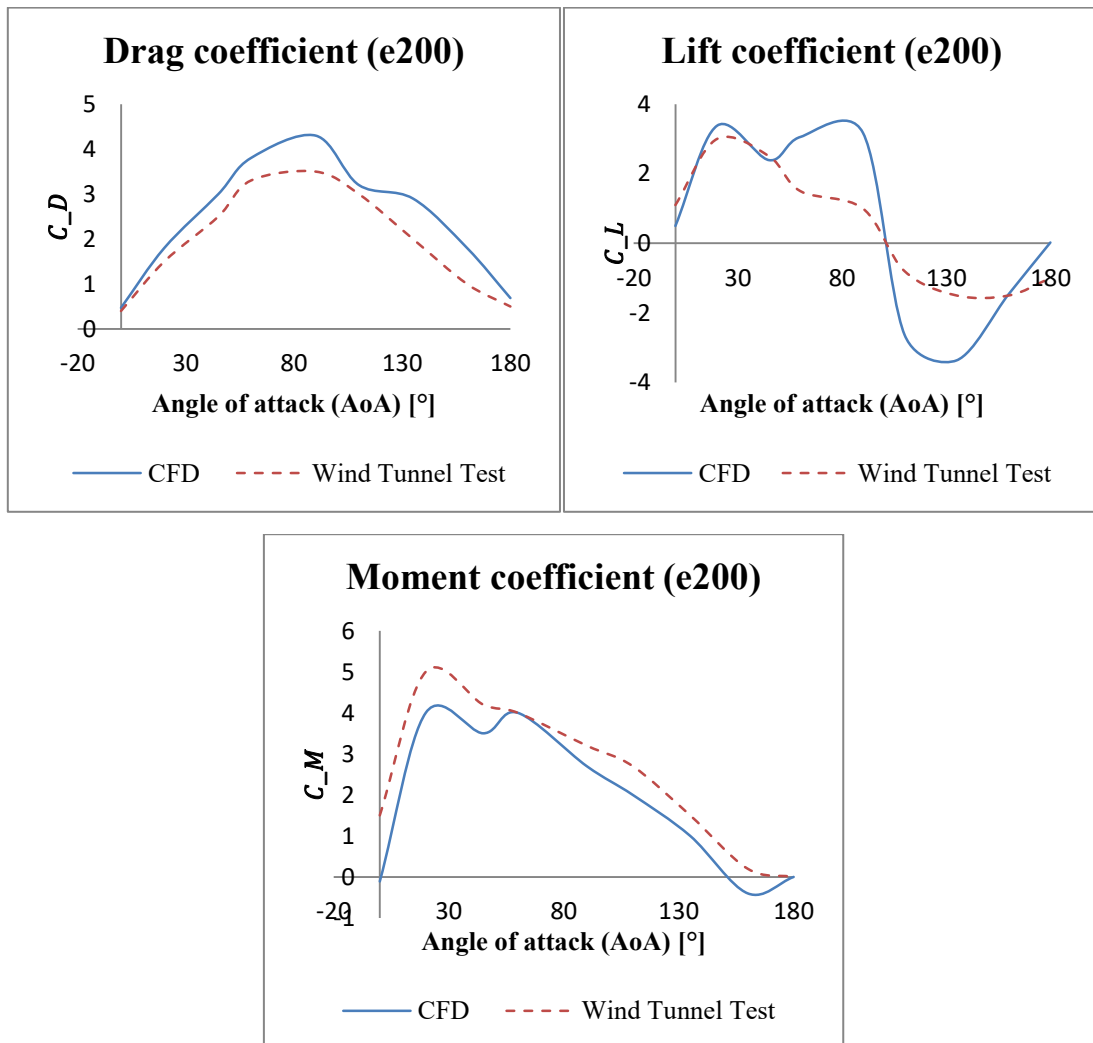


Figure 4.1.5 – Aerodynamics coefficients related to Wind Tunnel Tests results for e200

A comparing plot is presented in Figure 4.1.6 in order to show the comparison between the different trends of CFD results referring to the values of eccentricities.

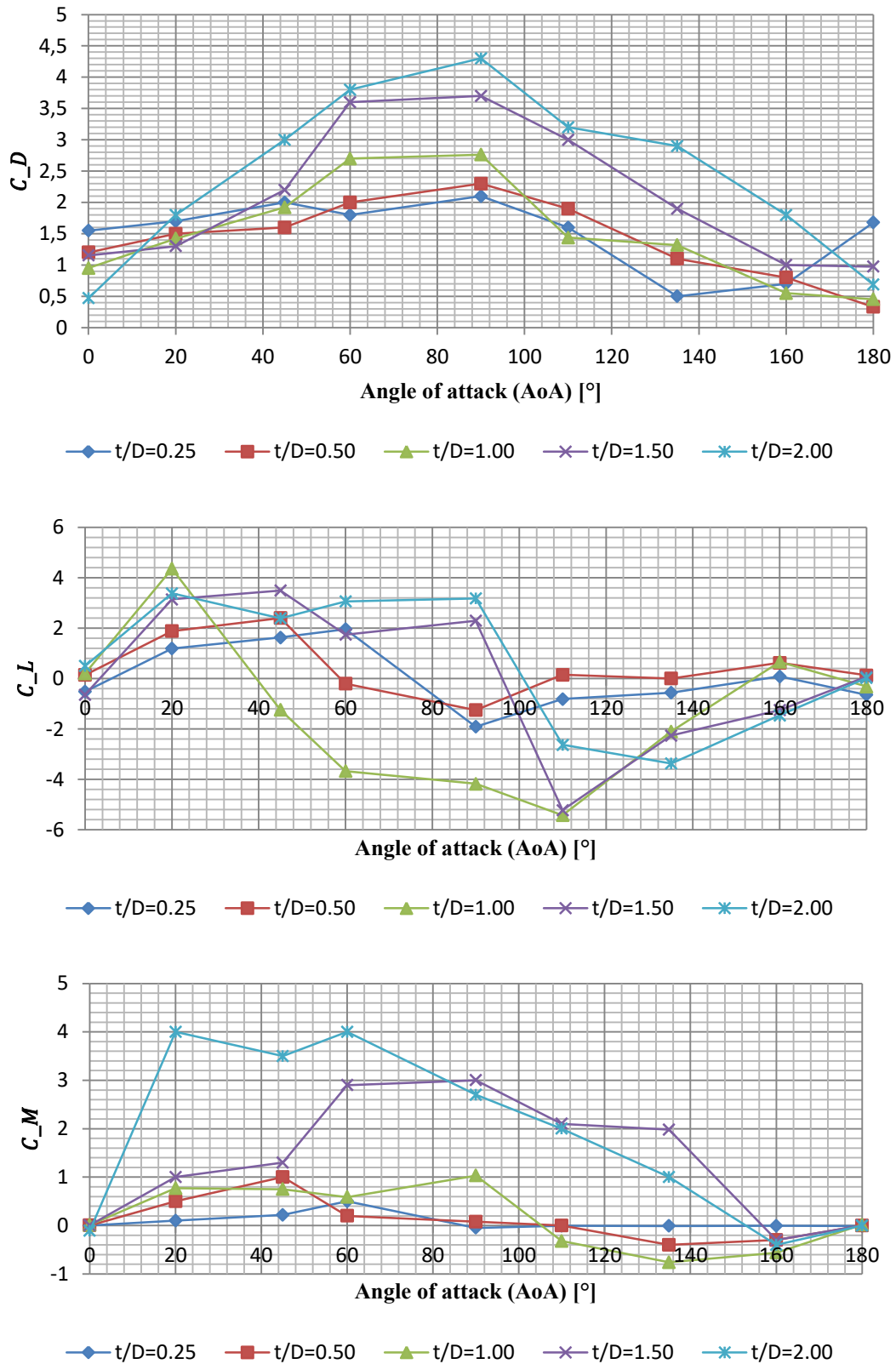


Figure 4.1.6 – Comparison between the several trends of aerodynamic coefficients for all the eccentricities studied, in relation to the variation of angle of attack

All contours presented refer to parameters about wind effects like Pressure [Pa], Velocity [m/s] and Turbulence [Turbulent Kinetic energy $J/kg=m^2/s^2$].

$t/D=1.50$ (e150) - $U=10$ m/s - $\alpha=0^\circ$ - $t=5\%$

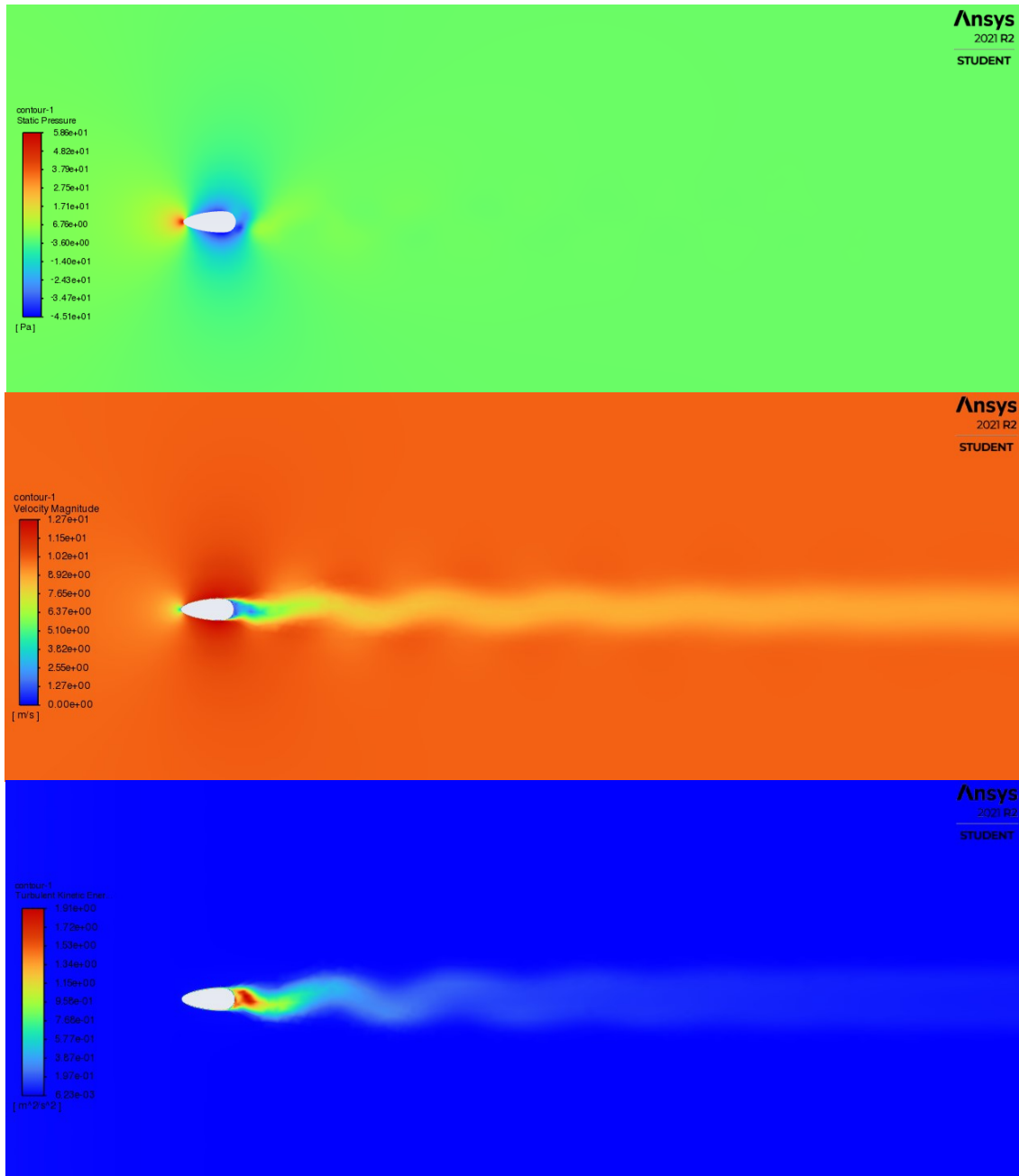


Figure 4.1.7 – Contouring dealing with Pressure [Pa], Velocity [m/s] and Turbulence [m^2/s^2] respectively, for ice eccentricities of 150% (e150) and $AoA=0^\circ$

$t/D=1.50$ (e150) - $U=10$ m/s - $\alpha=20^\circ$ - $t=5\%$

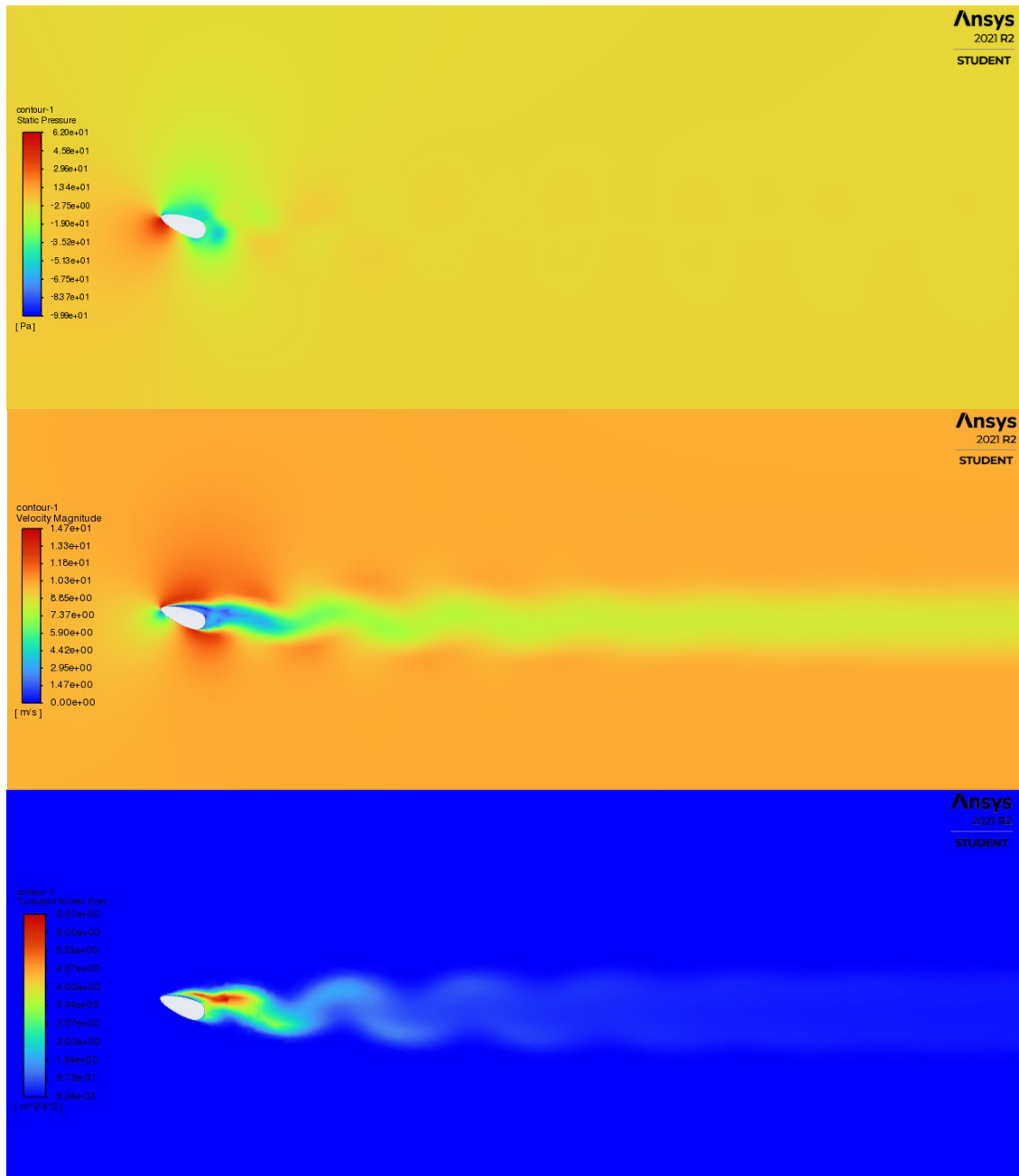


Figure 4.1.8 – Contouring dealing with Pressure [Pa], Velocity [m/s] and Turbulence [m²/s²] respectively, for ice eccentricities of 150% (e150) and AoA=20°

$t/D=1.50$ (e150) - $U=10$ m/s - $\alpha=45^\circ$ - $t=5\%$

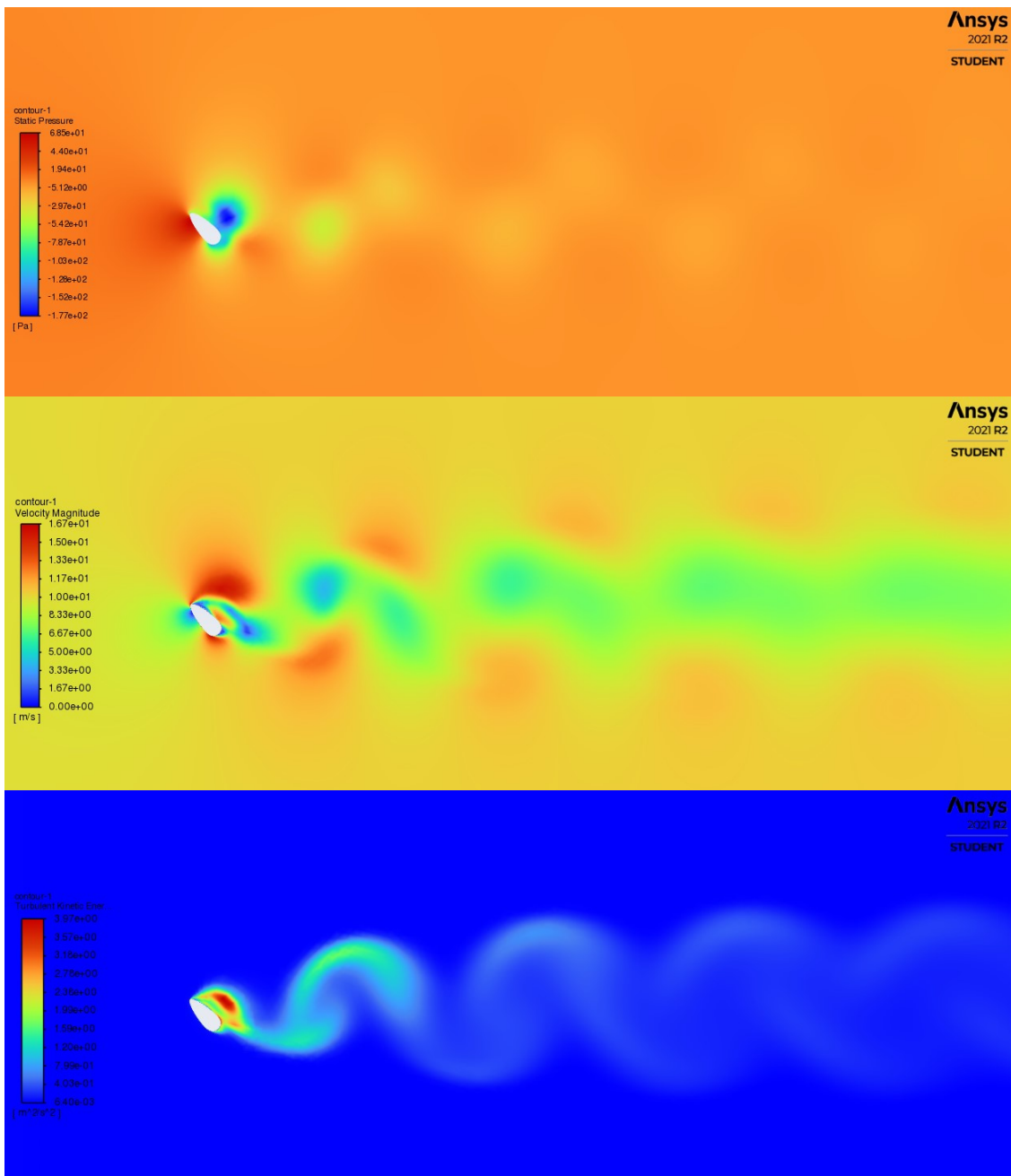


Figure 4.1.9 – Contouring dealing with Pressure [Pa], Velocity [m/s] and Turbulence [m²/s²] respectively, for ice eccentricities of 150% (e150) and AoA=45°

$t/D=1.50$ (e150) - $U=10$ m/s - $\alpha=60^\circ$ - $t=5\%$

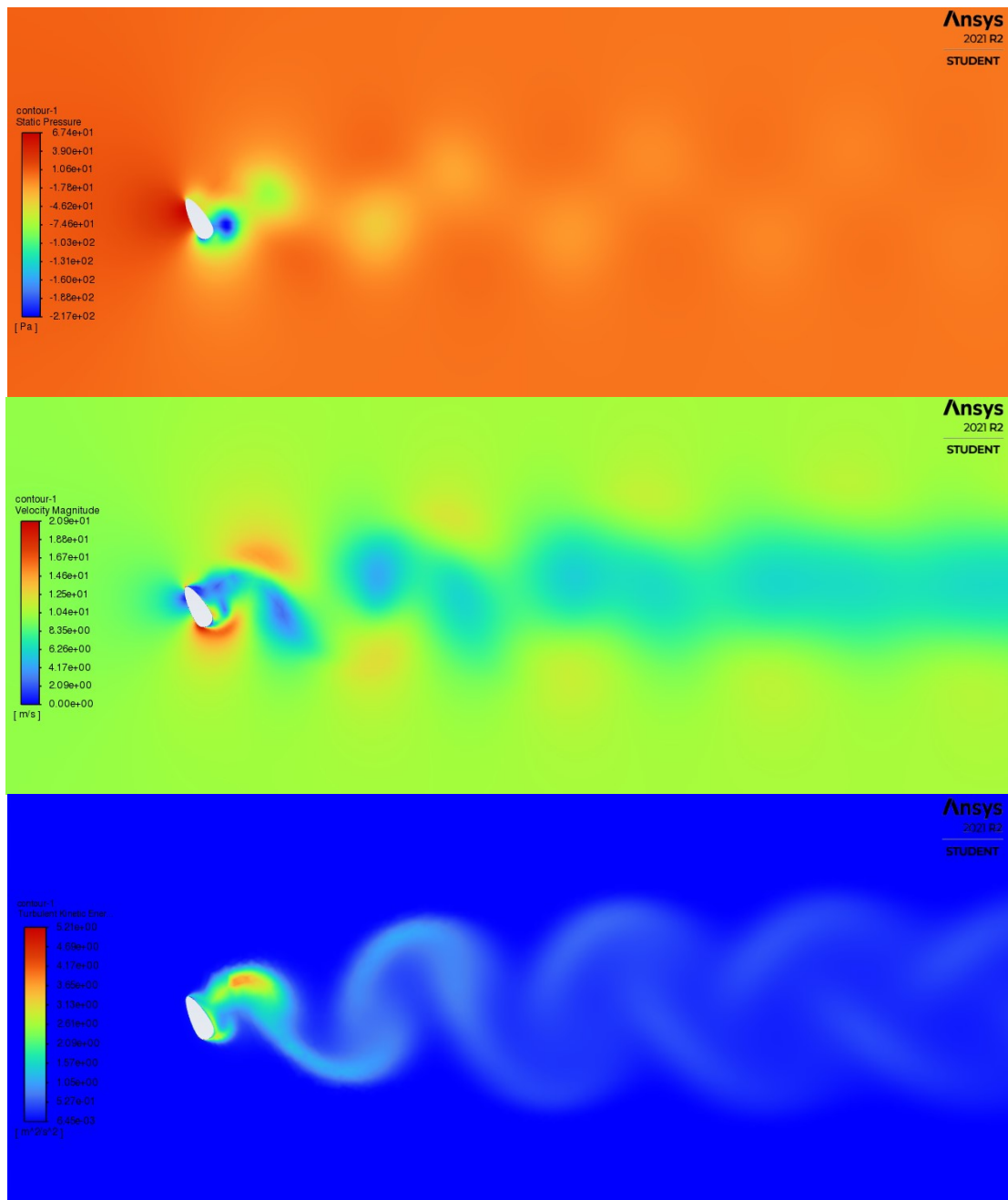


Figure 4.1.10 – Contouring dealing with Pressure [Pa], Velocity [m/s] and Turbulence [m^2/s^2] respectively, for ice eccentricities of 150% (e150) and $AoA=60^\circ$

$t/D=1.50$ (e150) - $U=10$ m/s - $\alpha=90^\circ$ - $t=5\%$

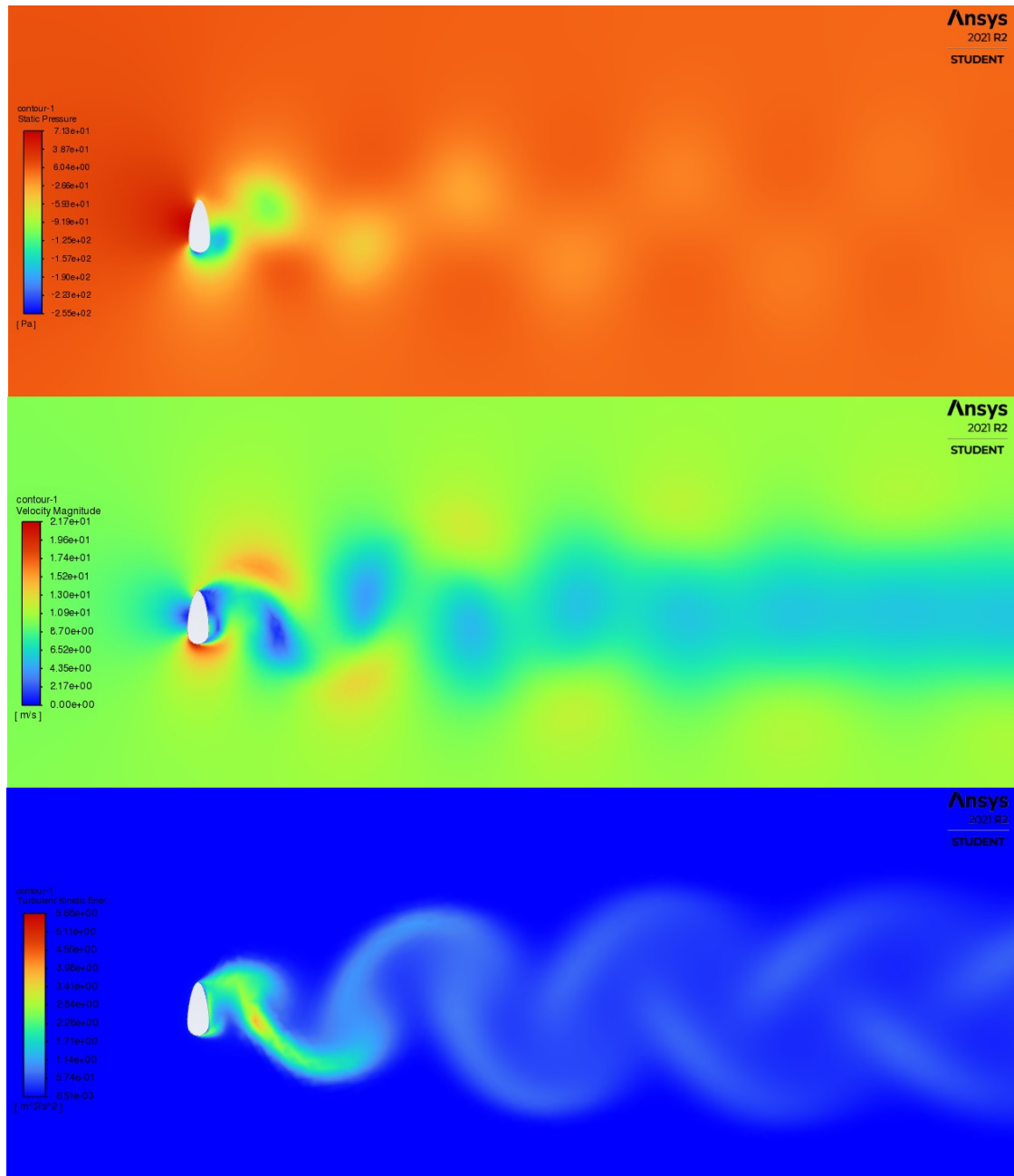


Figure 4.1.11 – Contouring dealing with Pressure [Pa], Velocity [m/s] and Turbulence [m^2/s^2] respectively, for ice eccentricities of 150% (e150) and $AoA=90^\circ$

$t/D=1.50$ (e150) - $U=10$ m/s - $\alpha=110^\circ$ - $t=5\%$

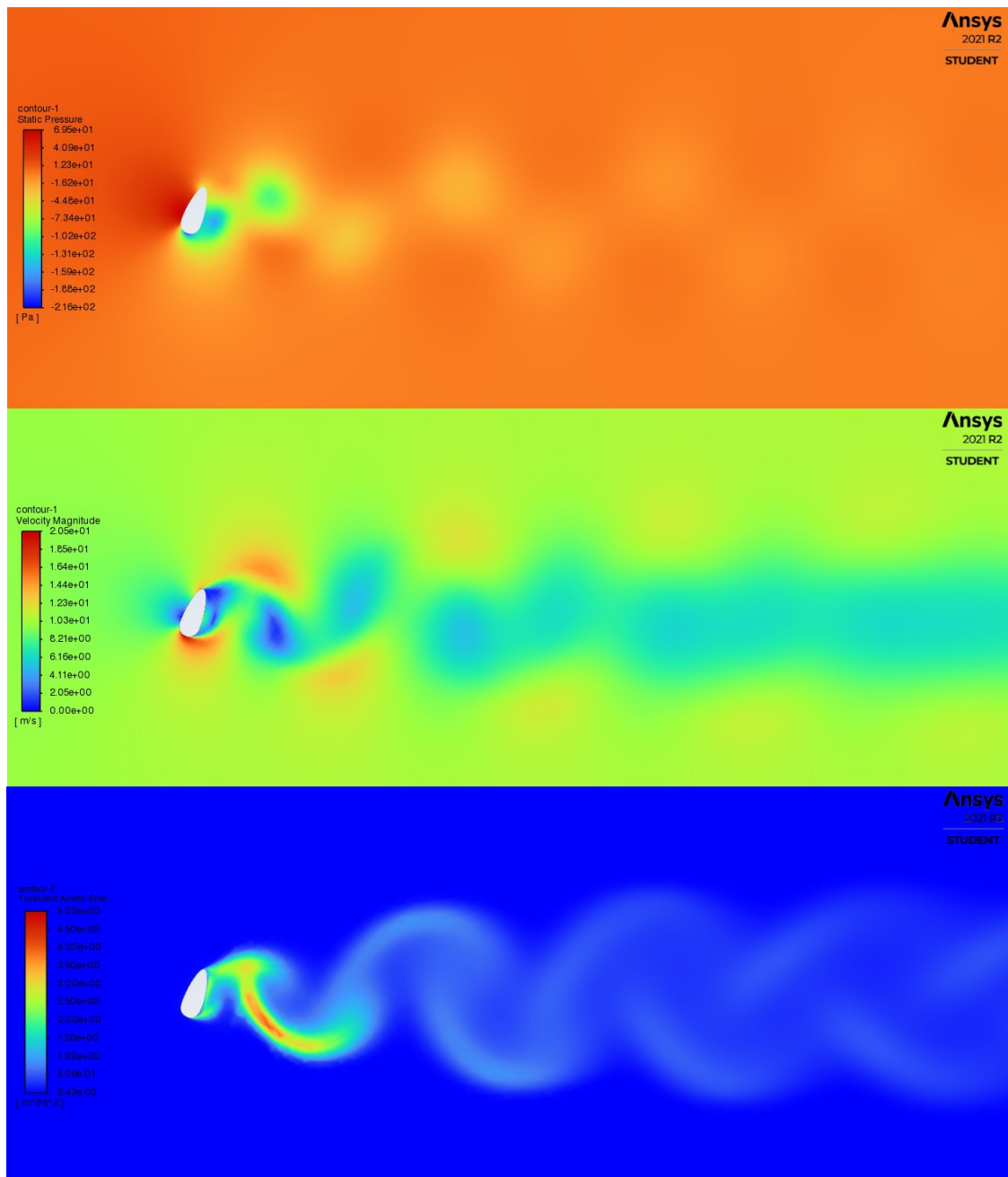


Figure 4.1.12 – Contouring dealing with Pressure [Pa], Velocity [m/s] and Turbulence [m^2/s^2] respectively, for ice eccentricities of 150% (e150) and $AoA=110^\circ$

$t/D=1.50$ (e150) - $U=10$ m/s - $\alpha=135^\circ$ - $t=5\%$

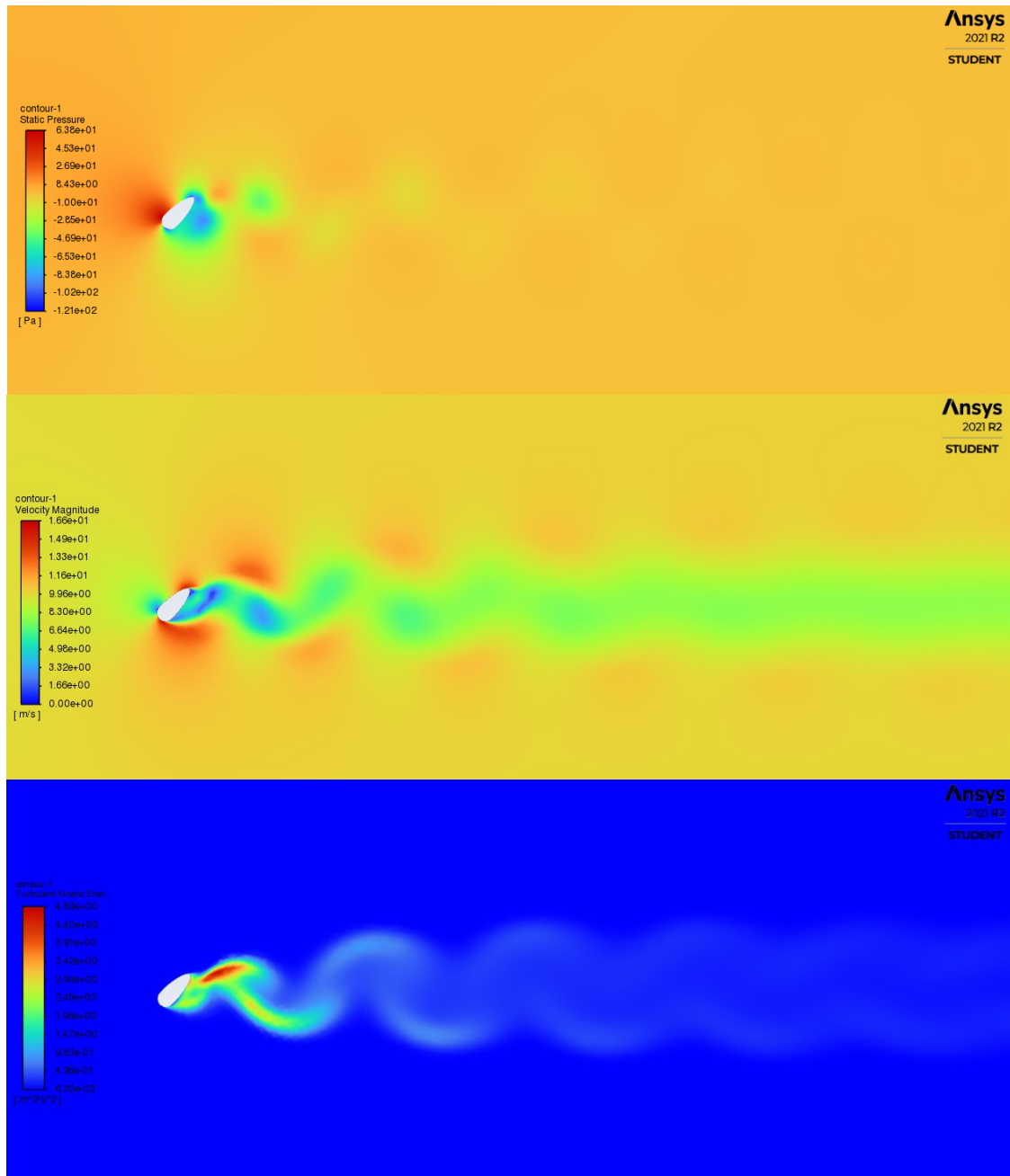


Figure 4.1.13 – Contouring dealing with Pressure [Pa], Velocity [m/s] and Turbulence [m²/s²] respectively, for ice eccentricities of 150% (e150) and AoA=135°

$t/D=1.50$ (e150) - $U=10$ m/s - $\alpha=160^\circ$ - $t=5\%$

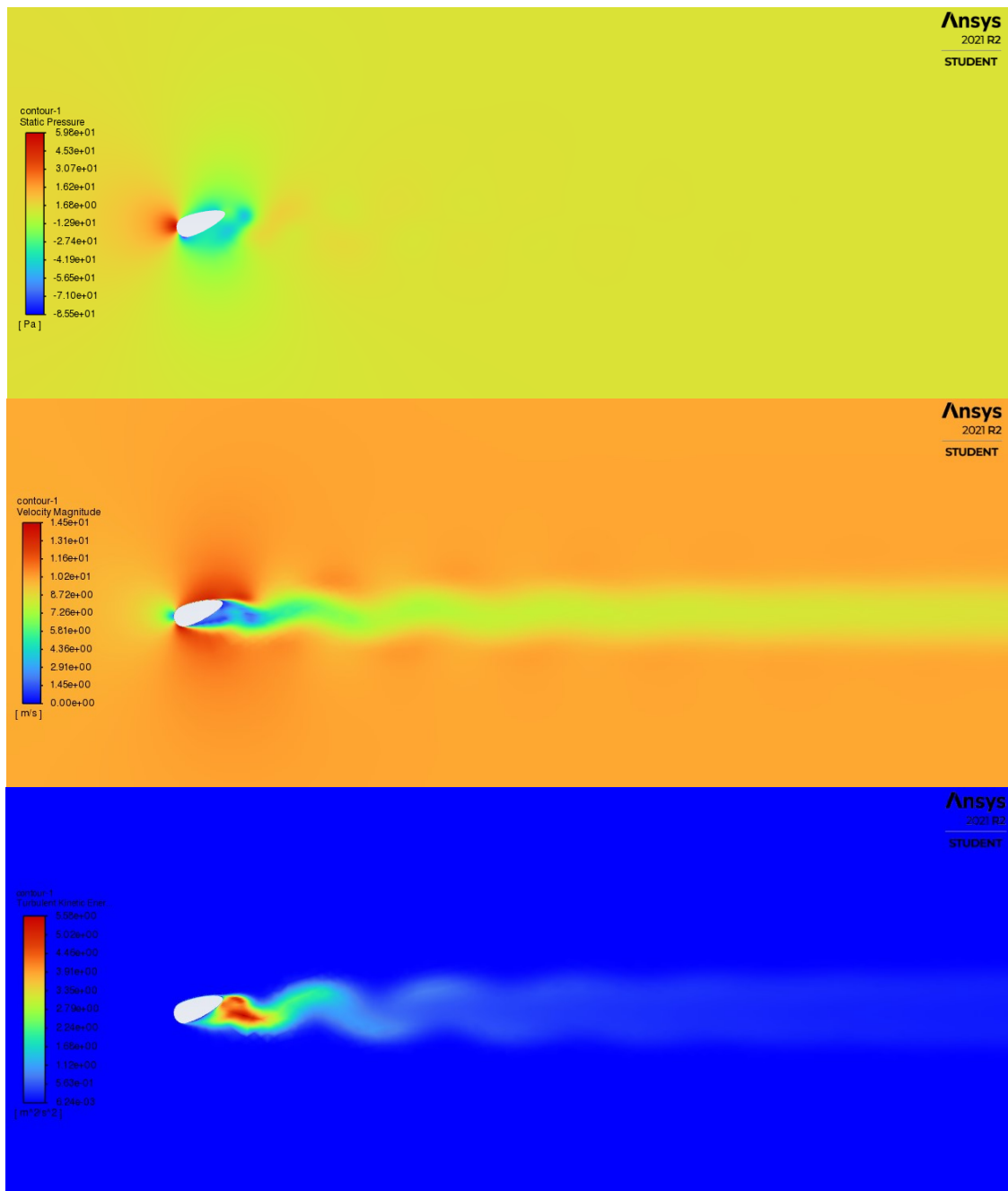


Figure 4.1.14 – Contouring dealing with Pressure [Pa], Velocity [m/s] and Turbulence [m²/s²] respectively, for ice eccentricities of 150% (e150) and AoA=160°

$t/D=1.50$ (e150) - $U=10$ m/s - $\alpha=180^\circ$ - $t=5\%$

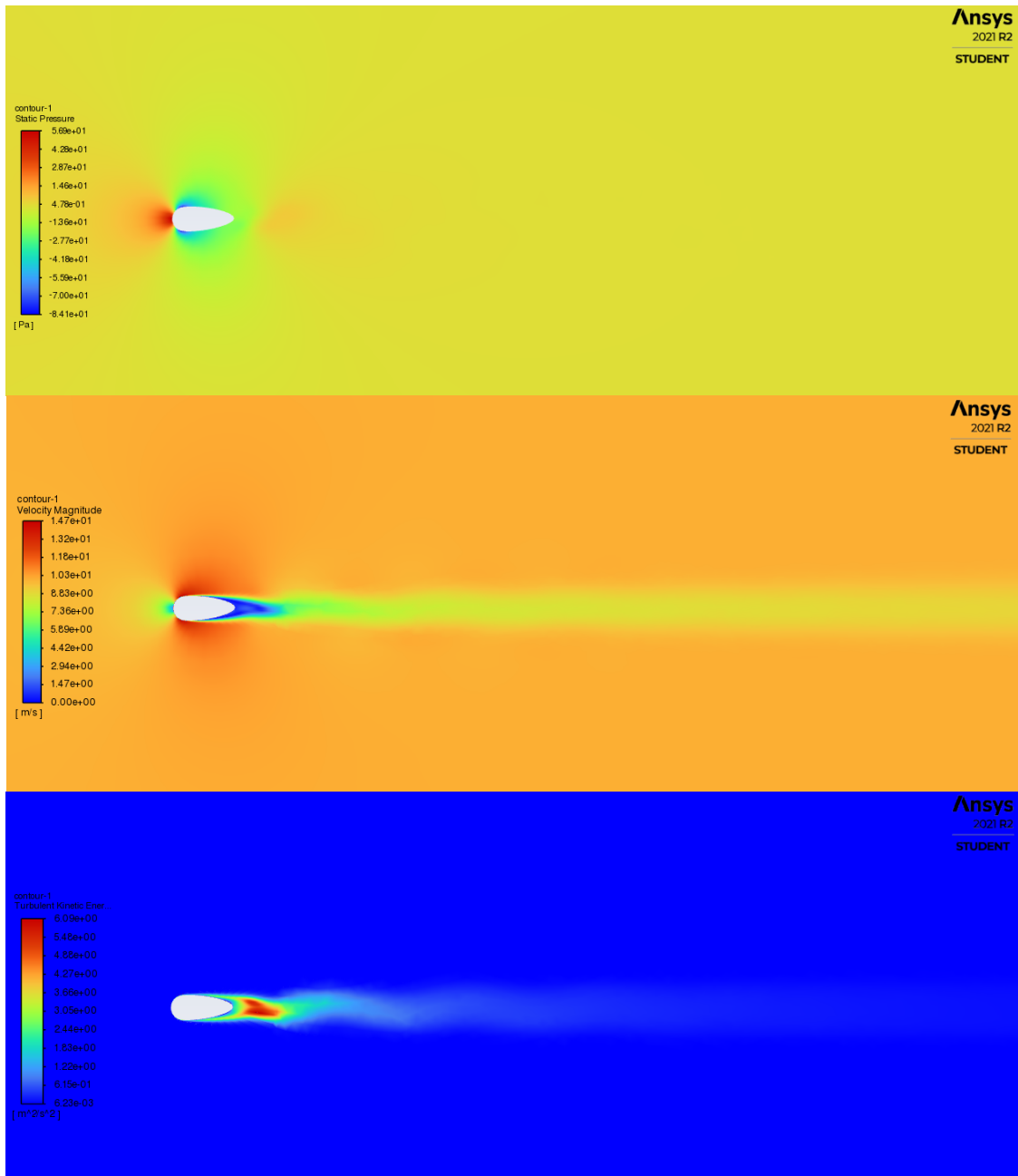


Figure 4.1.15 – Contouring dealing with Pressure [Pa], Velocity [m/s] and Turbulence [m²/s²] respectively, for ice eccentricities of 150% (e150) and AoA=180°

The results in terms of aerodynamics factors and coefficients were used to calculate vibrating forces, representing the air flow effects on the wire. As several authors have established in different documents, as said, the real trend of these forces is not possible to know. However, they can be well expressed by harmonic mathematical formulation since they change their sign and direction during the acting. Hence, choosing for instance the sinusoidal development, a simple equation along time can be written:

$$y = A \sin(\omega t) \quad (4.1.1)$$

Where A is the amplitude and ω the frequency of the wind load.

As already explained in the previous chapters, according to the orientation of the axis chosen for the model and the will to investigate only the main galloping vibrating mode which is the vertical one, the y -direction was the reference. In fact, this axis represents the only one in common between structural model and fluid dynamics model, since in the former it deals with the lift direction orthogonal to the wind velocity and in the latter it is orthogonal to the line longitudinal development.

Thus all the Lift coefficients were captured in their worst effects on the transverse section, generating Lift external forces through the already expressed formulation:

$$L = \frac{1}{2} \rho U^2 A C_L \quad (4.1.2)$$

This value represents the amplitude of the harmonic time history for the dynamic load, while the frequency used in the sinusoidal expression was obtained by the theoretical results through the Strouhal number, that embodies the vortex shedding frequency:

$$f = St \frac{U}{D} \quad (4.1.3)$$

This last one, as already said, is assumed 0.18 for this problem, since this value characterizes the case of cylindrical wire hit by the wind stream flow. It is important to highlight that U is the relative velocity of the flow respect to the conductor and D is the characteristic length [m]. In particular, D length is to be recognized as the orthogonal projection of the transverse section in relation to the wind speed. In other words, if α is the angle of attack created between U direction and the ice-accreted section, D length is obtained thanks to $\sin(\alpha)$, and it consists of a kind of equivalent diameter, as follows.

$$D = k d \sin(\alpha) \quad (4.1.4)$$

Where k is the amplifying factor according to the ice eccentricity studied (for example, the case of $e025$ the value of k is 1.25), d is the design diameter of the wire and α the angle of attack, as said. Obviously, D value acquires its maximum at $\alpha = 90^\circ$, where the

orthogonal projection is the same of the equivalent diameter, and has its minimum at $\alpha = 0^\circ$ and $\alpha = 180^\circ$, where the sinusoidal function is null.

Table 4.1.1 gives the trend of D values and the corresponding frequencies for dynamic load assumed.

Table 4.1.1 – Calculation of characteristic length and vortex shedding frequencies

α [°]	α [rad]	$\sin(\alpha)$	e025		e050		e100		e150		e200	
			k d sin(α)	f [Hz]	k d sin(α)	f [Hz]	k d sin(α)	f [Hz]	k d sin(α)	f [Hz]	k d sin(α)	f [Hz]
20	0,34889	0,34185	0,01006	198,742	0,01208	165,618	0,0161	124,213	0,02013	99,3708	0,02415	82,809
45	0,785	0,70683	0,02081	96,1207	0,02497	80,1006	0,03329	60,0755	0,04161	48,0604	0,04994	40,0503
60	1,04667	0,86576	0,02549	78,4751	0,03058	65,3959	0,04078	49,0469	0,05097	39,2375	0,06117	32,6979
90	1,57	1	0,02944	67,9406	0,03532	56,6171	0,0471	42,4629	0,05887	33,9703	0,07065	28,3086
110	1,91889	0,94003	0,02767	72,2753	0,03321	60,2294	0,04428	45,172	0,05534	36,1376	0,06641	30,1147
135	2,355	0,70795	0,02084	95,9679	0,02501	79,9732	0,03334	59,9799	0,04168	47,9839	0,05002	39,9866
160	2,79111	0,34335	0,01011	197,875	0,01213	164,896	0,01617	123,672	0,02021	98,9377	0,02426	82,4481

The development of the characteristic length and the frequency follows what it was expected for them, with a maximum value for $\sin(\alpha)$ at the angle of attack $\alpha = 90^\circ$ and at which a minimum frequency in Hz corresponds. It has to be specified that in this Table angles 0° and 180° are absent, since they would have diverged frequency values as the \sin would have been null at the denominator. It is clear that the value assumed in the structural model was the one at $\alpha = 90^\circ$, which also represents the orientation at which the most significant vortexes generate.

Figure 4.1.16 shows graphically the trend of vortex shedding frequency.

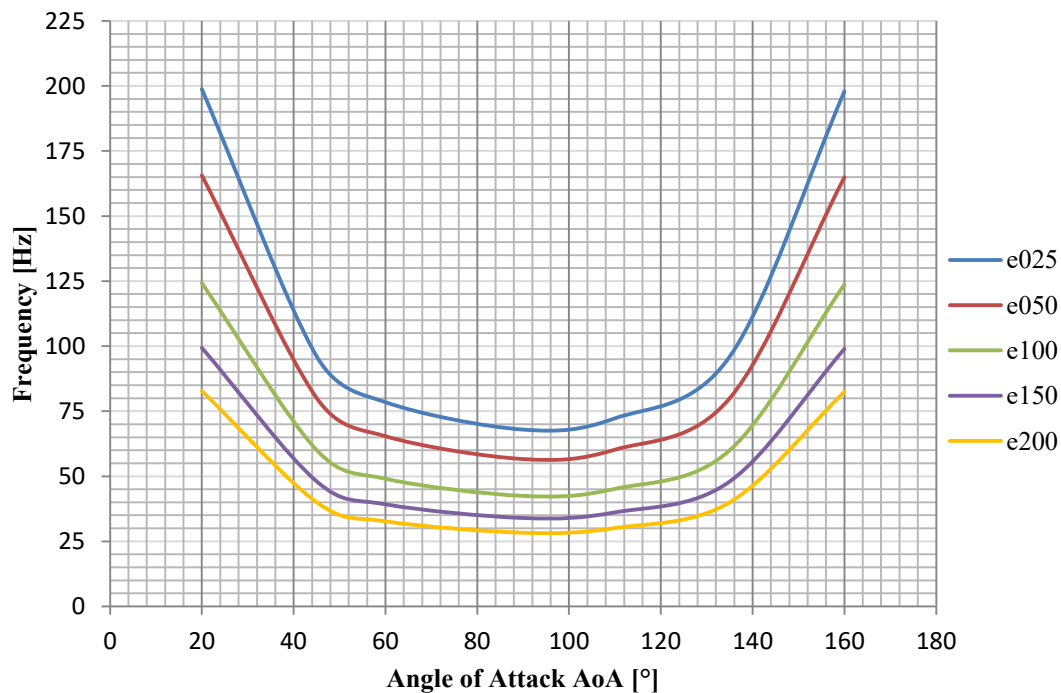


Figure 4.1.16 – Trend of vortex shedding according to theoretical solution

As expected, the trend is correctly symmetric in relation to the 90° angle.

Equation (4.1.1) requires a frequency expressed in terms of *rad/s*, thus the values were converted as well.

Alvise Rossi, as said, had the possibility to log into the use of Wind Tunnel Room, in which the wind conditions were applied with a significant precision and in a realistic way. The so called “Wind Tunnel Test” gave several results in terms of vortex shedding frequency, that were compared with the theoretical ones obtained in this Thesis.

Figure 4.1.17 shows the plot of comparison between them, even if only the cases of eccentricities *e025* and *e100* were recorded and reported in his document. Hence, the precision of the model adopted is expressed by just these two reference comparisons.

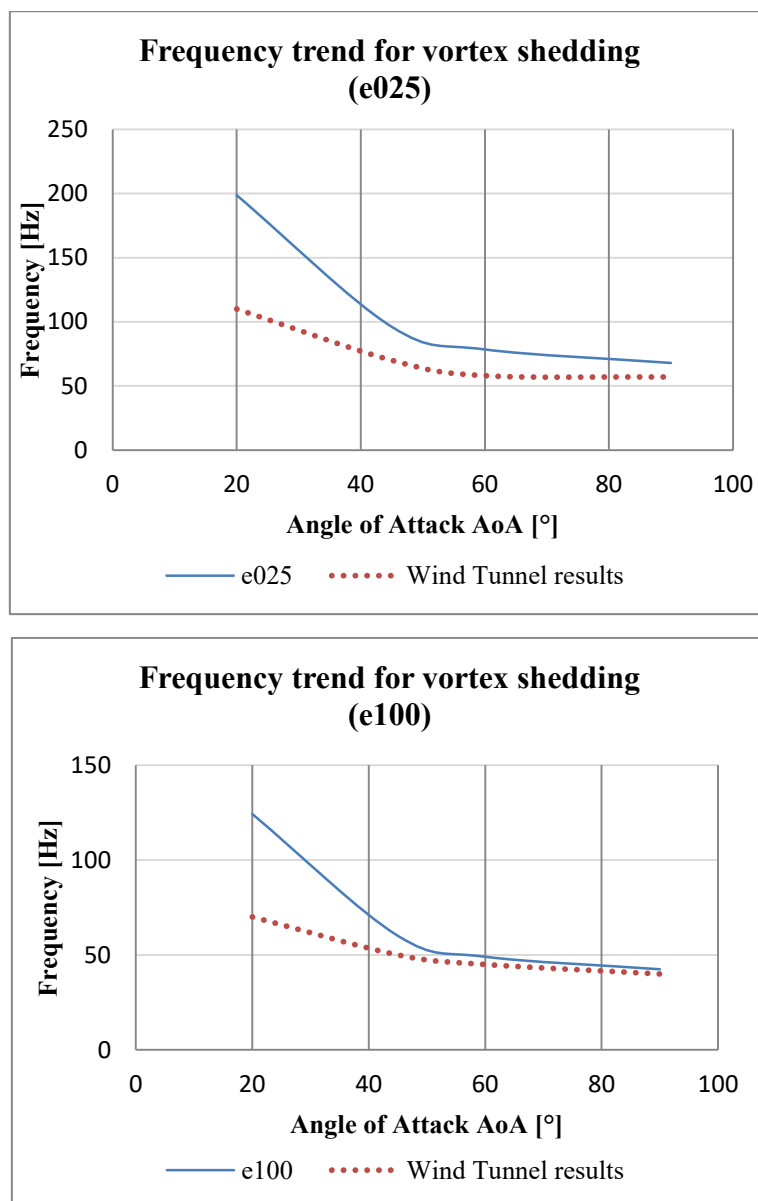


Figure 4.1.17 – Comparison between vortex shedding frequencies with Wind Tunnel Results

The analysis of results above highlight that the value of the vortex shedding varies with the angle of attack similarly to theoretical predictions. However, the frequencies for the range of small angles of attack are larger than the ones obtained by the physical simulation with the Wind Tunnel Test. This over-prediction, however, tends to reduce itself at bigger angles of attack, until to converge at 90°, where the discrepancy is minimal.

The set of frequencies coming from vortex shedding is far from a resonance condition and it is also coherent with the statements contained in Eurocode 1. Indeed, the Scruton number is quite high and the ratio between the critical vortex shedding velocity and the onset wind velocity for galloping is far from the critical range highlighted.

Table 4.1.2 points out all the values presented and discussed in Subsection 1.2.1 and Subsection 3.4, but also proposed in a structural application in [43], dealing with characteristic aerodynamic parameters and speeds.

Table 4.1.2 – Aerodynamic numbers and parameters according to Eurocode

δ_s	0.049	-
ρ	1.25	kg/m ³
m_i	1.35	kg/m
b_i	0.02355	m
Sc	190.8394	-
$n_{1,y}$	0.31	Hz
b	0.02355	m
a_G	1	-
$U_{C,g}$	2.786446	m/s
St	0.18	-
U_{Critic}	0.040558	m/s
FACTOR	68.70218	-

Where δ_s is the structural damping expressed by the logarithmic decrement, thus defined:

$$\delta_s = 2 \pi \xi = 2 \pi \frac{c}{C_c} = 2 \pi \frac{c}{2 m \omega} = 0.049 \quad (4.1.5)$$

With C_c critical dumping, defined as the first value of dumping feature which allows the structure to return in its initial position without vibrating effects.

As the Table shows, the geometric parameter b is linked to the absence of ice eccentricity, since it corresponds to the value of conductor diameter. Thus, Table 4.1.3 has the purpose to give an idea of the new aerodynamic parameters in relation to the several ice shapes considered in the case of study.

Table 4.1.3 – Aerodynamic critical speeds for ice shapes adopted

	<i>e000</i>	<i>e025</i>	<i>e050</i>	<i>e100</i>	<i>e150</i>	<i>e200</i>
b [m]	0.02355	0.029438	0.035325	0.0471	0.058875	0.07065
$U_{c,g}$ [m/s]	2.786446	3.483057	4.179669	5.572892	6.966115	8.359338
$U_{Critical}$ [m/s]	0.040558	0.050698	0.060838	0.081117	0.101396	0.121675

As it can be noticed, the crescent trend of the onset wind velocity for galloping tends to the U velocity adopted in the present case of study ($U = 10$ m/s). Since it represents the minimum value of wind speed at which galloping can occur, it is rational thinking that the transmission line studied is probably prone to this kind of instability.

4.2 Structural results

As just presented, the structural model was loaded with the external forcing coming from the CFD analysis, in terms of Lift forces with their own Lift coefficients.

It has to be pointed out that two kinds of load are acting on the span: the static self-weight of the transmission line, and then the one of ice eccentricities, and the dynamic load from the combination of wind and snow accreted.

The span was divided into four parts, with the aim to simulate the progressive development of icing load from a supporting tower to the other one. This choice is justified by the fact that 160 m in length of the span are significant and the possibility to register an ice accretion not over the whole line conductor but just on a few quarters of it is quite interesting and not so small. Hence, four cases considered, respectively within the configurations in which the span is half covered, alternative covered, concentrated covered at the middle and all-covered by the ice load. Figure 4.2.1 gives an illustration of the load cases just mentioned.

A non-linear dynamic analysis was carried out, according to a time step that needed to respect and follow the structural period of the line. Thus, a time step of 0.01 s was adopted as constant for the whole simulation, that was interrupted at 30 s. the aim was to not to over-load the software with a period that might be too big and at the same time with a time step too small. In fact, it has to be noticed that a time step of 0.001 s was assumed for a trial analysis with the will to validate the value above. The numerical results confirmed the ones found with the greater time step, that means the convergence

was just achieved with a lesser computational cost. Obviously a such condition is to be preferred.

The explanation about the 30 s as the whole time analysis is to be searched in the convergence of the solution in terms of oscillations. These ones, in fact, stabilize themselves after a few seconds in their values, thus the idea of the discrepancy from the static position is achieved almost immediately. On top of this, the will to quit the dynamic analysis after half minute.





<u>Load case 1</u>	
Half covered span	
<u>Load case 2</u>	
Alternative covered span	
<u>Load case 3</u>	
Concentrated covered span	
<u>Load case 4</u>	
All covered span	

Figure 4.2.1 – Load cases combination

Obviously, the most important and burdensome configuration for icing load is the fourth one, since it represents the case of whole span covered with thus the maximum gravitational ice load on it. However, also other three combination were considered as representative of a condition in which snow may be broken out by the wind dynamic forcing itself, due to high fragility characterizing the layers. Furthermore, they might represent a situation where special thermal devices are installed on the line with the aim to melt snow and free cable by excessive icing weight.

In these conditions the cable would be subjected to a different load state and thus it is rational to evaluate the effect of wind flow hitting a conductor with a non-uniform load applied.

Figure 4.2.2 represents a plot illustrating cinematic and static results for the $e025$ case, in terms of sag oscillations and reaction forces discharged to supporting towers in the main combination case (All-covered), due to wind turbulence and dynamic loading. Figure 4.2.3, Figure 4.2.4, Figure 4.2.5 and Figure 4.2.6 show the same graphical outputs for the other eccentricity cases.

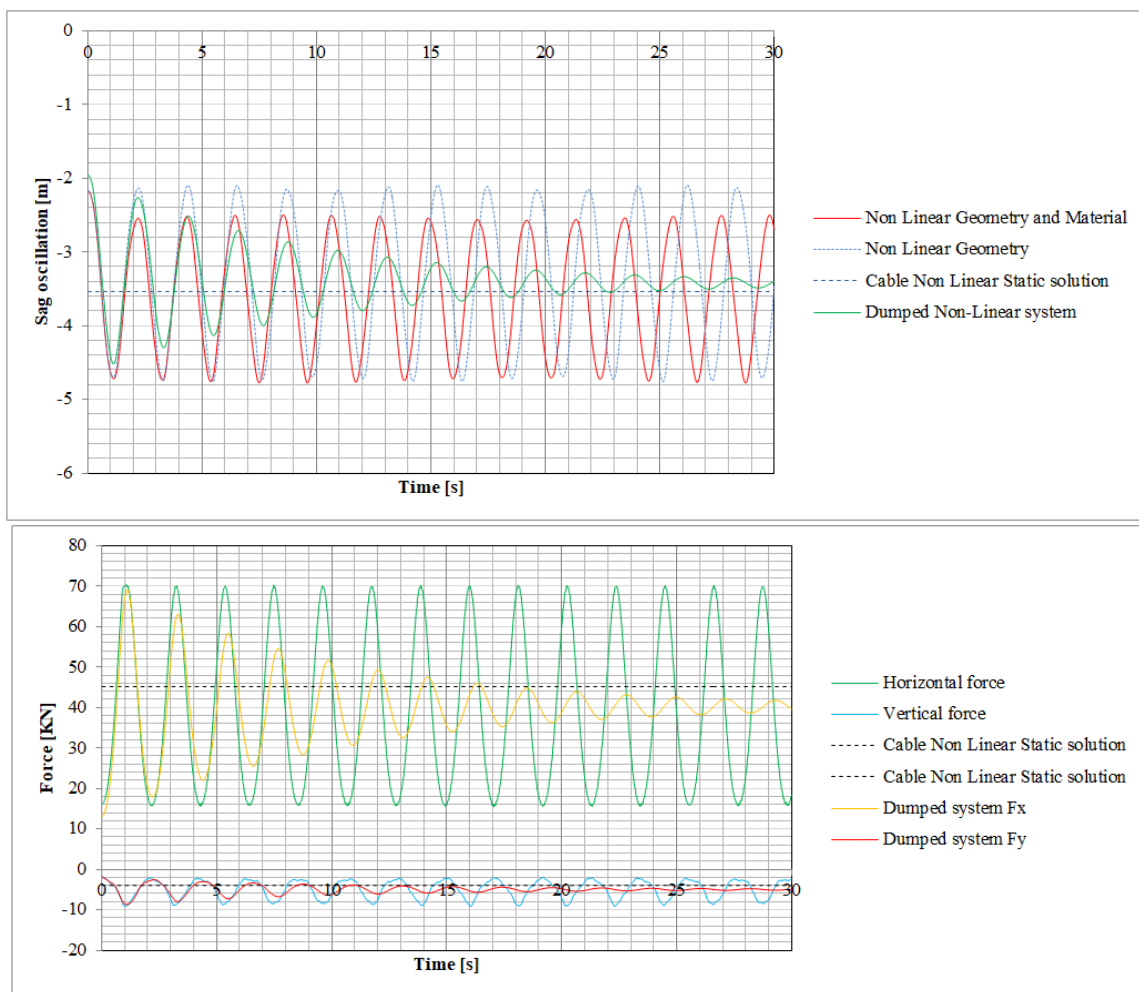


Figure 4.2.2 – Sag oscillation and forces discharged to supports, for the case of $e025$

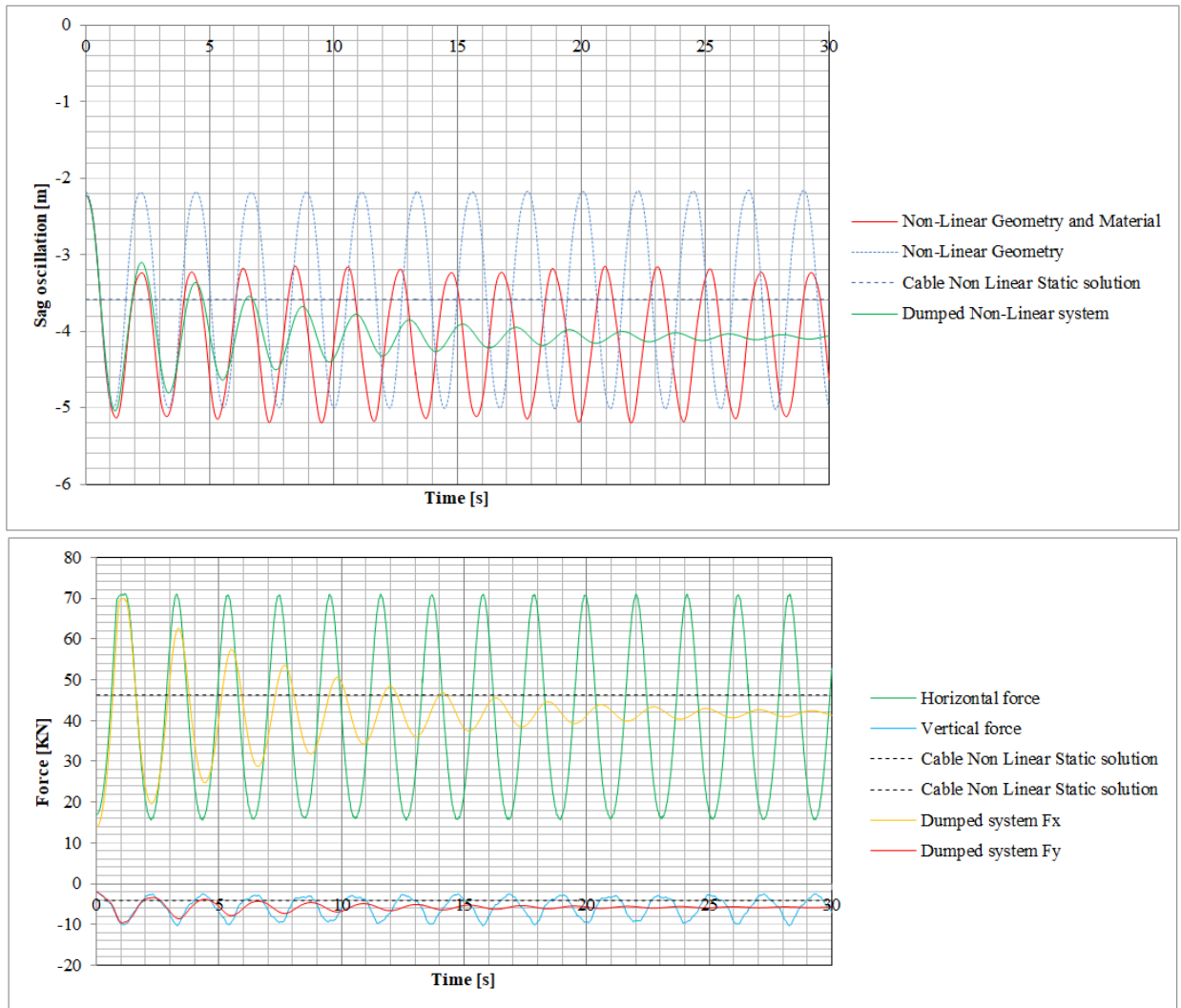


Figure 4.2.3 – Sag oscillation and forces discharged to supports, for the case of $e050$

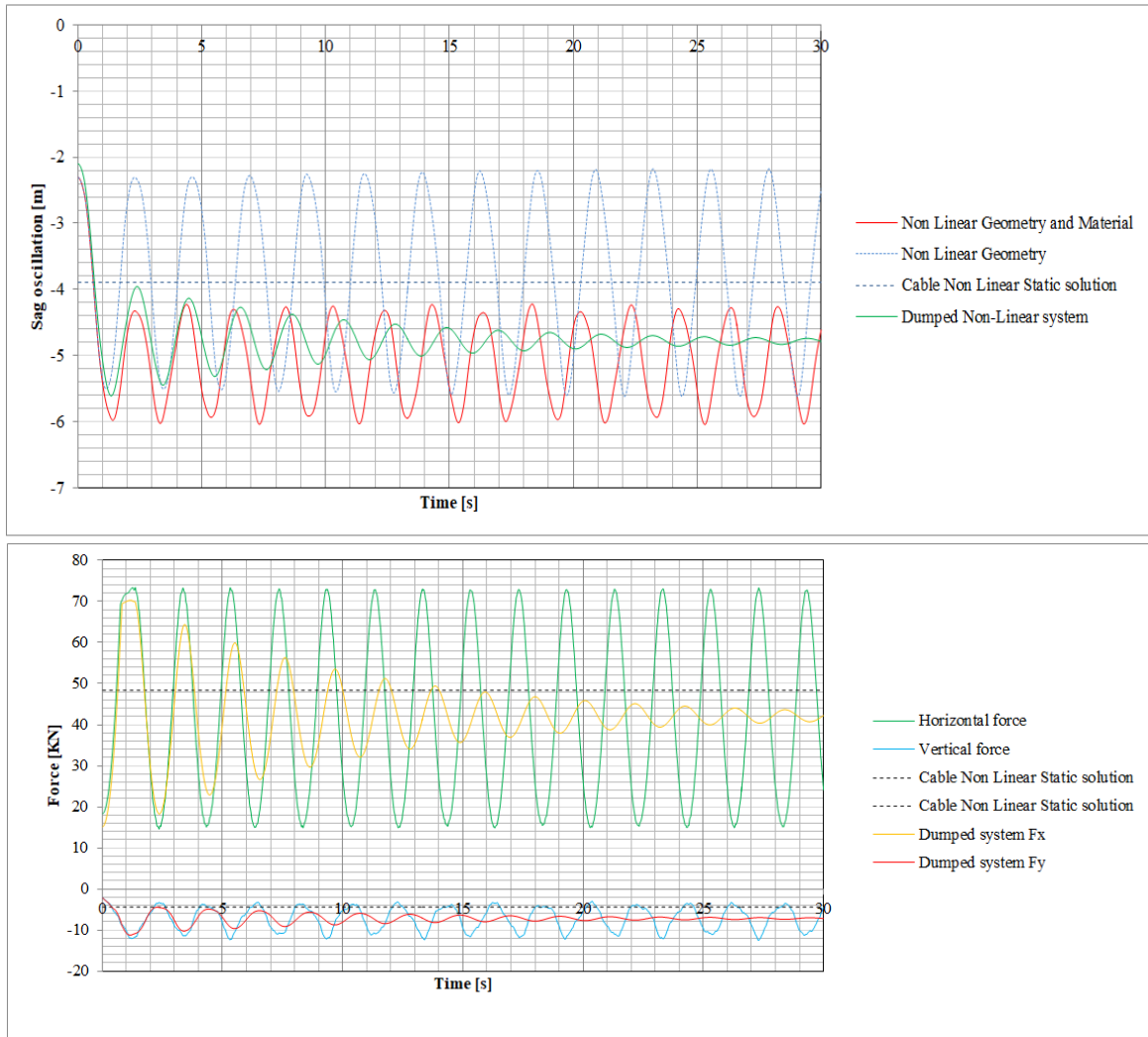


Figure 4.2.4 – Sag oscillation and forces discharged to supports, for the case of e100

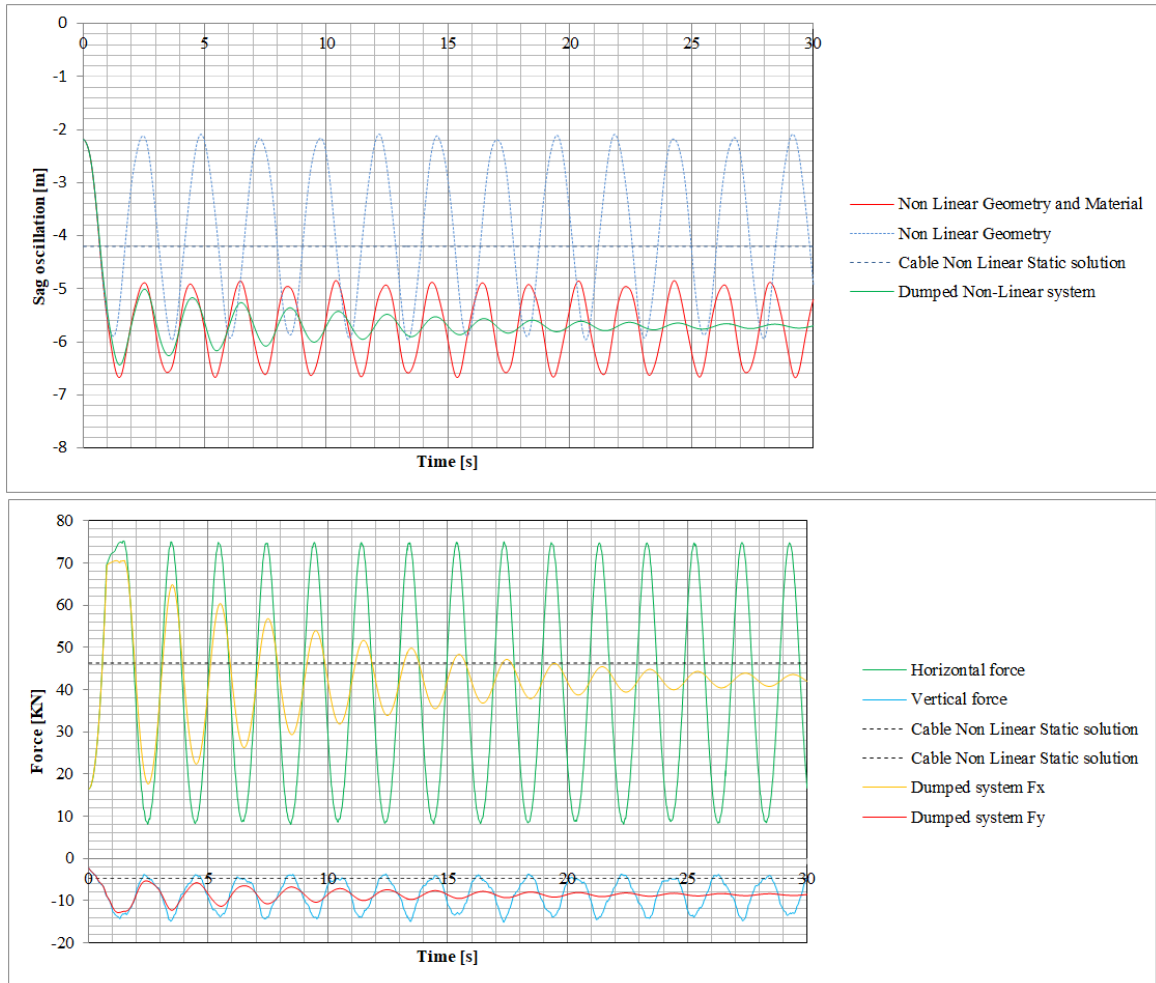


Figure 4.2.5 – Sag oscillation and forces discharged to supports, for the case of e150

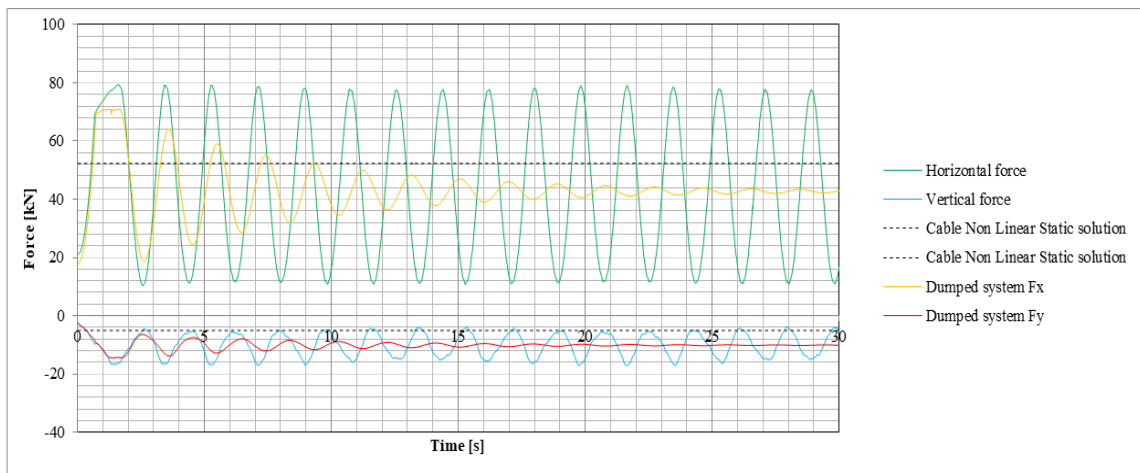
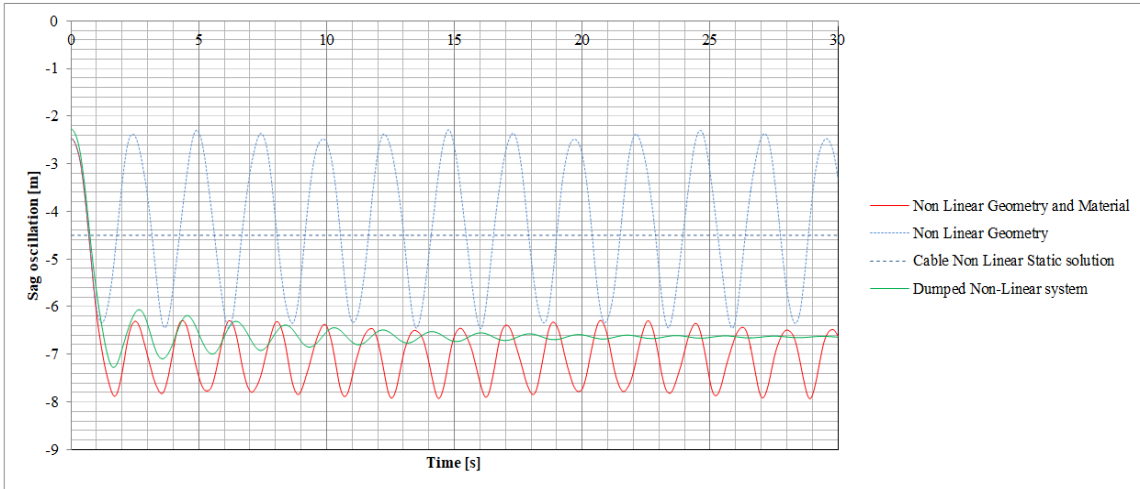


Figure 4.2.6 – Sag oscillation and forces discharged to supports, for the case of e200

As it can be noticed, the difference between non-linear static solution and non-linear dynamic one is clear and it reflects the expected trend, characterizing this kind of structural problem. In fact, the simple harmonic oscillations are gained around a static condition of initial balance, given by the self-weight of cable and snow accreted.

Furthermore, the dumped solution correctly represents a deletion of wire amplitudes but at the same time it records significant displacements as well. Hence, a type of intervention is requires anyway.

Moreover, the absence of structural damping is evident in terms of domain of vibrations: any kind of deletion dealing with displacements and deflections obtained by the analysis was not registered. Hence, the typical undumped solution is achieved and well presented.

Furthermore, there is not any kind of divergence in structural behaviour, clear sign that resonance problem is far. Indeed, the comparison between natural frequency of the span and wind turbulence, caused by vortex shedding, clearly points out that the gap is relevant and thus a resonance manifestation is avoided.

Another interesting result is to be researched in the alteration between the average values of non-linear geometry analysis and the both non-linear geometry with material one. In fact, it highlights a gap that becomes gradually bigger as and when the ice eccentricity increases. This discrepancy does not deal with just the mean values of distributions in time, but it affects also the magnitude of sag oscillation itself. However, at the same time the whole amplitude of structural vibrations becomes shorter as long as the icing load increases. This behaviour can be explained with the key role played by constitutive bond of Aluminium. In particular, it is evident that the conductor overcomes the yield point even with *e050* profile.

Table 4.2.1 – Values of strain state for each case of ice eccentricity

Type of profile	Maximum Strain reached [%]
<i>e025</i>	0.1901
<i>e050</i>	0.1955
<i>e100</i>	0.5931
<i>e150</i>	1.1834
<i>e200</i>	2.1618

As it can be noticed, *e025* presents a first state of yielding inside the conductor and at the middle span point. However, this value can be approximately confused with 0.2%, thus the ultimate state for substantially elastic domain. Instead, with *e100* profile starts several configurations in which the yielding is passed and plasticity comes out.

However, the ultimate tensile strength is extremely far even for the worst combination load case. Figure 4.2.8 shows the non-linear trend of strain percentage for all-covered span combinations.

The consequence of this increasing in terms of strain field is given by a consideration through the compute of Dynamic Amplification Factor (DAF). This one, defined as the ratio between the dynamic response and the equivalent static solution one, highlights the dynamic effect in this kind of analysis. What was expected is a value of DAF always bigger than one, since 1 means an absence of dynamic characteristics of the problem and thus a static phenomenon. Figure 4.2.7 is an illustration of DAF trend for each ice profile case.

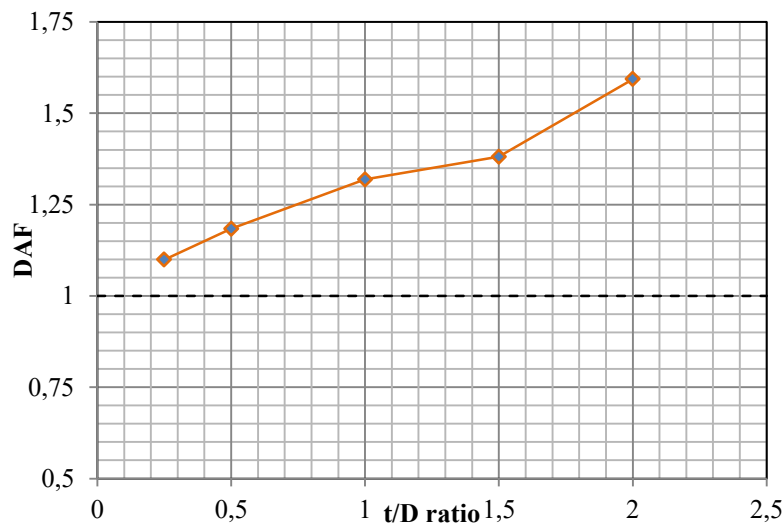


Figure 4.2.7 – Dynamic amplification factor trend

DAF ranges between 1.09 (*e025*) and 1.59 (*e200*), with an average value of 1.31, bigger than 1 as expected. A direct comparison with DAF for a similar case is given by Figure 4.2.8, where this factor refers to a multi-span transmission line system under synoptic wind considering various speeds [38].

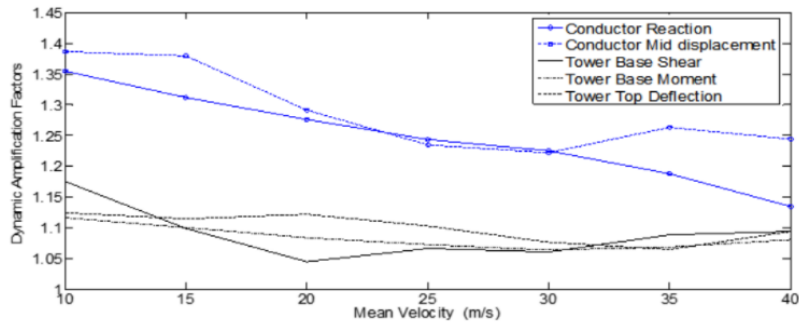


Figure 4.2.8 – DAF vs Mean velocity for a different case of study [38]

The trend is similar to the one obtained with galloping conditions. Also the amplitude of DAF reveals the same peaks for dynamic response.

Another consideration is made in terms of reaction forces discharged to boundaries, represented by supporting towers. Figure 4.2.9 shows the amplification in the static field, with the aim to give an idea of the magnitude increased about the load given to the steel towers.

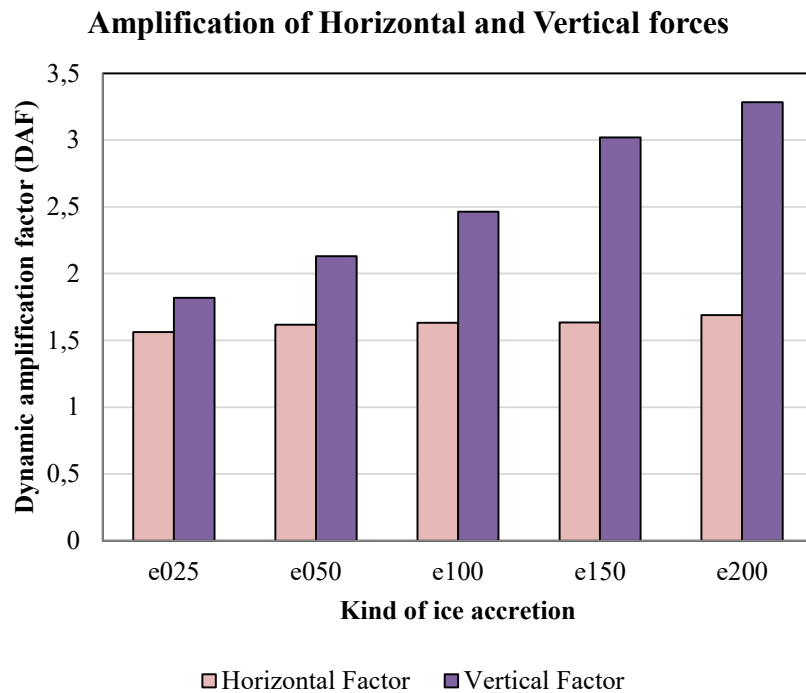


Figure 4.2.9 – Dynamic amplification factor trend for forces on supporting towers

DAF for vertical reactions ranges between 1.81 (*e025*) and 3.28 (*e200*), with an average value of 2.54. A more comprehensive valuation can be made on the base of results coming from similar cases of transmission line. In their publication about cable rupture in transmission line systems, Thiago Carlos and Joas Kaminski [37] report the trend of axial forces in conductors discharged to supporting towers for several combination in term of

rupture cables. Obviously, the case of cable failure is quite different from galloping phenomenon, however the dynamic response and approach are the same adopted with the aim to study structural behaviour. Figure 4.2.10 reports the trend of forces for this kind of dynamic effect.

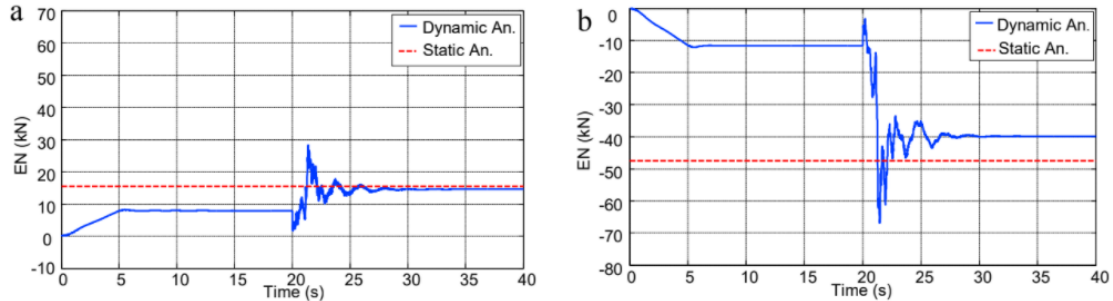


Figure 4.2.10 – Axial forces discharged to towers for a particular case of cable rupture [37]

As the figure highlights, the amplitude of forcing is on the same line of galloping results for this Thesis.

Table 4.2.2 highlights dynamic behaviour under the load case combinations for all kinds of profile. As it can be noticed, the maximum displacement and deflection recorded are less than the ones generated by the all-covered span, as predicted. Once again, the fourth configuration for icing load reveals itself as the most burdensome, pointing out the biggest DAF ever.

However, a significant discrepancy between the three load cases may be discussed, since the concentrated snow at the middle span seems to be the worst hypothesis for the cable. Indeed, the sag of span is the deepest point for the line and in that case it is more solicited than the others.

Table 4.2.2 – Comparison between icing load cases in terms of dynamic response

		Max v [m]	Max A [m]	Static sol. [m]	Strain [%]	DAF	F _x [KN]	F _y [KN]
<i>e025</i>	Load case 1	3.53	1.66	3.01	0.139	1.17	48.88	5.37
	Load case 2	3.49	1.62	3.03	0.142	1.15	51.32	6.04
	Load case 3	4.35	2.52	3.13	0.185	1.38	61.65	7.43
	Load case 4	4.66	2.58	3.53	0.19	1.32	69.59	7.56
<i>e050</i>	Load case 1	3.79	2.11	3.04	0.148	1.24	49.15	6.38
	Load case 2	3.78	1.98	3.06	0.143	1.23	51.55	6.41
	Load case 3	4.34	2.43	3.18	0.176	1.36	62.21	8.15
	Load case 4	5.11	2.03	3.58	0.20	1.42	69.55	8.99
<i>e100</i>	Load case 1	4.16	2.46	3.09	0.171	1.33	59.79	7.46
	Load case 2	4.15	2.27	3.11	0.177	1.34	61.48	9.68
	Load case 3	4.78	2.47	3.25	0.299	1.47	70.52	10.61
	Load case 4	6.18	2.03	3.89	0.59	1.55	72.55	10.67
<i>e150</i>	Load case 1	4.52	2.57	3.15	0.198	1.42	69.36	8.22
	Load case 2	4.55	2.54	3.18	0.199	1.43	69.64	11.54
	Load case 3	5.31	2.05	3.34	0.311	1.58	71.09	12.85
	Load case 4	6.54	1.55	4.21	1.18	1.58	73.52	13.26
<i>e200</i>	Load case 1	4.91	2.21	3.24	0.221	1.51	70.01	9.05
	Load case 2	4.88	2.24	3.20	0.235	1.53	71.89	12.24
	Load case 3	5.83	1.83	3.43	0.342	1.69	72.33	14.84
	Load case 4	7.73	1.25	4.50	2.16	1.71	79.81	15.21

As it can be noticed, green cells are representative of values under the yielding point for Aluminum material, yellow ones have the role to highlight the proximity to yield and finally the red cells point put the cases in which conductor plasticity occurs and thus it would be a design value for future developments. The wire indeed must be designed in order to be maintained in elastic domain.

A summary representation of the two extremities configuration is now given in Figure 4.2.11 for $e025$ and $e200$ respectively, in order to evaluate the amplification order also in graphical terms. Eventually, in Figure 4.2.12 there is a set of all the maximum displacements for vibration reached by every single ice eccentricity in hypothesis of all covered span.

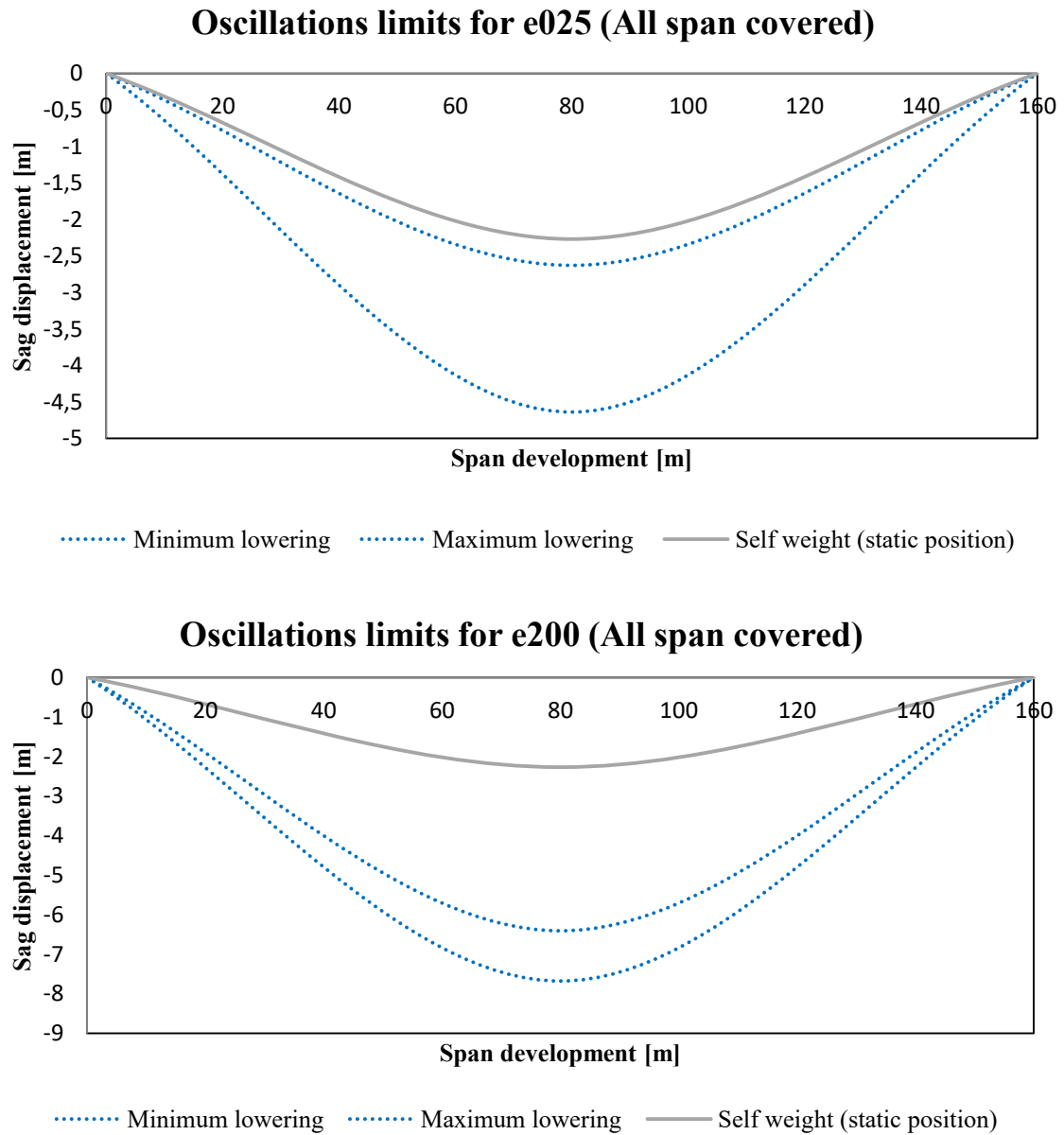


Figure 4.2.11 – Comparison between self-weight configuration and e025-e200 cases

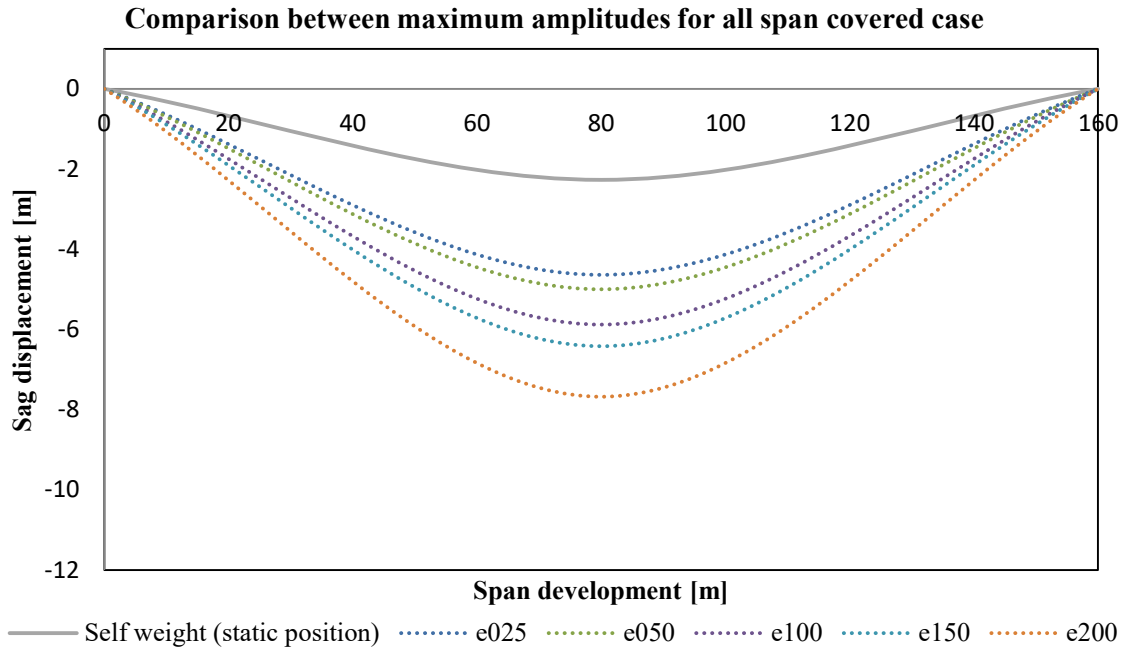


Figure 4.2.12 – Comparison between self-weight configuration and other profile cases

4.3 Resolution Tools

In front of these results obtained by the structural analysis, it is rational to think about several solutions in terms of engineering realistic approach. In fact, the amplitude of displacements recorded by the cable are too much large and in particular they yield to a plastic behaviour of conductors' rheological bond. This condition is not accepted for transmission lines, which need to be functional due to the importance that characterize them, as emphasized in Chapter 1.

Hence, a resolution method is required with the purpose of weakening sag oscillations.

A first intuitive approach is to increase wire section with the aim to contain stress values below to the yielding point, and thus remaining into the elastic domain.

However, it is clear that a such kind of solution leads to an increasing also of span weight, which can give rise problems not only on the dynamic field but also on static configuration since the initial balance would be compromise.

On a dynamic point of view, the increasing of cable mass would play a double antithetic role; it would indeed generate bigger inertial forces which give a significant contribute to the dynamic balance equation, but also the would represent other bigger forces the whole system need to be subjected to.

Thus, a second solution can be considered, in terms of thermal response. In particular, several thermal devices can be installed along the whole span and line, with the aim to be activated when significant ice-loads hit the structure.

In this case, hence, the devices would melt the snow accretion and relieve transmission lines by the external asymmetric bodies and weight. After all, the first three load case combinations represent the conditions in which ratios of span are not covered anymore by the ice accretion. This situation may occur for different reasons, for instances big conductor oscillations that expulse snow due to its very poor friction, or moreover just for the effects of thermal solution in particular zones of the span in which actually the ice load is completely melted instead of other parts.

Eventually, a third and more engineering solution can be adopted. The dumped system has revealed that transmission lines in Aluminium have poor dumping capacities, since the oscillations reduce their amplitude along time but the absolute displacements remain significant.

Hence, an external dumpers are required in order to increase the deletion of vibrations. Stockbridge advices, in this sense, are the most used solution to protect cable from oscillating complications. These kind of dumpers that have gotten their name from G.H. Stockbridge in 1924. Their design has evolved along the years but substantially the functional concept has always remained the same: two masses suspended of a specially designed wire, fixed to the conductor with a clamp [41].

When a dumper is placed on a vibrating cable, the vibration is transmitted from the terminal to the two masses causing their motions and creating this kind of vibration absorbing capacity. Figure 4.3.1 shows Stockbridge in its shape and typical position on transmission line systems.



Figure 4.3.1 – Stockbridge dumper

The two masses have the same values and are represented by two degrees of freedom, corresponded to the two main ways of motions of that system, shown in Figure 4.3.4.

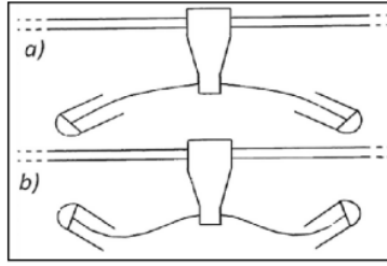


Figure 4.3.2 – The two ways of motions of a Stockbridge [42]

The dissipation effect of Stockbridge is represented by a force component in phase with the vibrating velocity [42]. This damping force modifies the behaviour of the conductor, deleting its oscillations.

Eventually, it is important to highlight that there is not a particular position in which the damper must be installed, since it depends on the vibrating frequency of the conductor.

It is therefore not possible to determine a priori an optimal position of the Stockbridge, but an optimal damper can be considered in terms of functionality. The dissipated energy can be written as follows [42]:

$$E_d = \pi F q \sin(\Phi) \quad (4.3.1)$$

Where F is the applied force, q is the displacement and Φ is the phase shift between the force vector and the displacement of a point considered. Thus, an optimal damper requires the following condition.

$$F_{opt} = \omega \sqrt{Tm} \quad (4.3.2)$$

Where F_{opt} represents the optimal force per unit length, ω is the frequency and T is the tension of the cable. In this condition, the optimal value is acquired when the \sin assumes the value 1. Thus, Φ must be $\pi/2$.

Figure 4.3.3 shows a typical behaviour of a Stockbridge damper.

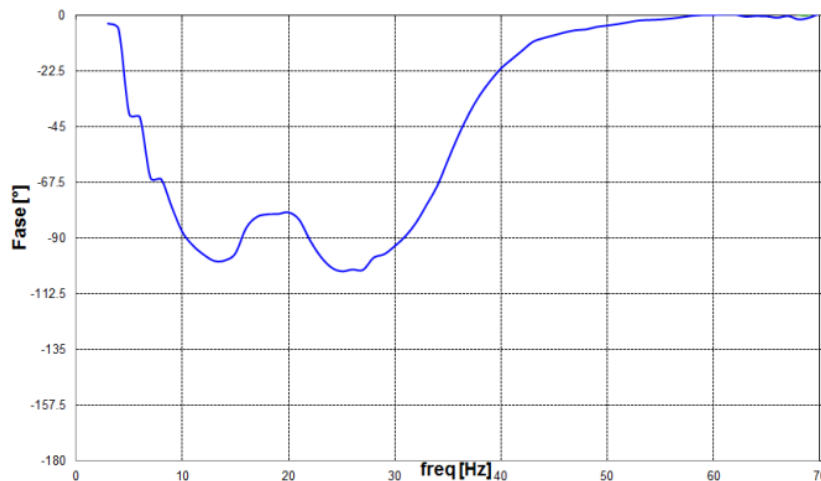


Figure 4.3.3 – Typical functionality of Stockbridge [42]

Chapter 5

Conclusions

This final chapter is aimed to point out the major outlooks of this Thesis and the whole research work dealing with Galloping phenomenon.

The Canadian transmission line system of Long Lake Hydro Project was the object of a structural and aerodynamics analysis, performed in order to investigate the dynamic behaviour of a wire due to wind and snow combination.

5.1 Summary

From a parametric and statistical analysis of climatic dataset, it was highlighted that the most important role in terms of galloping development was played by wet snow. By considering this kind of natural event as an increasing of transverse section of the wire, once dropped on the transmission line's conductor, several cases were performed in icing load. The eccentricities created by the iced layers were assumed in terms of both self-weight acting on the line and amplification factors on the geometrical field, since the cylindrical section acquires a half-elliptical shape. Five cases were considered for additional section thickness, with a magnitude of 25%-50%-100%-150%-200% times the conductor's diameter, giving rise to the profile names used respectively *e025*, *e050*, *e100*, *e150* and *e200*.

A constant value of wind velocity in free flow conditions was assumed equal to $U=10$ m/s, after studying a wind speed distribution during wet snow events, according to literature and dataset about climatic conditions of the site during the 20 years observation period, made by the research Canadian team.

The angle of attack generated by wind direction and the transverse section axis was considered in its variation on a range between 0° - 180° . This orientation is extremely

important in terms of creating aerodynamics differential effects, generated by the flow in hitting the iced-shape wire profile. Thus, 45 combinations were performed in CFD analysis considering the angle of attack and the kind of ice eccentricity.

The results obtained with ANSYS software allowed to record Lift coefficients necessary to calculate Lift forces, that were subsequently downloaded on the structural model in STRAUS7. By combining fluid dynamic and mechanical behaviour, a full analysis of galloping effects was carried out.

As the set of angles of attack highlights, galloping is more likely in the range that varies from 15° to 30° for small angles, and 160° - 180° for greater ones [1].

The trend of displacements registered reflect the harmonic response expected by the model, as oscillations around the initial non-linear static condition made by self-weight load. In terms of magnitude, maximum amplitude was recorded for the case of $e200$, where obviously icing load is extreme. This output consideration is the same for both undumped and dumped system.

As the initial classification have highlighted, the amplitudes of galloping vibrations are very large, in terms of meters. Aeolian and Wake-induced oscillations would have recorded amplitudes with an order of magnitude around millimeters or centimeters. However, even if the field of sag displacements records a significant oscillations, these ones are contained into a range that allows to point out a distance from resonance phenomenon. The trend of them is indeed a kind of limited stationary conditions without divergence of strains.

Even though resonance effects were not recorded, since the frequency of vortex shedding reveled quite far from the one of the span conductor, several problems can be signed up due to the wire oscillations. For instance, the overlapping of conductors can cause the interruption of transmission line services, but also fatigue damages. Moreover, on the field of force balancing, horizontal and vertical reactions can yield to instability crisis on supporting towers.

Hence, the resolution methods and tools proposed in Subsection 4.3 are the most adopted and rational expedient to cope with this kind of dynamic problems.

Obviously each solution needs to be evaluated on the economic field in terms of costs coming from each method, a condition that always drives every single decision in engineering struggles.

5.2 Future developments

A long series of future studies can be made on the Galloping theme, since both its lack of knowledge on the scientific international scene and the fact that this project was restricted to the only vertical in-plane oscillations.

Hence, a possible next step of this studying may be the extension of galloping effect to out-plane motions and torsional behaviour. Obviously, as said, the assumption of beam-plane analysis and the time available for the Thesis did not allow to investigate all the degrees of freedom for cable behaviour. Moreover, a more comprehensive comparison of aerodynamic results can be conceived, since the constant value of wind velocity may vary on a range established due to statistical investigation. Thus, a whole parametric analysis may be set up, in order to improve control and knowledge on galloping instability in terms of aerodynamic field.

Eventually, an alternative span of the line can be considered with the same approach, with the aim to compare behaviour under the same unstable conditions. Furthermore, as literature has signed and highlighted, since the Long Lake Hydro Transmission Line is developed on a continuous altitude variations, an extension of the studying for the case of supporting towers not lying at the same level can be pointed out.

The single conductor assumption may be also replaced by multiple cables characterizing the single span of the line. In fact, as just discussed, galloping phenomenon is able to activate overlapping problems for cables causing the interruption of the whole line services, and thus the energy delivered to activities and people. Hence, if conductors are arranged in a non-staggered manner, this kind of risk can occur.

Furthermore, two or three dimensions extension of the structural problem would allow to understand deeper galloping effects and oscillations amplitude, with also a more comprehensive knowledge of the error linked to the assumption of an analysis based on the linear theory of cable free vibrations. In this case, a global dynamic behaviour would be considered in its three-dimensional stiffness and a different approach in order to generate wind pressure.

Eventually, oscillations can be checked and even muffled, thanks to damping devices such as Stockbridge tools, as reported and discussed in the final part of Chapter 4. This kind of analysis allows to evaluate wire's harmonic response with the contribute of dumping capacity, which was neglected in the first simulation for this Thesis and then considered as an internal capacity of the conductor material. However, the use of special

dumping tools such as Stockbridge requires a particular analysis to be able to reproduce the global behaviour of the advice. In this sense, a refined 3-D model would be set up in order to investigate all the stress states available in Stockbridge and their dynamic contribute in terms of span vibrations, like most of documents and researches have done for them.

References

- [1] Alvise Rossi, “*Wind tunnel modelling of snow and ice effects on transmission lines*”. University of Denmark and Università degli Studi di Padova, Italia, 2018.
- [2] J. Lee, Ho-Yeon Jung, J.R Koo, Yoonjin Yoon, Hyung-Jo Jung, “*Prediction of Galloping Accidents in Power Transmission Line Using Logistic Regression Analysis*”. The Korean Institute of Electrical Engineering. 2017
- [3] Wagner T., “*Modeling of Wind Borne Ice Accretion on Power Transmission Lines*”. Department of Architecture, Civil Engineering and environmental Sciences University of Braunschweig – Institute of Technology, Braunschweig, Germany, 2020.
- [4] Preformed Line Products, “*Conductor Galloping Basics*”. Cleveland, Ohio, 2016.
- [5] Task Force B2.11.06, “*State of the art of conductor galloping*”. Paris, France, 2005.
- [6] Makkonen L., “*Models for the growth of rime, glaze, icicles and wet snow on structures*”. Technical Research Centre of Finland (VTT), 2000.
- [7] Units, Corso di Progetto di Strutture, Azioni sulle strutture, 2018-2019.
- [8] CIGRE-187, “*Design optimization of a 138 kV transmission line with optical phase conductors*”. CIGRE Canada Conference, Montréal, Québec, 2019.
- [9] Samy Krishnasamy and Svein M. Fikke, “*An objective approach for selecting ice or wet-snow design loads on transmission lines*”. The Royal Society, Mississauga, Ontario, Canada, 2021.
- [10] Sakamoto Y., “*Snow accretion on overhead wires*”. Central Research Institute for Electric Power Industry, Tokyo, Japan, 2000.
- [11] Daisulce Kuroiwa, “*Icing and Snow Accretion on Electric Wires*”. Research report CRREL 123, U S. ARM Y MATERIEL COMMAND, Hanover, New Hampshire, 1962.

- [12] Caijin Fan and Xingliang Jiang, “*Analysis of the Icing Accretion Performance of Conductors and Its Normalized Characterization Method of Icing Degree for Various Ice Types in Natural Environments*”. Laboratory of Power Transmission Equipment & System Security and New Technology, Chongqing University, Shapingba District, China, 2018.
- [13] N. Nikitas and J.H.G. Macdonald, “*Misconceptions and generalizations of the Den Hartog galloping criterion*”. University of Leeds, United Kingdom, 2013.
- [14] William C. Skamarock, Joseph B. Klemp, Jimmy Dudhia, David O. Gill, Dale M. Barker, Michael G. Duda, Xiang-Yu Huang, Wei Wang, Jordan G. Powers, “*A Description of the Advanced Research WRF Version 3*”. NCAR Technical Note, Boulder, Colorado, USA, 2008.
- [15] Borna A., “*Prediction of Galloping of Transmission Line Conductors by a Computational Aeroelastic Approach*”. McGill University, Montreal, Canada, 2014.
- [16] Lars Davidson, “*An Introduction to Turbulence Models*”. Department of Thermo and Fluid Dynamics in CHALMERS UNIVERSITY OF TECHNOLOGY, Goteborg, Sweden, 2018.
- [17] Unige, “Turbulence and CFD models: Theory and applications”. Dicat, Unige.
- [18] Wikipedia, “*Law of the Wall*”, https://en.wikipedia.org/wiki/Law_of_the_wall.
- [19] Physics, “*Physics stack exchange*”, <https://physics.stackexchange.com>.
- [20] T. Andrienne, “*Aeroelasticity & Experimental Aerodynamics, Lecture 7 – Galloping*”. University of Liège, Belgium, 2015.
- [21] H. M. Irvine and T. K. Caughey, “*The Linear Theory of Free Vibrations of a Suspended Cable*”. Department of Civil Engineering, University of Auckland, New Zealand, 1974.
- [22] Edutecnica, Meccanica, <https://www.edutecnica.it/meccanica/ela/ela.htm>.
- [23] Han Yuan, “*Static and dynamic stiffness analysis of cable-driven parallel robots*”. Mechanical engineer. INSA de Rennes, 2015.

- [24] Shoei-Sheng Chen, “*Flow-Induced vibration of circular cylindrical structures*”. ARGONNE NATIONAL LABORATORY, South Cass Avenue Argonne, Illinois, 1985.
- [25] Yogeshkumar M. Desai, “*Modelling of planar transmission line of Galloping*”. Department of Civil Engineering University of Manitoba. Vinnipeg, Manitoba, 1991.
- [26] Haym Benaroya and Rene D. Gabbai, “*Modelling vortex-induced fluid–structure interaction*”. Department of Mechanical and Aerospace Engineering, Rutgers University. New Brunswick, Gaithersburg, USA, 2007.
- [27] Bert Blocken, Ted Stathopoulos, Jan Carmeliet, Jan Hensen, “*Application of CFD in building performance simulation for the outdoor environment: an overview*”. Journal of Building Performance Simulation, 2011.
- [28] Bakker A. (2008) Lectures on Applied Computational Fluid Dynamics. www.bakker.org
- [29] Zienkiewicz O.C., Taylor R.L., “*The Finite Element Method – Volume 3: Fluid Dynamics*”. Woburn Massachusetts, 2000.
- [30] Umberto Cian, “*Analisi dinamica di un disco palettato di turbina con smorzamento per attrito*”. DIPARTIMENTO di INGEGNERIA MECCANICA e AEROSPAZIALE, Torino.
- [31] Petrosino Francesco, “*Analisi numerica delle forze aerodinamiche su configurazioni aeronautiche*”. Dipartimento di Ingegneria Aerospaziale, Università degli Studi di Napoli Federico II, Italy. 2008.
- [32] Sighard F. Hoerner, “*Fluid-Dynamic Drag*”. American Institute of Aeronautics and Astronautics (AIAA). New York, United States of America, 1965.
- [33] C. Borri and S. Pastò, “*Lezioni di ingegneria del vento*”. Firenze University Press, Università degli Studi di Firenze, Italy, 2006.
- [34] Holland H. Farr, “*Transmission Line Design Manual*”. DEPARTMENT OF THE INTERIOR, Water and Power Resources Service. Denver, Colorado, United States, 1980.

- [35] A. Guell, “*Mechanical Stresses in Transmission Lines*”. University of Illinois, Engineering Experiment Station. Urbana, Illinois, 1912.
- [36] M. Bozza, “*Introduzione all’analisi non lineare delle strutture*”. Copyright © ADEPRON.
- [37] Thiago B. Carlos and Joao Kaminski Jr., “*Dynamic response due to cable rupture in a transmission line guyed towers*”. Department of Civil Engineering, University of Coimbra and University of Santa Maria, Portugal and Brazil. 2017.
- [38] Saif Haddadin, Haitham Aboshosha, Ayman M. El Ansary, Ashraf A. El Damatty, “*Sensitivity of wind induced dynamic response of a transmission line to variations in wind speed*”. Western University, Canada. 2016.
- [39] Eurocode 1, “*Basis design and action on structures*”. Part 2-4: «Wind action». ENV 1991– 2 – 4, – CEN, 1994.
- [40] Solidworks, <http://help.solidworks.com/2014/Italian>.
- [41] Marco Onore, “*Smorzatore Stockbridge e soppressione delle vibrazioni dei cavi tesi: analisi numerica e sperimentale*”. Politecnico di Torino, Dipartimento di Ingegneria Meccanica. Torino, 2018.
- [42] Marco Buscemi, “*Studio di un sistema di controllo attivo per la riduzione delle vibrazioni nelle linee aeree di trasmissione dell’energia elettrica*”. Politecnico di Milano, Dipartimento di Ingegneria dell’Automazione. Milano, 2016.
- [43] A.M. Belostotsky, I.N. Afanasyeva, I.Yu Lantsova, S.O. Petryashev, N.O. Petryashev, “*Estimation of aerodynamic instability of building structures*”. *Procedia Structural Integrity*, Research Institute of Building Physics of the Russian Academy of Architecture and Construction Science. Russia, 2017.